Nearshore Mixing due to the Effects of Waves and Currents

By

Soroush Abolfathi

A thesis submitted in partial fulfilment of the requirements for the degree of Doctor of Philosophy in Engineering

University of Warwick, Department of Engineering

July 2016

CONTENTS

LIST OF FIGURES

LIST OF TABLES

DEDICATION

I would like to dedicate this thesis to my beloved parents, Ali and Nasrin for their unconditional love and for their selfless and invaluable support throughout my course of study.

ACKNOWLEDGEMENTS

The completion of this doctoral thesis would not have been possible without the guidance and support of the kind people around me. Above all, I would like to thank my family for their unconditional support over the past years.

This work would not have been possible without the help, invaluable criticism and advice of my principal supervisor, Dr. Jonathan Pearson, not to mention his valuable knowledge and expertise in the field of coastal engineering. I would like to thank Dr. Pearson for his willingness to spend much time supervising this project. Thank you for keeping me going when times were tough. Also, I must express my gratitude to my co- supervisor, Professor Ian Guymer for his invaluable support, scientific advice and encouragement throughout my time at Warwick.

I am indeed grateful to School of Engineering, University of Warwick for offering me a Ph.D. Scholarship which provided me with the financial support.

The great advice, support and patience of Dr. Petr Denissenko, has been invaluable on the technical side of this project, for which I am extremely grateful. Last, but by no means least, I would like to thank Dr. Jop Velaskomp and Mr. Ian Baylis for their help and patience with the experimental part of this study. Also, I would like to thank Dr. Andrew Bishop for all the entertainment that he provided during our time in D030 and for delaying my PIV experiments.

DECLARATION

I hereby declare that this thesis is all my own work except where I have otherwise stated and that this thesis has not been submitted for a degree at any other University.

Soroush Abolfathi

July, 2016

CONTRIBUTIONS TO KNOWLEDGE

Peer Reviewed conference proceedings.

1. ABOLFATHI S., PEARSON J. M., 2014. Solute dispersion in the nearshore due to oblique waves. Proc. of Coastal Eng. 1(34).
2. ABOLFATHI S., PEARSON J. M., 2016. A Lagrangian Particle-based models in Nearshore Mixing: A comparison to Laboratory Data, Proc. of Coastal Eng. (Accepted, In press)

Conferences

1. ABOLFATHI S., PEARSON J. M. & GUYMER I., 2014. Modelling mixing mechanisms in the nearshore. International Association of Hydro-Environment Engineering & Research, Coventry, UK. [Oral & Poster presentation]
2. ABOLFATHI S., PEARSON J. M. & GUYMER I., 2014. Pollution at the seaside: Mixing due to the effects of waves and currents. YCSEC (10), Cardiff, UK. [Best presentation prize, considered for publications in Journal of Maritime Eng., ICE]
3. ABOLFATHI S., PEARSON J. M., 2014. Solute dispersion in the nearshore due to oblique waves. International Conference on Coastal Engineering, ASCE, Seoul, South Korea. [Oral presentation]

Prizes and awards

- Young Coastal Scientist Award, YCSEC (2014)
- Travel Grant, School of Engineering, the University of Warwick (2014)
- Research Consumable grant, School of Engineering, the University of Warwick (2013)
- Victoria Fernandez Scholarship, the University of Warwick (2012)

NOTATION

Lower case

a	wave amplitude [m]
b	local dispersion coefficient [m^2/s]
c	concentration of diffusant [ml/l]
d	total water depth [m]
d_{tr}	depth to wave trough level [m]
e_m	molecular diffusion coefficient [m^2/s]
e	diffusion coefficient [m^2/s]
e_{wf}	turbulent diffusion generated by oscillatory wave motion [m^2/s]
g	gravitational constant = 9.81m/s^2 [m/s^2]
g	Group velocity [m/s]
k	wave number $2\pi/L$ [m^{-1}]
k_x	longitudinal dispersion coefficients [m^2/s]
k_y	transverse dispersion coefficients [m^2/s]
l	length [m]
m	beach slope
n	dimensionless ratio of wave group velocity to wave phase velocity
q	fractional thickness
q_w	maximum orbital velocity [m/s]
R^2	least-squared linear regression coefficient
s_o	bed slope
t	duration or time [s]
u	velocity in x-direction (varying with time) [m/s]
u_s	surface velocity in x-direction [m/s]
u_*	local bed shear velocity in x-direction [m/s]
v	velocity in y-direction (varying with time) [m/s]
v_*	local bed shear velocity in y-direction [m/s]
v_+	temporally averaged velocity in crest-trough level [m/s]
v_-	temporally averaged undertow velocity[m/s]
v_a	mean amplitude velocity [m/s]
w	velocity in z-direction (varying with time) [m/s]
x	horizontal distance, in direction of wave propagation [m]
y	horizontal distance, perpendicular to x, lateral direction [m]

z vertical distance, origin at water surface [m]

z_o bottom roughness parameter [m]

z_δ displacement parameter [m]

Upper case

A total cross-sectional area [m^2]

B diffusion velocity [m/s]

B_b breaker coefficient

C velocity of wave propagation (celerity) [m/s]

C Chezy bed frictional coefficient [$m^{1/2}$/ s]

D shear dispersion coefficient [m^2/s]

D_b wave energy dissipation per unit area

E overall mixing coefficient [m^2/s]

E total wave energy [J]

F fluorescent intensity

H wave height – distance from crest to trough [m]

Hs significant wave height [m]

J diffusive flux [m/s]

I temporal wave-averaged momentum [kg/m s]

K reflection coefficient

K_e turbulent kinetic energy [m^2/s]

L wave length [m]

L_m length scale [m]

N arbitrary constant

P non-dimensional parameter

P wave power per unit crest length [kW/m]

Q mass of tracer [kg]

Q_b fraction of the breaking waves

R_w dimensionless wave parameter

Re Reynolds number

S radiation stress [N/m^2]

T wave period [s]

T_s significant wave period [s]

V temporally averaged (over wave cycle) drift velocity [m/s]

Y_b surfzone width [m]

W local wind speed [m/s]

Greek Letters

γ	breaker depth index
δ	wave steepness = H/L
η	vertical displacement of water surface from mean surface elevation at $z = 0$ [m]
κ	von Karman universal constant
λ_a	relative acceleration threshold
μ	dynamic viscosity [kg/m s]
μ	position of centroid [m]
ν	kinematic viscosity [m^2/s]
ν_t	eddy viscosity [m^2/s]
ϑ	coefficient of proportionality
θ	angle [degree]
ϕ	Vertical distribution function
π	3.1416
ρ	fluid density [kg/m^3]
σ	standard deviation
σ^2	spatial variance [m^2]
τ	viscous shear stress [N/m^2]
τ_o	bed shear stress [N/m^2]
ω	wave angular frequency $=2\pi/T$ [s^{-1}]

Subscripts

+	onshore direction
-	offshore direction
b	breaking conditions
c	current
d	spatially depth averaged
i	oscillatory flow
o	deep water conditions
os	oscillatory flow
t	turbulent property
tc	tidal current
T	total
w	wave
x	longitudinal direction

y	transverse direction
z	vertical direction

Other notation

u'	e.g. u prime, denotes turbulent fluctuation of velocity
$\overline{u}$	e.g. u bar, local time average of velocity

GLOSSARY

ADV	Acoustic Doppler Velocimetry
BC	Boundary Condition
CFD	Computational Fluid Dynamics
EFG	Element Free Galerkin
FD	Finite Difference
DEM	Discrete Element Method
FEM	Finite Element Method
FLIC	FLuid-In-Cell
FOV	Field Of View
FPS	Frame Per Second
FVM	Finite Volume Method
LBE	Lattice Boltzmann Equation
LDA	Laser Doppler Anemometry
LDV	Laser Doppler Velocimetry
MAC	Marker-And-Cell
MLPG	Meshless Local Petrov-Galerkin
MLS	Moving Least Square
MPM	Meshfree Particle Methods
MWS	Mesh-free Weak-Strong form
PDE	Partial Differential Equation

PIC	Particle-In-Cell
PIM	Point Interpolation Method
PIV	Particle Image Velocimetry
PPM	Part Per Million
PPB	Part Per Billion
RMS	Root Mean Square
SF	Scale Factor
SPH	Smoothed Particle Hydrodynamics
SWL	Still Water Line
TKE	Turbulent Kinetic Energy
WCSPH	Weakly Compressible SPH

ABSTRACT

Analytical, experimental and computational studies were carried out to investigate the mixing and dispersion of neutrally buoyant tracer in the nearshore region due to the effects of waves and currents. The main objective of this study was to quantify the mixing processes in the nearshore region.

Theoretical approaches were developed to quantify the contribution of diffusive and dispersive mixing in the nearshore due to wave activity. An analytical model was developed to quantify the diffusive and dispersive mixing mechanisms based on mathematical solutions for the advection-diffusion equation.

Mixing under the combined effects of waves and currents were studied through measurement of hydrodynamic and fluorometric tracing experiments from a large-scale facility at the Danish Hydraulic Institute, Denmark. The experiments were conducted in a shallow water basin for a range of hydrodynamic conditions covering wave steepness between 2 – 5%. Data from detailed measurements were used to examine the spreading of a solute inside the surf zone and seawards of the breaker region. The overall depth-averaged on-offshore mixing coefficient obtained from the hydrodynamic experimental studies were compared to the mixing coefficients determined from the tracer measurements. It was shown that inside the surfzone, the shear dispersion is the dominant mixing factor, which is almost an order of magnitude greater than the diffusive mixing. The location of the breaker point and the wave height across the nearshore is shown to be important for determining the mixing coefficient.

Further detailed spatial and temporal variations of flow hydrodynamics across the nearshore were investigated through a series of laboratory experiments with the use of Particle Image Velocimetry. The experiments were undertaken in a dedicate wave flume at the University of Warwick. Through analysis of the PIV data, new information on the spatial variation of diffusion and dispersion in the shallow water column of the nearshore region was obtained. Flow visualisation of the PIV results identified three distinct hydrodynamic processes during the bore, undertow and the bore/undertow interaction, which were the primary mixing mechanisms in the nearshore region. The temporal variation of dispersion coefficient shows that intense shearing mechanisms exist during wave bore/undertow interactions.

The numerical capabilities of Smoothed Particle Hydrodynamics, a Lagrangian, meshless, particle-based method in modelling the nearshore hydrodynamics were explored in this study. The numerical data was used to quantify the mixing processes.

By using suitable estimates of turbulent diffusion and cross-shore wave-induced velocity, a theoretical approximation of the overall mixing within the surfzone and seaward of the breaker region can be obtained. A comparison between the theoretical model and previous laboratory and field studies on the nearshore mixing suggests that the mixing is proportional to wave height ($H^{1.5}$). It is demonstrated that inside the surfzone, the mixing is dominated by the vertical structure of the cross-shore velocity.

The pioneering Royal society works of Svendsen & Putrevu (1994) identified the temporally-averaged dispersion, as a function of distance from the shore. Using a combination of experimental, mathematical and numerical formulations, this study has identified and quantified for the first time, the temporal and spatial dispersive mixing processes in the nearshore (over the full wave cycle), within the challenging and complex environment of the surf zone. It has been shown that the cross-shore circulation provides lateral mixing that exceeds that of the turbulence by an order of magnitude inside the surfzone. The turbulence still remains an essential part of the flow since it is the primary driver which through the vertical mixing is responsible for defining the vertical velocity profiles, which then determine strength of the dispersion.

"When I meet God, I am going to ask him two questions: Why relativity? and why turbulence? I really believe he will have an answer for the first."

Werner Heisenberg

CHAPTER 1

INTRODUCTION

1.1 Synopsis

The nearshore zone experiences pollutant loading through both the shoreline and seaward boundaries. From the seaward boundary, pollutant loading is transported landward towards the surfzone by the so-called Stokes drift effect (Stokes, 1847). From the shoreline boundary, runoff pollution, which can contain faecal indicator bacteria and human viruses (Schiff *et al*., 2003) can drain into the surfzone. Consequently, pollution can congregate in the nearshore region, and as such, the water quality can affect the health of the general public who frequent beaches and thus is seen as a global problem (e.g. over a million beachgoers visit Santa Monica Bay beaches on a typical summer weekend – Schiff *et al*., 2003). However, the key mass exchange processes related to the pollutant transport and dilution within the nearshore water body are still not fully understood.

Coastal recreational waters should comply with the appropriate water quality standards. In Europe, these standards are defined by the updated EU Bathing Waters Directive (2006/7/EC). The updated directive includes a tightening of water quality standards and the requirement to provide information about bathing waters to the public. This necessitates those responsible for coastal recreational areas to implement pollution management plans. The World Health Authority (1998) reports on 22 worldwide studies that confirm a link between faecal indicator bacteria in recreational water and 'adverse health outcomes'. The nearshore zone is an area of high amenity value and therefore, there is a strong need to manage the conflicting demands of waste management, recreation and fisheries (Dixon, 2012; Rippy *et al*., 2013).

The nearshore zone is subject to a combination of both wave and longshore currents. This results in a complex three-dimensional flow field which is affected by the surface and bed generated turbulence, orbital motions of the wave, spatial variation of flow depth and vertical and transverse shear effects caused by longshore currents activities.

Although several field and laboratory studies have been undertaken to understand the mixing processes within the nearshore zone, quantifying all associated parameters are challenging due to the measurement limitations in this region. This project is specifically focussed to improve understanding and technical descriptions of the dispersal of neutrally buoyant pollutants. Through a range of theoretical, experimental and numerical investigations, the mixing processes under a range of wave-only and wave-current conditions are quantified.

1.2 Aims and Objectives

There have been comparatively few studies [Pearson *et al*., 2002 and 2009; Feddersen, 2006; Clark *et al*., 2010] to investigate aspects of mixing under waves and currents in the nearshore zone. Few field studies have been undertaken using tracers. However, the lack of detailed hydrodynamic data has made it difficult to interpret the mixing processes. Bowen and Inman (1974) suggested that seaward of the breaker region, the turbulence generated by waves is small compared to the current-generated turbulence. Svendsen and Putrevu (1994) performed a numerical study and proved that the cross-shore current generated by wave activities dominated the transverse mixing. They suggested that cross-shore currents could exceed the contribution of the mixing caused by turbulent activity by an order of magnitude. However, there was only little data available to fully validate their findings. This brief review suggests that although advances have been made in understanding the mixing processes, still little hydrodynamic and fluorometric data is available.

The objectives of this study are to elucidate the underlying mechanisms that leads to the mixing of neutrally buoyant pollutants in the coastal waters under different hydrodynamic conditions and to quantify those mixing mechanisms inside the surfzone as well as seaward of the breaker region, by use of experimental and numerical studies. In addition, this project aims to identify the current lack of knowledge in the theoretical modelling of wave mixing in the coastal region by identifying and studying those effective mechanisms in the nearshore, in order to provide a better understanding of the underlying physics of solute mixing and transport in coastal waters. The specific objectives of this research work are as follows:

1. To develop a theoretical approach for quantifying wave mixing parameters in the nearshore region.

2. To study mixing of buoyant pollutant under wave-current conditions for the first time, by critically analysing hydrodynamic and fluorometric data from large scale laboratory measurements, undertaken in shallow water basin of Danish Hydraulics Institute, Denmark in 2005 (Pearson *et al*., 2006). The data collection study measured a range of wave steepness and the dataset was used to examine the associations between the proposed theoretical mixing mechanisms with measured hydrodynamics and fluorometric data, identified in this study. Specifically to determine:

   a. The overall mixing coefficient from analysis of the fluorometric data.

   b. The Turbulent Kinetic Energy (TKE) and turbulent diffusion coefficient (e_y) for the hydrodynamic data.

   c. The overall shear dispersion coefficients (D_y) for the hydrodynamic data.

3. To measure detailed spatial and temporal variation of flow hydrodynamics across the nearshore region under a range of wave conditions, using Particle Image Velocimetry (PIV). Specifically to determine:

a. The temporal and spatial variation of diffusion coefficients across the nearshore

b. The temporal and spatial variation of dispersion coefficient across the nearshore

4. To validate the proposed theoretical model and mixing parameters with the state-of-the-art Lagrangian meshless particle-based numerical approach, developed within this study.

1.3 Overview of the Thesis Structure

This thesis comprises seven chapters:

- In Chapter 2 (Background theory and previous work), an overview of nearshore hydrodynamics and mixing under the effects of waves and currents is presented. A detailed review of the published literature on the fundamental theories and the previous work on different aspects of mixing in the nearshore is presented.

- In Chapter 3 (Theoretical approach), a theoretical approach is developed to quantify the nearshore mixing under different hydrodynamic conditions.

- In Chapter 4 (Mixing under combined effects of waves and currents – laboratory measurements and analysis), the large-scale laboratory study of mixing due to the combined effects of waves and currents is presented. This chapter analyses the data collected at Danish Hydraulic Institute (DHI) in 2005. The mixing due to the effects of waves and currents is quantified on the basis of the methodology postulated in Chapter 3.

- Chapter 5 (Hydrodynamic measurements) presents the results of the laboratory measurements performed in the Warwick University wave flume. The experiments were carried out to measure the hydrodynamic field in the nearshore region using Particle Image Velocimetry. The experiments presented in this chapter cover hydrodynamic conditions similar to the DHI experiment (Chapter 4). The hydrodynamic flow field obtained from the PIV measurements is utilized to demonstrate a revised mixing mechanisms which are present within a wave cycle. This provides an improved understanding of mixing processes in the nearshore due to the turbulence and shear dispersion.

- In Chapter 6 (Numerical approach), Lagrangian particle-based, Smoothed Particle Hydrodynamics (SPH) capabilities are employed to model the hydrodynamic behaviour of the flow in the nearshore region. This section covers the methodology of SPH numerical methods, the modelling procedures and application of SPH in quantifying the mixing mechanisms.

- Chapter 7 (Conclusions) of this thesis is devoted to the overall discussions and conclusions. In this chapter, the main findings and outcome of the work are discussed and the conclusions are explained.

CHAPTER 2

BACKGROUND THEORY AND PREVIOUS WORK

2.1 Synopsis

This chapter discusses nearshore hydrodynamics and its influence on the mixing in the nearshore due to the effects of waves and currents. The governing equations and underlying concepts are reviewed and discussed to understand the mixing and dispersion mechanisms in the nearshore environment. A detailed review of the previous theoretical, experimental and numerical studies conducted on mixing, dispersion and diffusion is discussed.

2.2 Nearshore Hydrodynamics

Nearshore hydrodynamics is a highly intricate topic in the field of coastal engineering that addresses waves and wave generated phenomena within the nearshore region. Waves breaking on a sloping beach near to the shoreline can release large amounts of energy which is predominantly expressed as turbulence in the water column (Svendsen & Putrevu, 1994). As waves approach the shore, the wave height and the wave momentum will reduce, while the wave interactions with the bottom topography significantly increase due to frictional effects. This transfer of momentum instigates the formation of longer period waves and currents (Svendsen & Putrev, 1996) that ultimately drive processes such as mixing and dispersion within the surf zone.

Detailed analysis of surf zone hydrodynamics requires a comprehensive understanding of the wave driving and breaking mechanisms. Understanding the hydrodynamic processes which lead into generation and dissipation of turbulence in the nearshore are key to solving complicated coastal and ocean problems. §2.2.1 - §2.2.4 will describe the key concepts of the nearshore hydrodynamics and wave/current systems.

2.2.1 Wave Energy

Coastal processes are mainly influenced and derived by the energy of the incident waves in the surfzone. Airy theory (1845) describes the energy of a wave, based on the displacement of water particles due to the wave motion. Airy (1845) theory states that as a wave passes through a point the particles in that location will be displaced, moving through an orbit that is dependent on water depth, before returning to their original position and hence not resulting in a net displacement of mass. The shape of the orbital path traversed by a particle varies with water depth, it has circular path offshore, while elliptical in shallow water. The wave energy could be defined as the sum of its potential and kinetic energies. The potential energy of a wave is a function of the variation in the free surface elevation of the water body due to the motion of the wave whilst the kinetic energy is derived from the orbital motion of the particles under the wave (Komar, 1998). In order to derive total energy density of waves, these factors should integrate over the wave length (Eq. 2.1).

$$E = \frac{1}{L}\int_0^L\int_0^\eta (\rho g z)dzdx + \frac{1}{L}\int_0^L\int_0^{-h}\frac{1}{2}\rho(u^2+w^2)dzdx \qquad (2.1)$$

where L is wave length, η is water surface elevation. Wave energy density E, will not remain constant while it travels towards the shallow water region and consequently breaks. Equation 2.1 indicates that energy density is very dependent on the wave height, which varies significantly during transition from offshore region towards the surfzone. The energy flux P, is the total energy of the wave which follows the laws of conservation of energy and opposed to the energy density E within the wave (Eq. 2.2).

$$P = ECn = EC_g \qquad (2.2)$$

where C represent the celerity, C_g is the group velocity and n is a dimensionless ratio of wave group velocity to wave phase velocity. The value of n varies between ½ in deep water and one in shallow water. P indicates the wave power per unit crest length and is useful as it is not susceptible to variation in the manner that E is, as the wave front approaches towards the beach (Komar, 1998).

2.2.2 Mass Transport and Momentum

One of the key flaws in the linear Airy theory is the assumption of particle motion in a closed circular or elliptical orbit. This assumption does not take into account the mean motion of the water in the surfzone towards the shoreline (Dean & Dalrymple, 2002). The elliptical particle orbits, actually involve a net shoreward progression in the nearshore region and therefore the particle motion path is not a closed loop. Mass transport towards the shoreline can be estimated according to equation 2.3.

$$M = \frac{1}{t_2 - t_1} \int_{t1}^{t2} \int_{-h}^{\eta} \rho u(x,z) dz dt \tag{2.3}$$

Dean & Dalrymple (2002) pointed out that evaluation of M for the mean water surface level will be zero. Equation 2.3 clearly shows that the mass transport in the direction of wave propagation is non-linear. Also, it shows that the mass transport of the waves with a higher energy content will be higher. Mass transport always has momentum associated with it, which could be defined according to equation 2.4.

$$M = \frac{1}{t_2 - t_1} \int_{t1}^{t2} \int_{-h}^{\eta} ((\rho u)u) dz dt \tag{2.4}$$

The transfer of momentum through the wave breaking process results in a force known as radiation stress (§2.2.3).

2.2.3 Radiation Stress

Longuet-Higgins and Stewart (1964) demonstrated radiation stress and defined it as the 'excess flow of momentum due to the presence of waves'. The occurrence is due to a large forward flux of momentum under the wave crest that is not balanced by the backward transport of momentum under the trough (Svendsen & Putrevu, 1994). Longuet- Higgins and Stewart (1964) designated the radiation stress as the sum of the momentum flux and the dynamic pressure. The dynamic pressure is calculated as the difference between the hydrostatic pressure and the absolute pressure and is used to ensure that the momentum being assessed is due solely to the presence of waves (Komar, 1998).

$$M + \frac{1}{2}\rho g h^2 = S_{xx} + \frac{1}{2}\rho g(h + \bar{\eta})$$
$$S_{xx} = E[\frac{kh}{\sin(kh)}] \tag{2.5}$$

The radiation stress is denoted by S_{xx}, the x axis is placed in the direction of wave advance whilst the y axis is parallel to the breaker line, $\bar{\eta}$ is the mean water level set-down in the trough offshore from the breaker line.

2.2.4. Currents

Nearshore currents are primarily driven by waves that are incident on the coastal region; however, tidal fluctuations and winds blowing in the longshore direction can also influence current magnitudes (Komar, 1998). The study of currents in the coastal region is a key concept in the determination of transport, mixing and dispersion of pollutants in the nearshore, as they could have direct impact on these processes. The total current in the nearshore zone can be represented as the sum of a number of forcing mechanisms, each acting on different scales, as shown in equation 2.6.

$$u = u_w + u_{tc} + u_b + u_{os} + u_i \tag{2.6}$$

The above equation represents the steady current u as the sum of the breaking waves action u_b, currents driven by strong local winds u_w, tidal current u_{tc}, infra-gravity waves u_i and oscillatory flows due to wind driven waves u_{os} (US Army Corps, 2002).

Nearshore currents are separated conceptually into two key classifications based on temporal and spatial variability. Quasi-steady currents are relatively stable in a temporal and spatial sense. They exist for extended periods of time and display nett long-term average velocities (Johnson, 2004). In contrast, a large number of variable nearshore currents also exist. These are characterised by shorter periods and a high degree of spatial and temporal variability, and thus they are associated with zero long term mean flows (Johnson, 2004).

There are two primary quasi-steady current systems, the first of which is the longshore currents and the second one is the rip currents. Longshore currents propagate parallel to the shore in the nearshore zone and are driven by waves approaching the shoreline at an oblique angle. The nearshore current system developed by obliquely incident waves is shown in Figure 2.1.

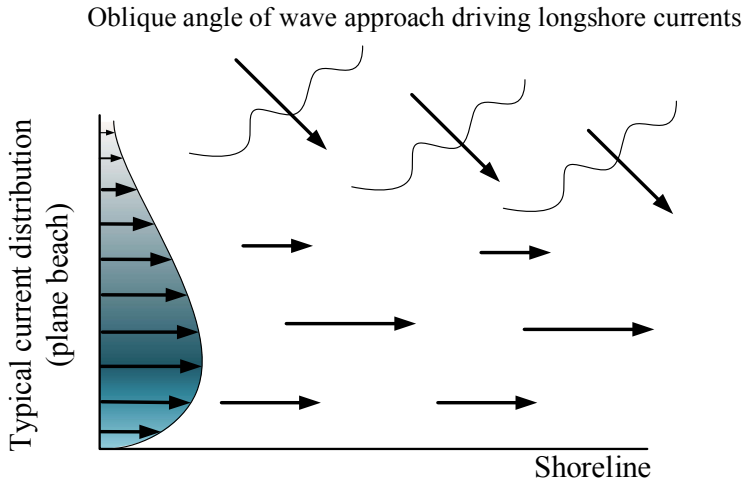

Figure 2.1 – Schematic of current pattern observed in the nearshore region under obliquely incident wave conditions

The longshore current (Fig. 2.1) is generated by changes in the momentum flux of the wave field in the alongshore direction, resulting in a transfer of momentum from the wave field to the mean longshore current (Johnson, 2004).

Rip currents are also classed as quasi-steady currents. Rip currents are strong, narrow offshore directed flows that pass through the surf zone often carrying sediment and debris that discolours the water compared to adjacent areas (Komar, 1998; Brander 1998, Short 1985). Rip currents are formed primarily due to longshore variations in radiation stress, the resulting imbalance of which between the free surface set-up and the radiation stress induces a region of narrow offshore directed flow. Figure 2.2 shows schematic of features driving rip current flow in the nearshore region, resulting in a nearshore circulation cell. Nearshore circulation cells are constrained within the surf zone, however their lengths are variable, with the spacing between rip

features ranging from one to eight times the width of the surf zone (Inman *et al*., 1971). Nearshore circulation cells are responsible for a continuous flow of water between the surf zone and the offshore zone and act as distributing mechanisms for contaminants present within the surf zone (Inman *et al*., 1971).

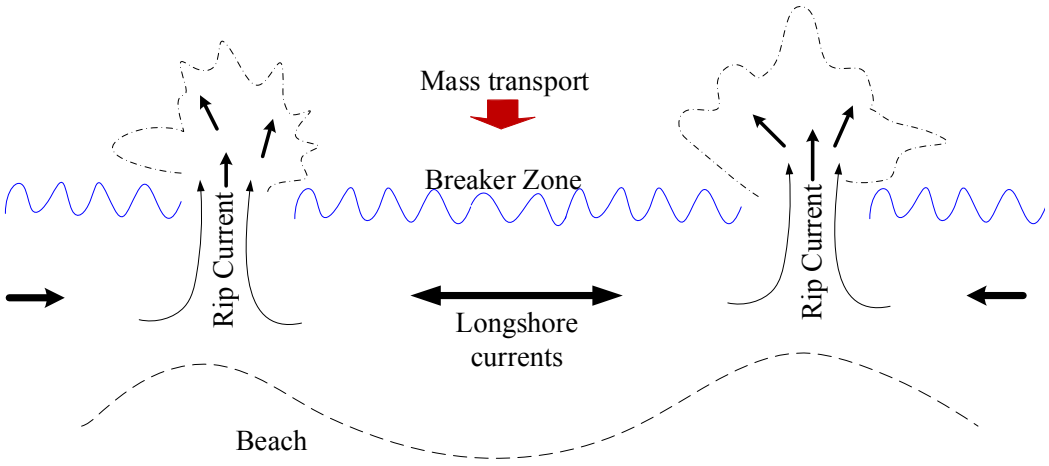

Figure 2.2 – Schematic sketch of a nearshore circulation cell

Variable currents are one of the nearshore circulation mechanisms which display flow with frequencies lower than the incident wave climate, but with a higher level of variability than the quasi-steady currents active in areas which are restricted by the incident wave climate and or topography (Svendsen, 2005). There are two classes of variable nearshore waves; infragravity waves and shear waves.

Infragravity waves are oscillations in the water level within the surf and swash zones that occur due to long period variations in the wave set-up caused by the passage of wave groups. A variety of energetic infragravity waves exist within the nearshore zone with periods of between 20 and 200 seconds including edge waves and surf beat (Johnson, 2004; Olsson, 2004; Svendsen & Putrev, 1996). Long period infragravity waves generally form standing waves on sloped beaches due to their low wave steepness (Horikawa, 1988).

Shear waves are another infragravity effect that can influence the magnitude of longshore currents. Shear waves are low frequency, wave like oscillations of longshore currents with periods and wavelengths of 100 seconds and 100 metres

respectively (Svendsen & Putrev, 1996). They are driven by the incidence of large waves upon the shoreline causing an oscillation in the velocity of flow within the longshore at a low frequency (Dean & Dalrymple, 2002). Shear wave motion relies on the action of cross-shore shear as a restoring force rather than gravity (Bowen & Holman, 1989; Dean & Dalrymple, 2002). This motion occurs in the horizontal plane and causes the longshore current to move back and forth across the surf zone. The total velocity variance in the longshore current due to the action of the shear waves can exceed that due to other infragravity effects such as edge waves or surf beat (Howd *et al*., 1991; cited in Johnson, 2002). It has also been suggested by Kirby *et al*. (1998) that resonant interactions may exist between shear waves and the other infragravity effects.

2.3 Mixing and Dispersion Transport Processes in the Nearshore

Mixing and dispersion are key transport processes within coastal waters and the surf zone. They are critical parameters to consider when investigating the ability of coastal waters to receive and dilute discharged material (List *et al*., 1990).

The energy required for driving mixing and dispersive processes in the nearshore region is derived primarily from wave action incident on the shore as well as wind and coastal currents (Inman *et al*., 1971). Within the surf-zone, waves interact with currents and other waves, which results in two well-defined mechanisms that drive mixing. The first of these is the turbulence generated from the breaking wave which drives rapid mixing along the path of the wave bore in an onshore direction. Secondly, wave-current interactions drive advective transport in both the alongshore and cross-shore directions forming circulative cells, these interactions are complex and are known to involve low frequency fluctuations (Oltman-Shay *et al*., 1989) of the current field and circulation through the vertical plane driving horizontal momentum mixing (Svendsen & Putrev, 1994; Takewaka *et al*., 2003). Circulative cells (see Fig. 2.2) consisting of longshore currents and seaward flowing rips are

responsible for a continuous interchange of water between the nearshore and offshore regions. As such they are key dispersal mechanisms for material injected into the surf zone. The intensity, frequency and direction of the incident wave climate, as well as the dimensions of the nearshore circulatory cells, have been found to be key variables impacting on the nearshore mixing processes (Inman *et al*., 1971).

The terminology used to describe mixing and dispersion in this research are defined according to Fischer *et al.* (1979). Some of the key mechanisms and their definitions are listed below:

- Mixing: Any process that leads to one parcel of water becoming intermingled with, or diluted by another, referring specifically to the action of dispersion and diffusion.
- Dispersion: The process of scattering particles or a cloud of contaminants through the combined effects of shear and transverse diffusion.
- Diffusion (Turbulent): The random spreading of particles through turbulent motion. Turbulent diffusion is considered to be somewhat analogous to molecular diffusion; however the scales of motion, described by 'eddy' diffusion coefficients, are significantly larger.
- Diffusion (Molecular): Refers to the scattering of particles through random molecular motion. This is described by Fick's Law of diffusion (Eq. 2.7), where q represents the solute mass flux, c is the mass concentration of a diffusing solute and υ is the co-efficient of proportionality also known as the molecular diffusivity.

$$q = -\upsilon \frac{\delta c}{\delta x} \tag{2.7}$$

- Advection: transport due to an imposed current system, including quasi-steady and variable currents in the nearshore region.
- Shear: The advection of fluid at varying velocities at different positions. Shear occurs in changes in current velocity and direction with depth in complex estuarine and coastal flow regimes.

2.4 Theory of Mixing

In this section, the role of molecular diffusion within aqueous related studies is considered, initially in a stationary fluid, and then examined whilst moving. The diffusion is modelled using a concentration gradient process based on an analogy to Fick's (1855) first Law. As pointed out by Fischer *et al.* (1979), molecular diffusion when considered by itself in hydraulic related studies is insignificant, and in many laboratory and field studies is assumed to be negligible. However, the mixing enhanced by other additional processes is considered to strongly resemble molecular diffusion albeit on a larger scale.

2.4.1 Molecular (Fickian) Diffusion

Consider a small parcel of neutrally buoyant tracer placed in still water, a large distance from any boundaries. With time the tracer spreads slowly and equally in all directions. The spreading of the tracer is known as molecular diffusion and results from the random molecular motion occurring within the fluid, the so-called Brownian motion effect, first observed by the botanist Robert Brown and developed statistically by Einstein (1905).

In 1855, Fick reported an analogy which related the molecular diffusion of salt in water to the diffusion of heat along a metal rod, described by Fourier's law of heat flow. Fick's law states:

> *The rate of mass transfer of a diffusion substance through a unit area of an isotropic media is proportional to the concentration gradient measured normal to the section.*

When considered in one dimension, Fick's Law can be described mathematically by

$$J_x = -e_m \frac{\partial c}{\partial x} \tag{2.8}$$

where J_x denotes the rate of molecular transport across the unit area (molecular diffusive flux); c the concentration of the diffusion substance; x the distance normal to the area across which the material is transported; and e_m the molecular diffusion coefficient. The minus sign indicates that diffusion occurs from a region of higher concentration to lower concentration.

Rutherford (1994) pointed out that although Fick's law is based on a hypothesis rather than an actual physical description, empirical studies show that the relationship between the molecular diffusive flux, J_x and the concentration gradient, $\partial c/\partial x$, defined in equation 2.8 are remarkably linear. The molecular diffusion within a fluid is dependent on density and temperature. Typical values of molecular diffusion, determined empirically in water, lie in the range $0.5 - 2.0 \times 10^{-9}\,\mathrm{m^2 s^{-1}}$ (Rutherford, 1994).

Consider a very small parcel of tracer within a fluid, as illustrated in figure 2.3. The control volume has the dimensions $\Delta x, \Delta y \,\&\, \Delta z$; the passage of molecules, or diffusive fluxes, entering the control volume through the boundaries located at x, y, z is given by $J_x, J_y \,\&\, J_z$; and the diffusive fluxes leaving the parcel of fluid located at $x + \Delta x, y + \Delta y \,\&\, z + \Delta z$ are given by $J_{x+\Delta x}, J_{y+\Delta y} \,\&\, J_{z+\Delta z}$. By definition, the mass of tracer, Q within the control volume at time t, may be given by

$$Q_t = c_t \Delta x \Delta y \Delta z \tag{2.9}$$

where c_t = the average concentration within the parcel of fluid at time t.

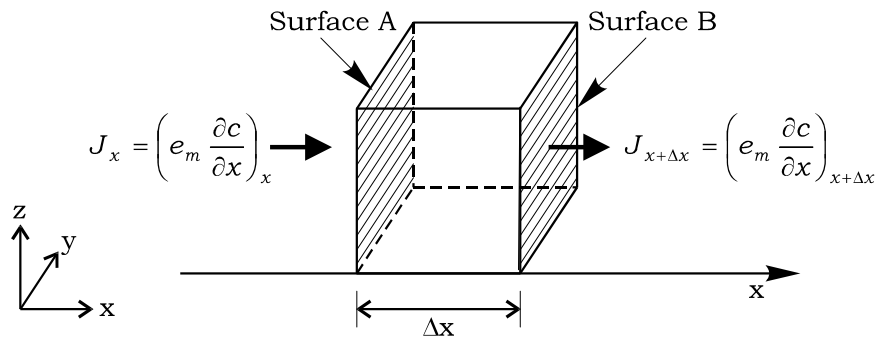

Figure 2.3 – Diffusive fluxes within small control volume of tracer, adapted from Rutherford (1994)

After a small time interval, Δt at time, $t + \Delta t$, let the mass be denoted by $Q_{t+\Delta t}$. By the application of the law of conservation of mass, during the time interval, Δt the rate of change of mass in the control volume may be given by (Rutherford, 1994):

$$\frac{\partial Q}{\partial t} = \frac{Q_{t+\Delta t} - Q_t}{\Delta t} \tag{2.10}$$

By recalling the law of conservation of mass, the passage of molecules into and out of the control volume during the time interval, Δt must equal $\partial Q / \partial t$, thus (Rutherford, 1994):

$$\frac{\partial Q}{\partial t} = (J_x - J_{x+\Delta x})\Delta y \Delta z + (J_y - J_{y+\Delta y})\Delta x \Delta z + (J_z - J_{z+\Delta z})\Delta x \Delta y \tag{2.11}$$

For simplicity, consider the passage of molecules into the control volume in the *x*-direction only. From equation 2.8, the diffusive flux into the control volume, through the surface A, yields $J_x = e_m(\partial c / \partial x)$. Now consider the diffusive flux leaving the control volume through surface B. The diffusive flux, $J_{x+\Delta x}$ can be evaluated by adopting a Taylor's series expansion. By assuming that the time interval, Δt is small, the second and higher order terms can be neglected. This leads to the result (Rutherford, 1994):

$$J_{x+\Delta x} = J_x + \left(\frac{\partial J_x}{\partial x}\right)\Delta x \tag{2.12}$$

Thus, the diffusive fluxes, or the passage of molecules moving into and out of the parcel of tracer can be evaluated (again for simplicity, evaluated in the *x* direction only), by recalling equation 2.8, rearranging equation 2.12 and multiplying each side of the equation by $\Delta y \Delta z$, to yield

$$(J_x - J_{x+\Delta x})\Delta y\Delta z = \frac{\partial}{\partial x}\left(e_m \frac{\partial c}{\partial x}\right)\Delta x\Delta y\Delta z \tag{2.13}$$

Equation 2.9 defines the mass of the tracer within the control volume, it is noted that the volume is constant, thus by adopting equation 2.9 and recalling the law of conservation of mass, leads to the result

$$\frac{\partial Q}{\partial t} = \frac{\partial c}{\partial t}\Delta x\Delta y\Delta z \tag{2.14}$$

So far, consideration of the passage of molecules entering and leaving the control volume has been restricted to the *x* direction only, however the same analytical procedure can be applied to the other two orthogonal directions. Combining equations 2.12, 2.13 and 2.14, and by recalling that in homogenous, isotropic conditions, the tracer spreads equally in all directions, enables the 'classical diffusion equation' to be derived (Rutherford, 1994):

$$\frac{\partial c}{\partial t} = e_m\left(\frac{\partial^2 c}{\partial x^2} + \frac{\partial^2 c}{\partial y^2} + \frac{\partial^2 c}{\partial z^2}\right) \tag{2.15}$$

2.4.2 Advective Diffusion

So far, it has been assumed that the parcel of fluid has been stationary and spreading of the tracer is generated by molecular diffusion alone. In an extension to the previous result (Eq. 2.15), now consider the movement of the control volume in laminar flow, moving at a constant velocity, with velocity components of *u*, *v* and *w* in the *x*, *y* and *z* directions.

In laminar flow it is assumed that the fluid flows in discrete layers, and thus it is assumed that the diffusion occurs as if the fluid were stationary, and that the

diffusion is constant in all directions. The movement or transport of a tracer cloud by an imposed current system is termed advection.

Again for simplicity, consider the passage of the molecules into the moving control volume in the *x* direction (Fig. 2.3). As the control volume is now moving, the rate of mass transport through the control volume is simply the diffusive flux as defined by equation 2.8 plus the advective flux (Fischer *et al*., 1979). The advective flux is the rate at which the imposed current transports the control volume. This rate is defined as the mean concentration within the control volume multiplied by the velocity in the *x*- direction, *u*. Thus, the total rate of mass transport through the control volume in the *x*-direction can be described mathematically by:

$$J_x = \left(- e_m \frac{\partial c}{\partial x} \right) + uc \tag{2.16}$$

Thus by utilising equation 2.16 and adopting the same analytical procedure to describe the mass transport in the other two orthogonal directions, and combining the result derived for stationary conditions (Eq. 2.15), leads to:

$$\frac{\partial c}{\partial t} + u\frac{\partial c}{\partial x} + v\frac{\partial c}{\partial y} + w\frac{\partial c}{\partial z} = e_m\left(\frac{\partial^2 c}{\partial x^2} + \frac{\partial^2 c}{\partial y^2} + \frac{\partial^2 c}{\partial z^2} \right) \tag{2.17}$$

Rate of change of concentration of point	Advection of tracer with fluid	Molecular diffusion

Equation 2.17 is more commonly known as the advection-diffusion equation. In a similar method adopted when the parcel of fluid was assumed to be stationary, equation 2.17 can be solved with suitable initial and boundary conditions together with known instantaneous velocities. In steady laminar flow this can be achieved relatively simply as the instantaneous velocity is constant. However, the advection-diffusion equation is of little direct use in aqueous related studies, as hydraulic flows are rarely laminar. Hence, to solve equation 2.17, requires an estimate of the

molecular diffusion coefficient together with knowledge of the instantaneous velocity vector, which is almost impossible to determine experimentally with sufficient accuracy in both time and space (Holly, 1985).

Thus, the determination of the fundamental advection-diffusion equation (Eq. 2.17) is of little practical use in aqueous related studies, in its present form. However, the mixing enhanced by other processes discussed in §2.4.4, is considered when both averaged spatially and temporally, to strongly resemble the random molecular diffusion albeit on a larger scale.

2.4.3 Turbulence

So far, a parcel of tracer has been considered, initially stationary and then examined whilst moving in laminar flow. The nearshore zone is subject to a combination of wave and longshore current effects. The flows within these areas are turbulent. Thus in this section some features of turbulent flow will be reviewed.

In open channel or pipe flows, in the vicinity of boundaries, as flow velocities increase, the velocity fluctuations change from a relatively simple form of regular sinusoidal movements to highly irregular movements which lead to the formation of large scale flow structures within the flow, or eddies. The eddies are formed in the regions of high velocity gradients, notably in the vicinity of boundaries. This leads to a diverse range of size and frequency of eddy motions throughout the flow.

The exact formation of how a small velocity fluctuation can produce such highly irregular turbulent flow structure of many times the magnitude of the original movement is unclear and is still the subject of current research. Csanady (1973) noted that certain larger eddies increased in magnitude with time and concluded that these larger eddies combined their energy with smaller eddies, which increased the resultant eddy. These large parcels of fluid movement then in-turn displace other fluid which inevitably has to fill the space vacated by the moving eddy. The movement of fluid into the space vacated by the moving eddy then generates additional smaller eddies which increase by combining together and the process

continues until the size of the smallest eddy does not possess enough energy to combine with another eddy, therefore ensuring stability of the velocity movement. Rutherford (1994) referred to previous studies of Fischer *et al*. (1979) and Chatwin & Allen (1985) who in turbulent river flows, suggested the smallest size of eddy to be the order of 10^{-4} to 10^{-3} m. Thus, so far it has been deduced that turbulence in pipe flow or open channel flow, is generated in the vicinity of boundaries. Thus it is expected that, for example in the vertical direction, the eddies cannot grow indefinitely, but are restricted in size to the depth of flow. Without going into further detail within this section, it is noted that turbulent flows are characterised by a diverse and complex number of eddies, of varying size and shape, and moving with differing velocities and direction.

Due to the complexities of turbulent flows, Reynolds defined the turbulent properties of the flow by adopting a statistical approach based on the small scale random particle fluctuations caused by the large scale eddy motion within the flow. Reynolds sought to isolate the velocity fluctuations from advection and derived the Reynolds equations of motion, more commonly known as the Reynolds' Rules of Averaging, given by Holly (1985):

$$u = \bar{u} + u' \tag{2.18}$$

where the $\bar{u}$ is an average of the longitudinal velocity over a representative period of time and u' is the instantaneous local deviation from the mean value. The turbulent intensity, or degree of turbulence within a flow at particular elevation, is given by:

$$u_m = \sqrt{(\overline{u'^2})} \tag{2.19}$$

u_m is sometimes referred to as a 'characteristic turbulent velocity', which indicates the behaviour of the eddy movements (Csanady, 1973). Reynolds' deduced that the turbulent velocity fluctuations generated forces or stresses within the flow, and proposed that the stresses could be described mathematically. The basic principle governing Reynolds' theoretical treatment was that momentum is conserved during the movement of fluid. For simplicity, consider the case of two-dimensional flow where it is assumed that only movements in the x and z direction occur. Figure 2.4

shows the movement of a small element of fluid passing through a small horizontal surface of area ΔA , whose dimensions are $\Delta x \times \Delta y$.

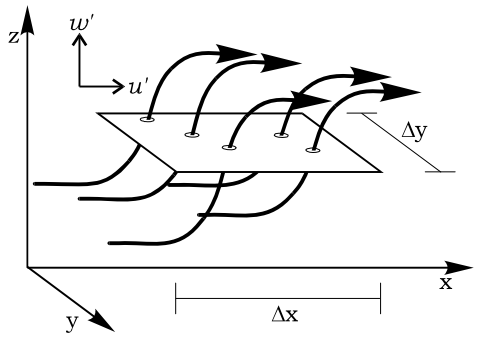

Figure 2.4 – Reynolds' stress eddy model, adapted from Chadwick & Morfet (1986)

During a small time interval, Δt it is assumed that the mass of fluid flowing through the surface in the *z*-direction is given by:

$$\rho w' \Delta A \Delta t \tag{2.20}$$

By adopting the Rules of Averaging, in the *x*-direction, the mass of fluid has the instantaneous horizontal velocity component of $\overline{u} + u'$. By definition the momentum (ΔM) of the mass of fluid is therefore given by:

$$\Delta M = (\rho w' \Delta A \Delta t)(\overline{u} + u') \tag{2.21}$$

The rate of change of momentum of the fluid over the small time interval, Δt is therefore given by:

$$\frac{\Delta M}{\Delta t} = (\rho \overline{w'} \Delta A \overline{u}) + (\rho \overline{w'u'} \Delta A) \tag{2.22}$$

Over the small time interval, the average rate of transport of momentum is related to the time averaged velocities of the turbulent fluid motion. Thus, by definition, although the mean of the velocity fluctuation in the *z* direction ($\overline{w'}$) is zero, the mean of the product ($\overline{w'u'}$) generally yields non-zero results. From Newton's second law, the rate of change of momentum equals a force, and stress is the ratio of force over area, hence, the average stress over the small time interval is given by;

$$\tau_t = \rho\overline{w'u'} \tag{2.23}$$

where τ_t is denoted by turbulent shear stress and is more commonly known as a Reynolds' stress.

2.4.4 Turbulent Diffusion

A full understanding of turbulent motion is still unavailable and has proved to be one of the most challenging and intractable problems of the physical sciences. Nevertheless, in this section, by applying suitable averaging techniques, such as assuming that the small-scale random turbulent particle fluctuations within flows resemble random molecular movements, an analogy between molecular diffusion and turbulent diffusion can be derived.

The advection-diffusion equation (Eq. 2.17) in § 2.4.2, mathematically describes homogenous molecular diffusion in laminar flow. Now consider the spreading of a tracer cloud in stationary homogenous turbulent flow. In stationary homogenous turbulent conditions it is assumed that the properties of flow, when averaged over sufficient time are identical along the three orthogonal directions of x, y & z.

Now consider a small control volume within a tracer cloud of sufficient size which encounters both turbulent velocity and concentration fluctuations within its volume as time elapses. To simplify turbulent mixing problems in practical studies, it is usual to simplify the problem by averaging with respect to time (Holly, 1985). The Reynolds' Rules of Averaging states that within the control volume, the following quantities may be expressed as;

$$u = \overline{u} + u' \tag{2.24a}$$

$$v = \overline{v} + v' \tag{2.24b}$$

$$w = \overline{w} + w' \tag{2.24c}$$

$$c = \bar{c} + c' \tag{2.24d}$$

By combining equation 2.17 and equation 2.24, yields (Rutherford, 1994):

$$\begin{aligned}&\frac{\partial(\bar{c}+c')}{\partial t} + \left((\bar{u}+u')\frac{\partial(\bar{c}+c')}{\partial x}\right) + \left((\bar{v}+v')\frac{\partial(\bar{c}+c')}{\partial y}\right) + \left((\bar{w}+w')\frac{\partial(\bar{c}+c')}{\partial z}\right) \\ &= e_m\left(\frac{\partial^2(\bar{c}+c')}{\partial x^2} + \frac{\partial^2(\bar{c}+c')}{\partial y^2} + \frac{\partial^2(\bar{c}+c')}{\partial z^2}\right)\end{aligned} \tag{2.25}$$

The fluctuating components about the mean values, denoted by primes in equation 2.24 are by definition, equal to zero, when averaged. Thus equation 2.25 may be simplified, to give (Rutherford, 1994):

$$\begin{aligned}&\frac{\partial\bar{c}}{\partial t} + \left(\bar{u}\frac{\partial\bar{c}}{\partial x} + \bar{v}\frac{\partial\bar{c}}{\partial y} + \bar{w}\frac{\partial\bar{c}}{\partial z}\right) \\ &= e_m\left(\frac{\partial^2\bar{c}}{\partial x^2} + \frac{\partial^2\bar{c}}{\partial y^2} + \frac{\partial^2\bar{c}}{\partial z^2}\right) - \underbrace{\left(\frac{\partial(\overline{u'c'})}{\partial x} + \frac{\partial(\overline{v'c'})}{\partial y} + \frac{\partial(\overline{w'c'})}{\partial z}\right)}_{\text{Turbulent diffusion}}\end{aligned} \tag{2.26}$$

Rutherford (1994) pointed out that although the mean of the velocity and concentration fluctuations are zero, the mean of their products generally yield non-zero results. It is noted that equation 2.26 is essentially the same as that derived for laminar flow conditions, the major difference is the last term of the right-hand side of the equation, which provides an additional transport mechanism, more commonly known as turbulent diffusion.

Taylor (1921) showed that turbulent diffusion could also be modelled based on a gradient-diffusion process. It was assumed that the small-scale random turbulent particle fluctuations within the flow resemble random molecular movements, and therefore an analogy between molecular diffusion and turbulent diffusion could be derived given that sufficient time had elapsed since the injection of the tracer and that the turbulence was statistically independent of time. In an analogy with molecular diffusion, the turbulent diffusion coefficients e_x, e_y & e_z in each of the three axial directions are introduced, and are defined by;

$$\overline{u'c'} = -e_x \frac{\partial c}{\partial x} \tag{2.27a}$$

$$\overline{v'c'} = -e_y \frac{\partial c}{\partial y} \tag{2.27b}$$

$$\overline{w'c'} = -e_z \frac{\partial c}{\partial z} \tag{2.27c}$$

Rutherford (1994) pointed out that although an analogy of molecular and turbulent diffusion can be adopted in aqueous related studies, molecular diffusion is a property of the fluid whereas turbulent diffusion is a property of the flow and thus varies with velocity, turbulence and the geometry of the flow. He suggested that a typical value of turbulent diffusion, determined empirically in water, is of the order of $10^{-3}\,\mathrm{m^2 s^{-1}}$ (c.f. molecular diffusion, $e_m \approx 10^{-9}\,\mathrm{m^2 s^{-1}}$). Thus by combining Equation 2.26 and 2.27 and assuming that molecular diffusion is negligible, leads to the result:

$$\frac{\partial \bar{c}}{\partial t} + \bar{u}\frac{\partial \bar{c}}{\partial x} + \bar{v}\frac{\partial c}{\partial y} + \bar{w}\frac{\partial \bar{c}}{\partial z} = e_x \frac{\partial^2 \bar{c}}{\partial x^2} + e_y \frac{\partial^2 \bar{c}}{\partial y^2} + e_z \frac{\partial^2 \bar{c}}{\partial z^2} \tag{2.28}$$

Equation 2.28 provides a basis of mixing processes within aqueous related studies. Despite its apparent simplicity, solving equation 2.28 requires estimation of the turbulent diffusion coefficients in the three axial directions, together with knowledge of the spatial velocity flow field.

2.5 Transverse Mixing due to Wave Activity in the Nearshore Zone

In this section, attention will focus on the transverse mixing processes (on-off shore) in the nearshore coastal zone. The coastal zone, whether along an open coastline or within the confines of an estuary is subject to both wave and current effects. This results in a complex three-dimensional flow field affected by the periodic orbital motions of the waves, together with vertical and transverse shear effects generated by long-shore currents and the spatially variable flow depth.

As a wave approaches the shoreline, it is modified in height and length. When the water depth and the wave height are of similar magnitude, the wave breaks. The region between the breaker point and the shoreline is known as the surfzone. Visual observations made by Bowen & Inman (1974) of solute tracers released into the nearshore region suggest that in the surfzone, the spreading of a tracer across this region was much larger than in the along-shore direction. Observations were also made that most of the dye stayed within the confines of the surfzone, only returning through intermittent rip currents. Outside the surfzone, seawards of the breaker point, they reported that the mixing was much lower when compared to surfzone mixing, and suggested that the contribution of additional turbulence generated by wave activity may be smaller than the turbulence generated by current effects. There have been relatively few mixing studies, yet alone transverse solute mixing within the nearshore zone. This, despite being the interface of the ocean where many man-made aqueous discharges are released from outfalls.

Although site specific field studies have been undertaken to elucidate the mixing processes within the nearshore zone, analysis is difficult because of the problems of measuring all the associated parameters. Additionally, due to the nature of the coastal environment, field studies carried out under the combined effects of waves and currents, have resulted in a lack of resolution of the individual contribution of wave activity and current action on the mixing processes. The purpose of this section is to introduce some of the governing equations under idealised wave motion, prior to reviewing detailed theoretical and experimental mixing studies in the nearshore region.

2.5.1 Wave Theory

Wind generated waves

The primary driving force which causes the formation and generation of waves in natural environments is the wind. The pressure within an air stream above the water surface fluctuates about a mean value causing small ripples and waves to form figure 2.5a.

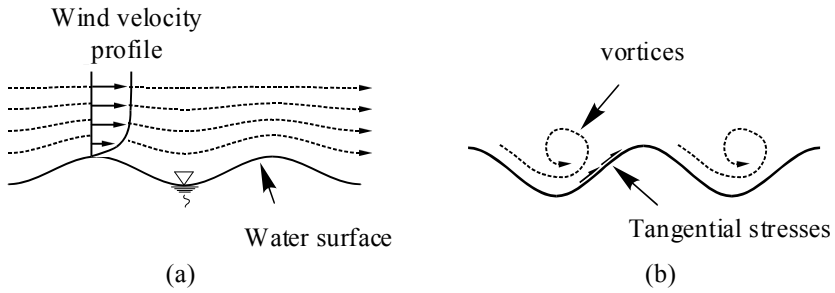

Figure 2.5 – Definition sketch of the generation of wind waves

If the air stream is of sufficient magnitude, the small waves may disturb the air stream patterns over the surface waters (Fig. 2.5b). This can result in the generation of air vortices which can lead to a greater transfer of energy due to the increased force on the water surface. This can cause the wave height to increase further. Empirical studies suggest that the approximate wave condition at a given location can be estimated for a given wind speed, direction, duration and fetch length.

Clearly, due to the variability of atmospheric conditions, it is only possible to determine an estimate of the wave conditions. Thus although wind is the primary force in generating waves, it is customary to consider the overall effects of wave activity on solute mixing processes by considering the wave motion generated by the wind rather than the wind itself. Therefore, the underlying concepts of wave motion within the context of this present study are discussed from the point of view of the hydrodynamic wave conditions rather than the atmospheric conditions generating the waves.

Waves within natural environments consist of complex varying motions. To determine a mathematical description of the motion, it is customary to assume that the complex motion consists of a number of simple wave forms of different periods, lengths and heights moving in different directions superimposed on each other. These simple wave forms are assumed to obey some form of wave equation, which allows a mathematical description of the both the surface elevation and the orbital motions beneath the surface to be determined. Several theories exist to describe wave motion. Within this section, two theories of linear wave theory of Airy (1845)

and the more sophisticated wave theory of Stokes (1847) will be discussed from the point of view of understanding the underlying concepts rather than a complete mathematical derivation.

Small amplitude wave theory (Airy wave theory)

A wave is defined as a disturbance travelling from a point in a medium to another point at a later time. The mathematical description of wave motion formulated by Airy (1845) gives considerable information for little mathematical endeavour. Thus for the purposes of introducing the governing terminology with respect to wave motion, the use of small amplitude or linear wave theory will be considered. Consider a small amplitude progressive wave moving towards the shoreline in the y-direction (Fig. 2.6). The velocity at which the wave crest travels towards the shoreline is given by the wave celerity, *C*. It is assumed that the water surface moves in a simple harmonic sinusoidal motion and the wave is defined by the following parameters:

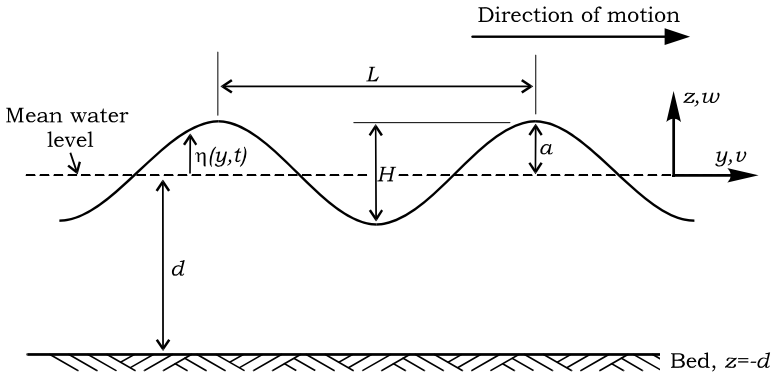

Figure 2.6 – Definition sketch for a small amplitude sinusoidal wave

d = Distance from bed to mean water level
$\eta(y,t)$ = Instantaneous vertical displacement of water surface above mean water level
a = Wave amplitude
H = Wave height $= 2a$ for small amplitude waves
L = Wavelength, distance between any two corresponding positions on successive waves
T = Wave period, the time interval for motion to reoccur at a fixed point
C = Velocity of wave propagation (phase velocity) $= L/T$
k = Wave number $= 2\pi/L$
ω = Wave angular frequency $= 2\pi/T$

In order to determine a description of motion within small amplitude waves, Airy adopted the following assumptions; (*i*) the amplitude is small compared with the wavelength [which results in the wave celerity being large when compared to the particle velocity], (*ii*) the water is homogenous, incompressible and the surface tension forces are negligible, (*iii*) the flow is irrotational (i.e. no shear stress), (*iv*) the bed [$y = -d$] is stationary, impermeable and horizontal, (*v*) the pressure along the air/sea interface is constant. Thus, the water surface profile, given as a function of position and time can be denoted as (Ippen, 1966):

$$\eta = \frac{H}{2}\cos 2\pi\left(\frac{y}{L} - \frac{t}{T}\right) = \frac{H}{2}\cos(ky - \omega t) \tag{2.29}$$

The relationship between the wavelength and the period can be derived by adopting the basic principles of continuity of mass and energy, and adopting the Laplace equation for two-dimensional flow, leading to the result;

$$L = \frac{gT^2}{2\pi}\tanh\frac{2\pi d}{L} \tag{2.30}$$

As the wave travels along the surface, the water particles beneath the surface also move. Airy's wave theory predicts such movements, and thus at a given location, (y,z) and periodic time interval, *t* within the wave cycle, the horizontal and vertical displacements at a mean depth, –*z* beneath a finite amplitude wave can be described by

$$y = \frac{H}{2}\frac{\cosh k(d+z)}{\sinh(kd)}\sin(ky - \omega t) \tag{2.31}$$

$$z = \frac{H}{2}\frac{\sinh k(d+z)}{\sinh(kd)}\cos(ky - \omega t) \tag{2.32}$$

These two equations describe an elliptical motion in which the particles rotate about a closed orbit and as such there is no net forward displacement of the water.

To simplify the hyperbolic functions in equation 2.31 and 2.32, it is customary to classify the waves according to the ratio of the water depth *d*, to the wave length, *L*. This ratio d/L is known as the relative depth. A common procedure adopted for small amplitude wave theory classifies the waves into three categories, namely; shallow, intermediate and deep water. If the relative depth exceeds $1/2$, deep water conditions are assumed to occur. When the relative depth is below $1/20$, the depth is small compared to the wavelength and it is assumed that shallow water conditions occur. In the range $1/20 < d/L < 1/2$, it is assumed that intermediate conditions occur, although the wave equations do not easily simplify. Table 2.1 presents the asymptotic values for shallow and deep water.

Table 2.1: Asymptotes of wave functions

Function	Asymptotes	
	Shallow water ($d/L < 1/20$)	Deep water ($d/L > 1/2$)
Sinh (*kd*)	*kd*	$\frac{e^{kd}}{2}$
cosh (*kd*)	1	$\frac{e^{kd}}{2}$
tanh (*kd*)	*kd*	1

By recalling the relationship between wavelength and period (Eq. 2.31) and noting that $C = L/T$, $k = 2\pi/L$ & $\omega = 2\pi/T$, the celerity can be written as:

$$C^2 = \frac{g}{k}\tanh(kd) \tag{2.33}$$

Using this result and the appropriate value in Table 2.1, the wave celerity, *C* can be reduced to;

$$C = \frac{g}{2\pi} T \qquad \text{(deep water)} \tag{2.34}$$

$$C = \sqrt{gd} \qquad \text{(shallow water)} \tag{2.35}$$

In addition, by recalling equations 2.32 and 2.33 and utilising the appropriate value in Table 2.1, the maximum orbital displacements under deep water conditions can be approximated to

$$y_{(\max)} = \frac{H}{2} e^{kd} \tag{2.36}$$

$$z_{(\max)} = \frac{H}{2} e^{kd} \tag{2.37}$$

Thus, equations 2.36 and 2.37 describe a circular path in which the horizontal and vertical displacements decrease exponentially with depth (see Fig. 2.7). Similarly in shallow water conditions, the maximum orbital displacements can be approximated to

$$y_{(\max)} = \frac{H}{2kd} \tag{2.38}$$

$$z_{(\max)} = \frac{H}{2} \frac{k(d+z)}{kd} \tag{2.39}$$

Thus, the maximum horizontal orbital displacement is constant from the surface to the bottom of the water column. However, the maximum vertical orbital displacement, varies from zero at the bed to $H/2$ at the surface (see Fig. 2.7c).

Figure 2.7 illustrates the orbital motions predicted by Airy's wave theory. In deep water (Fig. 2.7a), the turbulence generated by bed friction due to wave motion may be assumed to be negligible. Hence mixing due to turbulent diffusion may be small compared to other mixing processes which may be present.

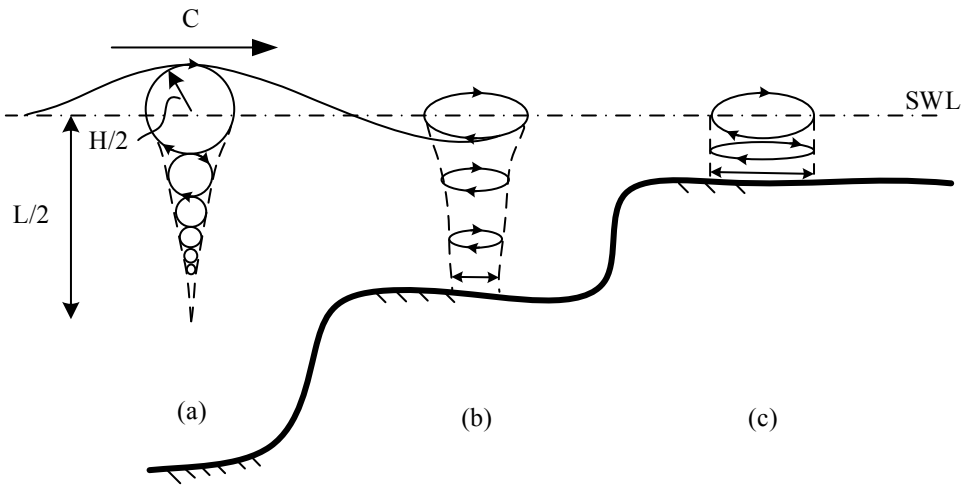

Figure 2.7 – Sketch depicting depth effects on particle orbits, (a) Deep water, (b) Water of intermediate depth, & (c) Shallow water, from Sorensen (1993)

As a wave approaches the shore line, the wavelength reduces, the period remains constant, and thus the wave celerity reduces. Due to the reduction in depth, the circular particle orbits in deep water become elliptical trajectories as the wave moves inshore. In shallow water the horizontal trajectories of the particles are constant with depth, and towards the bed, the elliptical trajectories become flattened. In the vicinity of the bed there is no vertical motion, and thus the particles follow a horizontal path (Eq. 2.39). The increase in velocity at the bed as the depth reduces, causes turbulence to be generated due to the alternating flow movements over the bed (Fig. 2.7c). This could increase turbulent diffusion, however, the extent of this increase is unknown, due to the limited theoretical and experimental knowledge currently available, and also due to other additional mixing processes which are present, which result in the difficulty of isolating the effect of any one influence. The role of the additional mixing mechanisms due to wave activity will be discussed in §2.5.3.

The wave breaker point

In the previous section, the basic equations to describe wave motion in shallow water were introduced. It was noted that as a wave travels from deep to shallow water, the wavelength decreases. Eventually, at a critical value, the wave becomes unstable and breaks. The expression which relates the ratio of wave height to wavelength is known as the wave steepness (δ) and is given by the simple relationship;

$$\delta = \frac{H}{L} \tag{2.40}$$

As a wave approaches the shoreline, due to the reduction in depth, the orbital particle velocities increase over the wave cycle (Eq. 2.38), whereas the velocity of propagation, or wave celerity reduces (Eq. 2.35). Galvin (1972) referred to the studies of McCowan (1894) who reported that for theoretical predictions, breaking occurs when the maximum particle velocity in the wave exceeds the wave celerity. According to Michell (1893), it can be shown that by the application of Stokes' wave theory (Stokes, 1847), the wave becomes unstable and breaks, when the angle of the wave crest reaches 120°, or written in terms of wave steepness, when $\delta = 0.142$. In shallow water conditions, by recalling equation 2.35 and $C = L/T$, and noting that the wave period remains constant irrespective of offshore location, gives

$$L = T\sqrt{gd} \tag{2.41}$$

Thus, in shallow water, the wavelength is determined by the water depth. Ippen (1966) referred to the studies of McCowan (1894), who adopted Stokes' theoretical breaking criteria, and applied the assumption to the theoretical wave motion described by Solitary wave theory. Thus, it was shown that the theoretical limiting breaking criterion in shallow water can be given by:

$$\gamma = \frac{H}{d} = 0.78 \tag{2.42}$$

This value is still commonly adopted in engineering applications, however in practical related studies it is found that the mean beach slope (m) influences both the breaker depth index (γ) and the type of breaking wave (Galvin, 1972). Thus, as pointed out by Goda (1970), who undertook an extensive experimental study in both the field and laboratory, the breaker index increases (γ) on steep beaches, while on flatter beaches the breaker index reduces. Fig. 2.8 illustrates the results compiled from the study, which indicates that the breaker depth can be parameterised by the deep water wave steepness and the beach slope (m).

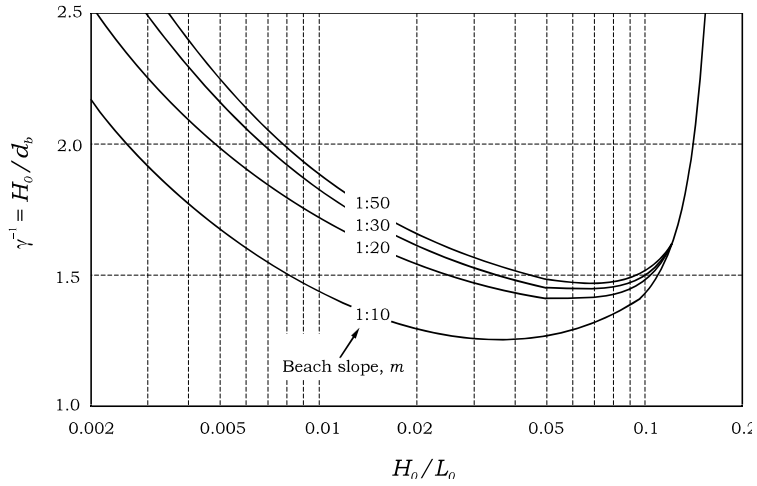

Figure 2.8 – Classification of wave breaking depth, adapted from Horikawa (1978)

The surfzone

The region between the breaker point and the shoreline is known as the surfzone. The motion of water particles within this region are complex, and although this region has been studied extensively, a full quantitative description of the hydrodynamics is still currently unavailable.

In the previous section it was noted that the wave breaker point was dependent upon the ratio of wave height to the water depth. However, the main controlling factor was the beach slope. The slope of beach influences the type of wave motion and hence the hydrodynamics within the surfzone. An early study to investigate surfzone hydrodynamics was undertaken by Wiegel (1963). Visual observations were made which classified breaking waves into three types, ranging from surging through plunging to spilling breakers. These conditions are illustrated in figure 2.9.

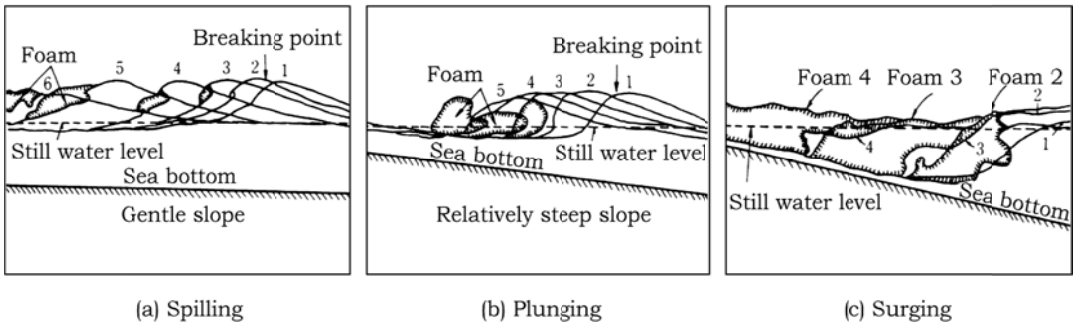

(a) Spilling (b) Plunging (c) Surging

Figure 2.9 – Classification of breaker types adopted from Horikawa (1978)

Patrick and Wiegel (1954) formulated a relationship, which classified the wave height and period to the beach slope. Thus, in shallow water conditions the breaker coefficient (B_b) was given by (Patrick & Wiegel, 1954);

$$B_b = \frac{H_b}{gmT^2} \tag{2.43}$$

where the subscript, *b* denotes breaking conditions, and *m* is the beach slope. Galvin (1972) undertook an experimental study on three plane laboratory concrete beaches, with varying slopes of 0.05, 0.10 and 0.20 to parameterise the breaker coefficient. The results are given in Table 2.2.

Table 2.2: Classification of breaker types [from Galvin (1972)]

Breaker classification	Breaker coefficient, B_b
Surging	<0.003
Plunging	0.003 – 0.068
Spilling	>0.068

Figure 2.9 illustrates that the beach slope greatly influences the hydrodynamics within the surfzone region. Based on these observations, it is therefore assumed that regardless of beach slope condition, increased turbulence occured in the surfzone, due to the breaking wave activity, and therefore increased mixing in this region is expected.

2.5.2 Wave-induced Currents

In the previous section, the use of Airy wave theory was adopted to introduce the fundamental concepts of wave theory. Airy's theory is of sufficient accuracy in deep water conditions. In practice, as the wave approaches the shore, the orbital trajectories are no longer closed orbits as predicted by Airy wave theory, but each water particle moves a short distance in the direction of the wave propagation by the end of each wave cycle. Thus, due to the wave motion, a wave induced current is generated. In this section, the higher order wave theory of Stokes (1847) will be presented to describe wave induced current in the nearshore zone, in the region seawards of the break point.

Finite amplitude wave theory (Stokes wave theory), seaward of the break point

A Eulerian co-ordinate system with respect to velocity or concentration measurements is one which is fixed in spatial location. In contrast, a Lagrangian co-ordinate system is one which moves along with an imposed current. In oscillatory flows, such as wave motion, there is a difference between the mean velocity recorded by Eulerian techniques and the mean velocity measured by a freely moving particle (Lagrangian). As pointed out by Longuet-Higgins (1970), the difference between the Eulerian and Lagrangian mean velocity is known as Stokes velocity or Drift (Stokes, 1847).

Thus, by adopting Stokes's higher order wave theory, the water surface profile (η), correct to a second order approximation, can be given by equation 2.44.

$$\eta = \frac{H}{2}\cos(ky - \omega t) + \frac{\pi}{8}\frac{H^2}{L}\frac{\cosh kd(2 + \cosh 2kd)}{\sinh^3 kd}\cos 2(ky - \omega t) \qquad (2.44)$$

The equations which describe the particle orbital motion beneath a finite amplitude wave, are denoted by:

$$y = -\frac{H}{2}\frac{\cosh k(d+z)}{\sinh(kd)}\sin(ky-\omega t) - \frac{\pi H^2}{4L}\frac{1}{\sinh^2 kd}\left(-\frac{1}{2}+\frac{3}{4}\frac{\cosh 2k(d+z)}{\sinh^2 kd}\right)\sin 2(ky-\omega t) - \left(\frac{\pi H}{L}\right)^2\frac{C}{2}\frac{\cosh 2k(d+z)}{\sinh^2 kd}t \quad (2.45)$$

$$z = \frac{H}{2}\frac{\sinh k(d+z)}{\sinh kd}\cos(ky-\omega t) + \frac{3}{16}\frac{\pi H^2}{L}\frac{\sinh 2k(d+z)}{\sinh^4 kd}\cos 2(ky-\omega t) \quad (2.46)$$

where the velocity of propagation, C is the same as the value denoted for linear wave theory. The final term of equation 2.45 features an additional net particle displacement term. Thus the net displacement (Δy_T) at the completion of each wave cycle is given by

$$\Delta y_T = \left(\frac{\pi H}{L}\right)^2\frac{C}{2}\frac{\cosh 2k(d+z)}{\sinh^2 kd}T \quad (2.47)$$

Thus, when averaged over the wave cycle the mean drift velocity ($\overline{V}$) or mass transport velocity of translation in the y-direction can therefore be given by

$$\overline{V}(z) = \frac{\Delta y_T}{T} = \left(\frac{\pi H}{L}\right)^2\frac{C}{2}\frac{\cosh 2k(d+z)}{\sinh^2 kd} \quad (2.48)$$

The Eulerian description of the predicted wave-averaged induced current assumed that the wave-averaged momentum, I, was concentrated in the crest to trough region of the wave (Longuet-Higgins & Stewart, 1960, 1964). Using linear wave theory, it can be approximated by:

$$I = \frac{E}{C} = \frac{H^2}{8}\rho\omega\coth kh \quad (2.49)$$

where E is denoted by the total wave energy per unit surface area, given by

$$E = 1/8\,\rho g H^2 \quad (2.50)$$

To balance the momentum the wave possesses, an equal and opposite force exists. Thus in wave conditions of finite depth, such as the coastal zone, the return flow or undertow can be approximated by,

$$v_{+} = \frac{I}{\rho d} \tag{2.51}$$

Assuming that the Eulerian mean return flow is distributed evenly throughout the entire depth, allows a Lagrangian description of the wave induced current at a particular elevation to be obtained. Combining equations 2.48, 2.49 and 2.51, yields in:

$$\overline{V}(z) = \frac{\omega k H^2}{8} \frac{\cosh 2k(d+z)}{\sinh^2 kd} - \frac{\omega H^2}{8d} \coth kd \tag{2.52}$$

Equation 2.52 is seen as a shoreward flow of water in the upper water column with a return seaward flow near the bed. Figure 2.10 illustrates a typical wave induced current profile over the water column as predicted by equation 2.52.

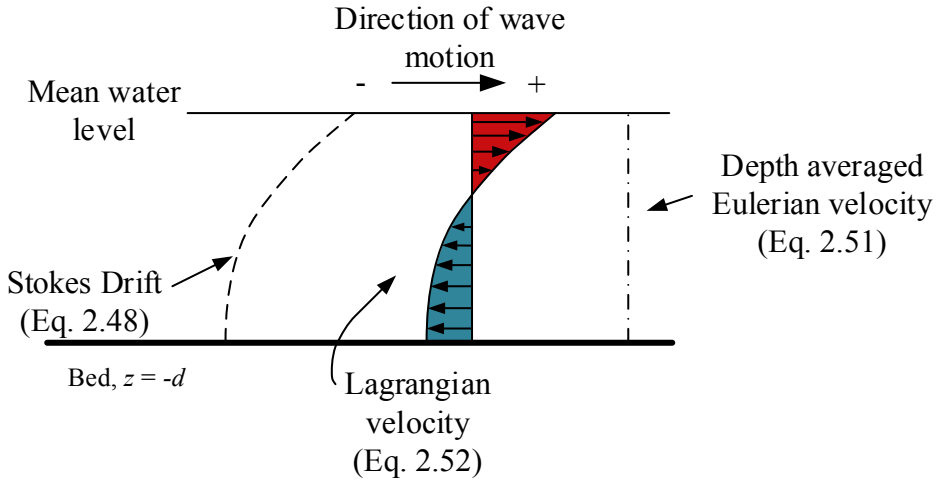

Figure 2.10 – Sketch depicting a typical Lagrangian velocity profile of the mass-transport in a progressive wave

The limitation of Stokes's wave theory is that it is assumed that the fluid is irrotational. Longuet-Higgins (1953) extended the analysis of Stokes to include the effects of the boundary layers at the free surface and the bed. After considerable mathematical derivation and treatment, it was shown that the mass transport at

particular elevation within the water column for a progressive wave can be given by the expression (Longuet-Higgins, 1953):

$$\overline{V}(z) = \frac{\omega k H^2}{4} F^{(p)}(z/d) \tag{2.53}$$

where;

$$\begin{aligned} F^{(p)}(z/d) = \frac{1}{4\sinh^2 kd}\Bigg[& 2\cosh 2k(d+z)+3 \\ & +\Big(3(z/d)^2+4(z/d)+1\Big)kd\sinh 2kd \\ & +3\Bigg[\frac{\sinh 2kd}{2kd}+\frac{3}{2}\Bigg]\Big((z/d)^2-1\Big)\Bigg] \end{aligned} \tag{2.54}$$

Figure 2.11 shows the non-dimensionalised vertical distribution of the mass transport velocity, predicted for three progressive waves. As the depth to wavelength ratio kd, reduces, the velocity in the lower part of the water column increases towards the shore.

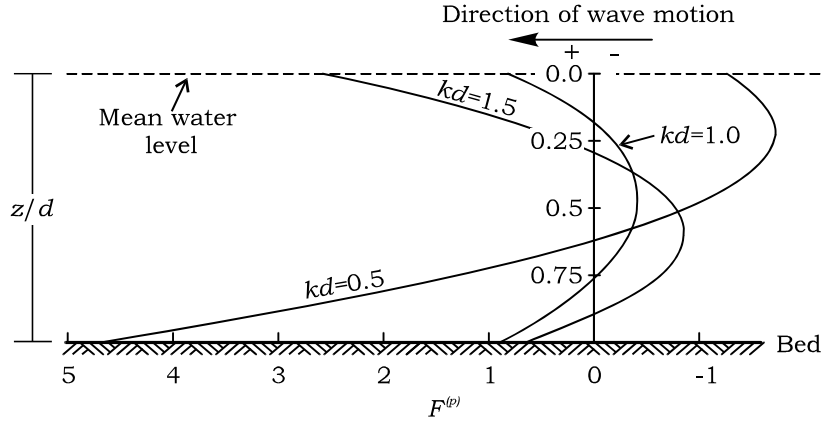

Figure 2.11 – Vertical distribution of the non-dimensionalised Lagrangian velocity in a progressive wave (kd = 0.5, 1.0, 1.5), adopted from Longuet-Higgins (1953)

Longuet-Higgins (1953) attempted to verify his solution with existing experimental measurements which were performed in 2D laboratory wave flumes and most of the measurements were made by photographing visible tracers. When compared to experiments (Bagnold, 1947) where the wave conditions were controllable and steady state conditions were assumed to occur, the theoretical predictions of the velocities near to the bed were within 15% of observed values.

Wave induced current in the surfzone

On a plane two-dimensional beach with the wave crests approaching parallel to the shore line, the water is carried shore-wards by the wave crest and is returned seawards by a shore normal return current, which is particularly strong towards the bed.

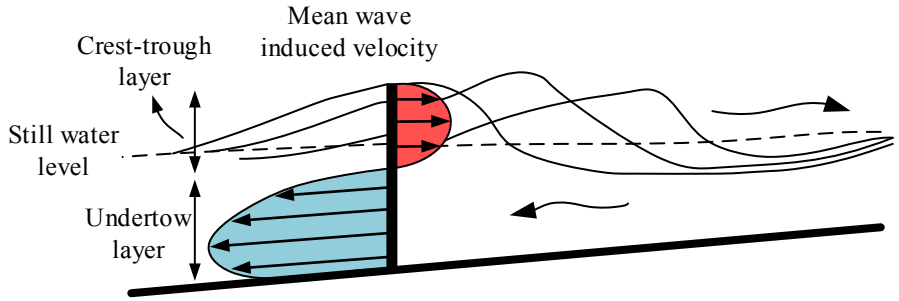

Figure 2.12 – Definition sketch of wave motion within the surfzone

Figure 2.12 illustrates the cross-shore mean wave induced secondary current (shore-normal) in the surfzone. Near to the surface in the crest-trough layer the mean velocity has a shoreward component, however as pointed out by Svendsen & Lorenz (1989), the Eulerian description of the mean velocity cannot easily be defined in the crest-trough layer as water is only present for part of the wave cycle. In the lower part of the water column, to satisfy continuity principle, the mean flow moves in an offshore direction.

In recent years several attempt has been made to quantify the magnitude of the wave induced currents in the surfzone. Longuet-Higgins & Stewart (1960, 1964) extended the earlier analysis of Longuet-Higgins (1953) who formulated mass transport for non-breaking conditions. To balance the momentum flux the wave possesses, an equal and opposite force must be present to satisfy equilibrium. In the surfzone, this is seen visually as rise in water level. This phenomenon can be described by equation 2.55 which is proposed by Longuet-Higgins (1972).

$$\frac{\partial S}{\partial y} + \rho g(d + \bar{\eta})\frac{\partial \bar{\eta}}{\partial y} = 0 \qquad (2.55)$$

where $\bar{\eta}$ is the difference between the still water level and the mean water level and S is the radiation stress in the direction of the wave motion given by (Longuet-Higgins, 1972):

$$S = E\left(\frac{2kd}{\sinh 2kd} + \frac{1}{2}\right) \tag{2.56}$$

By integrating equation 2.56, it can be shown that the mean sea level decreases as the wave approaches the breaker point. This mechanism is referred to as wave set-down and is given by (Horikawa, 1978);

$$\bar{\eta} = -\frac{H^2}{8}\frac{k}{\sinh 2kd} \qquad (d_b<d) \tag{2.57}$$

In the surfzone, the mean sea level increases and is referred to as wave set-up, given by (Horikawa, 1978);

$$\bar{\eta} = \left(\frac{1}{1+(8/3\gamma^2)}\right)(d_b - d) + \bar{\eta}_b \qquad (d<d_b) \tag{2.58}$$

where $\bar{\eta}_b$ is the wave set-down at breaking (Eq. 2.57). Figures. 2.13a and 2.13b illustrate a typical result from an experimental study undertaken by Bowen *et al*. (1968) to investigate the wave set-up and set-down as the wave approaches the shore. The results indicate that for the conditions tested, the theoretical curve (Eqs. 2.57 and 2.58) expressed the experimental results reasonably well. Chadwick & Morfet (1986) pointed out that, as a general rule, the maximum wave set-down is approximately 5% of the breaker depth and the maximum wave set-up is approximately 20% of the breaker depth. Fig 2.13c displays the theoretical mean return current across the nearshore zone as predicted by equation 2.51, it is clear that the transverse solute spreading of a depth averaged concentration field is influenced by secondary flows. Fig. 2.13c shows that the wave induced current is particularly strong inside the surfzone region which could be an important variable in the nearshore mixing processes. The role of wave induced current on the nearshore mixing will be discussed at the end of this chapter.

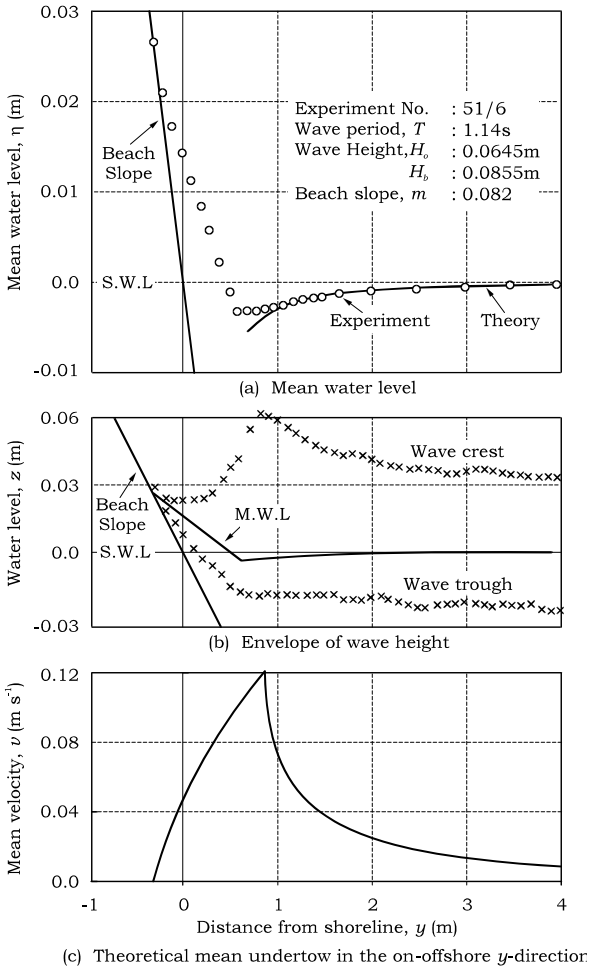

Figure 2.13 – Example of (a) experimental results on wave set-up and set-down, (b) wave height envelope, and (c) Theoretical mean undertow velocity {(a) & (b) from Bowen, Inman and Simmons, 1968}

Figure 2.14 summaries the results from the Hansen & Svendsen (1984) laboratory experimental study. The resultant Eulerian mean cross-shore velocity profiles illustrate that outside the breaker point, the horizontal velocity varies almost linearly between the bed and the wave trough layer. In the surfzone, due to the decreasing water depth, the cross-shore velocities are of a larger magnitude. It is also noted that the structure of the undertow changes, where can be seen that mean horizontal velocity is particularly strong towards the bed.

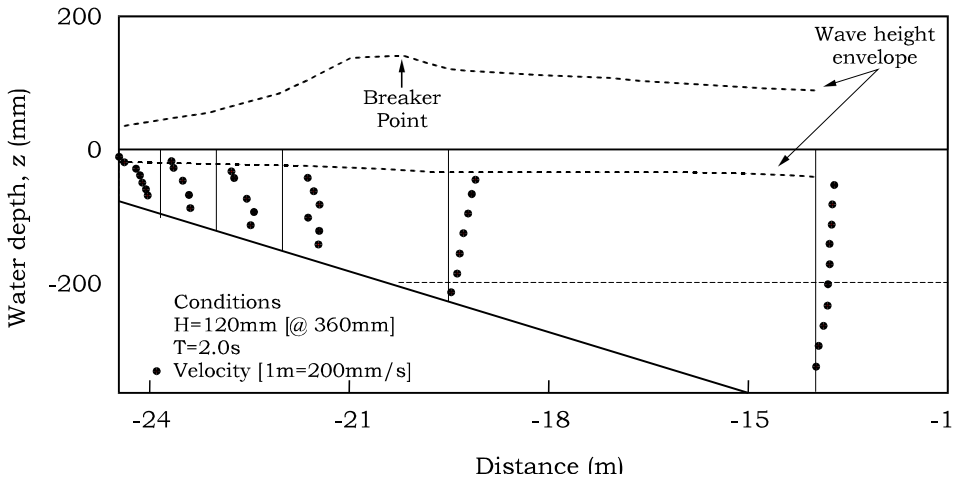

Figure 2.14 – Measured cross-shore mean Eulerian velocities in nearshore region, adapted from Hansen & Svendsen (1984)

2.5.3 Turbulence in the Nearshore Region

the previous section (§ 2.5.2) discussed wave motion and the resultant wave induced current. This section will consider the turbulence generated by wave activity, initially in the surfzone and then turbulence will be considered seawards of the breaker point. Finally, the section will conclude with a comparison and discussion of the various suggested forms of eddy viscosity.

Estimates of eddy viscosity in the surfzone

In § 2.4.4 it was noted that by adopting Reynolds analogy, the turbulent diffusion coefficient in the transverse direction (e_y) was of similar magnitude to the eddy viscosity (ν_t). Thus for the purposes of this present study it is assumed that the two variables are of the same magnitude. Hence, estimates of eddy viscosity values are usually derived from velocity measurement, while estimates of turbulent diffusion coefficients are usually obtained from direct measurement of a suitable tracer released into the flow. This section will therefore focus on the use of velocity measurements to determine eddy viscosity values in the surfzone.

The nature of breaking waves as they approach the shore generates turbulence and aeration. However, the difficulty in obtaining reliable estimates of eddy viscosity values within this region is that many velocity measurement devices are sensitive to air entrainment which leads in to spurious measurements. Thus, there have been comparatively few experimental studies to investigate the flow characteristics within the surfzone.

To date, attention has focused on waves which approach the shore with their crests parallel to the shore. In some coastal situations, waves are diffracted and refracted and may approach the shore line at an oblique angle. This results in two velocity components being generated, one perpendicular to the shore and one parallel to the shore. The velocity component perpendicular to the shore, results in the wave induced cross-shore circulation mechanism as discussed in the previous section. The velocity component parallel to the beach produces a current, known as the longshore current.

Galvin & Eagleson (1965) performed detailed experimental measurements of the longshore currents on a plane beach. The studies of Bowen (1969), Thornton (1970) and Longuet-Higgins (1970) utilised this data to suggest various forms of transverse eddy viscosity values. The observed current distribution of Galvin & Eagleson (1965), for one test series, is shown in figure 2.15, together with theoretical velocity profiles derived by Longuet-Higgins (1970) from his radiation stress theory (Longuet-Higgins & Stewart, 1960 & 1964). The non-dimensional parameter, P represents the inclusion of the horizontal mixing in the on-off shore direction, which will be discussed in detail later.

Figure 2.15 shows that although the generation of longshore currents from waves approaching the shore at an oblique angle is mainly confined to the surfzone, some residual current extends beyond the breaker line. Thus as pointed out by Longuet-Higgins (1970) an additional mechanism must be present to drive the longshore current beyond the breaker line.

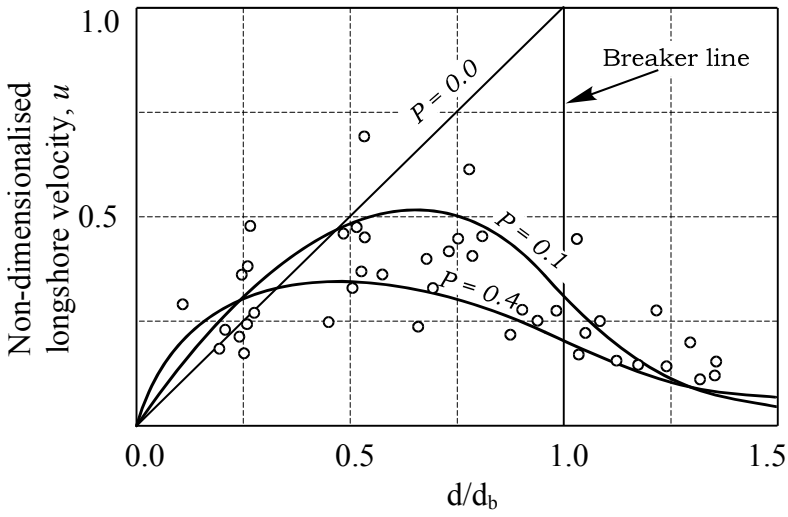

Figure 2.15 – Comparison of longshore velocities measured by Galvin & Eagleson (1965) with theoretical profiles derived by Longuet-Higgins (1970) , adapted from Longuet-Higgins (1970)

To balance the driving force of the waves within the surfzone, frictional forces are present in the form of bed friction. If only bed friction was considered in the formulation of theoretical longshore current predictions, a large discontinuity of the velocity prediction would be present at the breaker line, as shown in figure 2.15 by the non-dimensionalised parameter, $P = 0$. Bowen (1969), Longuet-Higgins (1970) and Thornton (1970) suggested that it was necessary to include an estimate of the lateral mixing in the on-offshore direction to describe the longshore current observations in theoretical predictions.

Bowen (1969) suggested that the eddy viscosity was assumed to be constant across the surfzone and beyond the breaker line. The justification was not reported, which suggested that by using an appropriate value of bed friction, an estimate of the eddy viscosity to best describe the observed data was used.

Thornton (1970) based analysis for the estimation of the lateral mixing coefficient on Prandtl's mixing length (Prandtl, 1952). It was proposed that the eddy viscosity could be evaluated based on the product of the water particle velocity and its orbital displacement. By adopting linear wave theory and assuming that the water particle motion retained its character as described by linear wave theory in the surfzone,

Thornton (1970) suggested that the eddy viscosity in the on-off shore direction, could be given by:

$$\nu_{ty} = \frac{H^2 \omega}{8 \sinh^2 (kd)} \cos^2 \theta \tag{2.59}$$

where θ is the approach angle to the shore. On a plane beach with a constant slope, equation 2.59 can be simplified to:

$$\nu_{ty} = \frac{gd\gamma^2}{8\omega} \tag{2.60}$$

Longuet-Higgins (1970) proposed that the size of the horizontal eddies in the surfzone could be related to the distance from the shore line and to the shallow water wave celerity. He proposed that the eddy viscosity could be given by:

$$\nu_{ty} = Ny\sqrt{gd} = \frac{Nd\sqrt{gd}}{m} \tag{2.61}$$

where N is a dimensionless constant. Figure 2.15 shows comparisons of longshore velocity measurements (Galvin & Eagleson, 1965) with theoretical predictions derived from Longuet-Higgins (1970). Although the exact formulation of the theoretical predictions are not discussed, within this present study, Longuet-Higgins (1970) demonstrated that the profile was dependent upon the non-dimensional parameter P, given by:

$$P = \frac{\pi}{2}\left[\frac{2mN}{\gamma C}\right] \tag{2.62}$$

where m is the bed slope and C is the Chezy bed frictional coefficient. In the analysis, it was assumed that the Chezy bed frictional coefficient was 0.01, the breaker index, γ was 0.82 and the slope of the beach (m) was 0.11. Longuet-Higgins (1970) showed that the observed velocity measurements were within the range relating to the curves of $0.1 < P < 0.4$. It was noted that the curves $P = 0.1$ and

$P = 0.4$ corresponded to $N = 0.0024$ and $N = 0.0096$ respectively. Although these values were within the expected range, it was clear that the selection of eddy viscosity (ν_{ty}) was insensitive to the prediction of theoretical longshore velocity profiles. Also, the selection of eddy viscosity was based on dimensional analysis rather than sound theoretical knowledge or measurement.

Battjes (1975) assumed that the length scale of eddies were more closely related to the depth than the horizontal distance offshore which was suggested by Longuet-Higgins (1970). Battjes (1975, 1983) reported that the lateral mixing within the surfzone was closely related to the turbulent energy dissipation of the breaking wave. For a gently sloping beach of constant slope, *m*, it was shown that the theoretical eddy viscosity, across the surfzone could be given by:

$$\nu_{tz} = M\left[\frac{5\gamma^2}{16}\right]^{1/3} m^{1/3} h\sqrt{gh} \qquad (2.63)$$

where *M* is a empirical constant ($M \approx 1.0$). The eddy viscosity predicted by equation 2.63 gives a result of similar magnitude to that theoretically predicted by Longuet-Higgins (1970) [Eq. 2.61].

To date, few experimental studies have been performed to determine the vertical eddy viscosity (ν_{tz}) in the surfzone. Svendsen (1987) summarised the measurements undertaken by Stive & Wind (1982), Hattori & Aono (1985), and Nadaoka & Kondoh (1982) who investigated the turbulent intensities, v_m and w_m of velocity under breaking waves, in the on-offshore and vertical directions respectively. Svendsen (1987) adopted the analysis of Prandtl (1952) to suggest that the turbulence generated mixing in the surfzone was dominated by the breaking wave. Thus, in an analogy with Prandtl's mixing hypothesis, the eddy viscosity (ν_t) could be estimated by a characteristic turbulent kinetic energy (k) and length scale (l_m), given by (Svendsen, 1987):

$$\nu_t = l_m \sqrt{k} \tag{2.64}$$

where k is defined by,

$$k = \frac{1}{2}(\overline{u'^2} + \overline{v'^2} + \overline{w'^2}) \tag{2.65}$$

and $\overline{u^2}, \overline{v^2}, \& \ \overline{w^2}$ are denoted by the turbulent velocity fluctuations. Svendsen (1987) noted that the relative strengths of the turbulent velocity fluctuations in each orthogonal direction varied, and adopted evidence provided by Battjes & Sakai (1981), which was also used by Stive & Wind (1982), to suggest that the relative strengths of the turbulent velocity fluctuation in each of the orthogonal directions (*x*, *y* & *z*) could be given by the ratio's (Svendsen, 1987).

$$\left(\frac{\overline{u'^2}}{2k}, \frac{\overline{v'^2}}{2k}, \frac{\overline{w'^2}}{2k}\right) = (0.32, 0.42, 0.26) \tag{2.66}$$

In all the experiments summarised, two velocity components were measured. Thus from equation 2.66, the turbulent kinetic energy (k) could be estimated from the two velocity fluctuations measured, and defined by

$$k = 1.33\left(\frac{1}{2}(\overline{v'^2} + \overline{w'^2})\right) \tag{2.67}$$

Svendsen (1987) suggested that breaking waves in the surfzone cause a rapid transformation of kinetic energy into turbulent energy, which then dissipates into heat as the wave crest moves up the beach slope. It was suggested that the turbulence generated by the breaking wave was initiated at the toe of the breaking wave front. Svendsen (1987) therefore proposed that the turbulent kinetic energy (*k*) was proportional to the celerity (*c*) of the wave crest in the surfzone. Hence, the results of the experimental studies cited by Svendsen (1987) depict the vertical spatial variation of $(k/gd)^{1/2}$ across the surfzone.

Figures 2.16a & 2.16b show the results obtained by Stive & Wind (1982) who performed measurements on a beach slope (m) of 1:40 under regular waves. A Laser Doppler anemometer was used for velocity measurements. The initial wave height was recorded with a value of $H = 0.145\,\mathrm{m}$ in both tests. The wave periods were measured with values of $T = 1.79s$ in test 1 and $T = 3.0s$ in test 2. Fig. 2.16c shows results reported by Hattori & Aono (1985), who measured velocities with a hot film anemometer. Unlike all the other results illustrated in Figure 2.16, the measurements undertaken by Hattori & Aono (1985) were performed on a horizontal shelf. The breaking wave was generated at the edge of the shelf using a beach with a slope (m) of 1:20, by placing it in front of the shelf. Figures 2.16d and 2.16e illustrate the results obtained by Nadaoko & Kondoh (1982). The measurements were performed on a beach with slope (m) of 1:20, and a Laser Doppler anemometer was used to measure the velocities. Two experiments were performed such that the conditions in the surfzone could be classified as plunging and spilling.

Svendsen (1987) demonstrated [by adopting Stive & Wind's (1982) measurements] that the temporal variation of the kinetic energy (k) over the wave cycle was almost constant, and thus it was assumed that for the majority of practical related studies a time-independent value of k would be of sufficient accuracy to describe the turbulent kinetic energy. It was also noted that in addition to the turbulence generated from the breaking wave, turbulence was also generated from the bottom boundary layer. However, by referring to the studies of Hansen & Svendsen (1984), the bed frictionl generated turbulence was an order of magnitude smaller that the breaker generated turbulence.

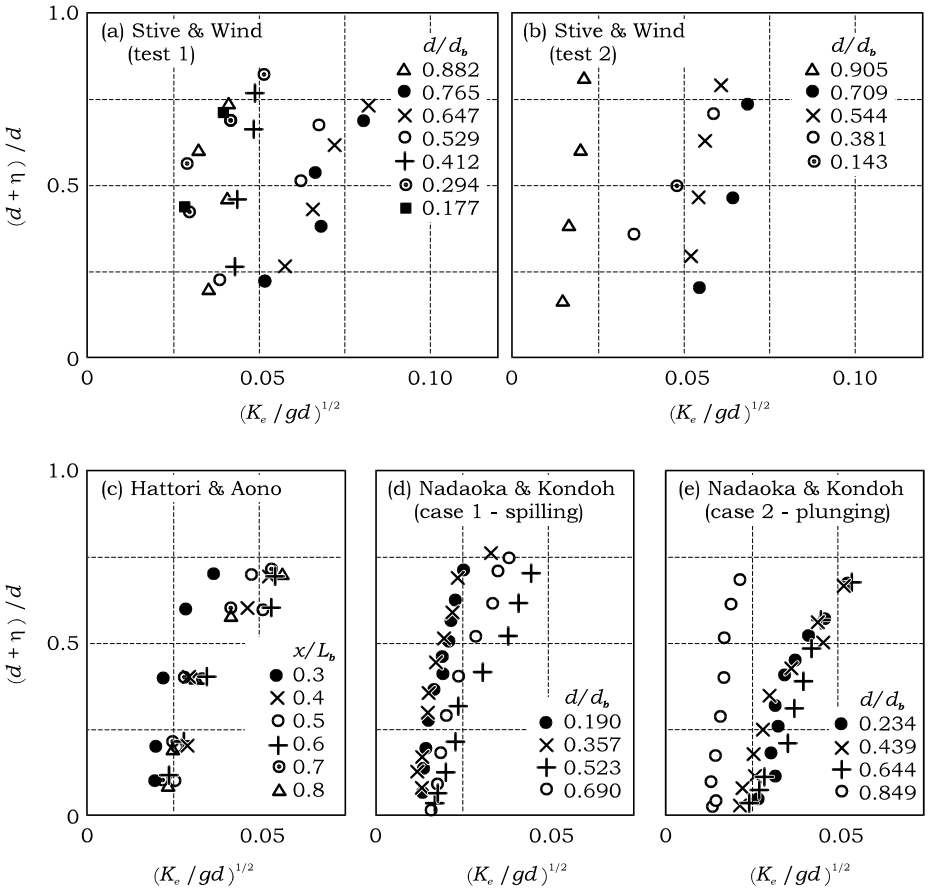

Figure 2.16 – Measurement of turbulent kinetic energies under breaking waves in surfzone, adapted from Svendsen (1987)

The experiments were performed under various test conditions such as spilling or plunging wave breaker types, and on two different beach slopes, which result in distinctly different hydrodynamic conditions. However, it is noticeable that there is little variation between tests in the recorded value of TKE. It is also evident from figure 2.16, that the vertical variation of k is small despite the turbulence being generated in the upper part of the water column. Based on these findings, Svendsen (1987) proposed that the length scale (l_m) of the eddies was closely related to the water depth (d) and suggested that

$$0.25d < l_m < 0.35d \tag{2.68}$$

Thus, by application of equation 2.64 it was concluded by Svendsen (1987) that under laboratory conditions, the variation of eddy viscosity (ν_t) across the surfzone generated by the breaking wave, could be characterised by the empirical relationship:

$$\nu_t = Md\sqrt{gd} \tag{2.69}$$

where M is a constant which lies in the range $0.01 < M < 0.03$.

The difficulty in accepting the findings reported by Svendsen (1987), is that when compared to the theoretical predictions of eddy viscosity derived by Bowen (1969), Thornton (1970) and Longuet-Higgins (1970) to explain longshore current distributions, a difference of at least an order of magnitude exists between the measured eddy viscosity values (Svendsen, 1987) and the eddy viscosity required to describe the observed longshore current data in mathematical predictions. Although the experimental studies cited by Svendsen (1987) could contain spurious results, it is unlikely any irregularities could explain an order of magnitude difference. Additionally, the results have been confirmed by three independent experimental studies. In § 2.5.2 it was noted that the surfzone is characterised by a cross-shore circulation mechanism. It would therefore appear that the unrealistically high values of eddy viscosity required to predict observed longshore current data in mathematical predictions, also incorporate the effects of the wave-induced cross-shore velocity, whereas the measured values of eddy viscosity incorporates only the effects of turbulent fluctuations.

Estimate of eddy viscosity seawards of the breaker point ($d>d_b$)

In the previous section it was noted that the turbulence was dominated by breaking wave effects in the surfzone. Seaward of the breaker point turbulence can be generated from two sources; the first is from the residual turbulence generated from the breaking, where the turbulence generated in the surfzone, is transported seawards by the undertow. A second source of turbulence is caused by the oscillatory wave motion flowing over the bed.

This section focuses on the determination of the eddy viscosity in the nearshore zone, seaward of the breaker line. Many of the analysis is derived from surfzone theoretical approximations of the eddy viscosity. It was shown in the previous section that, by adopting an appropriate value of the eddy viscosity within the surfzone, the longshore current could be modelled reasonably well to observed data. However, as suggested by Longuet-Higgins (1970) the selection of the eddy viscosity value was insensitive to the prediction of theoretical longshore currents.

Longuet-Higgins (1970) suggested that the eddy viscosity was related to the distance from shore, and assumed the same relationship beyond the breaker line, where the waves were not breaking. Much of the studies described in this section acknowledge that the wave induced turbulence is much less, seaward of the breaker line, and therefore propose that the eddy viscosity values reduces, when moving seaward.

Thornton (1970) assumed that the eddy viscosity decayed exponentially with distance from the shore. By adopting deep water wave conditions, it was suggested that the eddy viscosity seawards of the breaker point could be approximated by:

$$\nu_t = \frac{g d_b \gamma^2}{8\omega}\left[\frac{d_b}{d}\right]^{3/2} \tag{2.70}$$

James (1974) proposed that the eddy viscosity, beyond the breaker point was proportional to d^{-1}. The theoretical treatment of the eddy viscosity within the surfzone by Longuet-Higgins (1970) was adopted by James (1974), which led to the result that the eddy viscosity, beyond the breaker line could be given by:

$$\nu_t = \frac{N d_b^2}{md}\sqrt{g d_b} \tag{2.71}$$

For non-breaking wave conditions, De Vriend & Stive (1987) proposed that the turbulence within the flow was generated by the oscillatory wave motion over the bed, and suggested that the eddy viscosity, in its simplified form, could be given by:

$$\nu_t = 0.208\,\kappa d v_* \tag{2.72}$$

where v_* was the bed friction velocity in the on-off shore direction. Equation 2.72 has a similar form to the estimate for vertical turbulent diffusion, e_z given by Elder (1959) for open channel flows.

In the previous section, the theoretical variation of eddy viscosity across the surfzone derived by Svendsen (1987), was given by, $\nu_t = Md\sqrt{gd}$. Hence the mixing at the breaker point is given by, $\nu_{tb} = Md_b\sqrt{gd_b}$. To examine the decay of eddy viscosity with distance from the shore, Svendsen & Putrevu (1994) adopted the turbulent velocity measurements of Nadaoka & Kondoh (1982) to determine the cross-shore variation in eddy viscosity. The measurements showed that the turbulent intensity increased from the shoreline to a peak value at the breaker point, then decaying with distance beyond the breaker line.

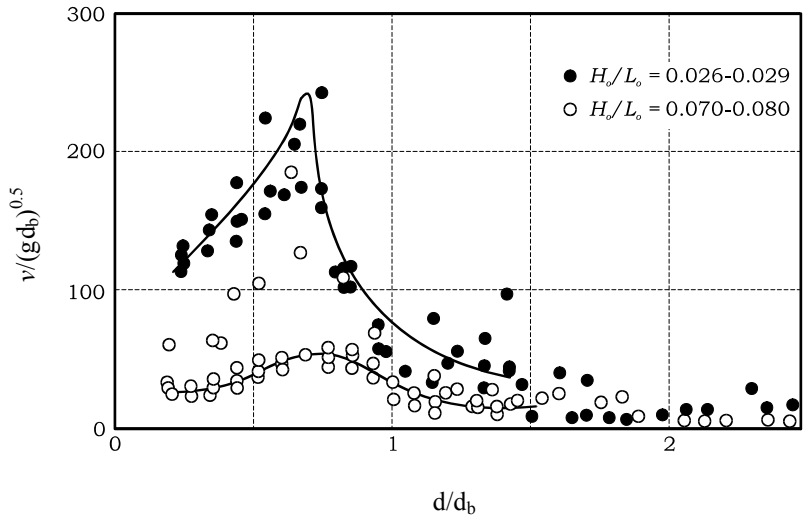

Figure 2.17 – Measurement made by Nadaoka & Kondoh (1982) of turbulent intensities in the nearshore region [adapted from Svendsen & Putrevu (1994)]

Figure 2.17 illustrates the results for Nadaoka & Kondoh (1982) measurements. It is clear that the surfzone contains high levels of turbulence, which is generated from the breaking wave. Seawards of the breaker point the turbulence decays, although considerable levels of turbulence are still present. This is probably the result of

turbulence generated in the surfzone which is transported seaward by the undertow. By continuing to move seaward, the magnitude of the undertow reduces. Thus, bed generated turbulence due to the oscillatory wave motion moving over the bed becomes the dominant process.

Svendsen & Putrevu (1994) therefore proposed that the variation of eddy viscosity with distance, seaward of the breaker line, could be given by:

$$\nu_t = (0.8(d/d_b)^{-4} + 0.2)\nu_{tb} \tag{2.73}$$

where $\nu_{tb} = Md_b\sqrt{gd_b}$ denotes the eddy viscosity at the breaker point. In a deep water region where the horizontal orbital velocities are negligible at the bed, it would be expected that the eddy viscosity generated by wave activity, reduces to zero. Equation 2.73 does not produce this effect at it has been derived from measurements in the nearshore region.

Figure 2.18 elucidates the proposed sources of turbulence within the nearshore region by adopting the suggested variation of eddy viscosity given by Svendsen & Putrevu (1994). As an example, the experimental conditions illustrated in figure 2.13 have been adopted [$m = 1/12, T = 1.14\text{s}, H_b = 0.085\text{m}$]. Figure 2.18a illustrates the assumed wave conditions. The surface elevation and associated orbital displacements outside the breaker point, have been predicted using Stokes' second order wave theory (Eq. 2.44 & 2.45). The breaker point and reduction in wave height due to energy losses in the surfzone have been predicted using the assumed theoretical breaking criteria, or breaker index, described by equation 2.42.

To predict the turbulence generated by the oscillatory wave motion over the bed, the theoretical analysis by De Vriend & Stive (1987) has been adopted (Eq. 2.72). In open channel flows, Kironoto & Graf (1994) reported that the bed shear velocity (υ_*) was approximately 10% of the depth mean flow. Thus, it is assumed that the shear velocity (υ_*) required in equation 2.72, is 10% of the average theoretical orbital velocity at the bed and that the orbital motion retains its character in the surfzone. The results obtained by adopting this simplified analysis are illustrated in figure

2.18b. Although not shown in figure 2.18b, the orbital motion at the bed reduces with increasing distance from the shore and hence, the eddy viscosity tended towards zero (1% of peak value) at approximately 17m from the shore line.

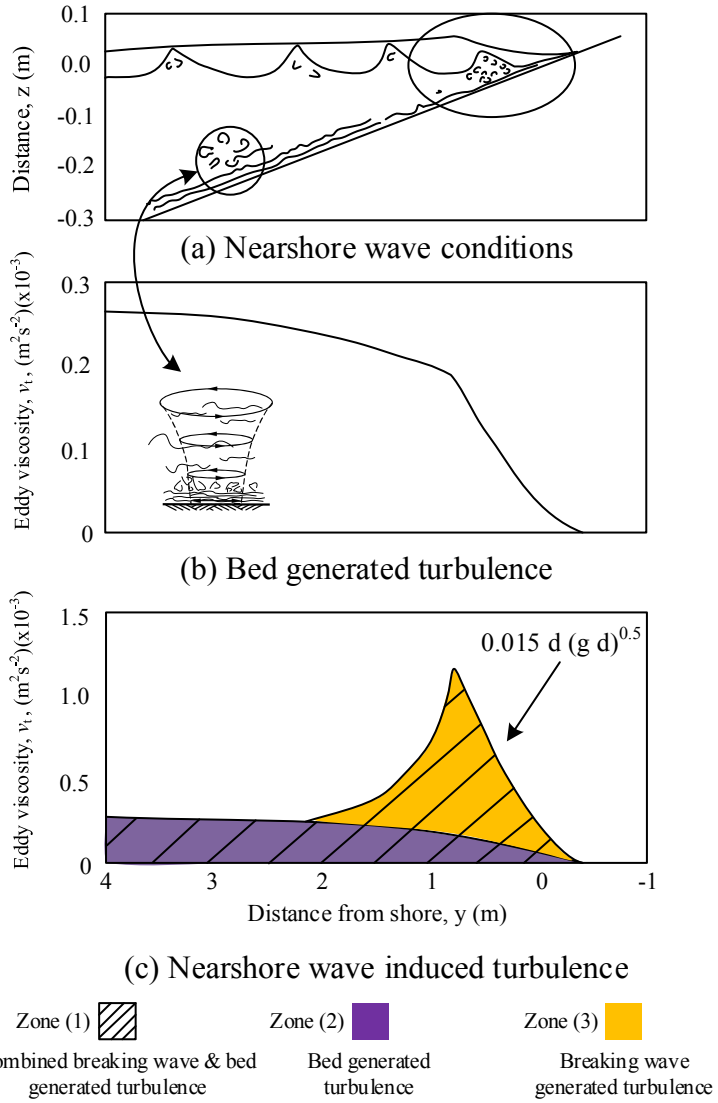

Figure 2.18 – Suggested sources of wave induced turbulence in the nearshore zone

Figure 2.18c illustrates the turbulence generated from the combined effects of breaker generated turbulence and bed generated turbulence. The analysis is based on the findings of the empirical studies adopted by Svendsen & Putrevu (1994) [Eq. 2.73]. Zone (1) illustrates the likely variation of eddy viscosity across the nearshore region, by adopting a value of $M = 0.015$.

In recognition that the suggested distribution of eddy viscosity was derived from measurements which include the effects of both wave breaker generated turbulence and bed generated turbulence, the theoretical description of bed generated turbulence utilised in figure 2.18b has also been plotted in figure 2.18c, denoted by zone (2). Calculation shows that at a distance of 3m from the shoreline, a value of $M = 0.015$ used in equation 2.73, gives a similar magnitude to that predicted by equation 2.72 for bed generated turbulence. Zone (3) illustrates the likely contribution to the combined wave generated turbulence, by the breaking wave. It is noted that within the surfzone, the breaking wave generated turbulence is approximately one order of magnitude higher than the bed generated turbulence, and is thus the dominant process. However, as one moves seawards to an approximate distance twice the surfzone width, and beyond, the predicted breaker generated turbulence is negligible, and thus the bed generated turbulence becomes the dominant process.

2.5.4 Experimental Study of Transverse Mixing

So far, it has been noted that the surface generated turbulence due to wave breaking processes and the bed generated turbulence due to bed frictions are the main sources of turbulence in the nearshore region. This section investigates experimental studies performed in the nearshore region to determine mixing estimates using solute tracers. A few solute tracer studies have also been included in deeper waters, where the breaking wave effects are negligible, in an attempt to determine the important parameters which influence the overall mixing processes.

The surfzone

Due to the highly non-linear nature of the surfzone, the variability and difficulties associated with measurement techniques, there are few experimental studies which undertake solute tracer measurements in the surfzone. This section investigates some important published studies which elucidate the transverse mixing processes.

Harris *et al*. (1963) undertook a series of experiments under field and laboratory conditions to investigate the mixing of a solute when released into the surfzone. Investigations concentrated on two sets of conditions whereby the waves either

approached the shore-normal or obliquely to the shoreline. For the purposes of this present study, discussion will concentrate on the shore-normal approach. Field study experiments were undertaken on a relatively straight, sandy coastline with a uniform underwater topography. In addition, a three-dimensional physical model was utilised to undertake further experimentation. Both the field and laboratory experiments produced similar observations. When waves approached normal to the coast, Harris *et al*. (1963) reported that long-shore currents were generated which moved in opposing directions along the beach, leading to the generation of intermittent rip currents.

Harris *et al.* (1963) noted that when the waves approached the shoreline normally to the beach, there were relatively long periods when long-shore and rip currents were not operating. During these periods, the measurements were undertaken. A radioactive tracer from a continuous point source was introduced into the surfzone. The subsequent spreading of the plume was detected by taking a number of discrete samples at a number of locations throughout the surfzone, these samples were later analysed. Visual observations showed that a slug of dye released into the surfzone, when compared to the along-shore direction, spread rapidly in the transverse (on-offshore) *y*-direction which was presumably as a result of the cross-shore wave-induced velocity transporting the tracer.

Harris *et al.* (1963) adopted the classical diffusion theory first developed by Taylor (1921) to analyse the results. By using an appropriate value of the diffusion coefficient (e_y), they attempted to visually fit the limited measured concentration values to the theoretical concentration profile. The results showed considerable scatter. However, as noted previously, a large cross shore circulation mechanism exists in the on-off shore direction. Thus, the reference to eddy diffusivity when related to concentration measurements, should perhaps be more correctly termed dispersion (D_y), as the effects of both diffusion and advection are clearly present.

To interpret the results, Harris *et al.* (1963) referred to the work of Harleman & Ippen (1960) who suggested that the eddy viscosity was proportional to the mean eddy size and to the rate of energy dissipation. The rate of energy dissipation, as

suggested by Harris *et al.* (1963) was proportional to the mean eddy size divided by the wave period. Based on the assumption that the eddy size was a function of the wave height, led to the result that the on-off shore mixing was proportional to the square of wave height divided by the wave period.

For the field studies, five tests were undertaken to determine the on-off shore mixing. The results in figure 2.19a, show the dispersion coefficient as a function of H^2/T. The results show considerable scatter, providing inconclusive evidence that dispersion was proportional to H^2/T. Harris *et al*. (1963) undertook further tests and analysis in a laboratory based experimental programme to determine and clarify the important variables in near-shore mixing processes. Similar test procedures to the field tests were adopted. The results for the laboratory based study are shown in figure 2.19b.

In the controlled laboratory conditions, and not withstanding some scatter, although showing some scatter, Harris *et al*. (1963) suggested that the dispersion was proportional to H^2/T.

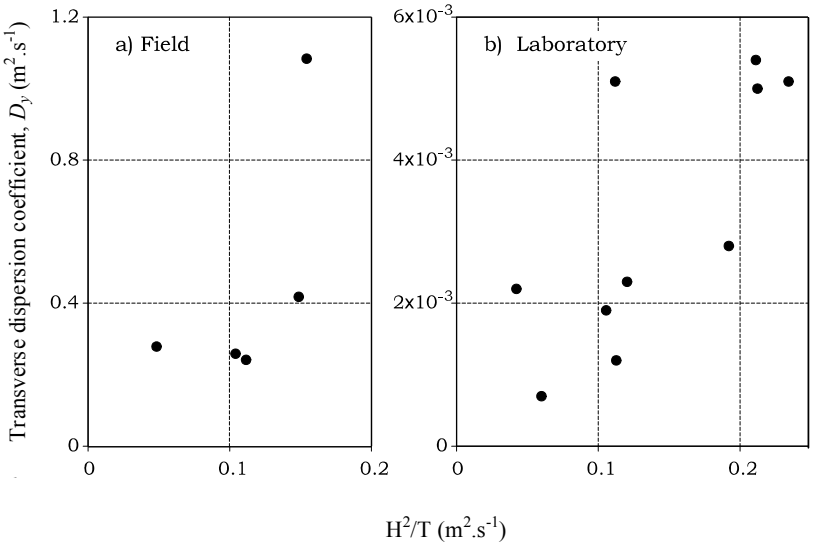

Figure 2.19 - On-off shore mixing characteristics for solute tracer studies in the surfzone (from Harris *et al*., 1963)

Field test studies within the surfzone of direct solute tracer experiments were reported by Inman, Tait & Nordstrom (1971). Solute tracer experiments were

conducted on two natural beaches; El Moreno Beach, Mexico and Scripps Beach, California. The beach at El Moreno had a relatively steep slope, $m = 0.04$ (1:25) and at Scripps Beach the slope was approximately $m = 0.0083$ (1:120) which resulted in significantly different mixing coefficients.

The measurement of the direction and magnitude of the waves entering the surfzone together with discrete concentration measurements were performed simultaneously. A slug of Rhodamine dye was released into the surfzone near to the breaker line and discrete samples of water were collected at various locations within the surfzone.

Preliminary investigations were made in which the mixing across the surfzone was much larger than in the longshore direction, again presumably as a result of the cross-shore circulation mechanism. They made observations in which a slug of dye released into the surfzone quickly dispersed across the zone, and only returned seawards through rip currents.

Inman *et al*. (1971) pointed out that it was difficult to isolate individual mixing mechanisms which contribute to the overall mixing processes. They suggested from observations that the mixing characteristics did not vary notably with time. In recognition of the complexity and the poorly understood mechanisms of breaking wave activity, they adopted an analogy to Fickian diffusion for the analysis technique. This simplified the analytical procedure in which they suggested that the results provided a reasonable fit to the observed measurements.

The diffusion coefficient, e_y (on-off shore direction) could be given by $e_y = \sigma^2/2t$ for a Gaussian concentration distribution (Fischer *et al*., 1979). In the absence of boundaries, it was also shown that the width of the concentration plume was equivalent to 4σ, where σ is the standard deviation of the tracer distribution. In the surfzone, Inman *et al*. (1971) treated both the shore line and the breaker line as boundaries, as observations showed that dye released into the surfzone stayed within the confines of the surfzone. To account for the boundaries, Inman *et al*. (1971) suggested the measured width of tracer distribution could be approximated to 2σ. Consequently, the surfzone width-averaged diffusivity, e_y was given by:

$$e_y = \frac{\sigma^2}{2t} = \frac{Y_b^2}{16t} \tag{2.74}$$

where Y_b denotes the width of the surfzone, and t is the time when the measured concentration at the boundaries of the surfzone equals one standard deviation of a theoretical unbounded Gaussian distribution. In Inman *et al*. (1971) analysis, they refer to the term diffusivity, e_y as the mixing parameter. Again, the term diffusion usually relates to the mixing generated by the turbulent fluctuations in the flow. In the surfzone, advection of the tracer due to wave-induced current is present, thus as with the Harris *et al*. (1963) study, the term diffusivity should perhaps be more correctly termed a dispersion coefficient. The exact location of the concentration sampling points were not reported in their analysis and only the final results were presented. The results of the study are shown in figure 2.20.

Figure 2.20 shows the comparison of the measured on-off shore dispersion, D_y, plotted against H_bY_b/T, where Y_b is the surfzone width. The results indicate that, as suggested by Inman *et al.* (1971), the width averaged dispersion coefficient is approximately equal to H_bY_b/T.

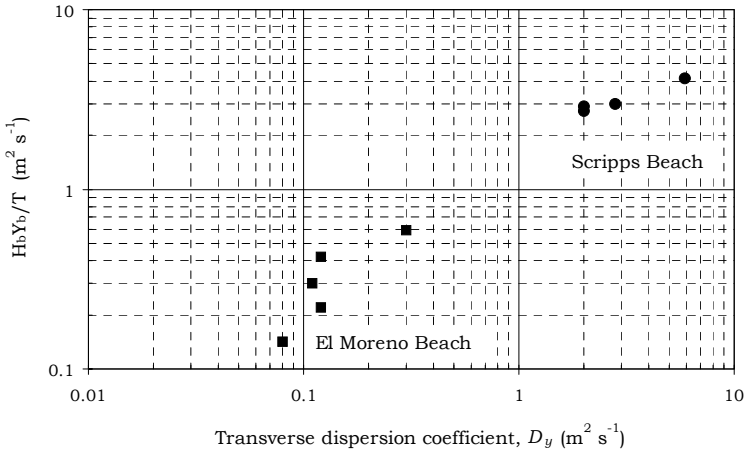

Figure 2.20 - On-off shore mixing characteristics for solute tracer studies in the surfzone (from Inman *et al*., 1971)

Tanaka *et al*. (1980) constructed a physical model to calibrate the dispersion of cooling water from a power station and compared results to field tests. A series of field studies under different wave conditions were performed, whereby small floats

were released into the surfzone, and subsequent the positions determined at certain time intervals.

Bowen & Inman (1974) summarised the studies of Harris *et al*. (1963) and Inman *et al.* (1971) and suggested that the width averaged transverse mixing coefficient, D_y was approximately equal to H_bY_b/T. The observed values of the previous studies of Harris *et al*. (1963) and Inman *et al.* (1971) together with the results of Tanaka *et al*. (1980) are shown in figure 2.21.

Figure 2.21 demonstrates that, as suggested by Bowen & Inman (1974), the transverse dispersion coefficient (D_y) follows the general trend of $D_y \propto H_bY_b/T$. However, further study of the results presented by Tanaka *et al*. (1980), show that the observed values were one order of magnitude lower than those of Inman *et al*. (1971). This difference may be due to the site specific nature of their study, or their adopted experimental procedure (such as the use of floats rather than a solute tracer) and analysis, which was not reported.

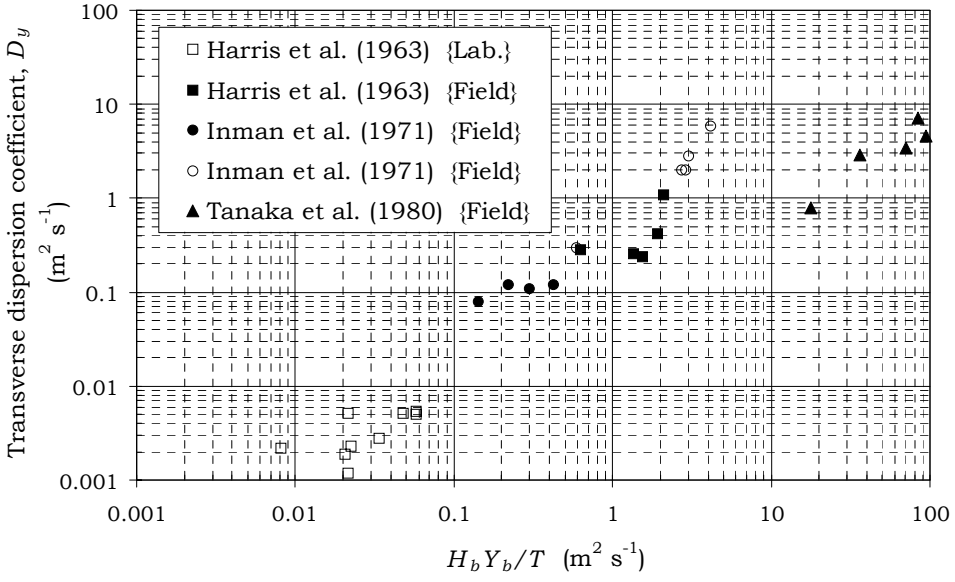

Figure 2.21 – Transverse (on-off shore) mixing characteristics for tracer studies in the surfzone

In recent years, Pearson *et al*. (2002) carried out a series of hydrodynamic and tracer measurements in the UK Coastal Research Facility (CRF) to investigated on-

offshore mixing. For locations inside the surfzone, Pearson *et al*. (2009) have shown that the transverse mixing is dominated by the effects of the cross-shore velocity and by adopting a theoretical approach, suggested that transverse mixing is proportional to $H^{3/2}$.

Spydell *et al*. (2009) undertook five days field study with use of GPS tracked drifters at Huntington Beach, California, to measure drifter's dispersion in the surfzone. They estimate diffusivities and dispersions, the results show that cross-shore diffusivity remains similar on all days. The longshore diffusivity was reported to increase monotonically for all time *t*. Spydell *et al*. (2009 and 2007) observations showed that alongshore diffusivity is higher than cross-shore diffusivity.

Clark *et al*. (2010) performed six days of field study with use of continuous dye releases to investigate cross-shore surfzone tracer dispersion in a wave driven alongshore current. Their observations show that tracer is advected with the mean alongshore current forming plumes that become wider and more diluted with the distance downstream. The concentration maxima for mean cross-shore profiles is often close to the shoreline with decreasing concentration towards offshore region. Clark *et al*. (2010) examined three potential mechanisms for cross-shore tracer dispersion in the surfzone. They concluded that, a breaking wave diffusivity show low correlation with the observations. The undertow driven shear dispersion estimates have high correlation with observations, but, under-predict the observed diffusivities and therefore, it cannot be the dominant term in cross-shore surfzone tracer dispersion. Clark *et al*. (2010) concluded that mixing-length parametrization based on 2D horizontal rotational velocities with use of surfzone width a length-scale has good correlation with observations. This suggest that mixing and dispersion in the surfzone is mainly due to eddies generated by shear instabilities or wave breaking.

Seawards of the breaker point ($d>d_b$)

So far, experimental solute transport studies in the transverse direction of the surfzone have been discussed. This section will review a number of experimental studies undertaken mainly in the field and in locations seawards of the breaker point.

Investigations will consider the mixing generated by waves in deep water where it is assumed that no upper bound limit of eddy size exists before examining the only known qualitative study of transverse mixing processes in the nearshore region.

A study to investigate the effect of wave activity in deep water conditions on the mixing processes was undertaken by Masch (1963). A laboratory based study was performed to investigate the surface mixing along the wave crest. The experiments were undertaken in a 30m long and 1m wide, closed wind-wave channel.

In order to determine the mixing processes along the waves crest, Masch (1963) utilised small polythene spheres released from a point source. The spheres floated on the water surface and were measured at given distances downstream from the injection point using a collection device, divided into a number of individual compartments, which spanned across the width of the channel. The resultant statistical distribution of the large number of particles released enabled the estimation of the lateral mixing along the wave crest under combined wind waves and currents.

Masch (1963) investigated the relationship of both water depth and wind speed on the diffusion processes. Over the range of depths (0.14 – 0.30 m) tested, it was found that the diffusion remained constant. Masch (1963) concluded that the turbulence generating the mixing, was mainly occurring at the surface and that the bed generated turbulence was of secondary importance. Since the measurements were taken at the surface where the primary driving force in the wave generation and resultant wave-induced currents were occurring, Masch's (1963) conclusion was not surprising. Masch (1963) demonstrated that the wind speed, W was closely related to the generated water surface current, u_s. It was shown that:

$$u_s \approx 0.027W \tag{2.75}$$

Masch's (1963) experiments were performed in an enclosed wind wave system which resulted in a return flow in the lower water column (undertow). It was noted

that changing the wind speed produced a corresponding change not only in the surface current u_s, but also the wave height (H) and wave period (T). Over the test section, it was reported that the waves were still developing, and thus, the significant wave height, H_s and T_s were calculated, defined as the average of the highest 1/3rd of wave heights.

Analysis showed that the dispersion (D_y) along the wave crest could be categorised by the simple relationship, $D_x \approx u_s^3 / g$. However, Masch (1963) noted that at any given surface velocity (u_s), the diffusion also increased with increasing wave activity. Although the simple relationship held for the conditions tested, he attempted to theoretically relate the dispersion to the physical properties of the waves generated. By assuming that the horizontal surface mixing could be characterised by the surface current and maximum horizontal orbital velocity of the wave, Masch (1963) showed that;

$$D_x \approx \frac{2\delta}{g\pi}\left(u_s \bar{q}_w^2 + \bar{q}_w^3\right) \tag{2.76}$$

where $\bar{q}_w$ denotes by the maximum orbital velocity of the wave and the wave steepness is given by $\delta = L/T$. In deep water conditions ($\omega^2 = gk$), the maximum orbital velocity can be simplified, to give; $\bar{q}_w = \pi H/T$.

Bowden *et al*. (1974) undertook a field based study to investigate the diffusive properties in deep water. They summarised the results from twenty-two tracer releases taken in several areas of the Irish Sea. A constant injection of Rhodamine dye was released from an injection point, near to the water surface, and moored to a buoy. The resultant concentration distribution was determined by traversing a sample vessel through the plume and continuously pumping a sample through a fluorometer, which was later analysed to determine the mixing characteristics.

Bowden *et al.* (1974) attempted to describe the data by assuming the dispersion was constant (i.e. $D_y = 0.5(d\sigma y^2 / dt)$), however the results showed considerable scatter,

and they found that the data could be better described by a power law function which better accounted for the large-scale eddy motion associated with unbounded domains, such as oceanic conditions. By measuring the velocity (u) in the direction of the plume, they converted the downstream distance from the source, x to a diffusion time and suggested that the dispersion coefficient could be given by;

$$D_y = \frac{1}{2} m a t^{(m-1)} \tag{2.77}$$

where a and m are constants to best describe the data. A value of $m = 1$, corresponds to a constant diffusivity, or Fickian diffusion.

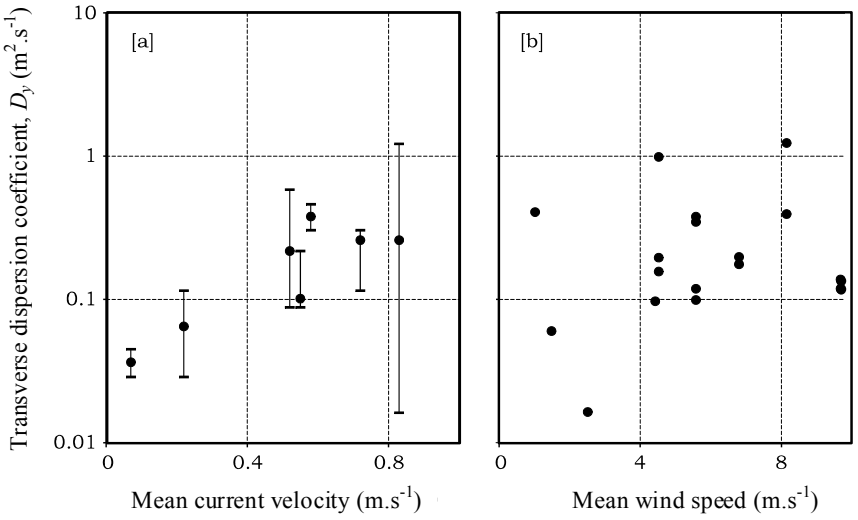

Figure 2.22 – Mixing characteristics for solute transport studies (from Bowden *et al*., 1974)

Observations from the experiments showed that the dispersivity increased with time. The results showed that the data could be best described by a power law function with $m = 2$. This allowed the dispersion to be expressed in the form $D_y = B^2 t$, where B is a constant labelled as diffusion velocity in their study. Figure 2.22*a* illustrates the relationship of the transverse dispersion with the mean current velocity. Although the data show considerable scatter, there is a general trend which suggests that the dispersivity is related to the mean velocity, which one would expect as Fickian diffusion is dependent on the turbulent velocity fluctuations.

Bowden *et al.* (1974) also investigated the effect of local wind conditions to the transverse solute mixing processes. The location and direction of the local wind conditions were not reported, but the results as shown in Figure 2.22*b*, show that the mixing processes are influenced by increasing wind conditions. Zeidler (1976) undertook a laboratory based experimental study to investigate the mixing characteristics of wave activity in the nearshore zone. The primary goal of the study was to investigate both the far field diffusive and advective behaviour of pollutants discharged to the sea. The experimental procedure and the location of the measurements with respect to the shore were not reported, but the results determined by Zeidler (1976) showed that diffusion generated by waves in the absence of currents was constant. Figure 2.23 shows the results of both the transverse dispersion (in the direction of wave propagation), D_y and the longitudinal dispersion (in the direction of the wave crest), D_x reported by Zeidler (1976). They demonstrated that the mixing in both orthogonal directions could be characterised by a dimensionless wave parameter, $R_{w,}$, given by;

$$R_w = \frac{H^2}{4T}(\sinh \omega h)^{-1/4} \tag{2.78}$$

The results as derived by Zeidler (1976), show that the dispersivity increased with R_w after reaching a critical value. It was also apparent that the mixing in the along the wave radius, D_y was approximately 4 times the mixing along the wave crest, D_x.

Elliott *et al.* (1997) summarised the results from twenty-three field studies, mostly of discrete tracer slug injections, performed at nearshore locations (water depth $< 15\,m$) around the coast of Ireland. The aim of the study was to determine the effects of water depth, tidal current and wind speed on the mixing processes.

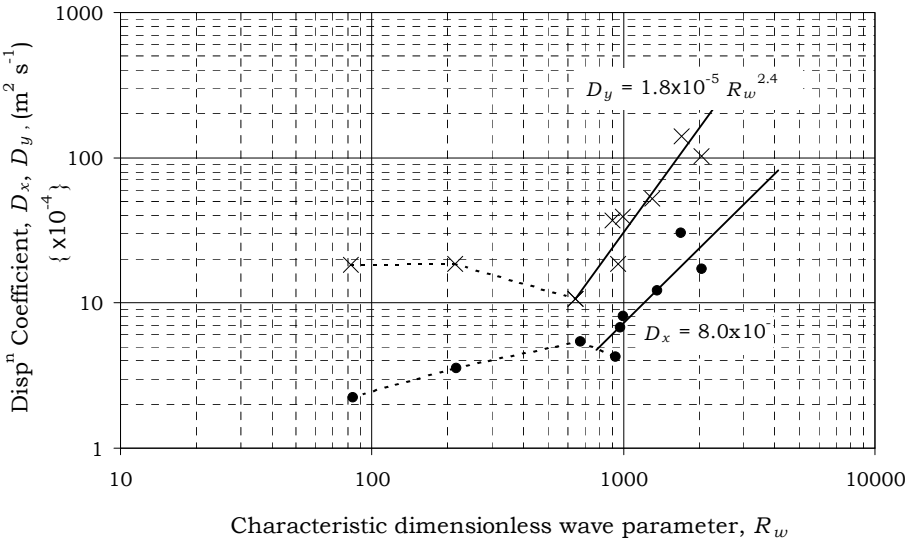

Figure 2.23 – Mixing characteristics for solute tracer studies adopted from Zeidler (1976)

A discrete slug of dye was released at the surface of the near shore location. The subsequent dye plume was monitored for a period of 2 – 5 *hrs*, by continually traversing both longitudinally and transversally through the plume with a small sampling vessel. The dye was monitored by continually pumping a water surface sample through a fluorometer, and the output recorded onto a chart recorder. The location of the sample craft was monitored continuously by using a shore-based tracking system. The longshore current was determined by using a velocity meter located on a moored vessel and an estimate of the wind was measured using a hand-held anemometer. Observations showed that the dye became vertically well mixed soon after the dye release.

Elliott *et al*. (1997) assumed that the width of the dye plume was defined at the location where the concentration reached 1% of the peak value. To simplify the analytical procedure, they used a method similar to Inman *et al*. (1971) in which it was assumed that the width of the concentration plume was equivalent to 4σ, where σ was the standard deviation of the tracer distribution. By assuming that the diffusive spreading was constant with time, they assumed that the diffusion could be given by $D_y = 0.5u(d\sigma_y{}^2 / dx)$, where u was the representative tidal current. The results for the transverse mixing coefficient under varying environmental conditions are shown in figure 2.24.

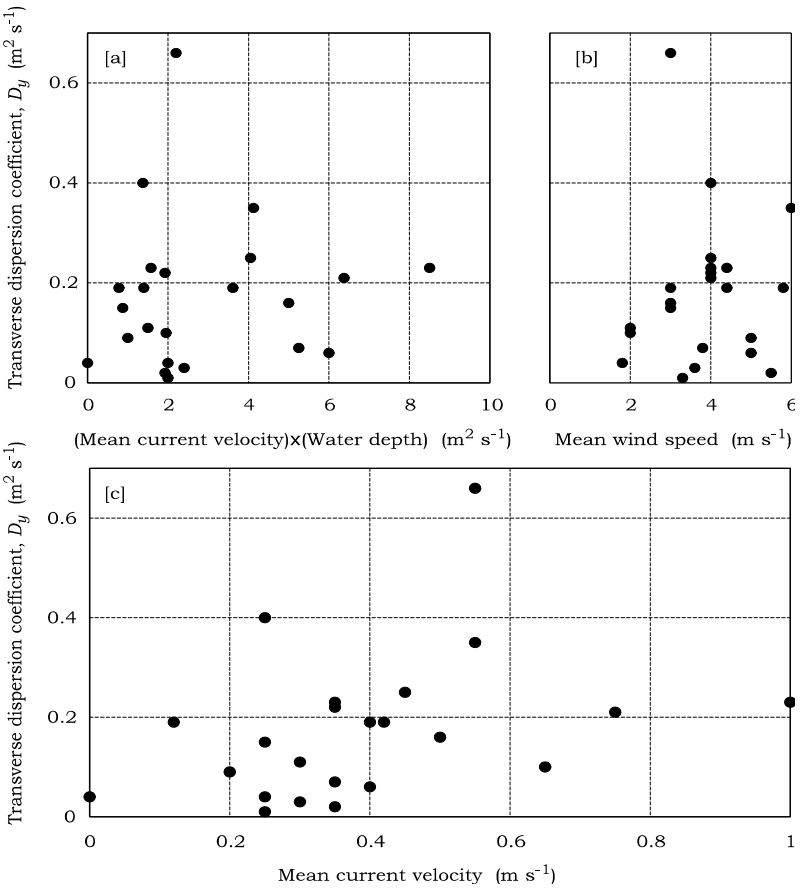

Figure 2.24 - On-off shore mixing characteristics for solute tracer studies in the nearshore zone adopted from Elliott et al. (1997)

The experiments had a bias towards low wind speeds (due to the size of sampling vessel), nevertheless the results as shown in figure 2.24*b* demonstrate that the mixing increases with wind speed. Figure 2.24*c* shows the relationship of transverse mixing with mean tidal current, and results show a general trend in that the mixing increases with current.

Elliott *et al*. (1997) determined the along-plume dispersion coefficient, D_x, and found that $D_x \approx 12D_y$. By incorporating the along and across-plume mixing effects, and accounting for the expected scatter of field results, they showed that a one-dimensional dispersivity, D_H could be described by, $D_H = 0.15u + 0.04W$, where W is the mean wind speed [m/s]. Thus, they concluded that the mixing was dominated by the tidal current and that the wind-induced mixing was of secondary importance, but suggested that this may have been a result of the measurements having a bias towards relativity low wind speeds.

Pearson *et al*. (2002) preformed a series of hydrodynamic and fluorometric measurements for locations seaward of the breaker region. They suggested that in the region seawards of the breaker point, the mixing increased with the square of the wave height (H). Pearson *et al*. (2002) results show that for longitudinal currents with no wave activity, the cross-shore diffusivity is approximately constant with an average value of $0.22du_*$, which is in line with the higher end of the Rutherford (1994) laboratory studies and also in good agreement with the diffusivity values of straight natural channels.

2.6 Summary

In this chapter, a review on mixing and dispersion in the nearshore was presented. The key nearshore parameters and mixing mechanisms were discussed. The review highlighted the existing knowledge on mixing and dispersion mechanisms in the nearshore and the gap in analytical model and experimental data for quantifying mixing mechanisms. In the next chapter, the theoretical approach for quantifying mixing due to the effects of waves and currents is presented.

CHAPTER 3

THEORETICAL APPROACH

3.1 Synopsis

In this chapter, the mechanisms which influence the mixing and dispersion in the nearshore region are discussed in detail mathematically and theoretically. The underlying concepts of mixing in the nearshore are discussed from the viewpoint of understanding the mixing mechanisms. A theoretical model based on hydrodynamics of the nearshore is postulated to quantify the mixing and dispersion due to the combined effects of waves and currents.

3.2 Mixing in the Nearshore

Nearshore regions have been subjected to pollution loading for decades. These contaminations are entering the coastal region from two sources of shoreline and offshore boundaries. Currently, only 27% of water bodies in England are classified as having ‘good status’, according to new standards set down by the EU Water Framework Derivative (Water Framework Directive, 2015). An understanding of the complex nearshore processes that effect the physical dispersion of the wastes in coastal waters can result in improving the water quality in the nearshore zone and advance water quality modelling (Abolfathi & Pearson, 2014).

The nearshore zone is the most dynamic part of a coastal region in which the wave breaking phenomena occurs. In this region, the hydrodynamic behaviour is influenced by a complex three dimensional flow field and a spatially variable flow depth. The combination of periodic orbital motions of the waves and the vertical and transverse shear effects are the primary reasons for the complex flow field. Figure

3.1 represents the schematic of the complex flow field in the nearshore region under the combined influence of waves and currents.

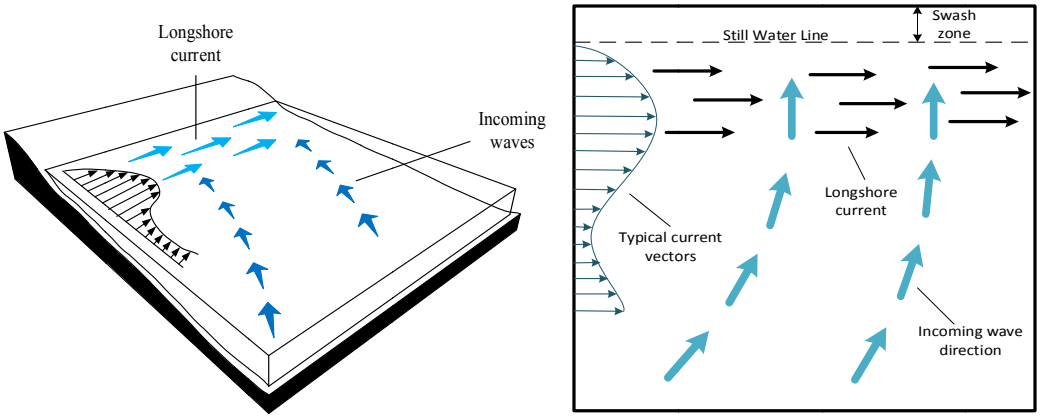

(a)

(b)

Figure 3.1 – Schematic view of (a) wave-current interaction in the nearshore region (b) complex flow field due to the effects of wave and currents

The nearshore region is a dynamic and constantly evolving environment which is shaped by interacting processes encompassing different spatial and temporal scales.

These processes are generated through complex feedback between wind, waves, currents and morphology.

Predicting the mixing coefficient in the nearshore region is challenging due to quantifying the bed and surface generated sources of turbulence, the effects of Stoke's drift, the interaction of the periodic orbital motions of the waves and the shearing effect resulted from longshore currents (Svendsen & Putrevu, 1994; Pearson *et al*., 2009; Abolfathi & Pearson, 2014). As discussed earlier in chapter 2, there are good fundamental theories for mean velocity determination in the nearshore region (Stokes, 1847; Longuet-Higgins & Stewart, 1960, 1964). However, limited data are available from measurements. Mixing processes have been theoretically described in recent years, but there are relatively few experiments to validate (details in §2.5.4) those findings. Furthermore, due to the lack of data, the coastal water quality models are limited in their predictive capability.

A wide range of mixing processes happen within coastal waters. The mean water depth, the bed roughness length z_o, the tidal frequency, the horizontal buoyancy gradient, surface buoyancy flux and the surface wind friction velocity, are the main parameters which contribute to the mixing phenomena (Spydell *et al*., 2007; Burchard, 2009; Souza *et al*., 2014). The surface wave parameters, surface elevation amplitude, horizontal buoyancy direction, phase difference between surface elevation and current velocity, also affect the mixing and dispersion in the nearshore region.

The nearshore is a region of high energy where the incident surface gravity waves break and dissipate their energy. In the nearshore zone, currents are primarily driven by wave actions near the breaker zone and include both cross-shore and long-shore currents. The key variables influencing the nearshore mixing processes are the intensity, frequency and direction of the incident wave climate, and most importantly, the dimensions of nearshore circulatory cells (Inman *et al*., 1971). Hydrodynamic processes within the nearshore have various time and space scales. The time scale of these processes can range between a few seconds (e.g., turbulence, wind generated waves) to 24hrs (e.g., tides and longshore currents), and the length

scale can vary from a few centimetres (e.g., turbulence) to hundreds of kilometres (e.g., tides, longshore currents). Figure 3.2 shows the time and length scales for some important hydrodynamic processes in the nearshore region.

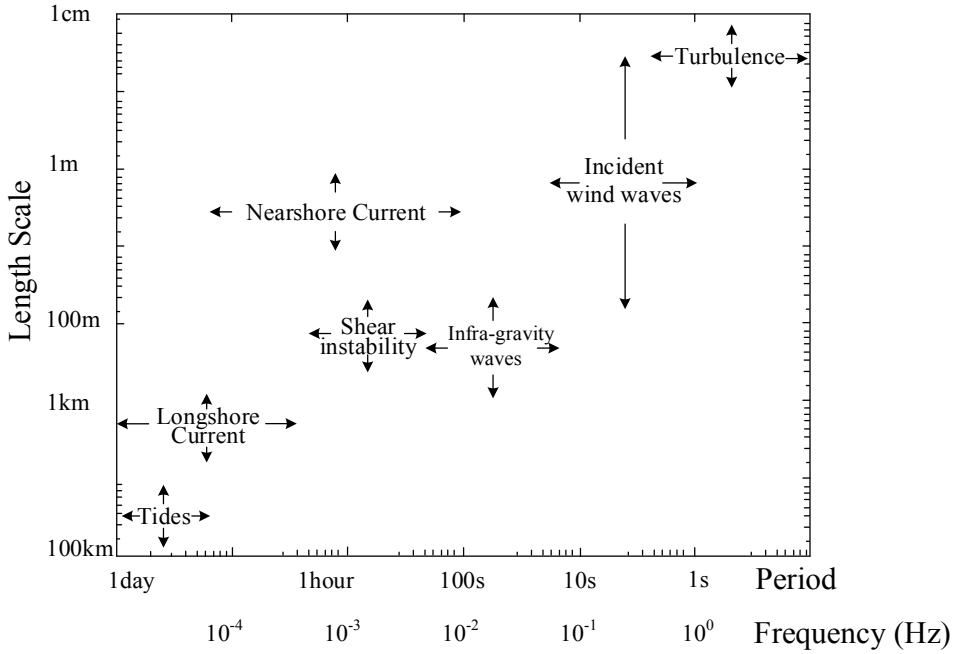

Figure 3.2 – The Temporal and spatial scales of hydrodynamic processes in the nearshore, adopted from Souza *et al*., (2014)

Longshore and cross-shore currents are the two main flow mechanisms that contribute to various transport exchanges within the coastal waters. Cross-shore currents include the undertow, mean current systems, which is derived from radiation stress (Longuet-Higgins & Stewart, 1960), and the setup gradients caused by the wave breaking and the associated onshore mass transport of water (Messelink & Black, 1995). The undertow may be considered as vertically segregated flows which consist of the wave-induced onshore mass transport in the upper layers of the water column and the offshore undertow close to the bed (Svendsen, 1984; Longuet-Higgins, 1970).

Obliquely incident waves near the beach generate the longshore currents. As discussed in chapter 2, Longshore currents are normally analysed based on a depth-

averaged approach proposed by Longuet-Higgins (1970). The deriving mechanism for the longshore currents is the alongshore momentum (radiation stress gradients, ∇S_{xx}) transfer from the incident wave field to the mean long-shore current. Thornton & Guza (1986) proved that the Longuet-Higgins (1970) solution is very accurate in predicting longshore currents on monotonic beach profiles.

The surface and bed generated turbulences resulting from wave activity in the nearshore are an important mixing process within the shallow coastal water column. In addition to the wave activities, coastal currents and wind are other major contributors to the mixing (Souza *et al*., 2014). Surface generated turbulence is produced by wave breaking in the surfzone, whereas the bed generated turbulence is mainly derived by mean currents at the bottom boundary layer (Inman *et al*., 1971). Turbulence generated in the nearshore leads to two main mixing mechanisms. The first suggested mechanism is proposed by Inman *et al*. (1971). They investigated the mixing in the surfzone and reported that the turbulence due to the wave breaking phenomena causes rapid mixing along the path of the wave bore in the cross-shore direction. They furthermore proposed cross-shore eddy diffusivity coefficient (Eq. 3.1) by normalizing and averaging the mixing value over the surfzone width Y_b:

$$e_y = \frac{H_b Y_b}{T} \tag{3.1}$$

where H_b represents the wave height at breaker point and T is the incident wave period. The second suggested mixing mechanism is caused by the wave-current interaction which induces transport in both the longshore and cross-shore directions. Wave-current interactions create circulation cells of longshore and rip currents (Fig. 3.3) in the seaward direction. Therefore, they are responsible for a continuous interchange of water between the nearshore and offshore region (Souza *et al*., 2014).

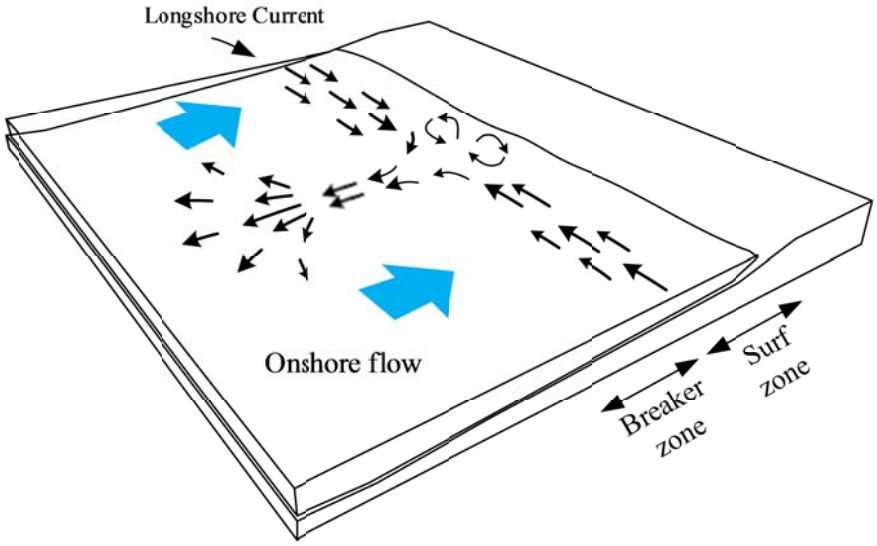

Figure 3.3 – Schematic of circulation cells of longshore currents and rip currents

Inman *et al*. (1971) found that for a beach with a constant longshore current, the eddy diffusivity v_t is a function of the longshore current velocity. They suggested that $e_y = H_b X_b / T$ and v_t ranges between 10 $m^2 s^{-1}$ and 100 $m^2 s^{-1}$ for open beaches. Feddersen (2007) undertook a field experiment with dye tracers and proposed cross-shore diffusivity of a passive tracer in the broken wave condition (Eq. 3. 2):

$$\frac{\alpha H_s^2}{\overline{T}} \tag{3.2}$$

where H_s is the significant wave height, $\overline{T}$ is the mean period and α is estimated to be 20.9 ± 5 based on Feddersen (2007) field measurements. For the longshore currents, Feddersen (2007) proposed that diffusivity is a function of alongshore current and surfzone width:

$$\zeta \left| \overline{v}_m \right| Y_b \tag{3.3}$$

where $\bar{v}_m$ is the maximum alongshore current, Y_b the surfzone width and ζ is a dimensionless parameter which is estimated to be 0.52 ± 0.08, from Feddersen (2007) field data. De Vriend and Stive (1987) studied turbulent diffusion by adopting the methodology developed by Fischer (1979) and Battjes (1983). They predicted the eddy viscosity by considering the effects of breaking waves and oscillatory bottom boundary layer.

Inman *et al*. (1971) stated that despite the highly energetic nature of the nearshore region with constant turbulence generation and dissipations, the scales of mixing are limited. Specifically in the nearshore region, the mixing happens in the surfzone where it is confined between the breaker region and the shoreline. Consequently, the mixing is limited to the width of the surfzone (Bowen & Inman, 1974).

Spatially variable currents in the nearshore region have been studied in a few studies by using a fixed frame of reference Eularian measurement technique. These measurements rely on deployment of an array of stationary sensors that measure the current properties from a fixed reference point. George *et al*. (1994) investigated turbulence in the surfzone by both laboratory and field studies as well as using a fixed frame of reference at a specific location. Trowbridge & Elgar (2001) utilised dual-sensor techniques that remove the contamination by surface waves to study near-bottom surfzone hydrodynamics. They examined an approximate alongshore momentum balance between wind stress and near-bottom turbulent Reynolds stress. Trowbridge & Elgar (2001) used an array of five upward-looking Sontek Acoustic Doppler Velocimeters (ADVs) that was mounted on a low-profile frame, and measured three-dimensional velocity vectors in a sample volume with a spatial scale of ~ 0.01m (Elgar *et al*., 2005). Feddersen *et al*. (2007) studied cross-shore tracer's dispersion in the surfzone with a Eularian approach over a range of time and space-scales. Generally, Eularian techniques are sensitive to the number of sensors utilized to record the spatial scales of motion. This imposes a restriction on the mixing and dispersion coefficients obtained from analysing the Eulerian measurements. However, Lagrangian approaches such as dye tracers and drifter measurements have also been employed in the study of mixing and dispersion in the nearshore.

Harris *et al*. (1963) was one of the first studies that investigate dispersion of dye by tracking fluorescent dye. Inman *et al*. (1971) and Bowen & Inman (1974) investigated different aspects of the mixing due to waves and currents in the nearshore area by using dye tracers in the field experiments. They defined three different mixing mechanisms due to the surface waves including the processes associated with the wave motion seaward of the breaking point, the mixing due to the breaking wave and the large scale mixing due to the movement of water in longshore and rip currents.

Rodriguez *et al*. (1995) employed Lagrangian tracers to study pollution dispersion in Spanish coasts. Takewaka *et al*. (2003) studied longshore currents in Japan by investigating dye diffusion in the longshore current field. Grant *et al*. (2005) studied alongshore transport of pollution at Huntington Beach by dye experiments and faecal indicator bacteria monitoring. Grant *et al*. (2005) showed that alongshore flux of surfzone water is at least 50 to 300 times larger than the cross-shore flux of surfzone water. Clark *et al*. (2014) used fluorescent dye and aerial imaging technique to study nearshore mixing.

Feddersen (2007) studied breaking wave induced cross-shore tracer dispersion in the surfzone. Spydell *et al*. (2007) carried out field experiments and utilized drifters to study about 200 m of the shoreline within the surfzone (at depths of less than 5m) and with the alongshore uniform bathymetry and waves. There is a large variation in the value of eddy diffusivity coefficient reported by the studies mentioned above (from 0.025 m^2s^{-1} [Takewaka *et al*., 2003] to 8 m^2s^{-1} [Inman *et al*., 1974]). Feddersen (2007) concluded that this large variation is due to the differences in the experimental methods and the difficulties of the dye tracing method.

Applications of Lagrangian drifters in studying the mixing and dispersion have been mainly limited to large-scale offshore and oceanic filed studies (Souza *et al*., 2014). Drifter technology has been adopted to measure diffusivity in estuaries and coastal waters (List *et al*., 1990; Tseng, 2001).

This section briefly presented the mixing processes and the background on mixing and dispersion studies in the nearshore region. In the following sections of this chapter, the theoretical approach adopted in this study for quantifying mixing mechanisms in the nearshore will be described.

3.3 Theoretical Approach

In this section, the mixing and dispersion is investigated from a theoretical point of view. The mixing mechanisms in the nearshore are studied with a special attention toward the mixing in the on-offshore direction. The existing theories and literature, which were discussed in chapter 2 are used to develop a theoretical approach for quantifying mixing mechanisms in the nearshore.

The advection-diffusion equation is the governing equation for contaminant transport in environmental fluid mechanics. For shallow waters in the coastal area, considering a wide beach with the homogeneous velocity vector and $u(z)$ and $v(z)$ varying with depth but not in the spatial directions x and y, we can write the equation for the advection and diffusion of a dilute solution of a non-reacting tracer. Equation 3.4 presents the two-dimensional horizontal Fickian advection-diffusion equation (Falconer *et al*., 1992; Rodriguez *et al*., 1995):

$$\frac{\partial \bar{c}}{\partial t} + \overline{U}_i \frac{\partial \bar{c}}{\partial x_i} - \frac{1}{h}\frac{\partial}{\partial x_i}(dE_{ij}\frac{\partial \bar{c}}{\partial x_i}) = -\frac{\bar{c}}{T_d} \qquad (3.4)$$

where i represents x in the on-offshore direction and j represents y, which is the longshore axis, d is the total depth of water, $\overline{U}_i$ is the depth averaged velocity, $\bar{c}$ represents the depth averaged mean concentration, T_d is the characteristic timescale and E_{ij} is the depth averaged diffusion-dispersion coefficient. As discussed earlier in chapter 2, the wave breaking phenomena is the dominant cause of mixing in the surfzone. It generates two strong mixing and dispersion mechanisms due to the surface generated turbulence of the breaking wave, and the shear dispersion induced by the vertically non-uniform structure of the period averaged flow (Karambas, 1999; Pearson *et al*., 2002 & 2009; Abolfathi & Pearson, 2014).

As pointed out in chapter 2 (§2.5.4), in the pioneering work of Harris *et al*. (1964), Inman *et al*. (1971) and Tanaka *et al*. (1980) on the nearshore mixing, there is no distinction between the turbulent diffusion and shear dispersion. Also, there is no complete theoretical approach to consider all the above mentioned mixing mechanisms. In this study, the turbulent diffusion (§3.4.1) and the shear dispersion coefficients (§3.4.2) are derived theoretically and the formulae are compared and validated with the existing data and the laboratory measurements.

3.4 Nearshore Mixing Processes

In equation 3.4, the mixing coefficient (E_{ij}) consists of turbulent diffusion and advective shear dispersion. Therefore, the combined mixing coefficient in the on-offshore and longshore directions can be given by equation 3.5:

$$\begin{aligned} E_x &= v_t + D_x \\ E_y &= v_t + D_y \end{aligned} \tag{3.5}$$

where v_t represents the depth-averaged horizontal eddy viscosity which represents the turbulent diffusion coefficient, D_x is the advective shear dispersion in the on-offshore direction and D_y is the advective shear dispersion coefficient in the longshore direction.

Fischer *et al*. (1979) postulated equation 3.6 for the dispersion coefficient, which is derived from the three dimensional advection-diffusion equation (Taylor, 1954). This solution is just valid for large times when the deviation of the concentration $c'(z)$ from its depth averaged value is small and therefore c varies very slowly and $\partial c/\partial x$ is almost constant over a long period of time (Fischer *et al*., 1979).

$$D = \frac{1}{d}\int_0^h u' \int_0^z \frac{1}{v_z} \int_0^z u' dz dz dz \tag{3.6}$$

In equation 3.6, v_z is the vertical eddy viscosity coefficient and u' represents the deviation of velocity from the depth averaged velocity. For the steady turbulent flow without any waves, the longitudinal shear dispersion and the turbulent diffusion coefficients have been studied by Elder (1959), Holly *et al*. (1984), Chikwendu (1986) and Pearson *et al*. (2002). The proposed formulae for this case are derived based on the assumption of a logarithmic velocity profile. All these relations are based on von Karman's constant, depth of water and the shear velocity. By adding the wave to this system, the turbulence generation due to the orbital motion of the waves and wave breaking will increase, which in turn affects the turbulent diffusion coefficient (Karambas, 1992). On the other hand, the presence of the waves and oscillatory flow will cause a non-uniform over the depth wave-induced current which will increase the advective shear dispersion (Chikwendu, 1986). As a result, in the nearshore area, existence of waves and currents increase the contribution of the turbulent diffusion and the shear dispersion in the overall mixing coefficient. § 3.4.1 and § 3.4.2 will investigate the effects of nearshore waves on quantifying the turbulent diffusion and shear dispersion coefficient.

3.4.1 Turbulent Diffusion

The turbulent diffusion coefficient is generally equal to the eddy viscosity coefficient [Svendsen and Putrevu, 1994; Karambas, 1999]. De Vriend & Stive (1987) derived equations for quasi three-dimensional modelling of nearshore currents and defined the turbulence viscosity as:

$$v_t = \bar{v}_t(x, y, t)\phi\left(\frac{z - z_b}{h}\right) \tag{3.7}$$

where, $\bar{v}_t$ is the depth averaged eddy viscosity and ϕ is the vertical distribution function. De Vriend & Stive (1987) combined the Boussinesq hypothesis with an algebraic relationship between the turbulence viscosity and the flow velocity considering an increase of the turbulence production and the eddy viscosity, due to

the wave orbital motion. Coeffey and Nielsen (1984) proposed a constant value of v_t for a part of a wave boundary layer (Eq. 3.8).

$$\bar{v}_t = M_h \delta (1 - \frac{\delta}{d}), \quad z - z_b < \delta \tag{3.8}$$

where, d is the water depth, z_b denotes the bottom level and M_h is a constant to be estimated from field data. Breaking waves results in additional turbulence production. Stive and Wind (1986) estimate the eddy viscosity of breaking wave below the trough level as a function of wave celerity and the water depth ($v_t = 0.01Cd$). However, they could not specify the vertical distribution of v_t. Battjes (1983) proposed that the horizontal diffusion coefficient in wave driven currents, which relate the turbulent diffusion to the mean rate of wave energy dissipation per unit area (D_b).

$$\bar{v}_h = dM_h (D_b / \rho)^{1/3} \tag{3.9}$$

In above equation, M_h is a constant to be estimated from experimental and field data and is of the order *O*(1). For the breaking waves which are in combination with currents, the vertical diffusion coefficient is suggested by De Vried and Stive (1987):

$$v_t = 0.208\kappa.d.w_* + M_h.d.(D_b / \rho)^{1.3} \tag{3.10}$$

Where κ is von Karmen constant, w_* is the current friction velocity. In equation 3.10, the first term of RHS is similar to the equations which are derived for turbulent diffusion coefficient of the open channel flow (Fischer *et al*., 1979). However, the additional mixing due to the orbital motion of the waves is incorporated through the wave and current friction velocity, w_*. The second term in RHS considers the effect

of the surface generated turbulence caused by the wave breaking. The rate of the wave energy dissipation studied by Battjes and Janssen (1987) is:

$$D_b = Q_b \rho \frac{1}{4T} g \frac{H^3}{h} \tag{3.11}$$

where ρ denotes the density of water, H is the wave height and Q_b represents the fraction of the breaking waves. Svendsen (1987) related the eddy viscosity to the turbulent kinetic energy (TKE) and the turbulent length scale (Eq. 2.64). Hence, the turbulent diffusion can be related to wave energy dissipation as:

$$v_z = l_m k^{1/2} \tag{2.64}$$

where l_m is the turbulent length scale (Svendsen, 1987) usually taken as a function of water depth (Putrevu & Svendsen, 1994) and k is the turbulent kinetic energy that shows the deviation of turbulent fluctuation velocity component from the mean velocity component. Equation 2.64 can be rewritten in terms of wave energy dissipation (D_b):

$$v_z = l_m \left(\frac{\beta}{C_d} \frac{l_m}{d}\right)^{0.33} \left(\frac{D_b}{\rho}\right)^{0.33} = M.d.\left(\frac{D_b}{\rho}\right)^{0.33} \tag{3.12}$$

$$\& \qquad M = a\left(\frac{\beta a}{C_d}\right)^{0.33}, \; l_m = ad \tag{3.13}$$

In which the turbulent length scale (l_m) is proportional to the local water depth. Pedersen *et al*. (1998) examined the turbulence under broken waves and determined the turbulent length scale to be between $0.25-0.3d$. Putrevu and Svendsen (1994) investigated length scale of the turbulence inside the surfzone and used similar length scale. In equation 3.12 and 3.13, M is turbulent constant equal to 0.025 in the region below the trough level (De Vried, 1987). C_d is a constant which is considered approximately 0.09 (Svendsen, 1987; Karambas, 1999). Svendsen (1987)

estimated the turbulent dissipation below the trough level by multiplying β (fraction) by the mean rate of wave energy dissipation per unit area (D_b).

Measurements of TKE in the nearshore region for breaking and non-breaking conditions show that the vertical variation of TKE over the depth is not substantial (Svendsen, 1987; Ting & Kirby, 1994; Karambas, 1999; Hattori & Aono, 1985; Nadaoka & Kondoh, 1982; Stive & Wind, 1982; Battjes & Sakai, 1981; Abolfathi & Pearson, 2014) and hence, it is a valid assumption to consider uniform distribution of the eddy viscosity over the depth. Svendsen and Hansen (1988) proposed the same assumption for the parabolic distribution of the undertow velocity. Using the above assumptions and based on equation 3.10, the eddy diffusivity coefficient below the trough level can be determined as:

$$v_{t-trough} = 0.208\kappa.d.w_* + 0.025d(D_b/\rho)^{1.3} \tag{3.14}$$

Only 2 – 5 % of the total wave energy dissipates below the trough level (Svendsen, 1987). In other word the fraction (β) under the trough level is 2 – 5% and therefore, equation 3.14 can be written for the wave crest by substituting $\beta = 0.95 - 0.98$ (total fraction is 1) and $\alpha = 0.3$. Equation 3.15 is the eddy viscosity coefficient above the trough level (Karambas, 1999).

$$v_{t-crest} = 0.208\kappa.d.w_* + 0.44d(D_b/\rho)^{1.3} \tag{3.15}$$

Svendsen (1994) proposed that it is a valid assumption to consider the characteristic length scale (l_m) to be equal in both vertical and horizontal directions. Therefore, the eddy viscosity coefficients in both vertical and horizontal directions are the same ($v_x = v_z$). Subsequently, the mean over the depth horizontal turbulent diffusion coefficient can be expressed as:

$$v_T = \frac{1}{d}\int_0^h v_x dz = \frac{d_e}{d} v_{t-crest} + \frac{d_r}{d} v_{t-trough} \tag{3.16}$$

where d_r represents the thickness of the water column below the trough level and d_e is the thickness of the water column above the trough level. In this study, it is assumed that the characteristic length scale of turbulence is similar in *x* and *z* directions. Svendsen and Putrevu (1994) concluded that turbulent diffusion is not the dominant mixing mechanism in the surfzone and they suggested that dispersive mixing mechanism is the main contributor to the mixing in the surfzone.

So far, the diffusive mixing mechanisms were discussed (§3.4.1). In §3.4.2, the theoretical and experimental data will be investigated to quantify the contribution of shear dispersion mechanism in the nearshore mixing. The performance of the theoretical approach developed is evaluated against existing laboratory and filed data at the end of §3.4.2.

3.4.2 Advective Shear Dispersion

The shearing effect in mean current can greatly enhance the dispersion of a passive tracer in the perpendicular direction to the shear (Spydell & Feddersen, 2012). This phenomena is called shear dispersion. Shear dispersion was first investigated by Taylor (1953) for laminar poiseuille flow in pipes. Most of the studies conducted on quantifying the shear dispersion coefficient have utilized the Fickian diffusion equation and are based on Eulerian approaches (Taylor, 1953; Aris, 1956; etc.). In recent years shear dispersion has been investigated from a Lagrangian point of view, mainly by employing the probability distribution function of particle displacements in bounded domains (Dewey and Sullivan, 1982; Feddersen, 2012; Camassa *et al*., 2010). All of these Lagrangian methods have confirmed and reproduced the Eulerian shear dispersion results.

Shear in the coastal ocean water is typically generated by bottom friction on the tidal currents, wave orbital motions and wind driven current. The dispersive shear mechanism is reported to be more significant than the turbulent diffusion mechanism

in terms of contributing to the mixing processes (Svendsen & Putrevu, 1994; Karambas, 1999; Pearson *et al*., 2009; Abolfathi & Pearson, 2014). The shear dispersion mechanism is mainly derived based on the non-uniform vertical structure of the time-averaged horizontal velocity over a wave period and the wave oscillatory motion. It is very strong in the nearshore region and especially in the surfzone. Figure 3.4 is the definition sketch of the vertical structure of mean horizontal velocity in the surfzone.

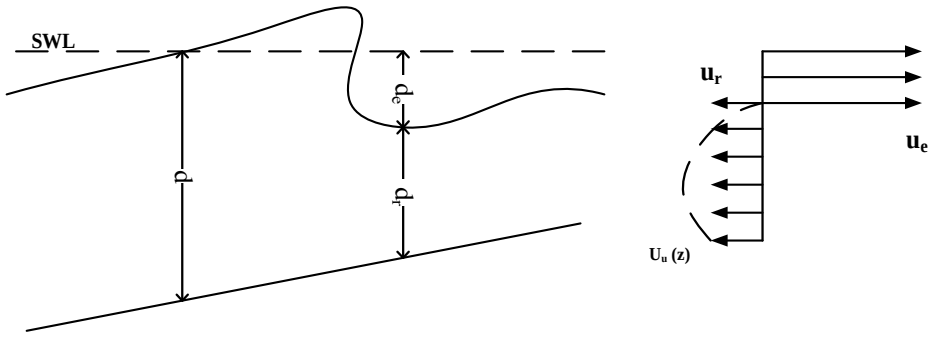

Figure 3.4 – Definition sketch of mean horizontal velocity inside the surfzone

In figure 3.4, u_e and u_r represent the velocity above and below the trough level, h is the mean water depth, d_r is the depth of undertow and d_e represents the thickness of the wave bore.

For the case of a fully mixed pollutant in the nearshore region, the total advective shear dispersion coefficient (D_x) in the on-offshore direction can be written as the sum of the dispersion coefficient due to the non-uniform over depth, on-offshore period mean secondary velocity profile (D_s) and due to oscillatory wave motion (D_o):

$$D_x = D_s + D_o \tag{3.17}$$

Following the assumptions made in § 3.4 for the logarithmic velocity profile of longshore current, the longshore dispersion coefficient can be estimated using an open channel flow expression for the turbulent flow (Karambas, 1999):

$$D_{yc} = D_y = 0.4041/k^3 du_* \tag{3.18}$$

Pearson *et al*. (2009) adopted the Fischer (1978) methodology and employed the Longuet – Higgins and Stewart (1964) theoretical velocity to predict the on-offshore dispersion coefficient in the nearshore region (Eq. 3.19).

$$D_y = \frac{gH^4}{768de_z} \tag{3.19}$$

Pearson *et al*. (2009) formula incorporates the effects of dispersive and diffusive mechanisms. The diffusion in equation 3.19 is estimated from Svendsen and Putrevu (1994) methodology and considering $e_z = e_y = \nu_t = Md\sqrt{gd}$. The constant *M* varies between 0.01 and 0.03 according to Svendsen and Putrevu (1994).

The interaction between the oscillatory flow and the vertical diffusion results in shear dispersion. Based on the two dimensional advection diffusion equation for the unsteady sinusoidal shear flow and with the assumption of linear velocity profile, Fischer (1979) proposed the following shear dispersion coefficient:

$$D_o = \frac{u_d^2 d^2}{\pi^2 \nu_T} (\frac{T}{T_c})^2 \sum_{n=1}^{\infty} (2n-1)^{-2} [(\frac{\pi}{2}(2n-1)^{-2} (\frac{T}{T_c})^2)^2 + 1]^{-1} \tag{3.20}$$

where *T* represents the wave period, u_d is the difference between surface wave velocity and the bottom wave velocity and $T_c = d^2/\nu_T$. Fischer *et al*. (1979) concluded that for the oscillatory flow after each reversal in a time interval of *T/2* , the concentration profile will change. However, T_c or mixing time is required before the concentration profile is completely adapted to changes in velocity profile. Therefore, if the wave period is very short compared to mixing time T_c, the concentration profile does not have the time to respond to the changes in the velocity profile and thus the shear dispersion is negligible (karambas, 1999; Fischer *et al*., 1979). Based on this theory, the lack of breaking wave theory does not permit an accurate estimation of velocity field. Nevertheless, based on existing wave modelling in the

breaker region as well as the laboratory and field research, the order of magnitude of D_o can be estimated. Considering a breaking wave, the horizontal velocity changes from the surface to the bottom. The velocity is equal to wave celerity C at the surface of the wave and reduces to much smaller value at the bottom which is of order of $0.2-0.3C$. The crest phase is usually $0.3T$ (Karambas, 1999), whereas the horizontal velocity is uniform for the rest of the cycle, and therefore the resulting dispersivity is zero. Karambas (1999) estimated the order of magnitude of D_o from equation 3.20 and by applying the typical breaking wave parameters and linear wave theory to estimate the bottom velocity (Stive, 1980). He proposed that the shear dispersion coefficient due to the oscillatory wave motion is a function of turbulent diffusion (Eq. 3.21).

$$D_o \cong 0.1 - 0.6\nu_T \tag{3.21}$$

As discussed earlier, the contribution of turbulent diffusion to the total mixing coefficient is small and consequently the advective shear dispersion mechanisms due to D_o cannot play any major role in the mixing phenomena in the nearshore region.

There are number of fundamental analytical methods for deriving longitudinal dispersivity of contaminants in shear flows. The first method was proposed by Taylor (1953) in his pioneering work on dispersion in laminar and turbulent flows. Elder (1959) employed the same methodology and extended it for three dimensional turbulent flow in open channels (Fischer *et al*., 1979). Aris (1956) developed a new technique to investigate shear dispersion based on concentration moment method. Chikwendu (1986) suggested a mathematical solution to calculate the shear dispersion for the flow in open channels and pipes.

The dispersion coefficient due to D_s can be quantified as the sum of two dispersive mechanisms due to mean opposite velocities (D_{s1}) and non-uniform distribution of undertow (D_{s2}) ($u_u(z)$, see Fig. 3.4).

$$D_s = D_{s1} + D_{s2} \tag{3.22}$$

In this study, the solution for the dispersion coefficient as the result of the mean opposite velocities (D_{s1}) is developed, based on the methodology described by Chikwendu (1986). Karambas (1999) and Pearson *et al*. (2002 and 2009) adopted theoretical velocities and Chikwendu's (1986) methodology to investigate shear dispersion coefficient.

An *N*-zones dispersion model is developed in this section based on Chikwendu (1986) methodology to determine the advective shear dispersion coefficient. The *N*-zone model will be used in chapters 4, 5 and 6 to quantify the contribution of dispersion mechanisms to the overall mixing for a range of experimental and numerical data.

Chikwendu (1986) method divides the flow into slow and fast zones and derives the shear dispersion coefficient for each of the zones. Each of these zones is moving with a depth-averaged velocities. Chikwendu (1986) employed two dimensional advection-diffusion equation for contaminant dispersion in open channel flow:

$$\frac{\partial c}{\partial t} = D_x(y)\frac{\partial^2 c}{\partial x^2} - u(y)\frac{\partial c}{\partial x} + \frac{\partial}{\partial y}(D_y(y)\frac{\partial c}{\partial y}) \tag{3.23}$$

where $u(y)$ is cross-sectional velocity distribution, c is the contaminant concentration and D_x and D_y are diffusivities in x and y directions, respectively. Each zone is assumed to be well-mixed with a specific velocity and concentration (Fig. 3.5). The coupled dispersion equations can be written as equation 3.24a and 3.24b:

$$\partial_t c_1 = D_{x1}\partial_x^2 c_1 - u_1\partial_x c_1 + b\beta_1(c_2 - c_1) \tag{3.24.a}$$

$$\partial_t c_2 = D_{x2}\partial_x^2 c_2 - u_2\partial_x c_2 + b\beta_2(c_1 - c_2) \qquad (3.24.b)$$

where D_{x1} and D_{x2} is the diffusivitiy in the fast and slow zones respectively, b is the mixing coefficient between the zones and $\beta_1 = h/h_1 = q_1^{-1}$ and $\beta_2 = h/h_2 = q_2^{-1}$.

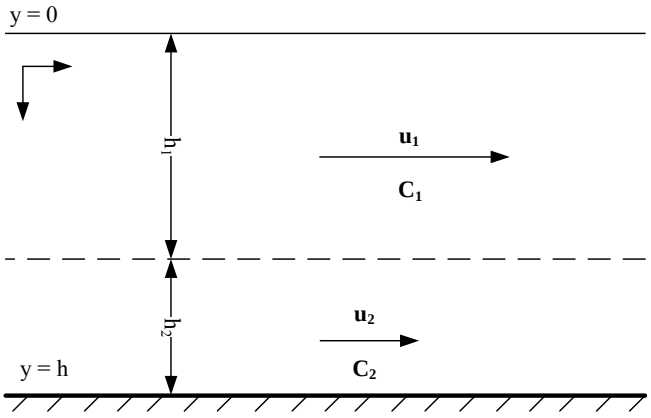

(a)

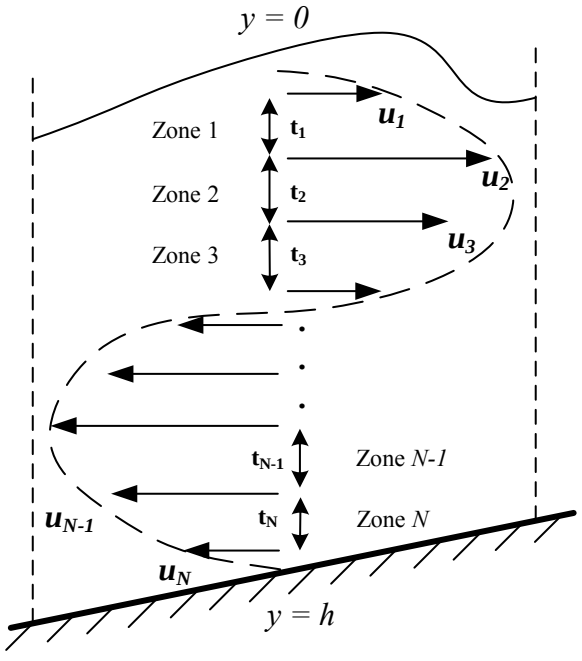

(b)

Figure 3.5 – Definition sketch of dispersion model (a) two zone model, (b) *N* zone model

Chikwendu (1986) found the exact mathematical solution for the system of equations above and concluded that at large times the contaminant concentrations approach a Gaussian distribution with a peak moving at the mean velocity $\bar{u}$.

$$D(2)=\frac{(q_1q_2)^2(u_1-u_2)^2}{b}+q_1D_{x1}+q_2D_{x2} \tag{3.25}$$

where q represents the fractional thickness of each zone. If the two dimensional flow is divided into N zones of well mixed parallel flow with the thickness of h_j, average velocities u_j, concentration of c_j and average longitudinal diffusivities D_{xj}, and $N\to\infty$ equation 3.25 results in N coupled dispersion equations as follow:

$$\partial_t c_1=D_{x1}\partial_x^2 c_1-u_1\partial_x c_1+b_{12}\beta_1(c_2-c_1) \tag{3.26.a}$$

$$\partial_t c_j=D_{xj}\partial_x^2 c_j-u_j\partial_x c_j+b_{(j-1)j}\beta_j(c_{j-1}-c_j)+b_{j(j+1)}\beta_j(c_{j+1}-c_j) \quad \text{for } j=2,3,...,N-1 \tag{3.26.b}$$

$$\partial_t c_N=D_{xN}\partial_x^2 c_N-u_N\partial_x c_N+b_{(N-1)N}\beta_N(c_{N-1}-c_N) \tag{3.26.c}$$

where:

$$\beta_j=\frac{h}{h_j}=\frac{1}{q_j}\ (j=1,2,3,...,N)\ \ \&\ \ b_{j(j+1)}=\frac{2D_{yj(j+1)}}{h^2(q_j+q_{j+1})}\ (j=1,2,...,N-1)$$

$D_{yj(j+1)}$ is the average vertical diffusivity between two consequent zones (j and $j+1$). This system of ODEs can be solved by use of Fourier transformation and large time exponent $\gamma(\lambda)$. As a result, the shear dispersion coefficient for N zones can be written as:

$$D(N)=\sum_{j=1}^{N-1}(q_1+q_2+...+q_j)^2[1-(q_1+q_2+...+q_j)]^2\times[u_{12...j}-u_{(j+1)...N}]^2/b_{j(j+1)}+\sum_{j=1}^{N}q_jD_{xj} \tag{3.27}$$

where $u_{12..j}$ is the mean velocity in the first j zones $[=(\sum_{k=1}^{j} q_k u_k)/(\sum_{k=1}^{j} q_k)]$ and $u_{(j+1)...N}$ is the mean velocity in the last N-j zones $[=(\sum_{k=j+1}^{N} q_k u_k)/(\sum_{k=j+1}^{N} q_k)]$. If the number of these zones tends to infinity, the thickness of each zone becomes infinitesimal and therefore the summations turn into the integral function. When N tends to infinity, the approximation of N zones model becomes an exact mathematical solution. Equations 3.28 to 3.32 present the mathematical procedure to get the exact solution (Eq. 3.32).

$$N \to \infty \quad , \qquad q_j \to \Delta q; \int_0^q dq = q \tag{3.28}$$

$$\sum_{j=1}^{N} q_j D_{xj} \to \int_0^1 D_x(q)dq \tag{3.29}$$

$$u_{12...j} \to \frac{1}{q}\int_0^q u(q')dq' = u_f(q) \tag{3.30}$$

$$u_{(j+1)...N} \to \frac{1}{(1-q)}\int_q^1 u(q')dq' \to \frac{1}{(q)}\int_0^q u(q')dq' = u_s(q) \tag{3.31}$$

$$D(\infty) = \lim_{N\to\infty} D(N) = h^2 \int_0^1 \frac{q^2(1-q)^2}{D_y(q)}[u_f(q) - u_s(q)]^2 dq + \int_0^1 D_x(q)dq \tag{3.32}$$

Equation 3.30 represents the average velocity in the faster layer of a two-layer model in which the fractional thicknesses are q and (1-q). Equation 3.31 is the average velocity in the slower layer of a two layer model, where the fractional thickness are q and (1-q). In this study, by use of equation 3.27 for N layer of parallel flow (which results in exact mathematical solution described in equation 3.32), the shear dispersion due to (D_{s1}) is quantified.

The shear dispersion mechanism due to non-uniform distribution of undertow (D_{s2}) can be quantified by adopting the solution for undertow proposed by Steetzel (1993).

Karambas (1999) adopted Steetzel (1993) solutions and defined undertow $u_u(z)$ as a function of bottom current velocity u_o, shear stress at the trough level τ_s and the bottom shear stress τ_b as:

$$u_u(z) = u_o + \frac{\beta}{\nu_z} z + \frac{1}{2}\frac{\alpha}{\nu_z} z^2 \tag{3.33}$$

where $\alpha = \frac{1}{\rho}\frac{\tau_s - \tau_b}{d_r}$ and $\beta = \frac{\tau_b}{\rho}$.

Shear stress at trough level can be estimated according to equation 3.34:

$$\tau_s = (0.5 + 7\frac{h}{L})\frac{D_b}{C} \tag{3.34}$$

In order to determine D_{s2}, the undertow velocity given by equation 3.33 needs to be substituted into equation 3.6:

$$D_{s2} = \frac{d_r^4}{\nu_z^3}[\frac{1}{30}(\frac{\tau_b}{\rho})^2 + \frac{1}{48}\frac{\tau_b(\tau_s - \tau_b)}{\rho^2} + \frac{1}{336}(\frac{(\tau_s - \tau_b)}{\rho})^2] \tag{3.35}$$

The overall mixing in the on-offshore directions can be written as the sum of the individual mechanisms that are discussed throughout this chapter:

$$E_{xx} = \nu_T + D_o + D_{s1} + D_{s2} \tag{3.36}$$

The theoretical mixing coefficient described in this chapter is compared to the experimental data of Tanaka *et al.* (1980) inside the surfzone (Fig. 3.6). The results indicate that the mixing is dominated by the shear dispersion, and also the non-

uniform distribution of undertow plays a significant role in the mixing of pollutants in the surfzone, confirming the existing knowledge [Svendsen & Putrevu, 1994; Karambas, 1999; Pearson *et al*., 2002 and 2009; Abolfathi & Pearson, 2014].

3.5 Summary

In this chapter, mixing mechanisms in the nearshore were discussed from a theoretical point of view by adopting the existing theories and experimental studies on mixing and dispersion in the nearshore. A theoretical approach for quantifying mixing mechanisms in the nearshore region is developed using the methodology described by Chikwendu (1986), Svendsen (1987), Svendsen & Putrevu (1994), Karambas (1999) and Pearson *et al*. (2002 and 2009). The theoretical approach derived and discussed in this chapter was evaluated and tested against the experimental data of Tanaka *et al*. (1980) and also against the existing empirical formulae of Battjes (1987) and Harris *et al*. (1964). In the next chapter (chapter 4), the experimental data obtained from hydrodynamic and fluorometric measurements from a large-scale wave-current facility at DHI, Denmark will be presented. The dispersive and diffusive mixing mechanisms will be quantified for the data using the methodology described in this chapter.

CHAPTER 4

MIXING UNDER COMBINED EFFECTS OF WAVES AND CURRENTS – LABORATORY MEASUREMENTS AND ANALYSIS

4.1 Synopsis

In this chapter, a laboratory-based investigation of mixing due to the combined effects of waves and currents is presented. The laboratory experimental procedures and the instrumentation are discussed in detail. The mixing coefficients are quantified for the hydrodynamic and fluorometric data. The dispersive and diffusive mechanisms in the nearshore are quantified through the hydrodynamic data analysis.

4.2 Laboratory Investigations

In this study, mixing of buoyant pollutants in the nearshore region has been investigated by means of both Eulerian and Lagrangian approaches in the shallow water basin at the Danish Hydraulic Institute (DHI). The data collection study was performed between February and April 2005 (Pearson *et al*., 2006). Detailed hydrodynamic measurements in the nearshore region were performed by using Laser Doppler Anemometry (LDA). Fluorometric dye tracing is carried out using Rhodamine water tracer dye to quantify the mixing coefficient under combined effects of waves and currents. The measurement section was $18m \times 18m$ and all the tests were performed on a 1:20 plain beach slope with an offshore water depth of $0.7m$. The bed of the facility consists of concrete screed with an assumed roughness element $1mm$ high. The facility was equipped with an absorbing piston-type wave-maker. The waves generated on the facility were long crested waves and produced by 36 computer controlled paddles (Fig. 4.1).

Figure 4.1 – Wave paddle system at large scale laboratory in DHI

The experiments were performed on the transverse sloping section of the facility where a parabolic longshore current was superimposed on increasing velocity in the offshore direction. The current parallel to the shore was generated by using a single pump set to 320 l/s (careful calibration was performed to find the exact pumping rate). In the cross-shore direction, y, the velocity increased as the water depth reduce. The measurements show that the mean Eulerian flow is in the offshore direction which indicates the presence of a cross-shore circulation mechanism.

Four test conditions were studied with a constant offshore wave height (H_o = 0.12m) and varying wave period (2.9, 1.85, 1.2 and 1.85_{rand} sec). The wave conditions were designed to represent different wave steepness S_{op} = 2, 3½, 5 and 3½ $_{Random}$ %, in order to study the hydrodynamic conditions across the European Union coastlines. Wave height measurements were simultaneously undertaken across the basin at 0.5m intervals to determine the wave characteristics in the region of the dye plume. The wave conditions were logged continuously for the duration of both the concentration and velocity data collection periods. This study mainly focused on monochromatic waves with the crests parallel to the shore, although one pseudo random wave condition with the steepness of 3½% was also investigated (Pearson *et al*., 2006).

4.2.1 Experimental Facility and Setup

In the configuration selected for the experimental investigations, the wave-current facility was designed to represent 0.7km of coastline at a 1:20 scale. The basin consisted of a plane concrete beach sloping at 1:20 and had a normal operating depth of z = 0.6m, although the depth could be altered from 0.3m to 0.8m. The facility had a static instrument carriage from which instruments were hung (see Fig. 4.2).

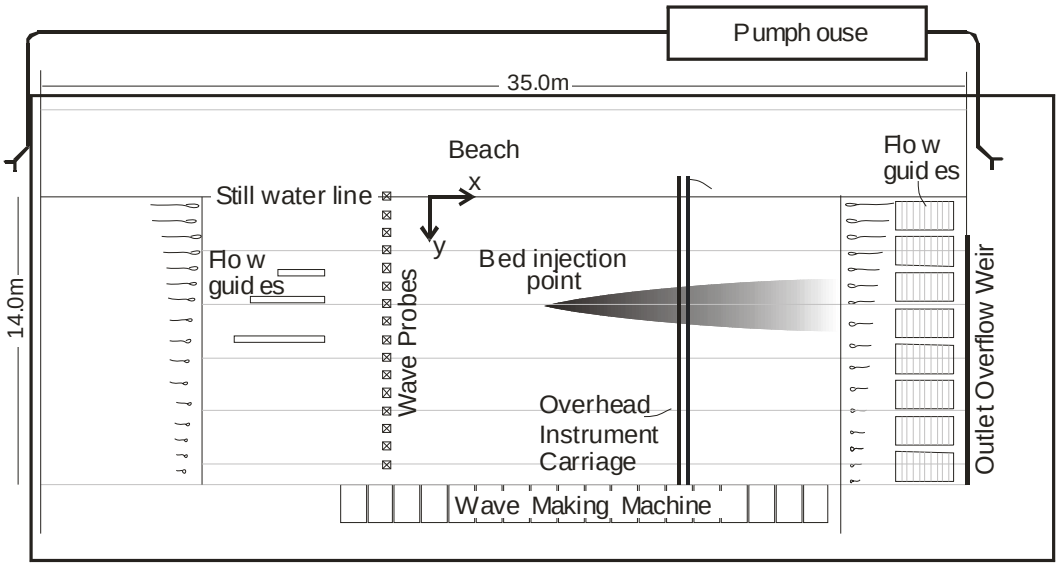

Figure 4.2 – Layout of the Wave Current Basin at DHI, Denmark

The shore-parallel current was generated by a single pump in a recirculating flow system. Water from the pump was stilled in a 10m wide sump. The flow from the pump was further controlled by use of flow straighteners. At the downstream end of the facility, wave adsorption/flow guides were used [see Fig. 4.3]. The waves were generated by 36 individual computer controlled wave paddles, each 0.5m wide. The electrically driven paddle elements were installed along one side of the facility. The paddle system was capable of generating monochromatic and random long crested waves with an angle of approach ranging from 0 up to $20^{\circ c}$.

Figure 4.3 – Wave guides/straighteners at downstream end of wave-current facility, DHI

4.2.2 Hydrodynamic Measurements

The velocity field in the surfzone and seaward of the breaker region forced by a laboratory generated wave were investigated from a Eulerian perspective using Laser Doppler Anemometry (LDA). The parabolic current was generated based on Chezy's equation and the waves approached at 90° to the generated current. The structure of the turbulence in the nearshore region was investigated by studying two dimensional velocity fields in the vertical plane from 180-200 consequent monochromatic waves that measured at six cross-shore locations in the nearshore region. Detailed velocity measurements were undertaken at 1.0 m intervals to describe the long-shore current. Additional velocity profiles at six sections away from the shoreline, $y = \{1, 2, 3, 4, 5, 6\}$m, were measured at the centreline of the basin for each wave condition. For the wave and current conditions a minimum of 20 points were measured in the vertical directions. No attempt was made to record both velocity and concentration measurements simultaneously. However, in some tests, a wave probe and LDA were deployed as concentration data were collected to confirm repeatability in the hydrodynamic conditions (Pearson *et al.,* 2006).

The coordinate system has been defined such that x is positive onshore along the beach face, where x=0 is located at the intersection of the still water level with the beach. The z direction is defined normal to the beach face and positive upward and

the y axis is determined by the right hand rule with y=0 at the lateral midpoint of the basin. Figure 4.4 is the schematic sketch of experimental coordinate system in x-z plane.

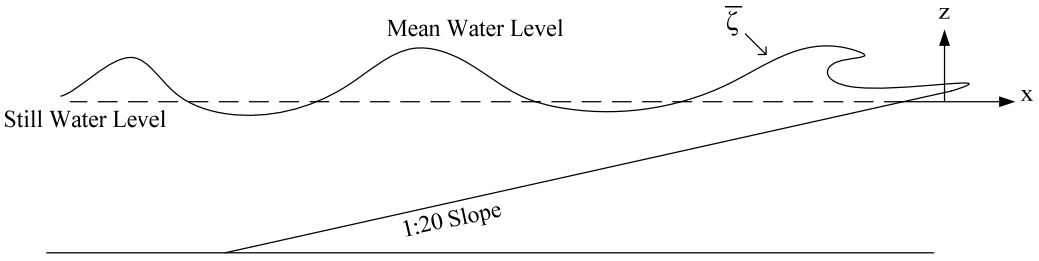

Figure 4.4 – Experimental coordinate system

In the DHI study, a Dantec Laser-Doppler Anemometry system was utilized to record the nearshore hydrodynamics. LDA is a device which is capable of capturing small scale turbulent velocity fluctuations (Fig. 4.5). For hydrodynamic measurements, a *5W* Argon-Ion laser was used to generate a light beam of discrete wavelengths, and a series of optics converted the beam into a suitable configuration for velocity measurements. The optics split the laser beam into a series of parallel pairs of beams of single wavelength (green [514.5*nm*] and blue [488*nm*]) and were passed down a fibre optic to the head positioned in the facility. Each wavelength corresponds to a different orthogonal plane (x and z). The LDA system logs a velocity record when a particle comes in the measurement volume and reflects the laser light. For each data log, the reflected light returns through the fibre optic to the LDA system and the signal converts and validates to a velocity record. The data rate is dependent on the number of particles in the flow. In the DHI experiment for the purpose of hydrodynamic measurements, the flow was seeded with Timiron which is a neutrally buoyant product. The data set shows that in some test cases the data recording rate exceeded 200*Hz*. However, inside the surfzone, the data recording rate was reduced due to wave breaking, bubble generation and air entrainment into the LDA probe.

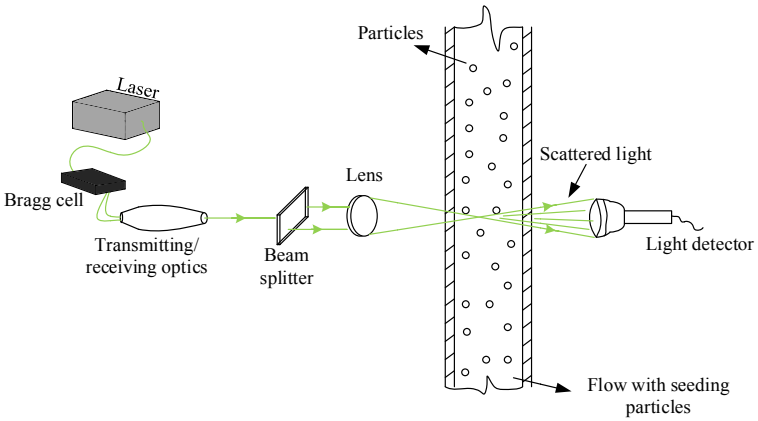

(a)

(b)

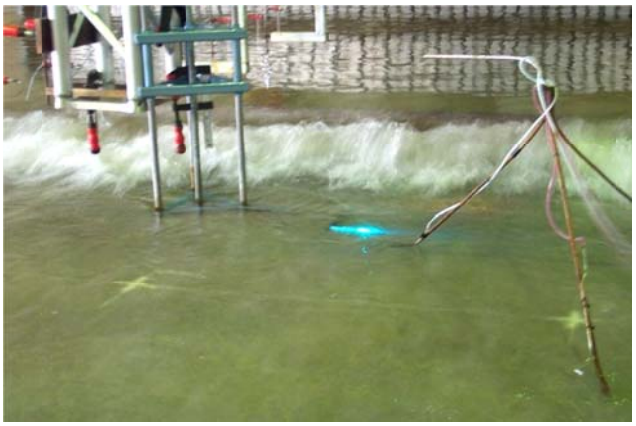

(c)

Figure 4.5 – (a) Laser Doppler Anemometry (LDA) system component, (b) LDA velocity measurement system, (c) laser probe installation inside the surfzone at DHI facility

4.2.3 Wave Gauge Measurements

Wave height measurements were simultaneously undertaken across the basin at $0.5m$ intervals to determine the wave characteristics in the nearshore region (Fig. 4.6). Eleven wave monitor modules, which were connected to twin wire wave probes were utilized to measure the water surface elevation at selected locations within the facility. Before each set of the experiments, the wave probes were calibrated and re-zeroed over four points (0, +100, -100, 0 *mm*) by moving the probe up or down. The output voltage from a wave probe monitor is directly proportional to the probe's depth of immersion. Automation of the wave probes' calibration system enabled the values of the least square regression line (r^2) for each instrument to be displayed instantly on the control platform. To ensure that the water elevation resolutions were down to $\pm 1mm$, in case any of the regressions values for each probes was below 0.9999, the calibration was rejected and the wave probes were re-calibrated (Pearson *et al.,* 2006). In this chapter, the region near the paddles is termed 'offshore', although, due to water depth, the waves are in the transitional region.

Figure 4.6 – Wave gauges configuration in DHI experiment

4.2.4 Fluorometric Measurements

In this chapter, the data obtained from dye tracer measurements in the DHI study was used to quantify the mixing and dispersion at various locations across the nearshore and for a range of wave steepnesses which were investigated throughout the study. Tracer concentration measurements were undertaken with a fluorometer (Turner Design Series 10) [see Fig. 4.7], which is a device to measure dye concentration.

The dye emits light with a wavelength different from the one which is striking it, and the fluorometer utilizes these fluorescent properties of the tracer to measure tracer concentration. For different types of benzo-organic dyes, the intensity of emitted lights can be detected by using proper filters and the output is measured as a voltage. All recorded voltages are converted to concentration values by calibrating the fluorometer with a known concentration of dye.

Figure 4.7 – 10 AU Turner Design Fluorometer utilized in DHI experiment

During the data collection study (Pearson *et al*., 2006), a constant head injection of Rhodamine Water Tracing dye was introduced to the basin from a small brass tube (3mm) at approximately mid depth, and at various distances from the shoreline (Fig. 4.8). The subsequent spreading of the tracer was then recorded by pumping one litre samples into sterilised containers for later analysis. The facility had a re-circulating flow system which caused the continual build-up of background dye concentrations. Hence, to minimise the temporal build-up during the test, ten discrete samples were

collected simultaneously with their sample tubes placed at approximately mid depth and spaced at a transverse distances of 50*mm* apart (Pearson *et al.,* 2006). To eliminate additional mixing generated by extracting the samples within the facility, the flow rate of the pumps was adjusted so that the velocity at the inlet of the pipe matched the longshore current velocity. It took approximately two minutes to collect ten samples, and the array of tubes were stepped across the plume at half-metre intervals. Approximately 60 samples were collected for each transverse section. Pearson *et al.* (2006) investigated up to five transverse sections at different longitudinal locations for each test condition in order to describe the lateral mixing.

Figure 4.8 – Continous injection of Rhodamine WT dye at various locations across the nearshore

Figures 4.8 and 4.9 show the concentration measurement system used in DHI study. The system was setup to continually sample the tracer in the facility via 3mm brass tubes placed in the flow (Fig. 4.9a). Peristaltic pumps were utilized to take the sample from the water (Fig. 4.9b). The samples were collected in containers for later analysis in the fluorometer. Pearson *et al*. (2006) reported that the system of continually extracting samples could only be used when a longitudinal current was superimposed on the waves. Therefore, under wave only condition, the advection caused by the sample tubes would generate currents greater than those generated by the waves.

Figure 4.9 – (a) Sample extraction tubes in facility, (b) pumping system for extraction

Smart and Laidlaw (1977) studied water tracing dyes and suggested that the fluorescent intensity of water tracing dyes varies inversely with temperature. Experimental studies showed that for Rhodamine WT dye, the fluorescent intensity, F, is given by:

$$F = F_o \exp^{-0.027\,t} \tag{4.1}$$

where F is the fluorescence reading at temperature t, and F_o is the fluorescence at $0^\circ C$. Thus, a $1^\circ C$ change in temperature can result in a 3% change in fluorescent intensity. Hence, careful monitoring of the water temperature throughout the calibration procedure and testing at DHI was reported to ensure temperature variation remained negligable between calibration and testing.

To calibrate the Turner Design fluorometer instrument, a 5 litre sample of fresh basin water was taken and allowed to reach the ambient temperature of the facility water. Known volumes of Rhodamine WT dye were added to the sample and mixed thoroughly and the sample was passed through the fluorometer (Pearson *et al.,* 2006). Figure 4.10 shows a typical calibration plot for the 10AU fluorometer.

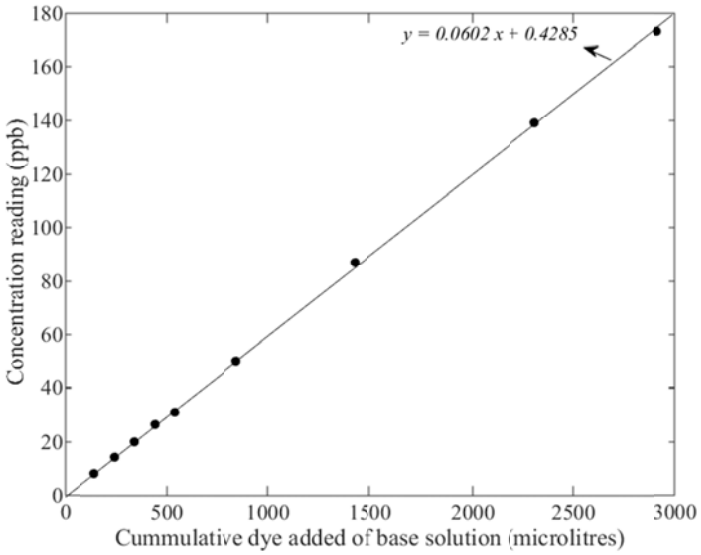

Figure 4.10 – Typical calibration plot of fluorometer

4.2.5 Test Conditions

This study mainly focuses on monochromatic waves with the steepness of 2 – 5%. However, one test condition was conducted to investigate the pseudo random waves (S_{op} = 3 ½ $_{Random}$ %). Table 4.1 summarizes all the conditions that have been tested in the DHI study.

Table 4.1 – Summary of experimental studies at DHI

1- Current only *x = dist. From injection, y = dist. From SWL, z = dist. From bed*	
Vertical LDA profiles (*x-y direction*) {y}	*2, 4 & 6* m
Vertical LDA profiles (*x-z direction*) {y}	*3 & 5* m
Transverse dye profiles {y}	*2, 3, 4, 5 & 6* m
Vertical dye profiles {y}	*5* m

2- Current + Regular waves $H_{nominal}$ = 0.12m, T=1.2s & S_{op} = 5%	
Vertical LDA profiles (*y-z direction*) {y}	*1.08,2.08,3,4,5 & 6* m
Vertical LDA profiles (*x-z direction*) {y}	*3 & 5* m
Transverse dye profiles {y}	*2, 3, 5 &* 5_{bed} m
Vertical dye profiles {y}	*5* m

3- Current + Regular waves $H_{nominal}$ = 0.12m, T=1.85s & S_{op} = 3.5%	
Vertical LDA profiles (*y-z direction*) {y}	*1.08,2.08,3,4,5 & 6* m
Vertical LDA profiles (*x-z direction*) {y}	*3 & 5* m
Transverse dye profiles {y}	*2, 3 & 5* m
Vertical dye profiles {y}	*5* m

4- Current + Regular waves $H_{nominal}$ = 0.12m, T=2.9s & S_{op} = 2%	
Vertical LDA profiles (*y-z direction*) {y}	*1.08,2.08,3,4,5 & 6* m
Vertical LDA profiles (*x-z direction*) {y}	*3 & 5* m
Transverse dye profiles {y}	*2, 3 & 5* m
Vertical dye profiles {y}	*5* m

5- Current + Random waves $H_{nominal}$ = 0.12m, T=1.85s & S_{op} = 3.5%	
Vertical LDA profiles (y-z direction) {y}	1.08,2.08,3,4,5 & 6 m
Vertical LDA profiles (x-z direction) {y}	3 & 5 m
Transverse dye profiles {y}	2, 3 & 5 m
Vertical dye profiles {y}	5 m

4.3 Experimental Data Analysis

The experimental setup and measurement procedures for DHI fluorometric and hydrodynamic measurements have been discussed extensively in §4.2.2 - §4.2.5. In this section, all the hydrodynamic and fluorometric data collected in the DHI study is

presented and analysed. The overall mixing coefficients are quantified from dye tracer data. The diffusive and dispersive mixing mechanisms in the nearshore are quantified from hydrodynamic data by developing analysis algorithms based on the methodology described in chapter 3. The overall mixing obtained from hydrodynamic measurements is compared to the fluorometric data for all test conditions (Table 4.1).

4.3.1 Hydrodynamic Data

4.3.1.1 Primary Flow under Current Only Condition

For the current only condition, the measurements were performed at z = -80 mm relative to the still water line. The similarity in general trend and the shape of the measurements for different longitudinal locations confirms that almost a steady uniform flow is present. The wave-current facility had a horizontal bed in longitudinal direction and therefore, it was not possible to generate truly uniform flow (Pearson *et al*., 2006). The analysis of the collected data shows that the flow velocity appears to increase by approximately 5% over the 10m control section of the facility. The analysis of the flow shows that the three cross-shore profiles located in the centre are very similar and hence there is no acceleration in the central region of the basin. However, the flow may be drawn at the downstream end of the facility and forced in the upper region. The variation of longitudinal velocity with cross-shore distance is presented in figure 4.11.

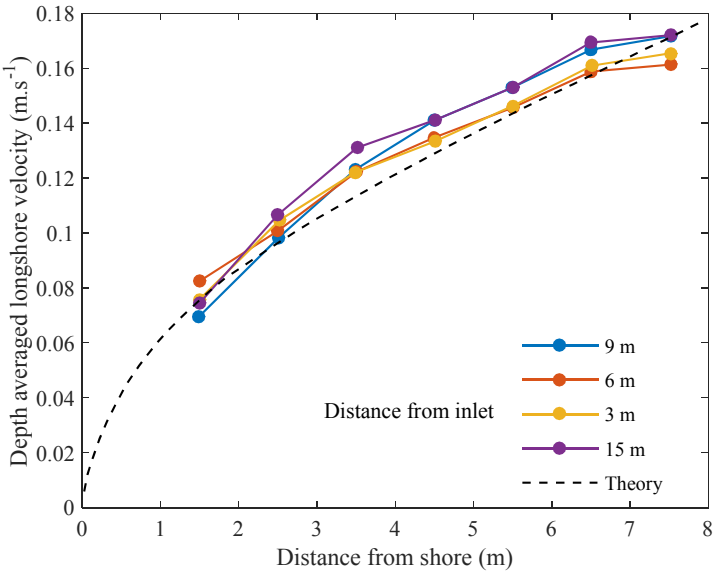

Figure 4.11 – Longshore velocity profiles for current only condition at x = {3,6,9,15}m from flow inlet

4.3.1.2. Longitudinal Flow Velocity under Current Only Condition

As discussed in §4.2.2, the flow velocities were measured by using a 2D Dantec LDA system. Detailed velocity measurements were undertaken at 1m intervals to describe the longshore current. Additional velocity profiles were measured at six locations away from the shoreline y{1,2,3,4,5,6}m, at the centreline of the basin for each wave condition. No attempt was made to record both velocity and concentration measurements simultaneously. However, for some tests, a wave probe and LDA were deployed as concentration data were collected to confirm repeatability in the hydrodynamic conditions (Pearson *et al.*, 2006).

Figure 4.12 represents the profiles of the longitudinal flow velocity at three locations from the shore under the current only condition. It is evident that the velocity profile increases with the distance from the bed and therefore they are following the general trend of two dimensional flows.

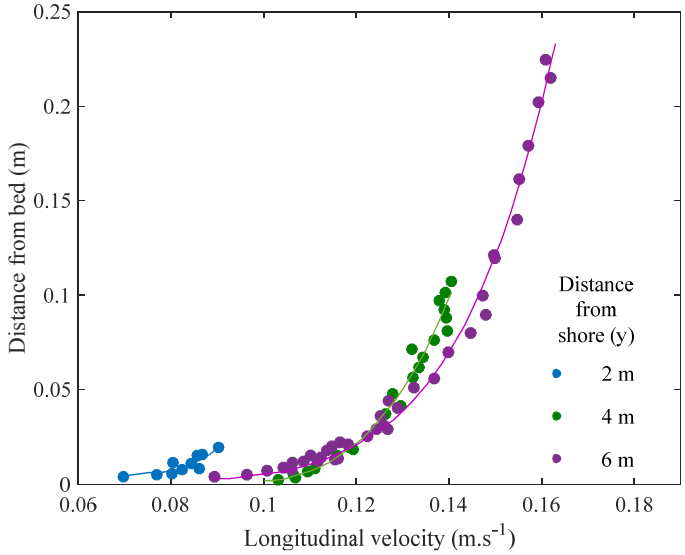

Figure 4.12 – Longshore velocity profile for current only condition at y = {2, 4 & 6} m from shoreline

4.3.1.3. Cross-Shore Velocity Profiles under Current Only Condition

Cross-shore velocity profiles at three locations from the shoreline are illustrated in figure 4.13, for the current only condition. The figure shows that only little secondary flows are evident which proves that the longitudinal flow under current only condition was setup correctly during DHI experiment.

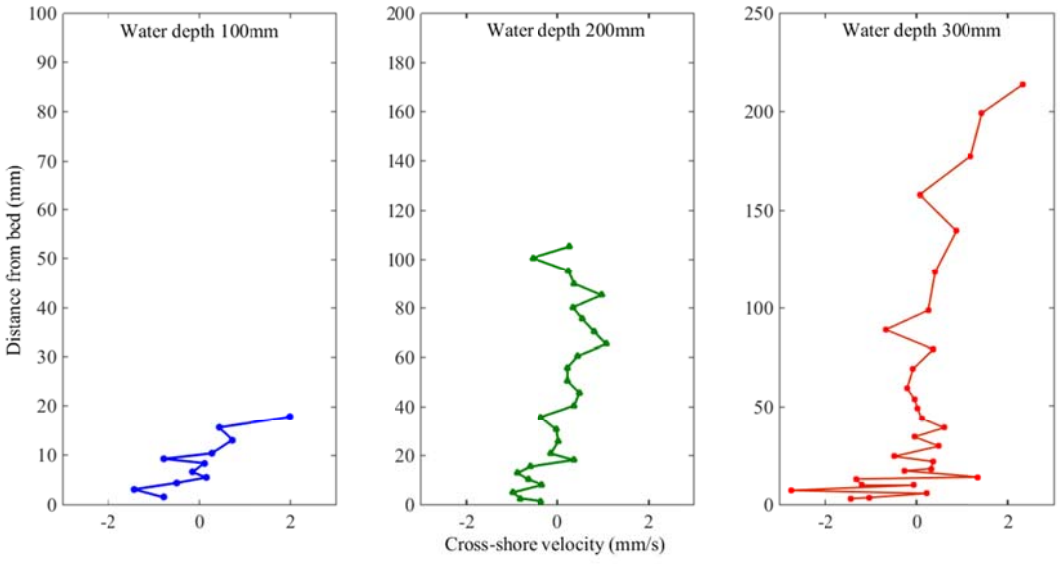

Figure 4.13 – Cross-shore velocity in on-offshore direction at y={2,4,6}m for current only condition

4.3.1.4 Cross-Shore Velocity Profiles under Wave-Current Conditions

The temporal mean cross-shore velocity profiles for $y\{1,2,3,4,5,6\}$m in on-offshore direction are shown in figures 4.14 to 4.17 for all 4 wave conditions tested in DHI study. The measurements inside the surfzone and seaward of the breaker point are shown in separate plots. In the cross-shore direction, y, the velocity increases as the wave height increases. The measurements show that the mean Eulerian flow is in the off-shore direction, indicating the presence of a cross-shore circulation mechanism. The theoretical Eulerian cross-shore flow in the off-shore direction can be given by $v_+ = Q / h_{tr}$, where Q is wave mass-flux $[Q = gH^2 / 8c]$, C is the wave celerity and h_{tr} is the depth below trough level. The comparison between measured and theoretical results shows that the Eulerian measurements are within the expected range.

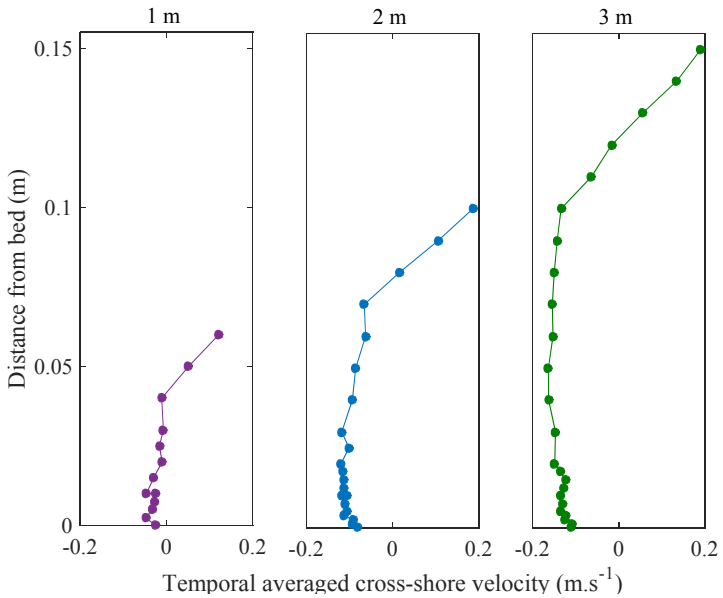

(a)

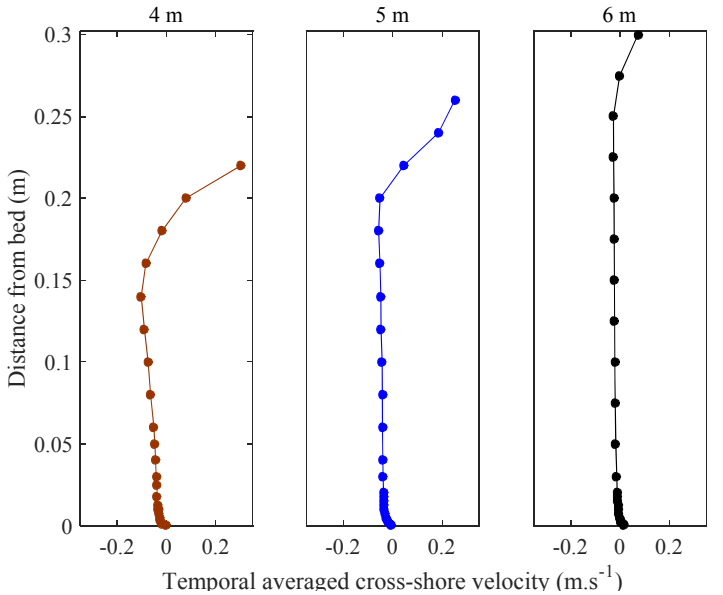

(b)

Figure 4.14 – Temporal averaged Cross-shore velocity in on-offshore direction for S_{op} = 2% (a) inside the surfzone y={1,2,3}m (b) seaward of the breaker region y={4,5,6}m

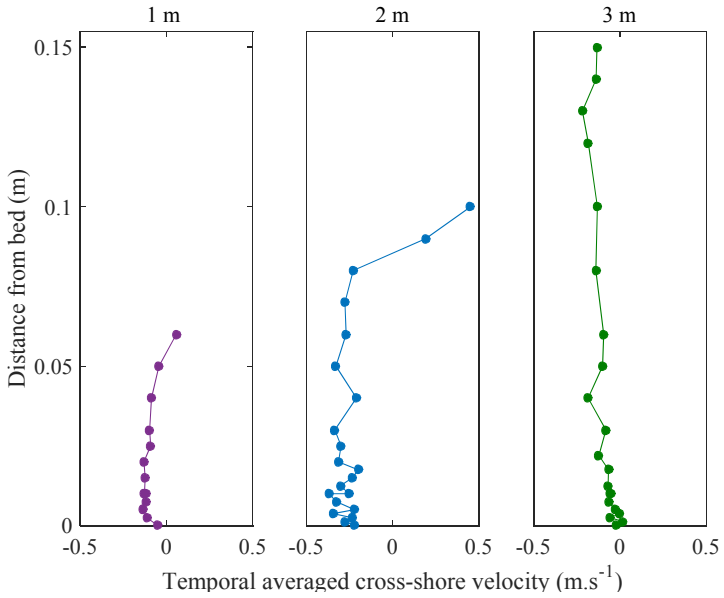

(a)

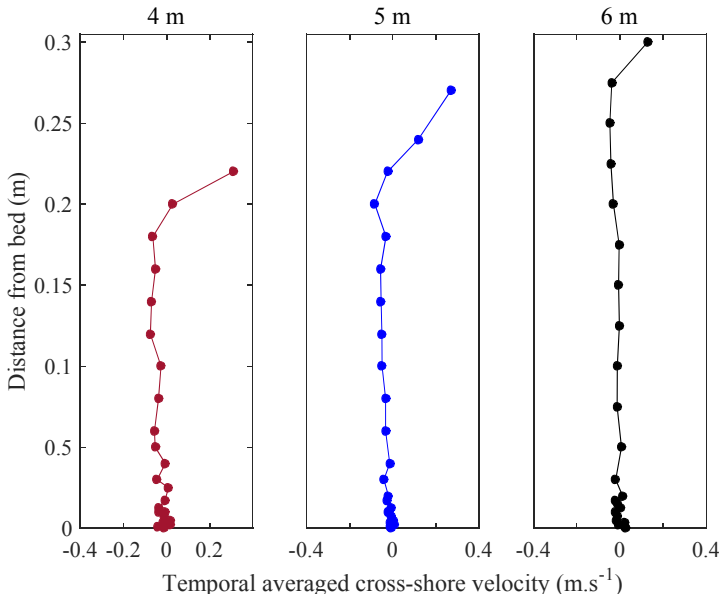

(b)

Figure 4.15 – Temporal averaged Cross-shore velocity in on-offshore direction for S_{op} = 3½ % (a) inside the surfzone y={1,2,3}m (b) seaward of the breaker region y={4,5,6}m

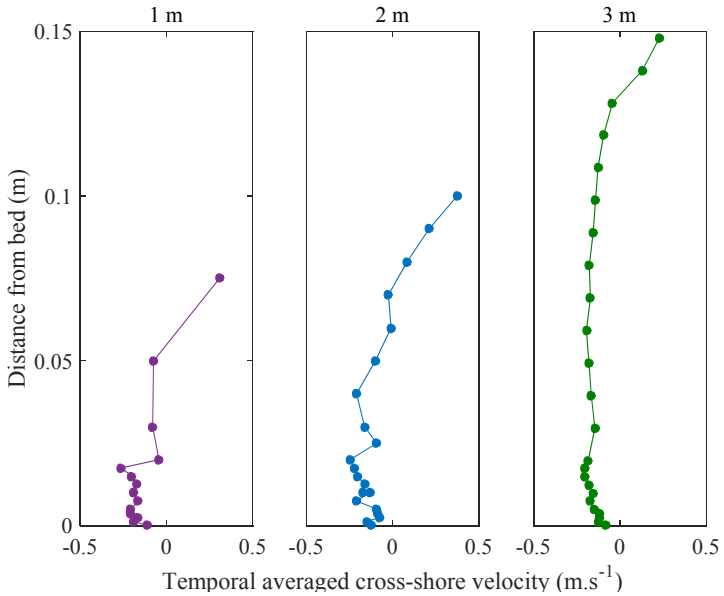

(a)

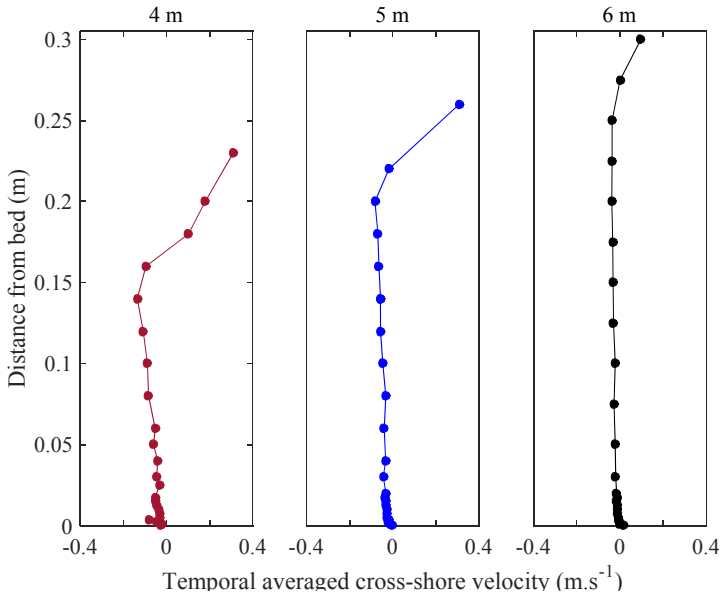

(b)

Figure 4.16 – Temporal averaged Cross-shore velocity in on-offshore direction for S_{op} = 5% (a) inside the surfzone y={1,2,3}m (b) seaward of the breaker region y={4,5,6}m

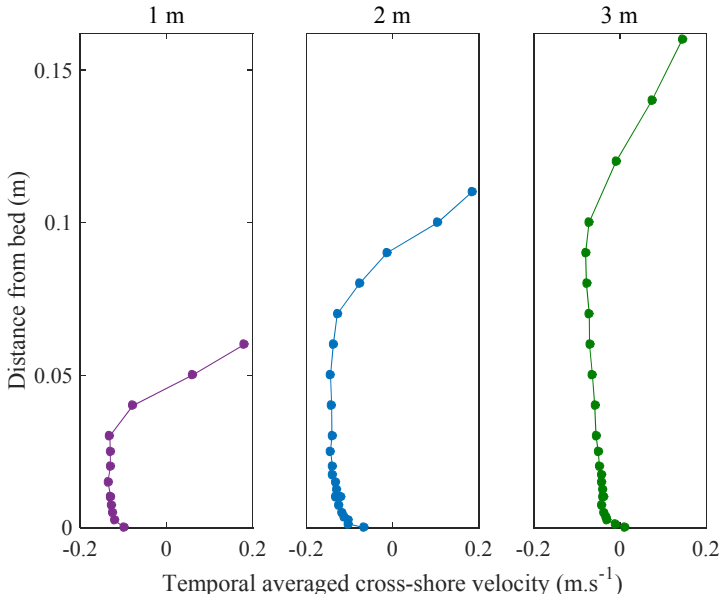

(a)

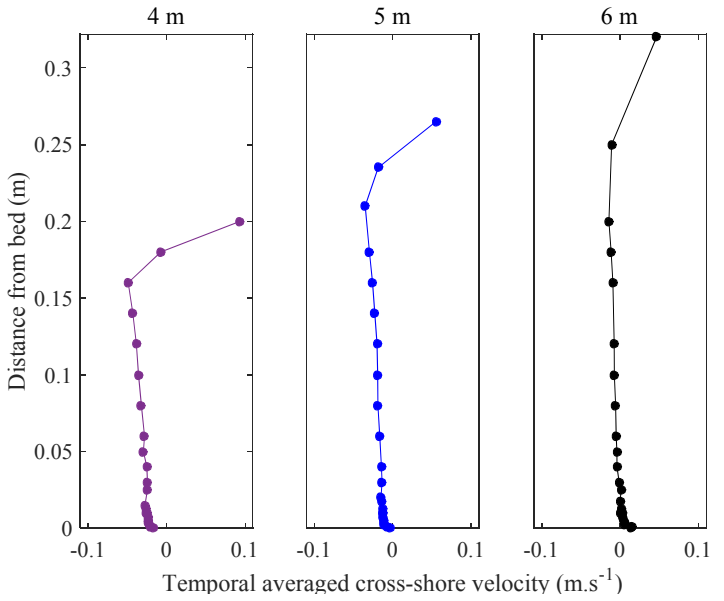

(b)

Figure 4.17 – Temporal averaged Cross-shore velocity in on-offshore direction for S_{op} = 3½ $_{random}$% (a) inside the surfzone y={1,2,3}m (b) seaward of the breaker region y={4,5,6}m

As discussed in §4.2.2, two components of the velocity in the on-offshore and vertical directions across the nearshore were recorded using LDA system. Figures 4.18 to 4.21 show the temporal averaged values for the vertical component of the cross-shore velocity, for all measured wave conditions inside the surfzone and

seaward of the breaker region. The recorded measurements for the upper part of the water column, in the region of the wave crest, showed some unrealistic spikes which were due to bubble generation and air entrainments to LDA probe. These unrealistic velocity records in the data for the crest part were removed from the dataset for later analysis.

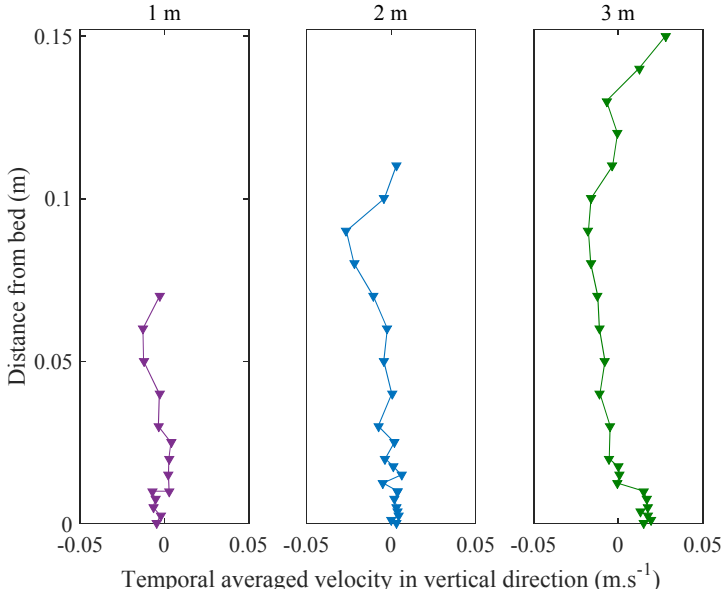

(a)

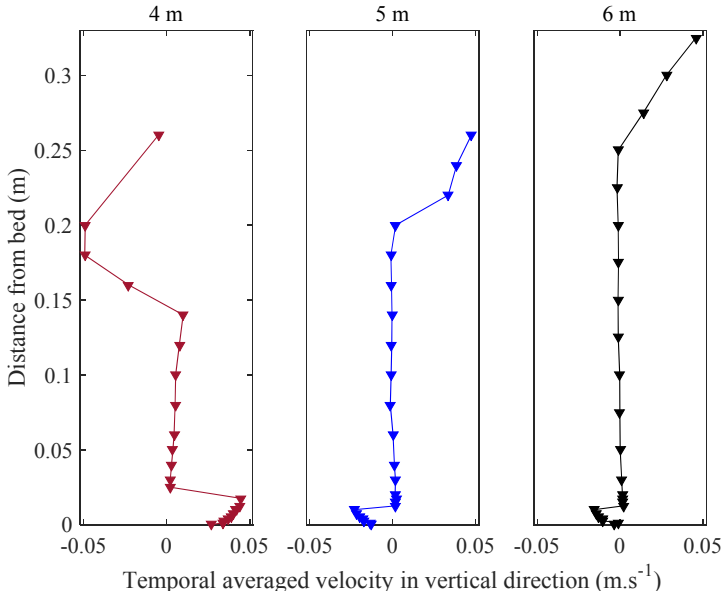

(b)

Figure 4.18 – Temporal averaged vertical velocity in on-offshore direction for S_{op} = 2% (a) inside the surfzone y={1,2,3}m (b) seaward of the breaker region y={4,5,6}m

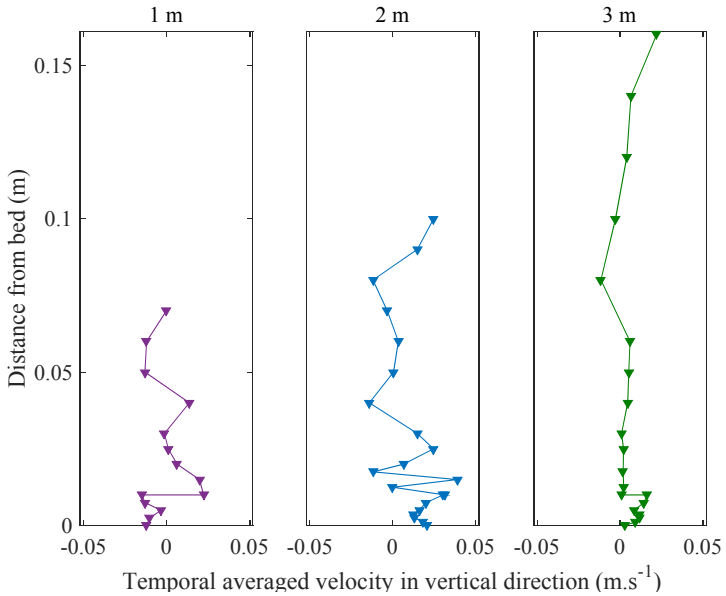

(a)

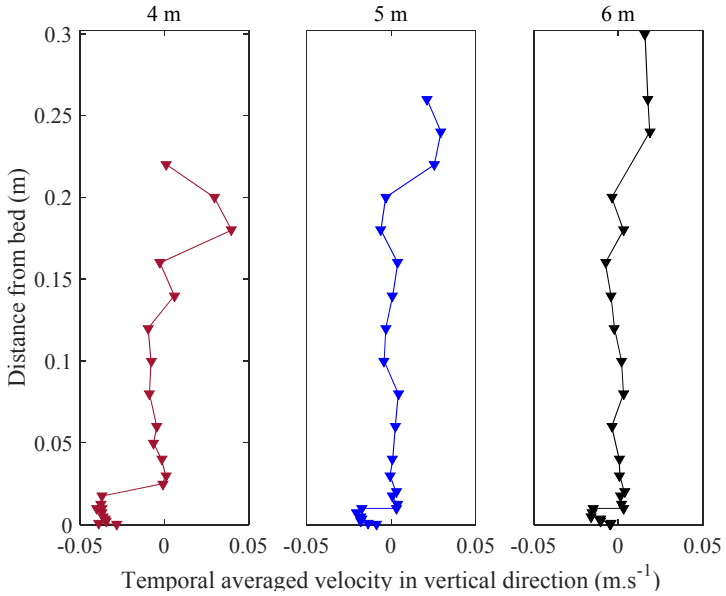

(b)

Figure 4.19 – Temporal averaged vertical velocity in on-offshore direction for S_{op} = 3½ % (a) inside the surfzone y={1,2,3}m (b) seaward of the breaker region y={4,5,6}m

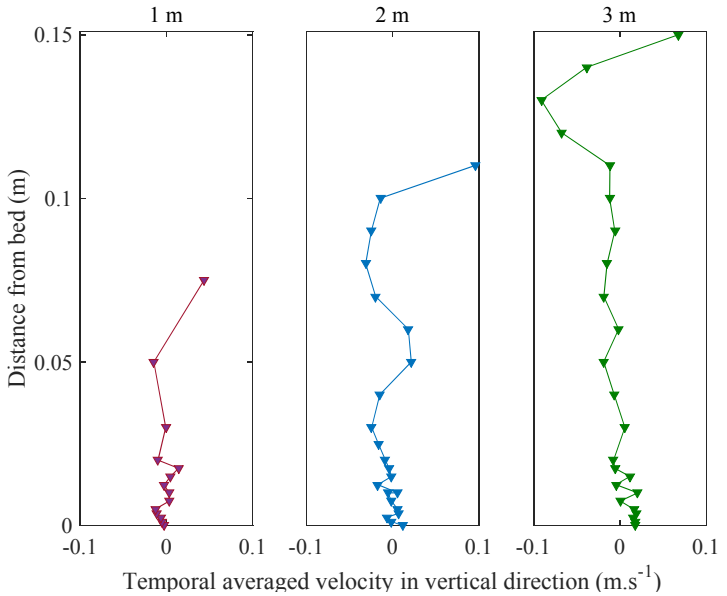

(a)

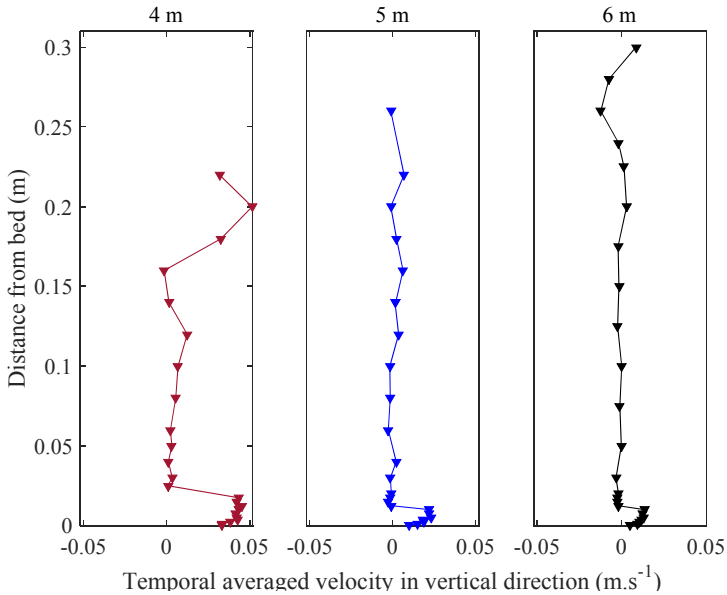

(b)

Figure 4.20 – Temporal averaged vertical velocity in on-offshore direction for S_{op} = 5% (a) inside the surfzone y={1,2,3}m (b) seaward of the breaker region y={4,5,6}m

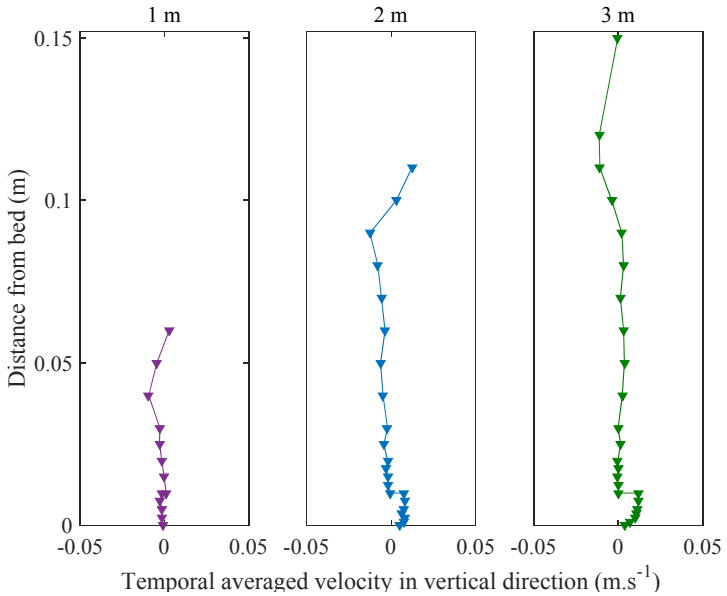

(a)

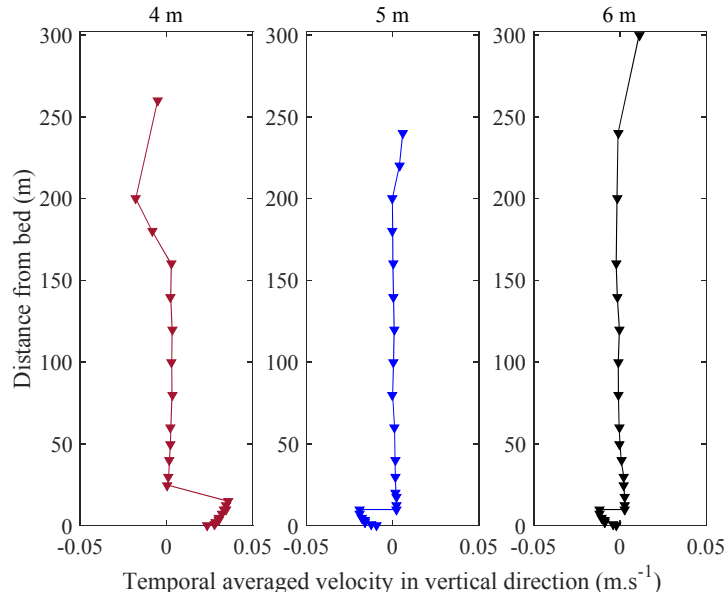

(b)

Figure 4.21 – Temporal averaged vertical velocity in on-offshore direction for S_{op} = 3½ $_{\text{Random}}$% (a) inside the surfzone y={1,2,3}m (b) seaward of the breaker region y={4,5,6}m

4.3.1.5 Wave Conditions

The water surface profiles were recorded simultaneously across the basin mild section at 0.5m intervals to determine the wave characteristics in the region of the dye plume (Fig. 4.22). The wave conditions were logged continuously for the duration of both the concentration measurements and the velocity data collection periods.

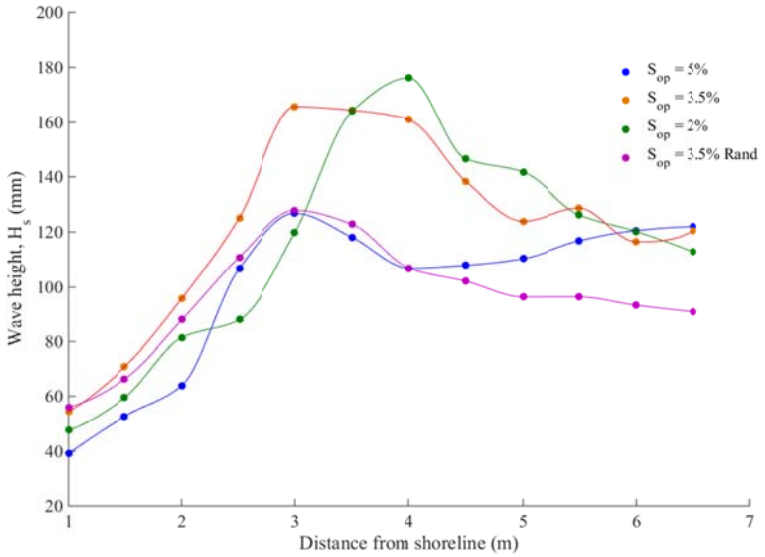

Figure 4.22 – Wave height measurements across the nearshore region for all the wave conditions

Figure 4.22 depicts the wave conditions for all four test cases across the control section. Table 4.2 shows the wave characteristics at the furthest wave gauge, y = 6.5m from the shoreline (SWL). This region has been termed 'offshore', although the waves are in the transitional region due to the water depth (d=0.35m).

Table 4.2 – Measured wave conditions in the offshore region of basin (y=6.5m)

Nominal Wave Steepness S_{op}	Offshore wave height H_o [m]	Offshore wave Period T_p [sec]	Offshore wave steepness S_{op} [%]
5.0%	0.122	1.20	5.49
3.5%	0.121	1.85	3.53
2.0%	0.112	2.90	2.08
$3.5\%_{Random}$	0.90	1.40	3.47

4.3.2 Solute Concentration Data

The behaviour of solute contaminant in the nearshore region has been invesitgated during the DHI experiments with the tracer measurement at various locations inside the surfzone and seaward of the breaker region. Dye tracer measurement were carried out with a constant head injection of Rhodamine Water Tracer dye to the basin from a small tapping point at approximately mid-depth (§ 4.2.4).

For each wave condition, the transverse mixing characteristics have been determined at three distinct locations including the surf-zone, breaker-point, and offshore, which correspond to distances of $y=\{2,\ 3,\ 5\}m$ from the shore line, respectively. Figures 4.23 to 4.27 present the results of tracer studies for all wave conditions tested during DHI study.

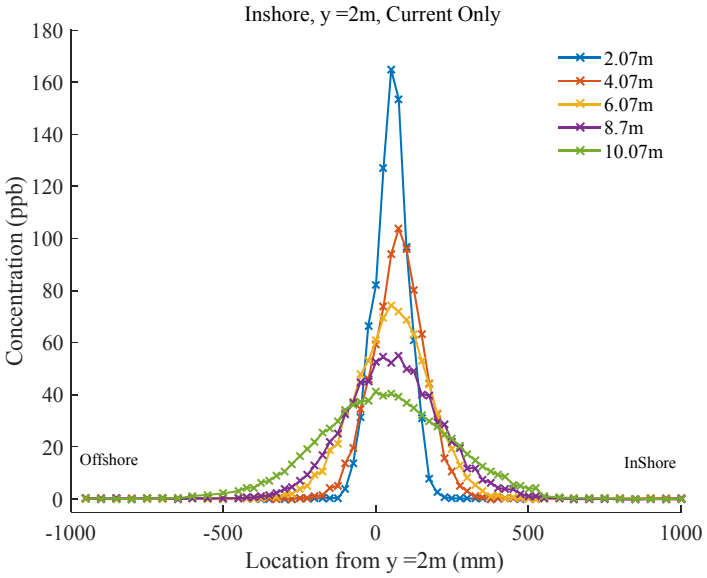

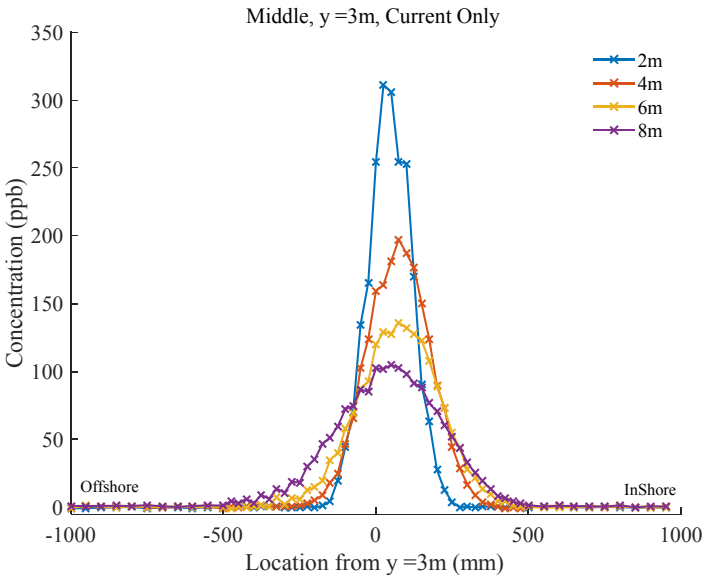
Middle, y =3m, Current Only
Concentration (ppb)
Location from y =3m (mm)
2m
4m
6m
8m
Offshore
InShore
350
300
250
200
150
100
50
0
-1000
-500
0
500
1000

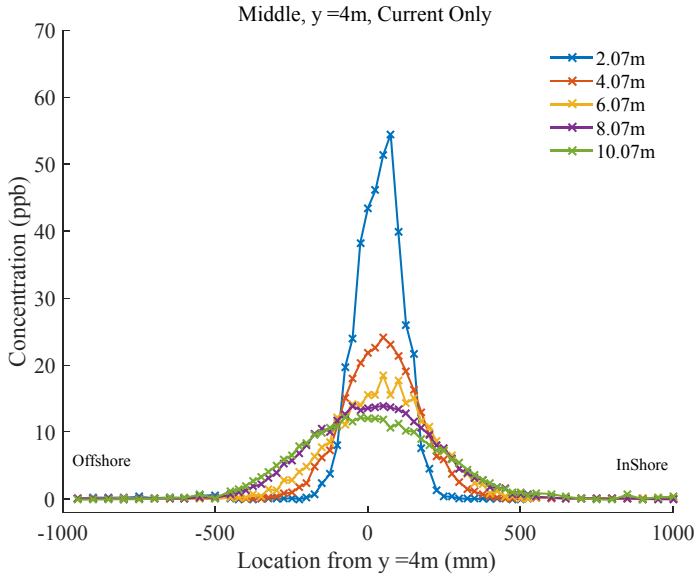
Middle, y =4m, Current Only
Concentration (ppb)
Location from y =4m (mm)
2.07m
4.07m
6.07m
8.07m
10.07m
Offshore
InShore
70
60
50
40
30
20
10
0
-1000
-500
0
500
1000

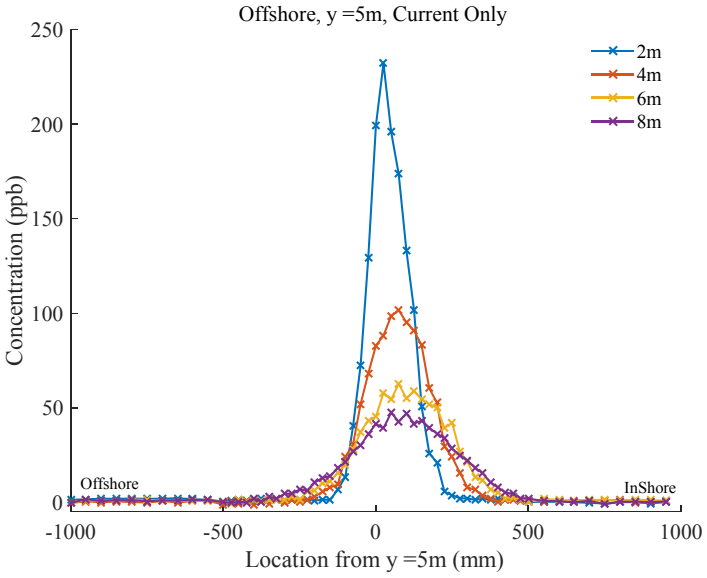
Offshore, y =5m, Current Only
Concentration (ppb)
Location from y =5m (mm)
2m
4m
6m
8m
Offshore
InShore
250
200
150
100
50
0
-1000
-500
0
500
1000

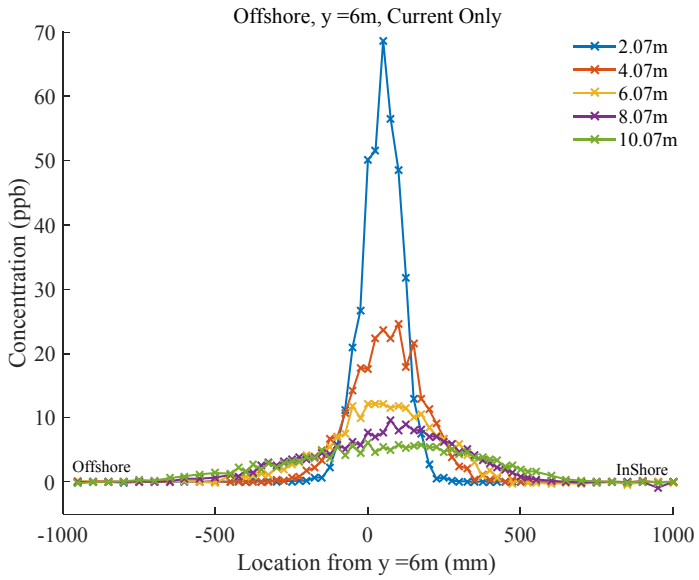

Figure 4.23 – Concentration measurements for Current only condition at y = {2, 3, 4, 5, 6}m from shore line

Figure 4.23 shows the concentration measurements for the current only condition at y = {2, 3, 4, 5, 6}m from shore line. For each location, the variation of tracer concentration is plotted with regards to the distance inshore and offshore from the study.

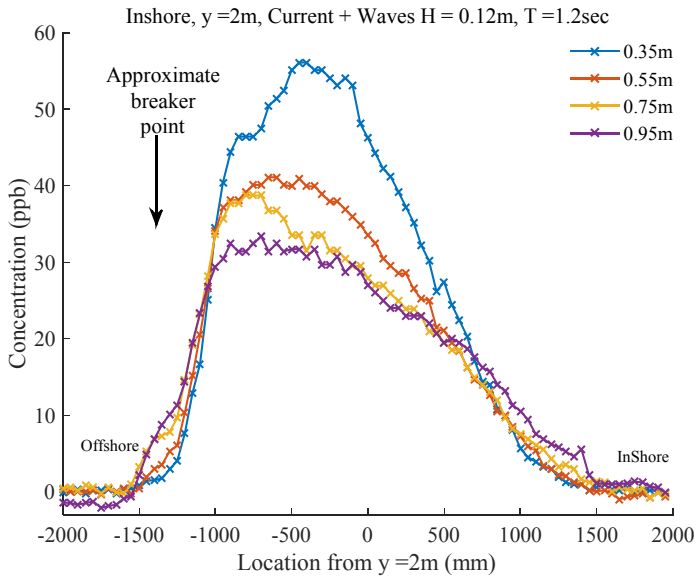

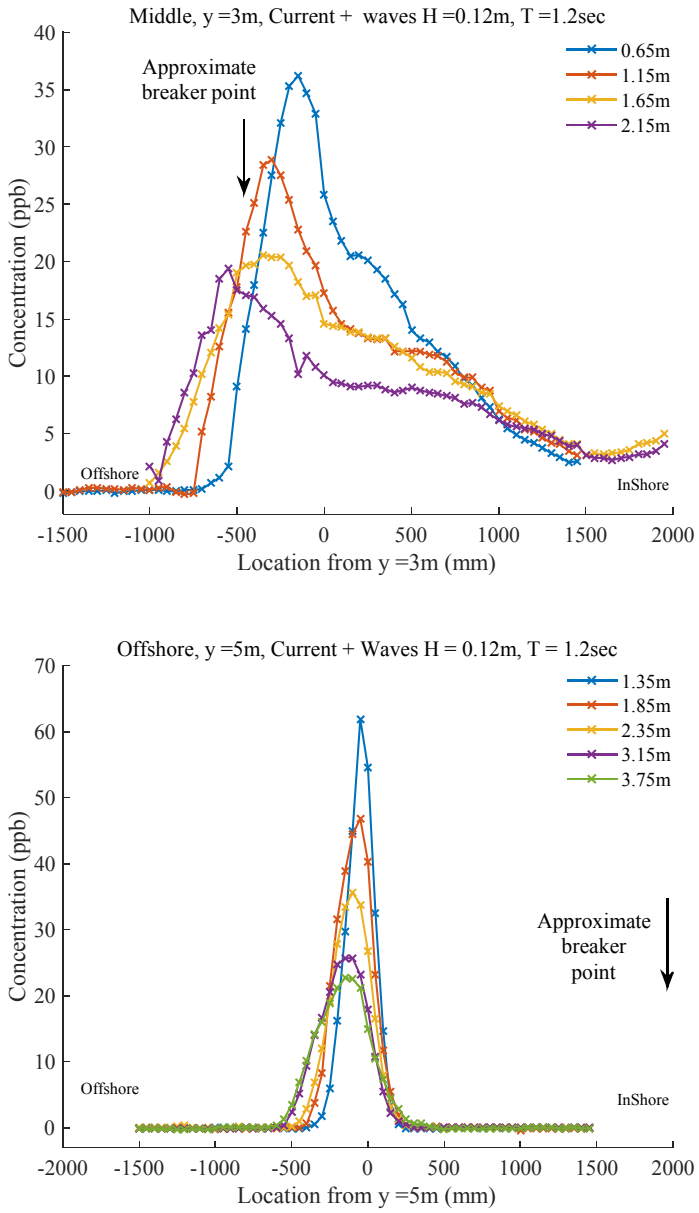

Figure 4.24 – Concentration for 3 injection points; surfzone, breaker point and offshore Wave condition – monochromatic waves with H = 0.12m and T=1.2sec

Figure 4.24 illustrates the results of tracer study for the monochromatic waves with the offshore wave height of 0.12m and wave period of 1.2sec. The tracer concentrations have been measured for three different injection points, inside the surfzone, breaker point and a location seaward of the breaker region for y = {2, 3, 5}m. The approximate location of the breaker point is shown for each study location. The injection point is at the origin of each graph.

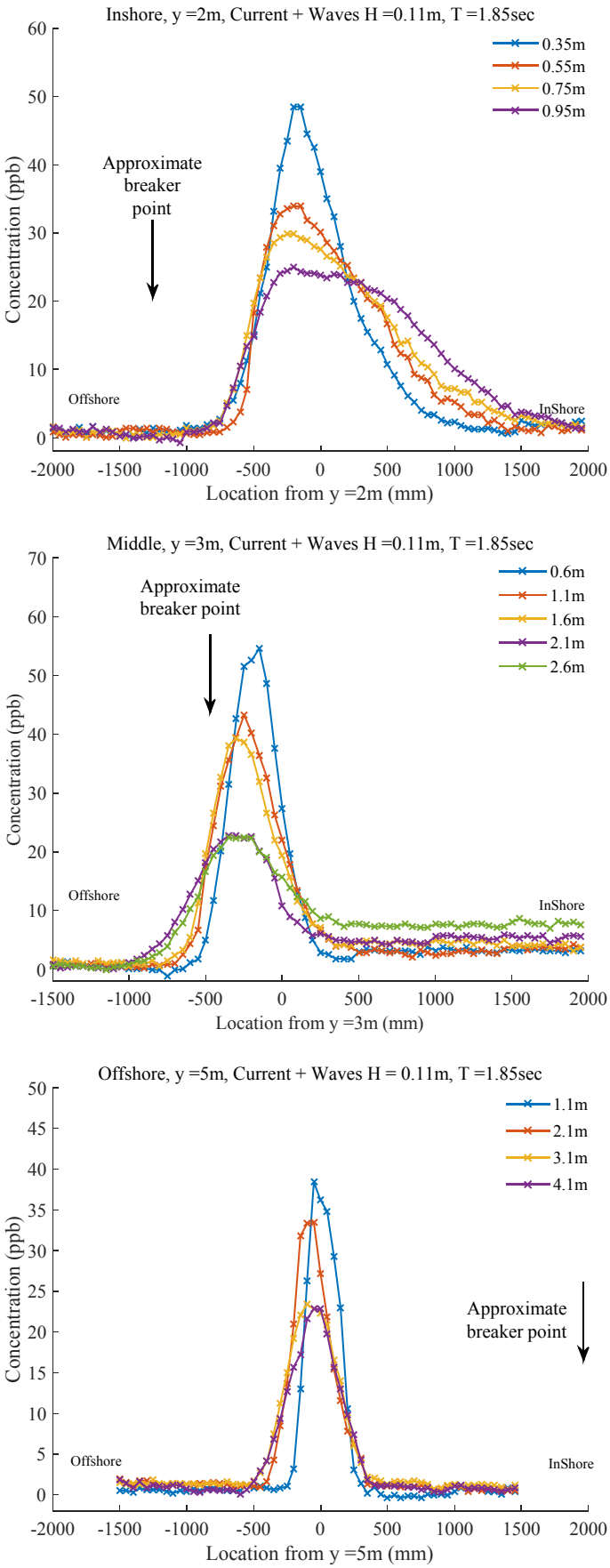

Figure 4.25 – Concentration for 3 injection points; surfzone, breaker point and offshore Wave condition – monochromatic waves with $H = 0.12$m & $T = 1.85$sec

Figure 4.25 shows the tracer measurements for monochromatic waves with an offshore wave height of 0.12m and the wave period of 1.85sec. The analysis of fluorometric data for three locations from the shoreline is presented to understand the tracer behaviour in the surfzone, breaker point and offshore region. For this condition, the dye was injected at 2, 3 and 5m from the still water line. The approximiate breaking point is shown in the graph for each location.

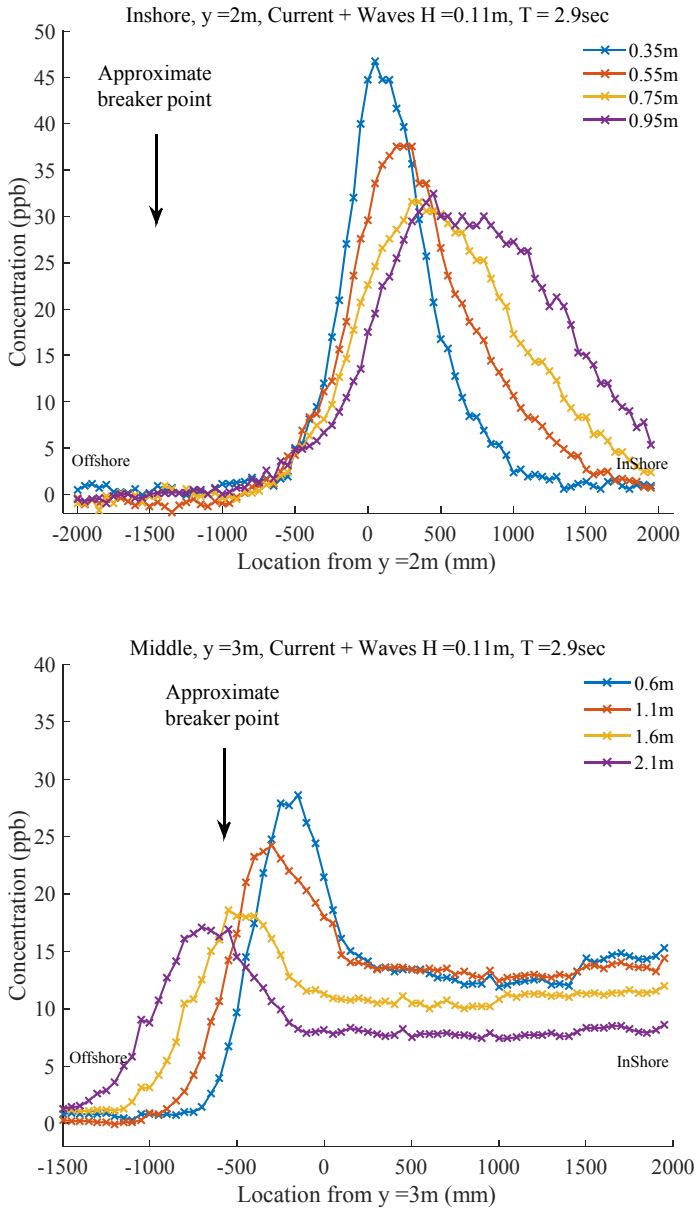

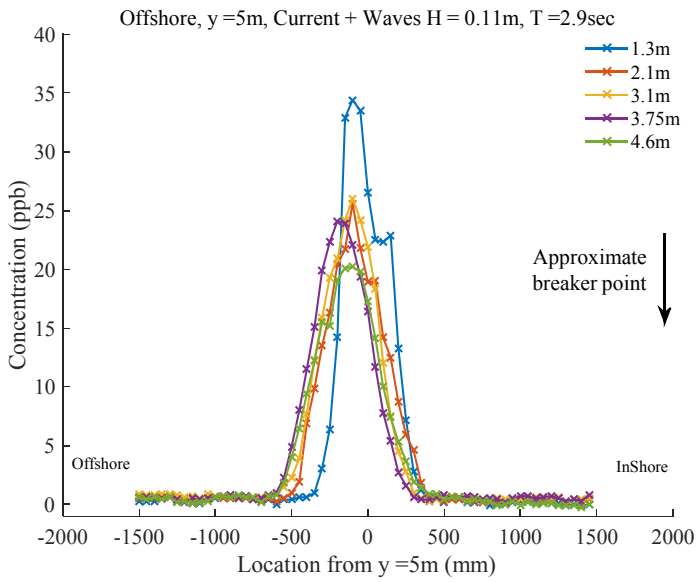

Figure 4.26 – Concentration for 3 injection points; surfzone, breaker point and offshore Wave condition – monochromatic waves with $H = 0.12m$ & $T = 2.9$sec

Figure 4.26 shows the concentration measurements for regular waves with offshore height of 0.12m and period of 2.9sec. For a comprehensive overview of tracer behaviour across the nearshore, three points including the surfzone, at the breaker point and in the offshore region have been investigated.

Figure 2.27 represents the tracer studies for irregular waves with the wave steepness of 3½%. Three locations at y = {2, 3, & 5}m have been investigated for the tracer measurements. The tracer concentrations shows that inside the surfzone, the tracer concentration stays higher shoreward of the injection point. However, the results show that the concentration drops rapidly for the offshore locations.

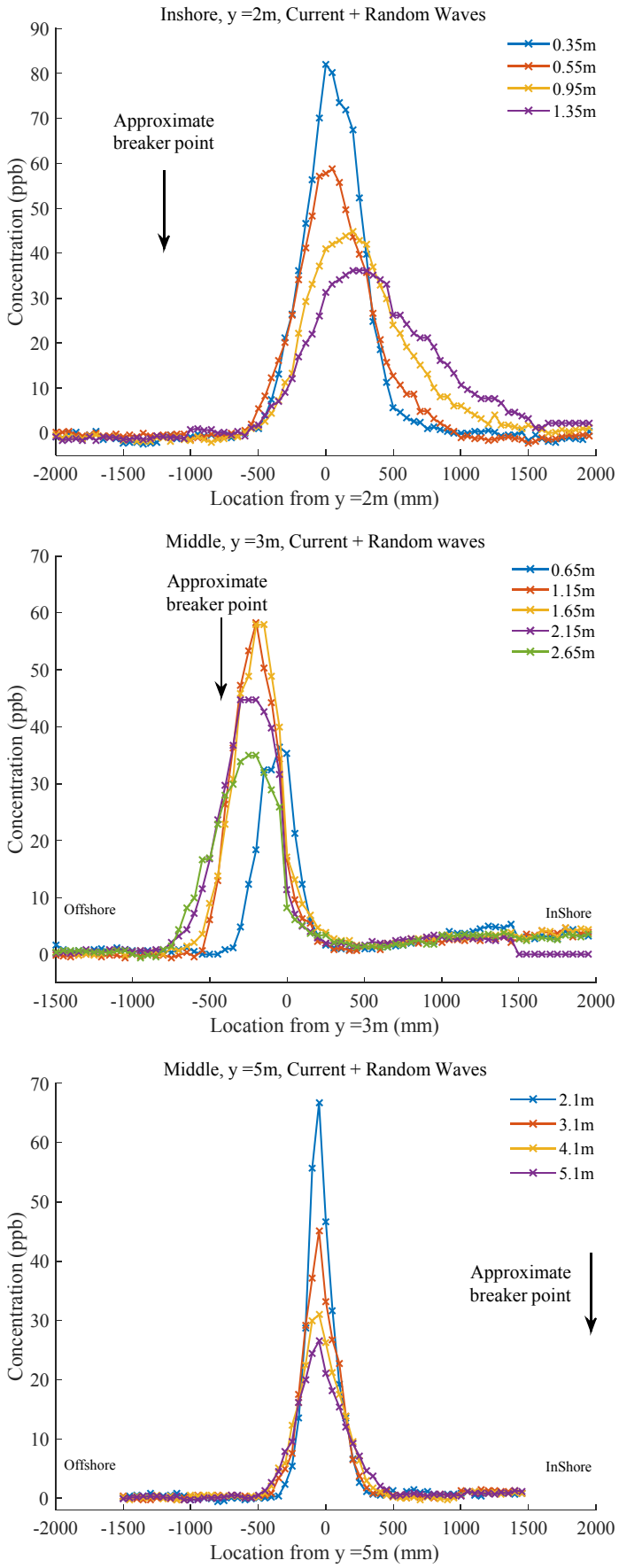

Fig: 4.27 – Concentration for 3 injection points; surfzone, breaker point and offshore
Wave condition – monochromatic waves with S_{op} = 3½%$_{\text{Random}}$

The variance of transverse concentrations against the distance from the injection points were determined for all tested conditions. Figure 4.28 presents the transverse concentration variance for all tested conditions and injection points. The value of R^2 for all tested conditions and injection points are plotted in figure 4.28.

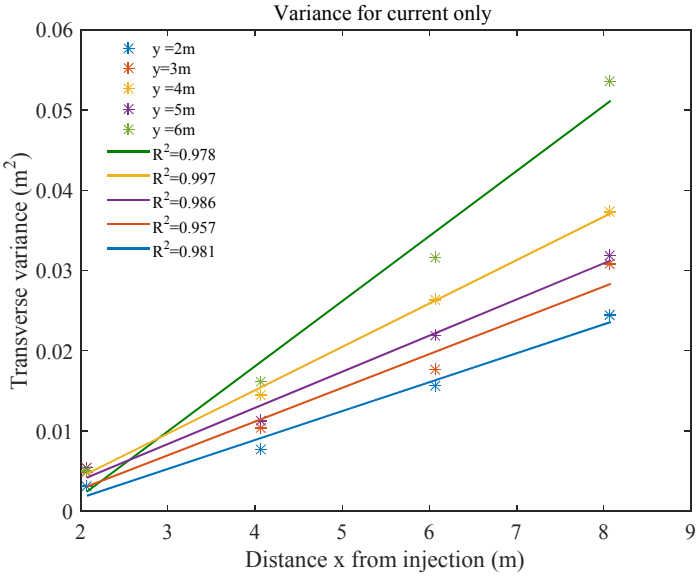

(a)

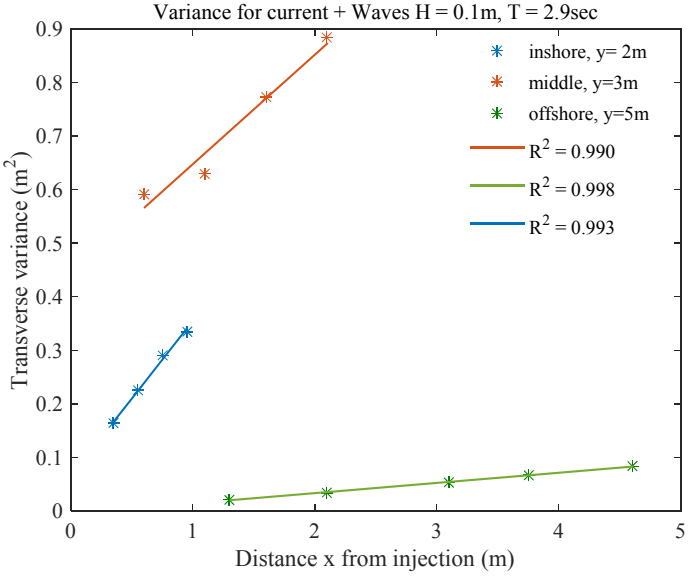

(b)

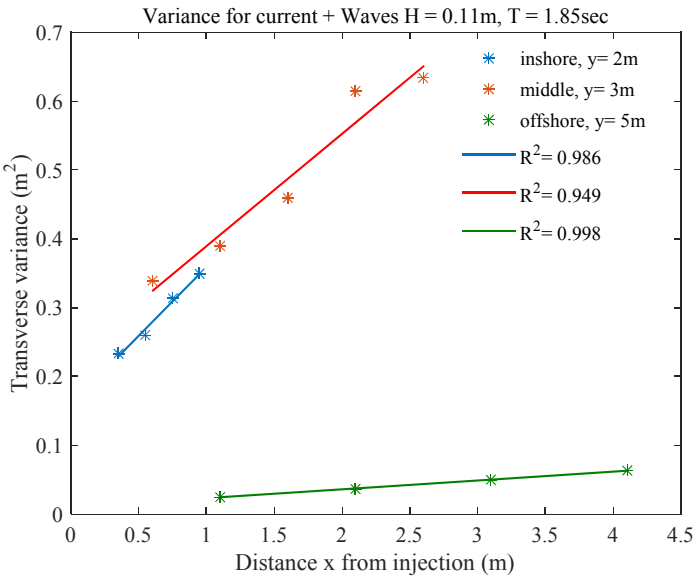
Variance for current + Waves H = 0.11m, T = 1.85sec
Transverse variance (m^2)
Distance x from injection (m)
inshore, y= 2m
middle, y= 3m
offshore, y= 5m
R^2= 0.986
R^2= 0.949
R^2= 0.998
0
0.1
0.2
0.3
0.4
0.5
0.6
0.7
0.5
1
1.5
2
2.5
3
3.5
4
4.5

(c)

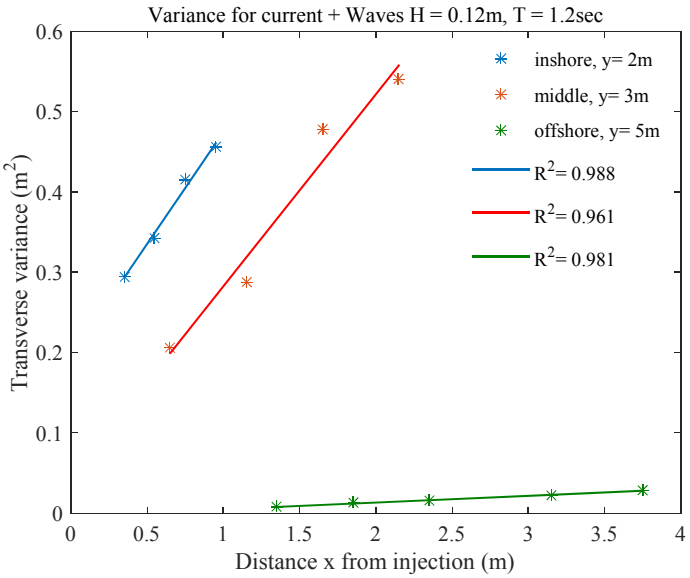
Variance for current + Waves H = 0.12m, T = 1.2sec
Transverse variance (m^2)
Distance x from injection (m)
inshore, y= 2m
middle, y= 3m
offshore, y= 5m
R^2= 0.988
R^2= 0.961
R^2= 0.981
0
0.1
0.2
0.3
0.4
0.5
0.6
0.5
1
1.5
2
2.5
3
3.5
4

(d)

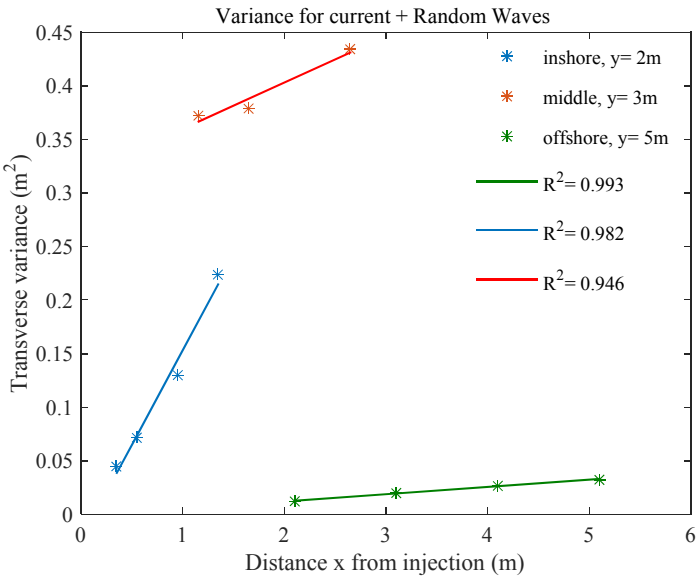

(e)

Figure 4.28 – Relationship between the variance of the transverse concentration profiles and longitudinal distance for (a) current only condition, (b) monochromatic waves, S_{op} = 2%, (c) monochromatic waves, S_{op} = 3½ %, (d) monochromatic waves, S_{op} = 5% and (e) Random waves, S_{op} = 3½ $_{\text{Random}}$%

4.3.3 Mixing Coefficient of Fluorometric Study

In coastal waters and nearshore region where the depth of water is relatively small compared to the flow width, the solute becomes vertically well mixed within a short distance from the source (point source discharge). Many researchers have adopted the analogy of turbulent mixing processes to Fickian diffusion in the coastal region (Fischer *et al*., 1979; Rutherford, 1994; Pearson *et al,*. 2002 and 2009). In order to reduce the complexity of considering and measuring all the associate parameters in spreading of dye, the depth variation in the solute concentrations can be ignored. Therefore, considering the variations of solute concentrations in the transverse and longitudinal directions, the depth averaged advective-dispersion equation can be written as:

$$d\frac{\partial c_d}{\partial t} + d\frac{\partial}{\partial x}(uc)_d + d\frac{\partial}{\partial y}(vc)_d = \frac{\partial}{\partial x}\left(d\left(e_x\frac{\partial c}{\partial x}\right)_d\right) + \frac{\partial}{\partial y}\left(d\left(e_y\frac{\partial c}{\partial y}\right)_d\right) \tag{4.2}$$

where, c is the concentration of diffusant, d is the total depth, e represents the diffusion coefficient, u and v are time-varying velocity in x and y direction respectively, k_x and k_y are longitudinal and transverse dispersion coefficients and D is the overall mixing coefficient. Equation 4.2 considers the molecular diffusion to be negligible and it takes into account the effect of spatial averaging of velocities on the spreading of a tracer. Taylor (1954) proposed an analysis method of solute tracer which combined the effects of both turbulent diffusion and shear dispersion. Fischer *et al*. (1979) studied a continuous vertical line source of solute injection and proposed the theoretical solution for the transverse spreading (Eq. 4.3)

$$c_d(x,y) = \frac{Q}{d\sqrt{4\pi D_y x u_d}}\exp\left(-\frac{y^2 u_d}{4D_y x}\right) \tag{4.3}$$

where x and y denote longitudinal and vertical directions respectively, c_d represents the depth averaged solute concentration, D_y is dispersion coefficient in the y direction, u_d is longitudinal depth averaged velocity and Q is the mass inflow rate of solute per unit width. Equation 4.3 results in a Gaussian distribution shape for concentration, and therefore the measure of spread about the bed can be quantified by calculating the spatial variance (σ^2) of the distribution:

$$\sigma_y^2 = \frac{\int_{-\infty}^{\infty}(y-\mu)^2 c_d(y)dy}{\int_{-\infty}^{\infty} c_d(y)dy} \tag{4.4}$$

The position of the centroid (μ) of the distribution can be determined from:

$$\mu = \frac{\int_{-\infty}^{\infty} y c_d(y) dy}{\int_{-\infty}^{\infty} c_d(y) dy} \tag{4.5}$$

As the mathematical feature of a Gaussian distribution, the spatial variance (σ^2) increases linearly with the distance from the source (Abolfathi and Pearson, 2014). Therefore, the transverse mixing coefficient can be defined as the rate of change of variance (Eq. 4.6).

$$D_y = \frac{u_d}{2} \frac{d\sigma_y^2}{dx} \tag{4.6}$$

D_y in equation 4.6 incorporates the combined effects of turbulent diffusion and shear dispersion. This equation has been used extensively in open channel flow (Fischer, 1967) and nearshore coastal region (Pearson *et al*., 2002, Pearson *et al*., 2009; Abolfathi and Pearson, 2014).

Figures 4.23 to 4.27 demonstrate the resultant above background concentration profiles for the four tested wave-current conditions as well as the current only condition. The spatial variance of each concentration profile has been determined based on equation 4.4 and the results for all tested conditions and locations are presented in figure 4.28. The results show that the increase in the transverse variance with regards to distance is approximately linear, although, some scattering exist. The transverse mixing coefficient has been determined by using u_d as depth-averaged velocity at the dye injection point. Tables 4.3 to 4.5 show the resulting mixing coefficients for all tested conditions.

Table 4.3 –Transverse mixing results for a continuous injection of tracer inside the surfzone, 2m from the shoreline under waves of varying T, with an H_o =0.12m

Nominal Wave Steepness S_{op}	Offshore wave height H_o [m]	Offshore wave Period T_p [sec]	Long. velocity (u_d) [m/s]	Bed shear velocity (u_*) [m/s]	$\frac{d\sigma_y^2}{dx}$ [m]	Transverse dispersion coefficient D_y [m^2/s]	$\frac{D_y}{du^*}$
0	-	-	0.09	0.0045	0.0036	1.620E-04	0.36
5.0%	0.122	1.20	0.09	0.0045	0.279	1.195E-02	27.9
3.5%	0.121	1.85	0.09	0.0045	0.200	8.566E-03	20.0
2.0%	0.112	2.90	0.09	0.0045	0.290	1.44E-02	29.0
$3.5\%_{Random}$	0.090	1.85	0.09	0.0045	0.177	7.961E-03	17.7

Table 4.4 –Transverse mixing results for a continuous injection of tracer at breaker region, 3m from the shoreline from the shoreline under waves of varying T, with an H_o =0.12m

Nominal Wave Steepness S_{op}	Offshore wave height H_o [m]	Offshore wave Period T_p [sec]	Long. velocity (u_d) [m/s]	Bed shear velocity (u_*) [m/s]	$\frac{d\sigma_y^2}{dx}$ [m]	Transverse dispersion coefficient D_y [m^2/s]	$\frac{D_y}{du^*}$
0	-	-	0.15	0.0075	0.0042	3.150E-04	0.28
5.0%	0.122	1.20	0.15	0.0075	0.239	1.261E-02	15.9
3.5%	0.121	1.85	0.15	0.0075	0.163	8.609E-03	10.9
2.0%	0.112	2.90	0.15	0.0075	0.205	1.079E-02	13.6
$3.5\%_{Random}$	0.090	1.85	0.15	0.0075	0.0432	3.240E-03	2.88

Table 4.5 –Transverse mixing results for a continuous injection of tracer, 5m from the shoreline from the shoreline under waves of varying T, with an H_o =0.12m

Nominal Wave Steepness S_{op}	Offshore wave height H_o [m]	Offshore wave Period T_p [sec]	Long. velocity (u_d) [m/s]	Bed shear velocity (u_*) [m/s]	$\frac{d\sigma_y^2}{dx}$ [m]	Transverse dispersion coefficient D_y [m^2/s]	$\frac{D_y}{du^*}$
0	-	-	0.165	0.00825	0.0045	3.710E-04	0.18
5.0%	0.122	1.20	0.165	0.00825	0.0084	6.930E-04	0.36
3.5%	0.121	1.85	0.165	0.00825	0.0128	1.056E-03	0.51
2.0%	0.112	2.90	0.165	0.00825	0.0191	1.576E-03	0.76
$3.5\%_{Random}$	0.090	1.85	0.165	0.00825	0.0068	5.610E-04	0.27

It is evident from the dye analysis results (Tables 4.3 to 4.5) that the mixing coefficient is significantly higher inside the surfzone than seaward of the breaker region. The results demonstrate that there is a 25-fold increase in the mixing over the offshore region at the breaker, whereas in the centre of the surfzone a 50-fold increase is observed.

4.4 Theoretical Model for Nearshore Mixing

This section focuses on quantifying the diffusive and dispersive mixing mechanisms from the hydrodynamic data collected in the DHI experiments. The turbulent diffusion and shear dispersion are quantified for all hydrodynamic conditions tested in DHI experiment based on the methodology derived in chapter three (§3.4).

4.4.1 Turbulent Kinetic Energy

The diffusion processes in the nearshore region are important factors which contribute towards the overall dispersion coefficient. As discussed earlier in chapter 2 and 3, the turbulent diffusion coefficient is generally equal to the eddy diffusivity coefficient for the case of nearshore flow. Svendsen (1987) pointed out that eddy viscosity could be estimated as a function of turbulent kinetic energy (Eq. 2.64). In this section, turbulent kinetic energy is determined for all tested wave conditions to quantify the contribution of diffusive mixing processes on the overall mixing coefficient.

The turbulence structure is studied in this section using the two-dimensional velocity records from LDA measurements. The LDA system was set to achieve a 200*Hz* data recording rate. However, the sampling rate for LDA is highly dependent on the seeding and the presence of bubbles in the flow. Despite careful consideration for the seeding, in some conditions and locations, especially inside the surfzone and in the upper part of the water column, the existence of bubbles and air entrainments to the LDA probe resulted in a poorer data acquisition rate. Figure 4.29 shows an example of a 2D velocity record inside the surfzone and seaward of the breaker region near the free surface of water.

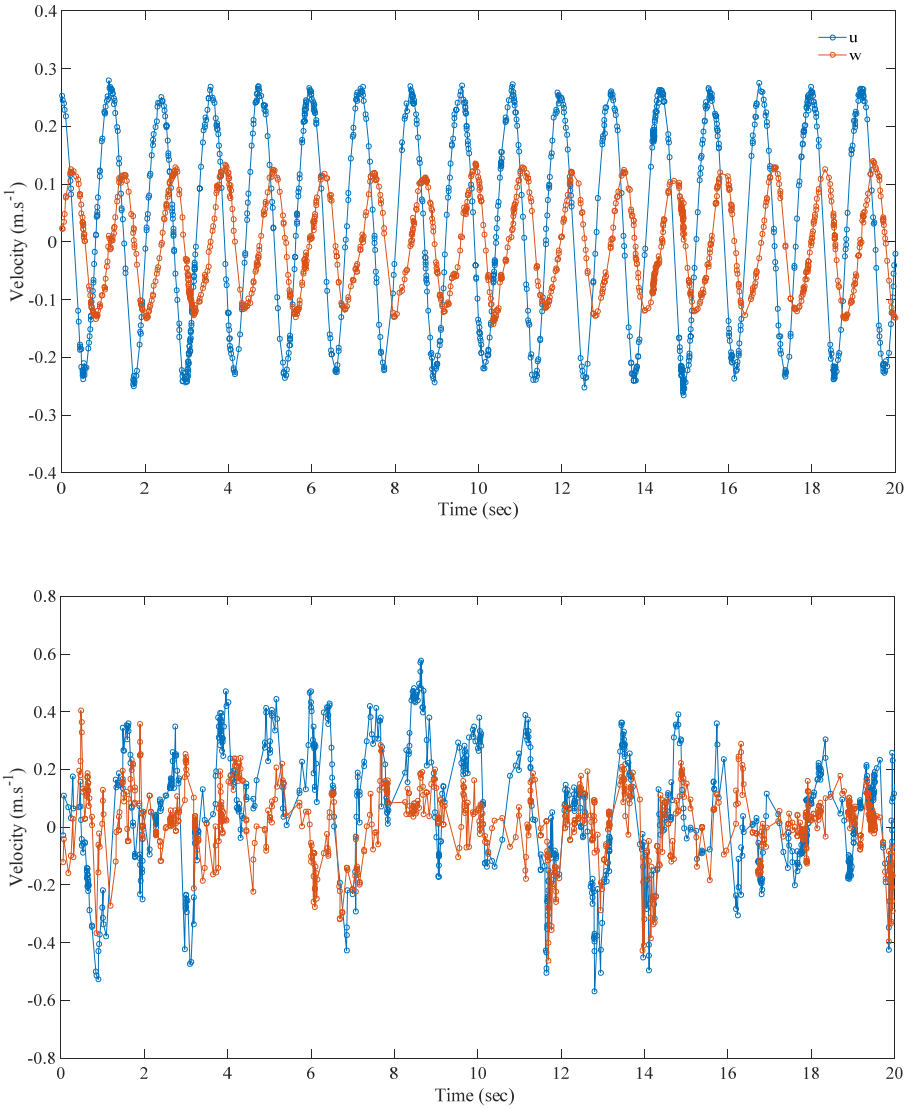

Figure 4.29 – An example of 2D velocity (*u*, *w*) records from LDA experiments – *H* = 0.12m & T = 1.2sec. (Top) measurements at 6m from SWL (Bottom) measurements inside the surfzone at 2m from SWL – red line is *w* and blue line represents *u*

For each on-offshore location, the LDA data is recorded at several points (up to 25 points) over the vertical from the bed to the wave crest elevation. For those measurement points close to the water surface, the LDA probe was outside the water during the undertow phase, and therefore the data acquisition rates were poor. For each measurement point, the data were recorded for over 180 consecutive waves. Figure 4.30 is an example of a velocity time-series which shows the on-offshore velocity component (*u*) measured inside (right) and outside (left) the surfzone. Only

10 consecutive waves are presented in the figure in order to show details of time series shape.

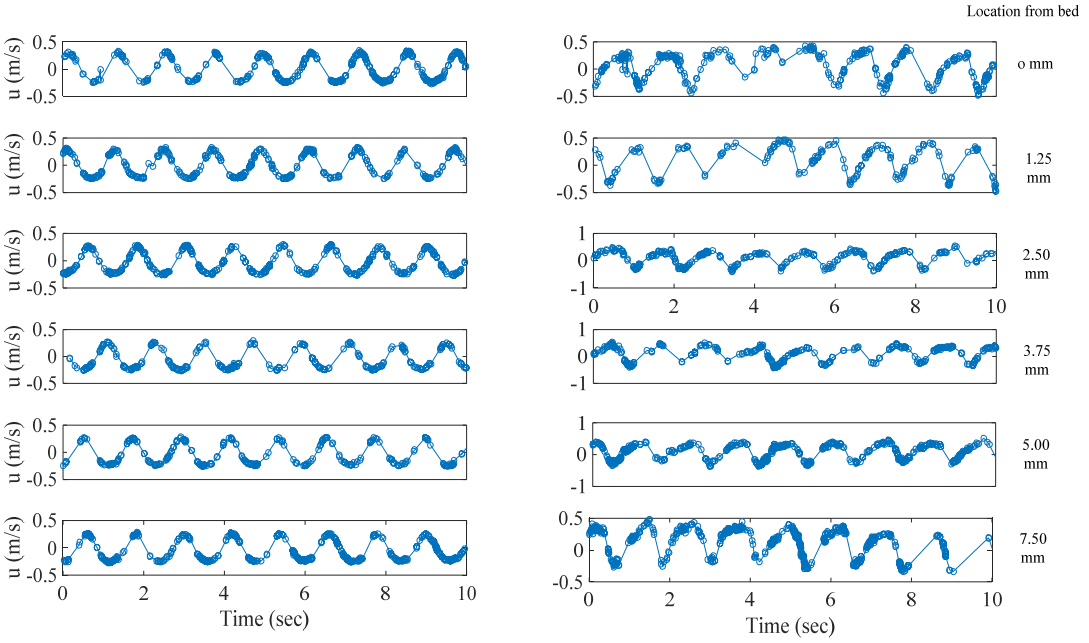

Figure 4.30 – An example of on-offshore velocity (u) records for H = 0.12m & T = 1.2sec (Left) outside the surfzone, at 5m from SWL, (Right) inside the surfzoe, at 2m from SWL

Turbulent Kinetic Energy (TKE) is essentially the deviation of the instantaneous velocity records from the mean velocity. Due to the nature of the complex three dimensional velocity fields in the nearshore region, determining the turbulence structure is a challenging task to achieve accurately. The turbulence field in the nearshore region is complex due to the interaction of waves and longshore currents and the periodic orbital motions of waves.

The raw hydrodynamic data obtained from measurements with the LDA technique, especially inside the surfzone, often contains some spikes which are recorded due to Doppler noise floor, aliasing of Doppler signal together with the presence of bubbles and air entrainment to the LDA probe. The presence of spikes in the data set can result in over estimation of turbulence and TKE. Therefore, it is important to detect and remove the spikes. § 4.4.1.1 present the method adopted in this study to deal

with spurious velocity records. Following the development and implementation of the despiking algorithm, the TKE estimation technique will be described in § 4.4.1.2.

4.4.1.1 Despiking Algorithm for LDA Data

Existence of spikes in the hydrodynamic data is a common problem that has been reported in several studies. In this section, a number of different methods for detecting and tackling the spike problem are considered and discussed. For a case with a single point spike, simple despiking algorithms can be utilized. However, in this work, LDA data has multi-point spikes and therefore, careful consideration was needed to detect and deal with these spikes. Figure 4.31 shows an example of unprocessed LDA data including multipoint spikes.

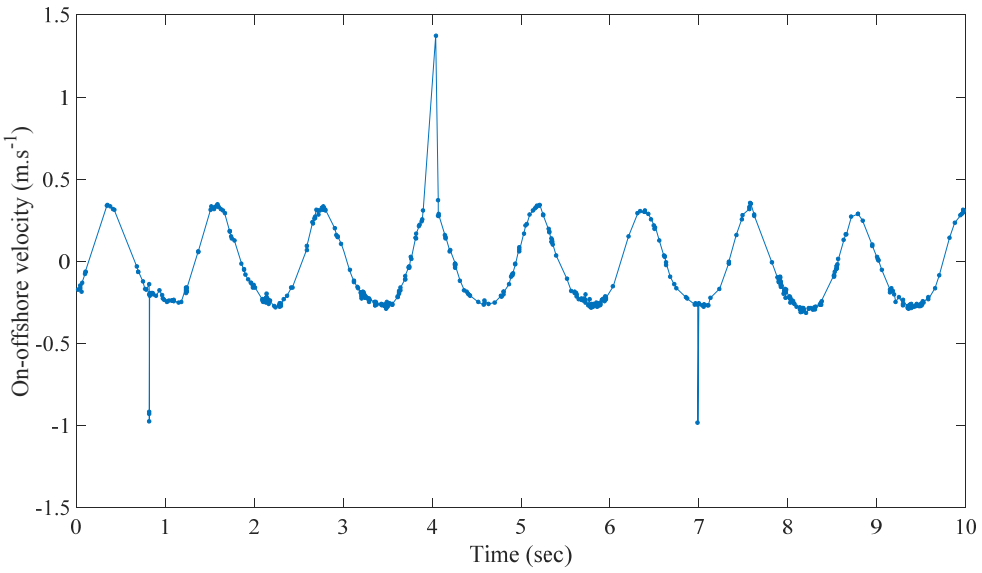

Figure 4.31 – An example of multipoint spikes in LDA data - on-offshore velocity (u) records for H = 0.12m & T = 1.2sec outside the surfzone, at 4m from SWL

Several studies have been conducted to develop an efficient method for dealing with the spikes of ADV data [McKinney, 1993; Donoho & Johnstone, 1994; Abarbanel, 1995; Addison, 1997; Roy *et al.*, 1999; Nikora and Goring, 2000; Goring and Nikora, 2002]. The electrical engineers were the first to develop despiking methods, wild point editing method (Otnes & Enochson, 1978), RC Filter and Tukey 53H

method are the most practised methods by electrical engineers. Nikora and Goring (2000) proposed an algorithm for despiking Acoustic Doppler Velocimetry data based on an Acceleration Thresholding Method. The method is derived on the basis that under normal flow conditions the instantaneous acceleration in a stream must be of the same (or less) than the acceleration of gravity (*g*). If the instantaneous acceleration for any particle is higher than gravity, the sediment grains should be thrown about violently, which is not the case in nature. The Nikora and Goring (2000) method determines the accelerations using a backward differencing technique in which the spikes are those points with the accelerations higher than *g* or *2g*. However, the method has limitations (Goring and Nikora, 2002). The method was improved by adding an extra condition so that a point could be considered as a spike if the acceleration exceeded a threshold $\lambda_a g$ and the absolute deviation from the mean velocity of the point exceed $k\sigma$. λ_a is a relative acceleration threshold, σ is the standard deviation and k is a constant (Goring and Nikora, 2002). This modified approach is successful for records where the spikes are very different from fluctuations in the data. However, the choice of thresholds is quite complicated and subjective.

For this study, a phase-space thresholding method was employed to remove spikes from data. Before applying the despiking algorithm, the mean and long-period fluctuations of the data were removed. On the completion of the spike removal processes, the mean and long-period fluctuations were returned to the data. The phase-space thresholding method (Goring and Nikora, 2002) employs a three-dimensional Pioncare map where the variable and its derivatives are plotted against each other. In this method, a universal criterion is defined to enclose the plotted data in an ellipsoid. The points outside the ellipsoid are labelled as spikes. In the phase-space thresholding method, the number of iterations goes down until the number of points, which are identified as spikes, falls to zero. Figure 4.32 shows an example of a Pioncare map plotted for LDA data obtained from DHI experiment. The red points in figure 4.32 represent the spikes and the blue points are good data. Once the spikes are detected, the algorithm will replace the spike in the data using a polynomial of best fit through the data on both sides of the spike, followed by interpolation across the spike with this polynomial.

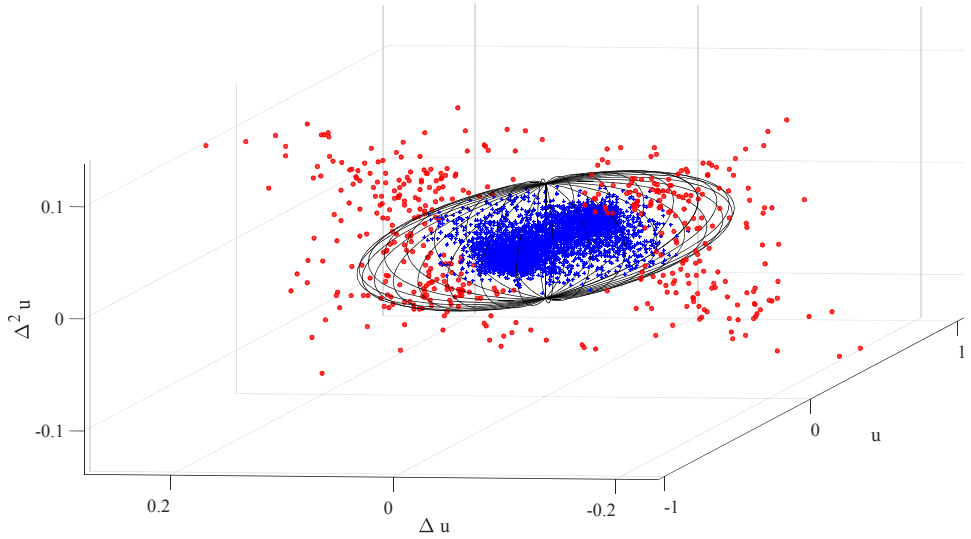

Figure 4.32 – Pioncare map for the data with H = 0.12m & T = 1.2sec inside the surfzone, at 3m from SWL

4.4.1.2 TKE Algorithm

Turbulent Kinetic Energy (TKE) is defined as the kinetic energy per unit mass of the turbulent fluctuations (u') in the flow:

$$TKE = k = \frac{1}{2}(\overline{u'^2_x} + \overline{u'^2_y} + \overline{u'^2_z}) \tag{4.7}$$

General information about TKE in the nearshore due to the wave activities and previous studies on TKE measurements were presented in chapter 2 (§2.4.3 - §2.4.4). In this section, the turbulent kinetic energy is determined from velocity time-series of LDA data and the results are compared to the existing data.

TKE is basically characterized by the root-mean-square of velocity fluctuations. Hence, TKE could be estimated by measuring the deviation of instantaneous velocity fluctuations from the mean velocity of a data record. There are several methods for determining the TKE from velocity records which are all based on separating the mean signal from the turbulent fluctuation signal. Amongst these methods, ensemble averaging and spectral analysis are the most practised techniques for estimating

TKE. Ensemble averaging techniques can define the mean time-varying wave components of the flow and has been utilised widely in coastal engineering problems [Stive, 1980; Stive & Wind, 1982; Svendsen, 1987]. For periodic waves, ensemble averaging can be executed by sampling at the same phase value from many successive waves. This method allows low-frequency vortices with a length scale comparable to the water depth to be recorded as a turbulent fluctuation signal (Svendsen, 1987). However, ensemble averaging techniques may result in overestimation of turbulence due to the fact that wave period in the surfzone, even for monochromatic waves, is not constant. One of the well-established methods in evaluating turbulent intensity and TKE is spectral analysis [Battjes & Sakai, 1981; Nadaokah & Kondoh, 1982; Sou *et al*., 2010] by use of Fourier Transforms and signal processing techniques. However, due to the Nyquist theorem (Meade *et al.*, 2000) and the choice of cut-off frequency in the signal processing, it is very likely to neglect some of the high frequency fluctuations and therefore an unrealistic estimation of turbulence typically results. Hence, there is a possibility of under-estimating or over-estimating the turbulence that exists in this method. Also, in this study, due to the existence of non-uniform distributed data points and missing velocity records inside the surfzone, determining the turbulence structure with use of Fourier transforms and spectral analysis was limited.

In this section, algorithms were developed for determining the turbulent kinetic energy from LDA data. The TKE was evaluated for each wavelet individually and averaged over 180 – 200 consecutive recorded waves. Each individual wavelet was recognized by using a zero-crossing algorithm. The TKE was calculated from deviations of the instantaneous velocity records from the mean velocity signal. For locations inside the surfzone (y={1, 2, 3}m), specifically those measurement points close to the free water surface, the existence of bubbles and air entrainments to the LDA probe reduced the data record and non-uniformity in time. A resampling technique with use of interpolation between each pair of recorded data at a constant time-step was adopted to retrieve the mean signal. Figure 4.33 shows an example of an LDA unprocessed signal against the resampled data for the monochromatic waves of 5% steepness inside the surfzone and close to the free water surface.

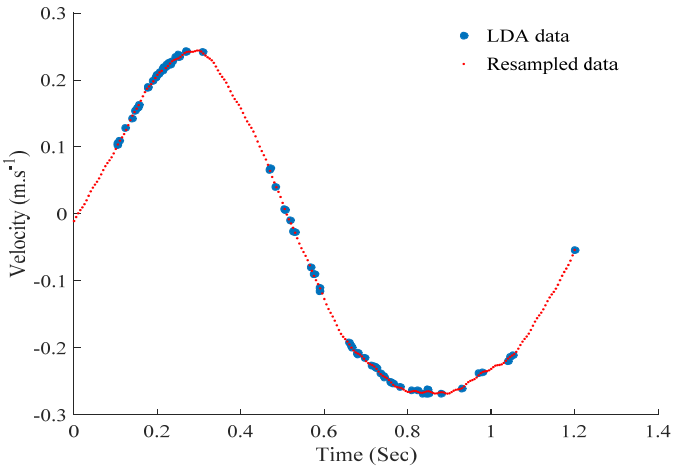

Figure 4.33 – An example of data resampling for LDA data inside the surfzone at 2m from SWL, S_{op} = 5%

The mean value of the LDA signal was determined by Fourier series (Eq. 4.8). The system of equations used to define the mean velocity (Eq. 4.8) is closely described by Fourier series without the constant (intercept) term.

$$V_{mean} = \sum_{i=1}^{n} a_i \sin(b_i x + c_i) \tag{4.8}$$

where n varies from 1 to 8, and thus the number of fit parameters can change from 3 to 24. The number of fit parameters was chosen according to the number of data points for each location and wave condition. TKE was then estimated using a windowing technique which splits the time series into a number of discrete wavelets with a limited number of data points. The variations of turbulent kinetic energy over the depth of water column for the DHI study is presented in figure 4.34.

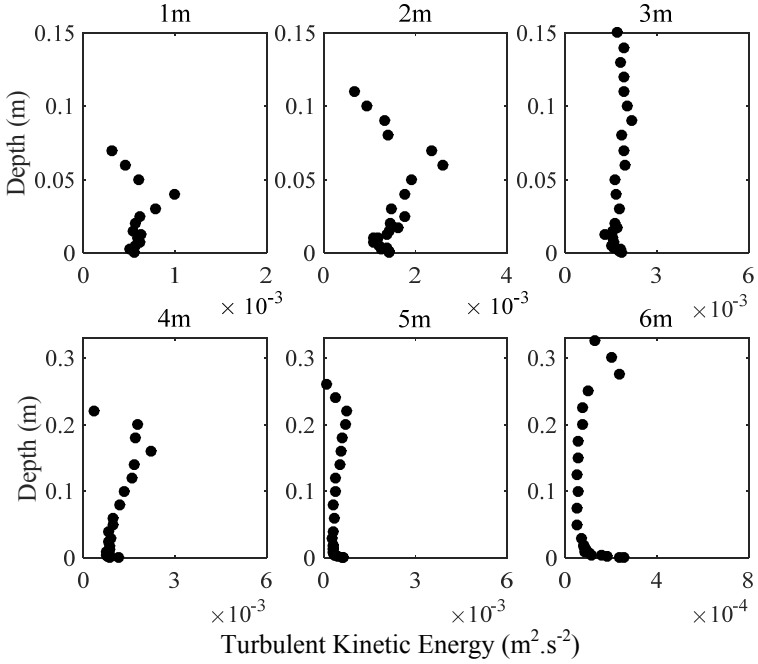
1m
2m
3m
4m
5m
6m
Depth (m)
Turbulent Kinetic Energy (m².s⁻²)

(a)

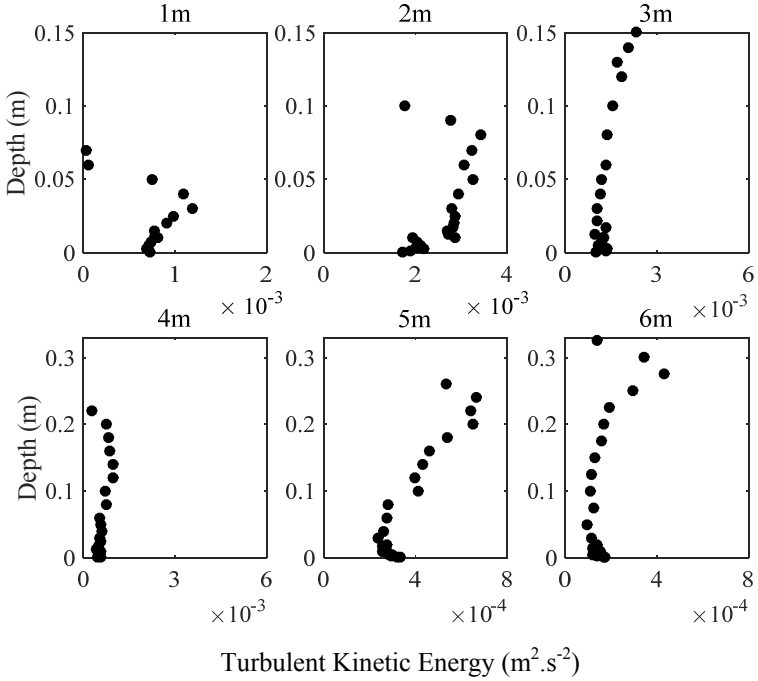
1m
2m
3m
4m
5m
6m
Depth (m)
Turbulent Kinetic Energy (m².s⁻²)

(b)

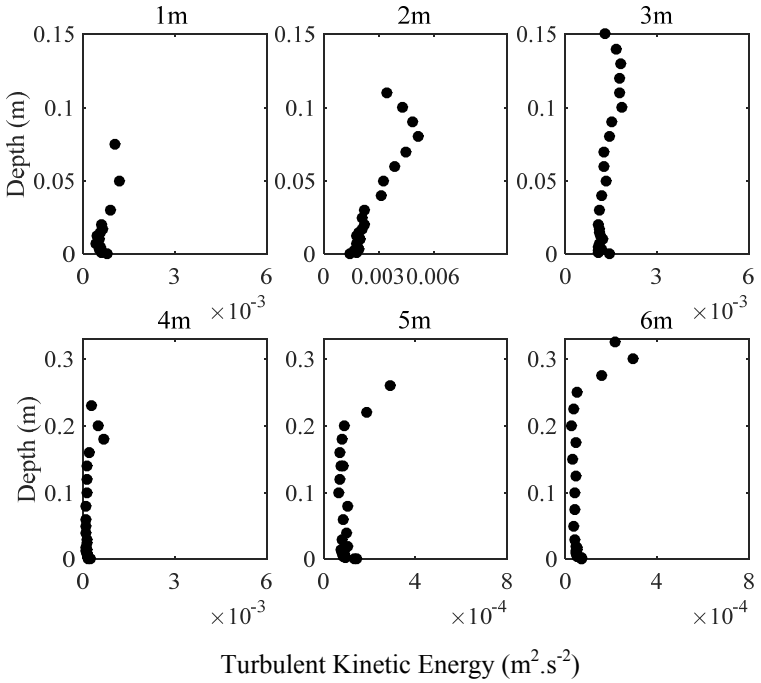

(c)

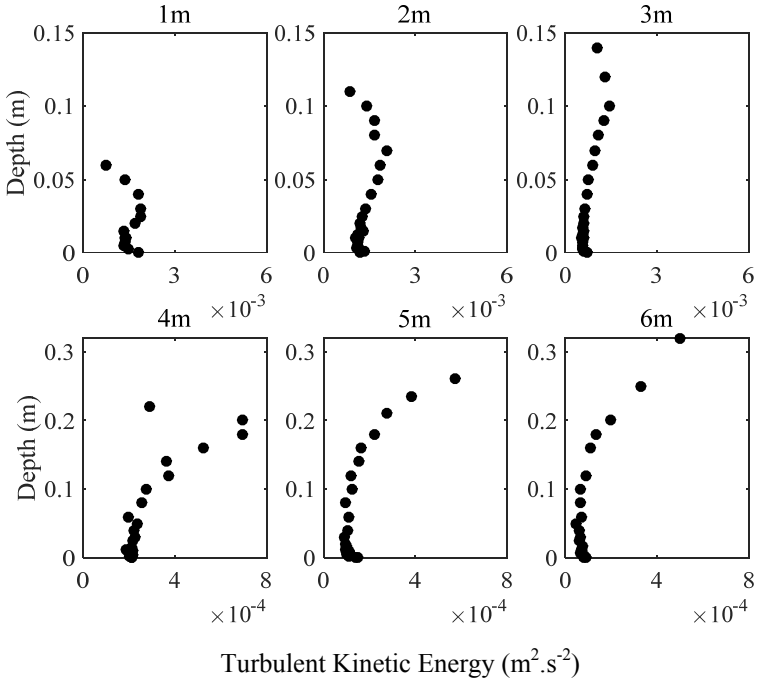

(d)

Figure 4.34 – Variation of TKE over depth of water column across the nearshore for the case of: (a) S_{op}=2%, (b) S_{op}=3½ %, (c) S_{op}=5% and (d) Pseudo random waves

Figure 4.34 represents the TKE variations across the nearshore for the monochromatic waves of 2, 3½, 5% and the random waves of 3½ % steepness,

respectively. The TKE variations across the nearshore demonstrate that the magnitude of turbulence outside the surfzone were decreased by an average of ~80% in comparison to the turbulence generated shoreward of the breaker.

As noted previously, for those locations inside the surfzone, especially towards the free surface, it is possible that hydrodynamic measurements are not representing the actual turbulence level. This was due to air entrainment and existence of bubbles. Hence, turbulence measurements are biased towards those phases of the wave cycle with lower turbulence levels. Figure 4.35 shows an example of the LDA recorded for on-offshore velocity during a wave cycle for the monochromatic waves of 3½% steepness at 2m from the shore and 5mm below the still water line. It is evident, that there are missing velocity records between 0.2 – 0.4sec and 0.6 – 1sec which might be associated to high turbulence phases of the cycle. Hence, it could be interpreted that there is an uncertainty in the accuracy of turbulence measurement inside the surfzone.

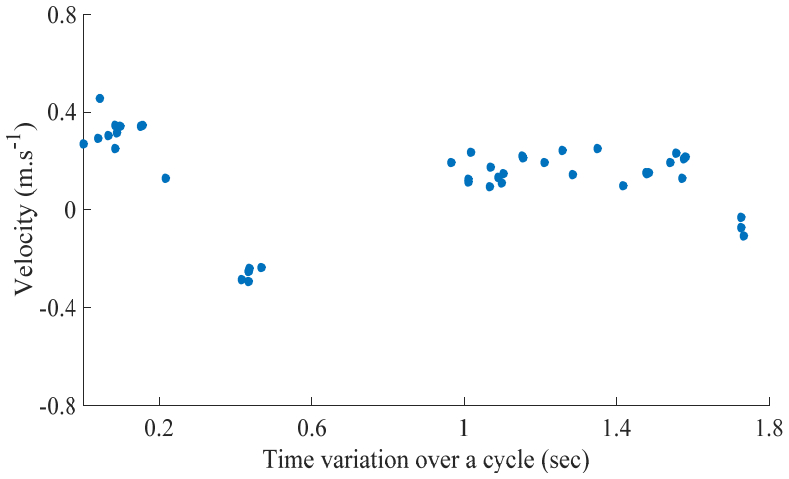

Figure 4.35 – Scarce on-offshore velocity records at 2m from shore and 5mm below the SWL for the case of H_0= 0.12m and T = 1.85sec

The results for the turbulent kinetic energy estimated from DHI hydrodynamic data are compared to the TKE measurements reported by Nadaokah & Kondoh (1982). Nadaokah & kondoh (1982) undertook a series of hydrodynamic measurements in a laboratory flume with a plane 1:20 beach slope using the LDA technique. They investigated plunging and spilling breaker waves and estimated TKE variations over

the depth of water column across the nearshore. Nadaokah & Kondoh (1982) employed a spectral analysis method and extracted the turbulent motion of the signal by filtering out frequencies below 10Hz. Hence, it is very likely that turbulent kinetic energies were underestimated in the Nadaokah & Kondoh (1982) results. Figure 4.36 compares the TKE reported by Nadaokah & Kondoh (1982) with the TKE determined in this study from LDA data. This figure focuses on the turbulence structure inside the surfzone up to the wave breaker region.

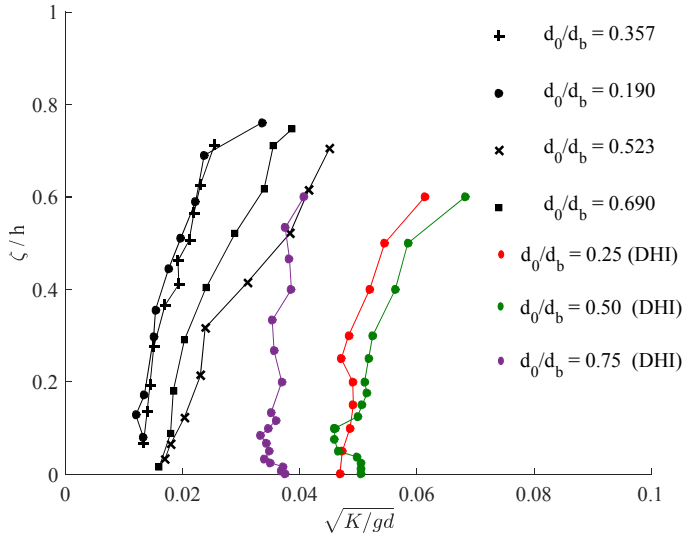

(a)

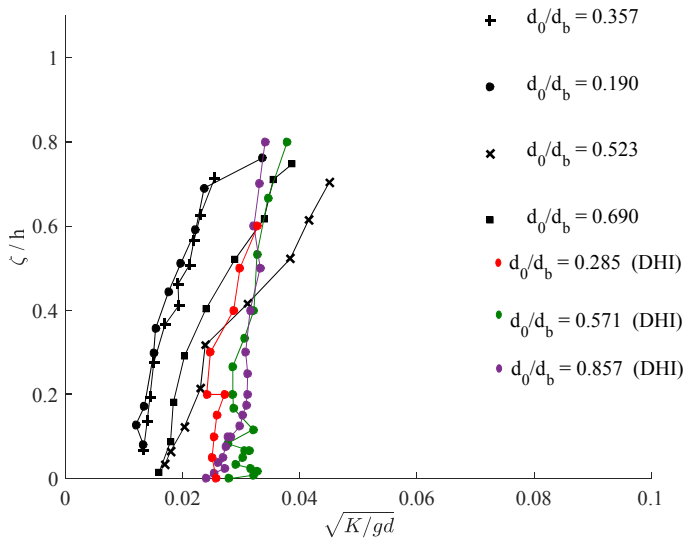

(b)

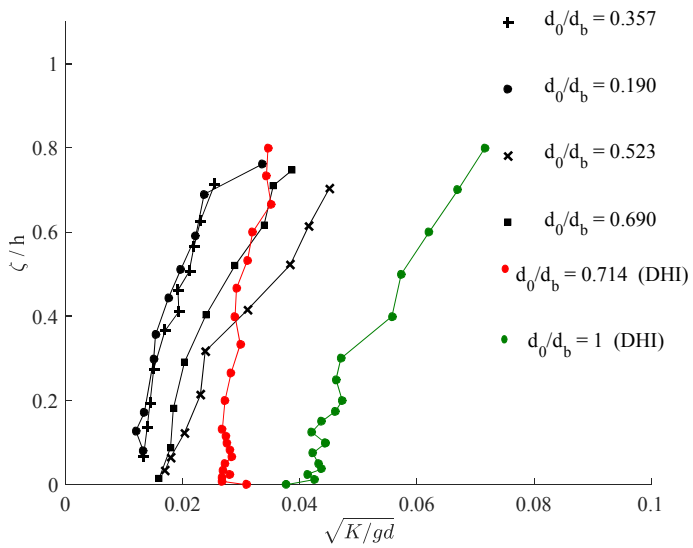

(c)

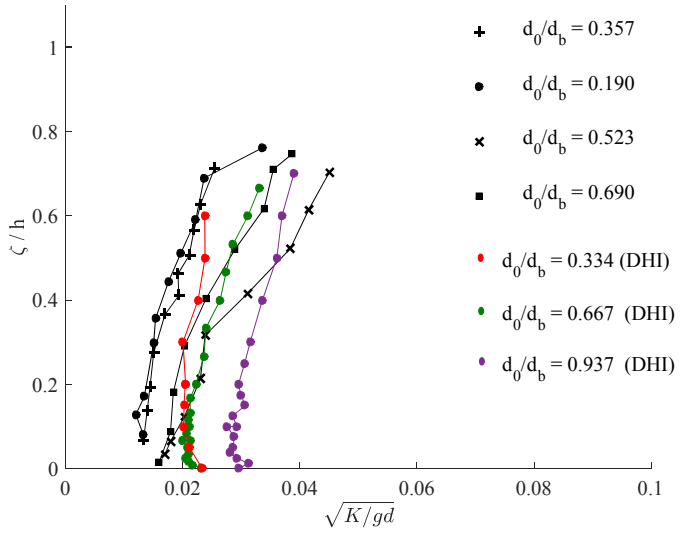

(d)

Figure 4.36 – Comparison of TKE reported by Nadaokah & Kondoh (1982) with the DHI measurements for the case of a) S_{op} = 2%, b) S_{op} = 3½ %, c) S_{op} = 5% & d) S_{op} = 3½ $_{\text{Random}}$%

The position of each set of measurements in figure 4.36 is indicated by the ratio of undisturbed local water depth (d_o) and undisturbed water depth at the breaker point (d_b). Figure 4.36(a) indicates that for the monochromatic waves of 2% steepness, $\sqrt{k/gd}$ is higher in the inner surfzone compared to the breaker region ($d_o/d_b = 0.75$). Figure 4.36(b) shows that the magnitude of $\sqrt{k/gd}$ has small variations inside the

surfzone (13%) for the monochromatic waves of 3½% steepness. Figure 4.36(c) demonstrates that for regular waves of 5% steepness, the value of $\sqrt{k/gd}$ drops by 64% from the breaker point to the inner surfzone. The results indicate that for waves with higher steepness (S_{op}=5%) most of the turbulent energy is being dissipated at the breaker region (Fig. 4.36c), while for the waves of lower steepness (S_{op}=2%), the kinetic energy is being transported to the inner surfzone (Fig. 4.36a).

The comparison between Nadaokah and Kondoh (1982) measurements and DHI data (Fig. 4.36) shows that for the conditions tested at DHI study, TKE values are higher than those values reported by Nadaokah and Kondoh (1982). It is evident from figure 4.36 that the TKE values reported in this study are in good agreement with the trend of data reported by Nadaokah and Kondoh (1982). The difference between TKE reported by Nadaokah and Kondoh (1982) and the current study is potentially due to the fact that the frequency signals below 10Hz are ignored, leading to neglecting some smaller scale turbulence, in Nadaokah and Kondoh (1982) estimation of TKE. The results depicted in figure 4.36 indicate that the variation of $\sqrt{k/gd}$ with vertical distance in the water column is very small, which confirms the existing data [Nadaokah and Kondoh, 1982; Stive and Wind, 1982; Svendsen, 1987].

The TKE measurements also show that inside the surfzone (y=1, 2, 3m), high turbulence intensity are observed for all tested conditions. This shows that there is a diffusive mixing mechanism due to the wave activities and turbulence generation. For those locations seaward of the breaker region, the results from DHI data confirms significant drops in the TKE (Fig. 4.34). TKE results confirm the existing knowledge and well-established measurements of surfzone turbulence [Battjes, 1975; Battjes 1983; Svendsen et al., 1978; Svendsen, 1987; Nadaokah & Kondoh, 1982; Hattori & Aono, 1985].

The analysis of temporal variation of TKE shows that when the wave front reaches the measurement location, TKE will increase. Once the wave front pass the measurement point, the TKE will gradually decay until the next wave reaches the

observation point. When the next breaker passes, the new turbulence is then added to the remaining TKE from the previous wave.

4.4.2 Turbulent Diffusion

Determining the turbulent diffusion coefficient will elucidate the contribution of the turbulence structure in the total mixing coefficient. In this section the turbulent diffusion coefficient is determined for all wave conditions which were studied during the DHI experiments. The turbulent diffusion obtained from hydrodynamic data is compared to the theoretical approach proposed by Svendsen and Putrevu (1994).

4.4.2.1 Eddy Viscosity

The turbulent diffusion coefficient is generally considered to be equal to the eddy viscosity coefficient (§3.4.1). Battjes (1983), Svendesen (1987) and Svendsen & Putrevu (1994) quantified the vertical diffusion coefficient as a function of turbulent kinetic energy (k) and the turbulent length scale (l_m) [see §2.5.3 for more details]. In this study, the diffusivity is determined based on the Svendsen (1987) methodology (Eq. 2.64).

$$v_t = l_m \sqrt{k} \tag{2.64}$$

The length scale is considered based on the methodology of Svendsen (1987) which proposed that the length scale of eddies is closely related to the water depth (d). The range of length-scale inside the surfzone proposed by Svendsen (1987) is described in §2.5.3 (Eq. 2.68).

$$0.25d \le l_m \le 0.35d \tag{2.68}$$

The length-scale of turbulence varies across the nearshore zone. Inside the surfzone, the turbulence propagates into the deeper layer of the water column. However, outside the surfzone, the turbulence dissipates at the free surface and does not propagate into deeper layers of water. Hence, the characteristic length-scale could reduce for those locations seaward of the breaker point. In this study, the lower range

(=0.25d) of l_m proposed by Svendsen (1987) was adopted for determining the eddy viscosity seaward of the breaker region, and the higher end (=0.35d) of l_m in equation 2.68 was considered for those locations inside the surfzone.

The eddy viscosity for this study was calculated by adopting the depth-averaged TKE from the LDA data and the characteristic length-scale based on methodology described in previous paragraphs. The results were compared with the theoretical formulae suggested by Svendsen & Putrevu (1994) [Eqs. 2.69 and 2.73].

$$\nu_t = 0.01 d\sqrt{gd} \text{ ; inside the surfzone} \tag{2.69}$$

$$\nu_t = [0.8(\frac{d}{d_b})^{-4} + 02]\nu_{tb} \text{ ; outside the surfzone} \tag{2.73}$$

where $\nu_{tb} = 0.01 d_b\sqrt{gd_b}$ is the eddy viscosity at breaking point, d is depth of SWL and d_b is depth of water at breaker point. The outputs of the Svendsen & Putrevu (1994) formulae for eddy viscosity are significantly dependent on the choice of breaker point. In this study, the breaker point was taken from laboratory data. Figure (4.37) presents the eddy viscosity values computed from DHI data and compares them with the diffusivity values obtained from Svendsen & Putrevu (1994) theoretical approach.

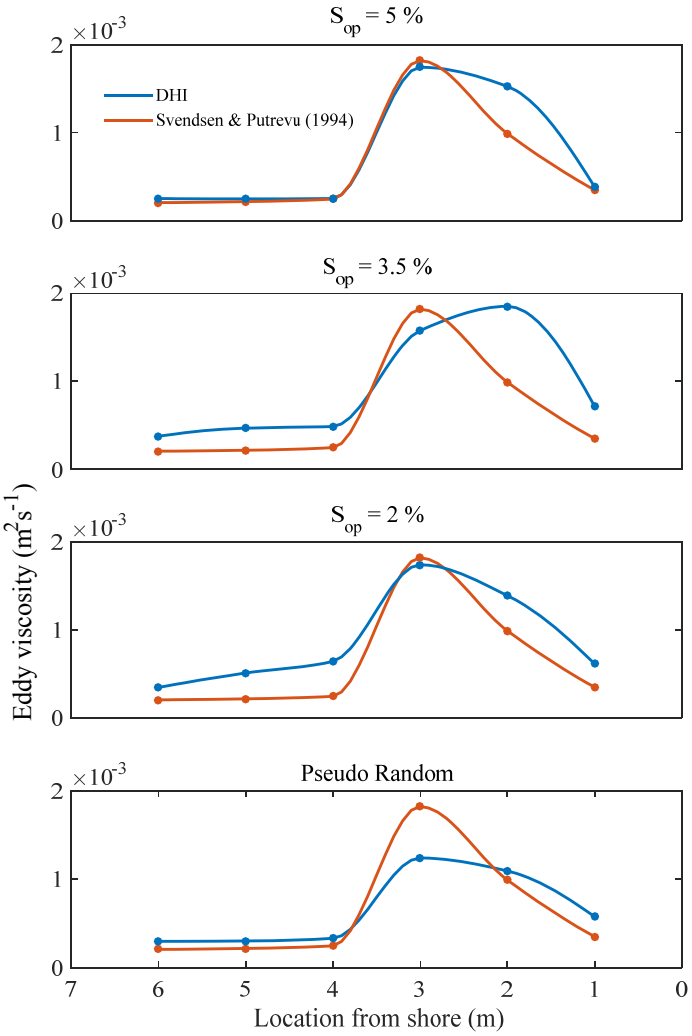

Figure 4.37 – Comparison of measured eddy viscosity from DHI data with Svednsen & Putrevu (1994) theoretical formulae

Figure 4.37 indicates that maximum eddy viscosity is occurring at the breaker region and the diffusivity significantly drops seaward of the breaker region. The results show that good agreement exists between the diffusivity measured from DHI data and the theoretical eddy viscosity proposed by Svendsen and Putrevu (1994). It is observed from figure 4.37 that for the random waves, the eddy viscosity values inside the surfezone are lower than those from the Svendsen & Putrevu (1994) formula. This is because under random waves, each wave breaks at a different location, hence rather than getting a focused breaker point, an averaged breaker zone is forming. It is also evident from figure 4.37 that close to the shoreline (y =1m),

diffusivity measured in this study is higher than those values proposed by Svendsen and Putrevu (1994).

In this section, the diffusive mixing mechanism has been quantified for DHI data. The TKE and eddy viscosity obtained from LDA data was compared to well-established theoretical and experimental data. The comparison of the results show that TKE values determined for DHI data were in line with the existing data and knowledge of the nearshore turbulence. Also, the diffusivity values obtained for DHI data are in good agreement with the theoretical formulae of Svendsen and Putrevu (1994). The next section will focus on quantifying dispersive mixing mechanisms for DHI data.

4.4.3 Shear Dispersion

In the nearshore region, wave processes are dominating the mixing of solute pollutants due to the finite depth of water. As described in §3.4, the mixing under wave-current condition is caused due to wave induced surface and bed generated turbulence and also due to the shearing effects from the vertical variation of velocity in the water column. As a result, the total mixing coefficient was defined as the sum of turbulent diffusion and shear dispersion (Eq. 3.5). This section focuses on quantifying the contribution of shear dispersion in the overall on-offshore mixing coefficient.

In this study, the shear dispersion coefficient was quantified for DHI data, using the mathematical solution proposed by Chikwendu (1986). An *N*-zone dispersion model was developed and adopted for quantifying the shear dispersion coefficient. The development of the *N*-zone model was described in detail in chapter 3 (§3.4.2). The dispersion model utilized the vertical variation of the flow hydrodynamics from LDA measurements. The flow depth is divided into *N* zones of parallel, well-mixed flow with constant velocity. A temporal averaging technique was employed to calculate the mean velocity value for LDA measurement points over the water column. Therefore each zone of depth h_j has a constant velocity of u_j. Figure 4.38 shows the schematic of the *N*-zone model developed in this study.

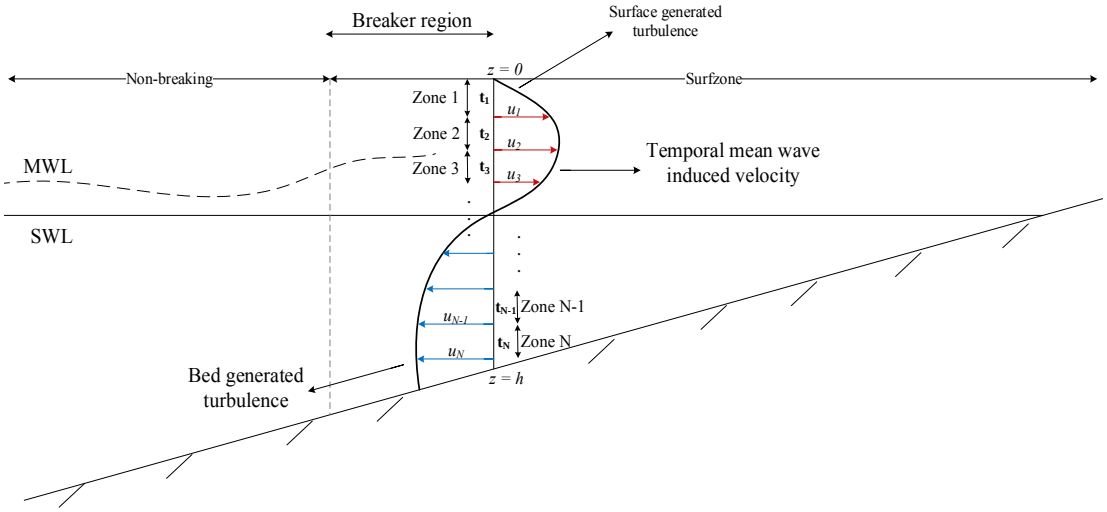

Figure 4.38 – schematic of *N*-zone model for calculation of dispersive mixing

The vertical variation of undertow was utilized to investigate the contribution of dispersive mechanisms in the overall mixing coefficient. The wave bore velocity measurements were not considered due to poor data resolutions in the upper part of the water column. Figure 4.39 shows the undertow velocity inputs which were obtained from temporal averaging of LDA data for all wave conditions tested in the DHI experiments.

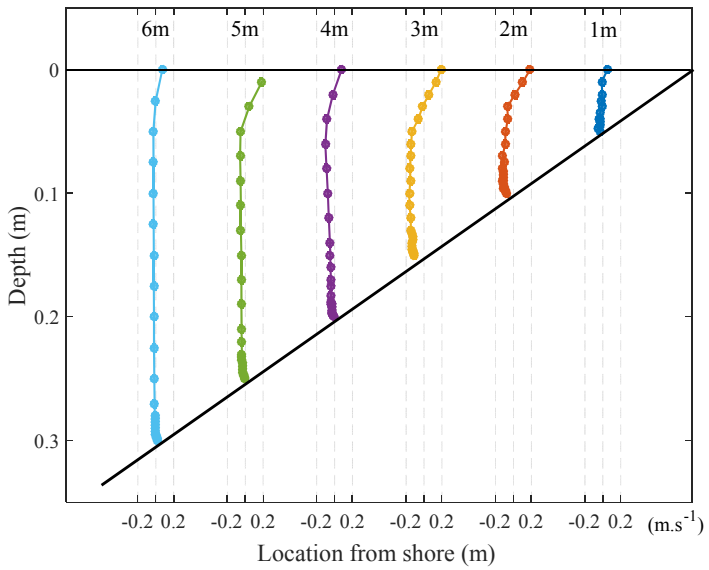

(a)

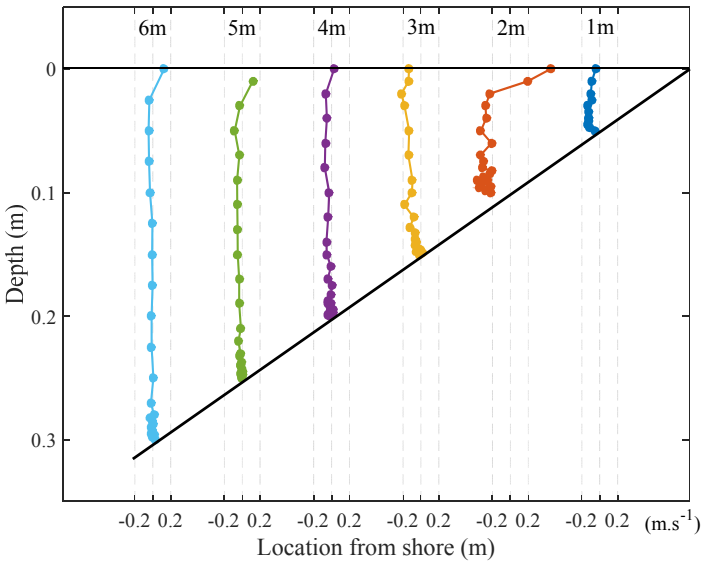
6m
5m
4m
3m
2m
1m
0
0.1
0.2
0.3
Depth (m)
-0.2 0.2
(m.s-1)
Location from shore (m)

(b)

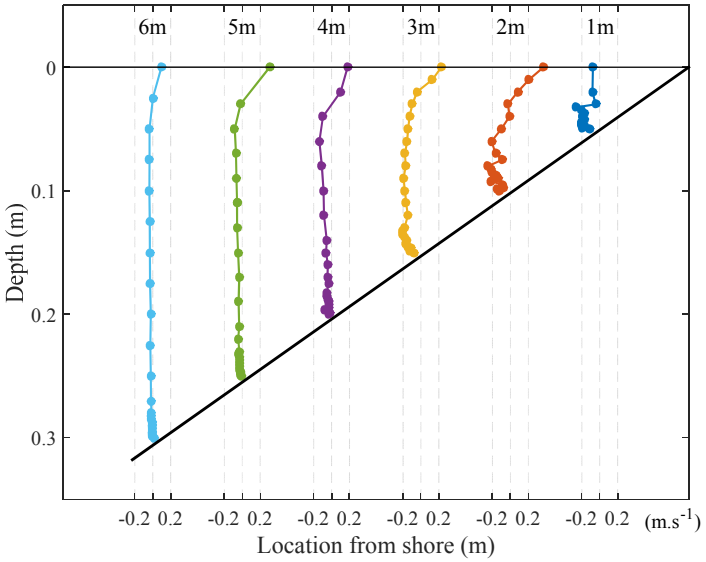
6m
5m
4m
3m
2m
1m
0
0.1
0.2
0.3
Depth (m)
-0.2 0.2
(m.s-1)
Location from shore (m)

(c)

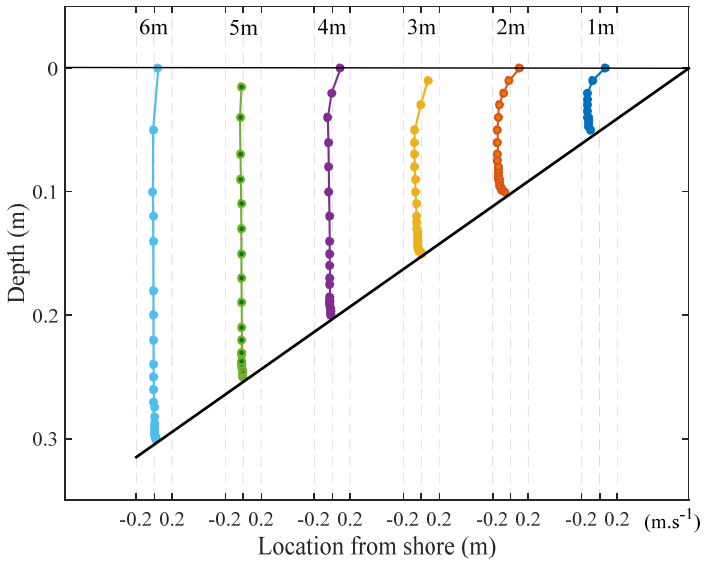

(d)

Figure 4.39 – Temporal Averaged undertow velocities for LDA measurements across the nearshore, a) S_{op} = 2%, b) S_{op} = 3½ %, c) S_{op} = 5%, d) S_{op} = 3½ $_{\text{Random}}$%

Figure 4.39 depicts the undertow velocities which were obtained from LDA measurements. These recorded velocities were adopted to quantify the shear dispersion by use of the *N*-zone model (Eqs. 3.28 to 3.32). The shear dispersion model requires diffusivity values for each layer of the flow as an input. Here, two approaches were considered for diffusivity. The first dispersion model was developed by using a depth-averaged eddy viscosity. Table 4.6 presents the dispersion coefficient predicted by use of hydrodynamic data and a constant depth-averaged eddy viscosity for all layers of the water column. The *N*-zone model results were also compared to the dispersion coefficient obtained from tracer measurements (§4.3.3).

The second model is derived by incorporating a depth-varying diffusivity into the *N*-zone model. Table 4.7 presents the shear dispersion coefficient determined for DHI data using undertow velocities and depth-varying eddy viscosity. The results of dispersion coefficients calculated from hydrodynamic data were compared to the fluorometric study.

Table 4.6 – Comparison of the shear dispersion coefficients determined with *N*-zone model (undertow values and depth-averaged ν_t) with the dye measurements

Condition		Shear Dispersion ($m^2.s^{-1}$)						
		Location from SWL (m)						
H (m)	T (sec)	1	2	3	4	5	6	
0.12	1.2	8.51E-3	9.68E-3	9.47E-3	5.23E-2	2.13E-3	1.85E-3	Model
		N.A	1.19E-2	1.26E-2	N.A	6.93E-4	N.A	Dye
	1.85	3.19E-3	6.78E-3	8.00E-3	4.45E-3	1.71E-3	1.21E-3	Model
		N.A	8.56E-3	8.60E-3	N.A	1.05E-3	N.A	Dye
	2.9	6.27E-3	9.19E-3	8.49E-3	1.20E-2	6.54E-3	1.68E-3	Model
		N.A	1.24E-2	1.07E-2	N.A	1.57E-3	N.A	Dye
	Random	2.89E-3	6.05E-3	2.64E-3	1.48E-3	1.17E-3	1.34E-4	Model
		N.A	7.96E-3	2.40E-3	N.A	5.61E-4	N.A	Dye

Table 4.7 – Comparison of the shear dispersion coefficient determined with *N*-zone model (undertow values and depth-varying ν_t) with the dye measurements

Condition		Shear Dispersion ($m^2.s^{-1}$)						
		Location from SWL (m)						
H (m)	T (sec)	1	2	3	4	5	6	
0.12	1.2	8.94E-3	1.03E-2	1.02E-2	5.64E-3	2.20E-3	1.93E-3	Model
		N.A	1.19E-2	1.26E-2	N.A	6.93E-4	N.A	Dye
	1.85	3.40E-3	7.13E-3	8.32E-3	4.67E-3	1.76E-3	1.00E-3	Model
		N.A	8.56E-3	8.60E-3	N.A	1.05E-3	N.A	Dye
	2.9	6.31E-3	9.27E-3	8.67E-3	1.27E-2	7.42E-3	1.92E-3	Model
		N.A	1.24E-2	1.07E-2	N.A	1.57E-3	N.A	Dye
	Random	3.18E-3	6.58E-3	2.69E-3	1.52E-3	1.17E-3	1.58E-4	Model
		N.A	7.96E-3	2.40E-3	N.A	5.61E-4	N.A	Dye

The comparison between the mixing coefficients obtained from tracer studies and the results of *N*-zone dispersion model with constant and depth-varying eddy viscosity show that in the case of monochromatic waves with 2% steepness, the shear dispersion model underestimated the mixing coefficients obtained from the tracer study inside the surfzone (y=2m) and at breaker region (y=3m) by $3.161E^{-3}m^2/s$ $2.119E^{-3}m^2/s$, respectively. The dispersion model overestimated the dispersion coefficient in the offshore region (y=5m) by $5.849E^{-3}m^2/s$. For the monochromatic waves of 2% steepness, employing depth-averaged and depth-varying eddy viscosity did not improve the prediction of the model in comparison to dye work.

In the case of regular waves with 3½% steepness, the comparison of results between the dispersion model with depth varying diffusivity and fluorometric measurements shows that for the breaker region (y=3m) and inner surfzone (y=2m) the dispersion model underestimated the dispersion by $2.820E^{-4}m^2/s$ and $1.436E^{-3}m^2/s$, respectively. The results show that for the monochromatic waves with S_{op} =2%, there is no significant difference between the model with depth-averaged and depth-varying eddy viscosity. Seaward of the breaker region at 5m from the SWL, the dispersion model overestimated the tracer data by $7.06E^{-4}m^2/s$.

For monochromatic waves of 5% steepness, the dispersion model underestimated the dispersion at the breaker region and in the inner surfzone. The results of the *N*-zone model show that the dispersive mechanism only varies by $1.079E^{-3}m^2/s$ across the surfzone (y=1, 2, 3m) in the case of monochromatic waves with S_{op}=5%.

The comparison between fluorometric data and *N*-zone model results for random waves show that seawards of the breaker region, the model overestimated the dispersion coefficient by $6.14E^{-4}m^2/s$. Inside the surfzone at 3m from SWL, the dispersion model overestimated dispersion by $2.90E^{-4}m^2/s$. At 2m from the shoreline, the difference between the model prediction and tracer measurements increases by $1.38E^{-3}m^2/s$.

The results obtained from shear dispersion model (Tables 4.6 and 4.7) show that the model is in good agreement with the dye tracer measurements. Using depth-averaged eddy viscosity or depth-varying eddy viscosity did not improve the predictions of the shear dispersion model significantly. For all wave conditions, the model with depth varying diffusivity predicted slightly higher dispersion coefficients inside the surfzone.

Figure 4.40 illustrates the variation of dispersion coefficient across the nearshore for all wave conditions tested in the DHI study. Here, the spatial and temporal variation of velocity in the wave crest part could not be included in the dispersion model due to the limitations of LDA technique. It is evident from figure 4.40 that the *N*-zone model applied in this work is capable of predicting the dispersion coefficient and is in good agreement with the dye measurements. The predicted dispersion coefficients are following the general trend of the tracer data.

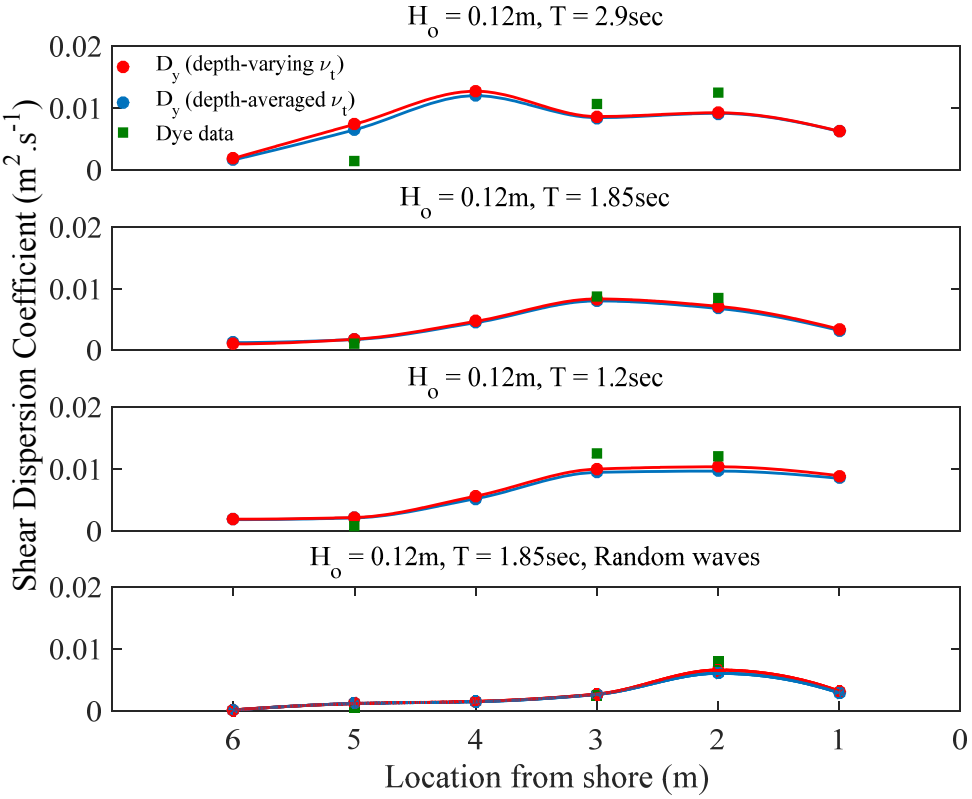

Figure 4.40 – Comparison between shear dispersion coefficients obtained from undertow measurements and the dye measurements

4.4.4 Comparison of Mixing with Existing Data

In this section, the shear dispersion coefficient obtained from DHI data are compared with the theoretical dispersion model proposed by Pearson *et al*. (2009) and the existing laboratory and field data described in the literature review (chapter two).

The theoretical model adopted here is derived based on the methodology derived by Pearson *et al*. (2009), where the flow over the water column is considered to be in two layers, consisting of an onshore velocity (v_+) and offshore velocity (v_-) and by using Fischer's (1978) dispersion model (Eq. 4.9) for an idealized flow in the nearshore.

$$D_y = k_y + e_y = \frac{(v_+ - v_-)^2 d^2}{48 e_z} + e_y \tag{4.9}$$

Pearson *et al*. (2009) adopted Longuet – Higgins and Stewart's (1964) theoretical velocity and the Svendsen and Putrevu (1994) theoretical predictions of diffusivities and proposed the overall on-offshore mixing coefficient:

$$D_y = \frac{gH^4}{768 d e_z} + e_y \tag{4.10}$$

The overall mixing coefficient in Pearson *et al*. (2009) model considers both dispersive and diffusive mixing mechanisms. The effects of both horizontal and vertical diffusion (e_y and e_z) are considered to be equal.

The mixing coefficients obtained from DHI data analysis inside the surfzone are compared with the theoretical approach described above [Eq. 4.10] and existing experimental data. Figure 4.41 shows the relationship between the measured on-off shore dispersion and the wave height at breaking.

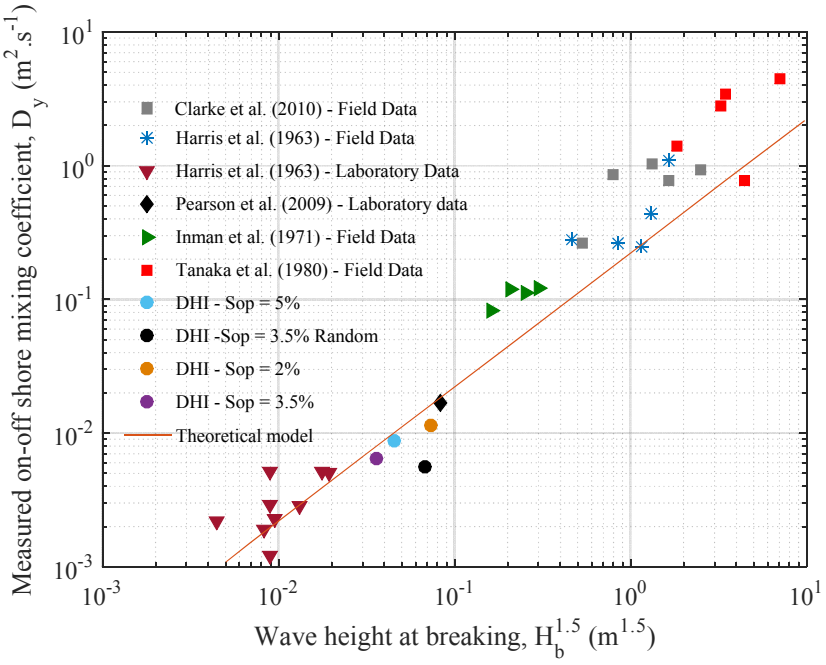

Figure 4.41 – Comparison of on-off shore mixing in the surfzone

Figure 4.41 shows that the overall dispersion coefficient obtained from DHI data are in good agreement with the theoretical formula proposed by Pearson *et al*. (2009). Also, despite the various surfzone hydrodynamic conditions presented in figure 4.41, it is evident that the dispersion coefficient obtained from DHI data follows the general trends of data.

4.5 Summary

In this chapter, mixing under combined effects of waves and currents were investigated with the use of experimental data collected at DHI, Denmark. The experimental study, which was performed in 2005 in the shallow water basin of the large-scale facility at the Danish Hydraulic Institute was described in details. The experimental setup, instrumentation and data logging procedures were described. The results of hydrodynamic measurements and tracer studies from the DHI experiments were presented and discussed.

The mixing under current only condition and combined effects of waves and currents were determined from dye tracer measurements at locations inside the surfzone, breaker point and in the offshore region.

According to the nearshore processes and the methodology developed and described in chapter 3, the diffusive and dispersive mixing mechanisms were quantified for the hydrodynamic data obtained from DHI study. The overall on-offshore mixing coefficients were determined from hydrodynamic data and then compared to the mixing coefficients obtained from analysis of dye work.

In §4.4.1, the turbulence structures in the nearshore were investigated for the hydrodynamic data. Several algorithms were developed to determine turbulent kinetic energy across the nearshore for the hydrodynamic conditions tested. The results of TKE were compared to Nadaokah & Kondoh (1982) data. Good agreement were found between the TKE determined for DHI data and the existing data.

The turbulent diffusion coefficients (§4.4.2) were investigated across the nearshore with use of TKE results. The turbulent diffusion coefficients obtained from the DHI data were compared to those determined from the Svendsen & Putrevu (1994) theoretical formulae. The comparison showed that turbulent diffusion obtained in this study were in line with the theoretical values.

The shear dispersion coefficients (§4.4.3) were determined for all wave conditions studied in DHI experiment. The mathematical solutions proposed by Chikwendu (1986) were adopted for determining shear dispersion coefficients. The undertow velocity profiles and eddy viscosity from LDA measurements were utilized for determining the shear dispersion coefficient. Comparison between the dispersion model and dye work show that, despite dispersion model predictions following the general trend of tracer measurements, some scattering exist in the model predictions. Due to limitations of the LDA measurement technique, it was not possible to consider the bore hydrodynamics and the results of the dispersion model are limited only to the undertow.

From the evidence presented in this chapter for the mixing in the nearshore due to the combined effects of waves and currents, it can be concluded that the measured results from this study follow the general trends of previous experimental and theoretical studies. Comparison between the dispersive and diffusive mixing mechanisms show that the dispersive mechanisms are the dominant contributor of nearshore mixing. The overall on-offshore mixing obtained from hydrodynamic data are qualitatively in good agreement with solute tracer studies performed in the DHI facility.

CHAPTER 5
HYDRODYNAMICS MEASUREMENTS

5.1 Synopsis

This chapter presents the application of Particle Image Velocimetry (PIV) in obtaining flow hydrodynamics in the nearshore region. The hydrodynamic measurements were employed to determine the velocity and turbulence structure across the nearshore and understand the behaviour of diffusive and dispersive mixing mechanisms. The hydrodynamics in the nearshore were investigated in a 1:20 experimental wave flume. Two-dimensional velocity fields in the water column from 20 consecutive monochromatic waves were measured at three cross-shore locations shoreward of the breaker region, and at two locations seawards of the breaker zone. Similar wave conditions to the DHI experimental study were investigated in the PIV experiments.

A short background on the PIV measurements in the nearshore region, the experimental setup, data acquisition and analysis procedures are presented in this chapter. The turbulent diffusion and shear dispersion mechanisms postulated in this study, were quantified for the data obtained from the PIV measurements.

5.2 Background

The nearshore region is a very dynamic region influenced by both breaking waves and currents, and thus the hydrodynamics of this region are complex. Detailed knowledge of nearshore hydrodynamics can help to have a better understanding of mixing and dispersion processes in the nearshore. Despite the importance of nearshore hydrodynamics at the coast, the velocity fields and turbulence in this region are still not fully understood.

Relatively few laboratory studies have been conducted to investigate the nearshore hydrodynamics using Laser Doppler Velocimetry (LDV) measurements. The Nadaoka & Kondoh (1982) laboratory investigations were one of the first hydrodynamic studies using LDV in the surfzone. Their studies confirmed the existence of large-scale turbulence generated from surface sources and small-scale turbulence generated from bottom boundaries. Ting & Kirby (1994, 1995 and 1996) performed a series of laboratory measurements to investigate the turbulence characteristics of spilling and plunging breaker waves. Their studies demonstrated that the turbulent kinetic energy (TKE) is transported landward under a plunging breakers. Their measurements showed a seaward transport of TKE for spilling breaker. Stive & Wind (1986) studied cross-shore mean flow velocities in the surfzone using LDV measurements. They concluded that shear stress at the trough level dominates the flow such that a mean seaward flow also arises near the bottom.

Particle Image Velocimetry (PIV) is one of the hydrodynamic measurement techniques which developed significantly during the past decade. PIV has the ability to provide hydrodynamic information over a flow field at many points and determine the vorticity field and spatial correlations (Nezu & Onitsuka, 2001). The historical development of PIV can be found in a series of papers written by Willert and Gharib (1991), Adrian (1991), Lourenco (1988) and Westerweel (1993). Adrian (1996) published a bibliography of the historical development of PIV and Raffel *et al*. (1998) reviewed different PIV techniques. Despite all significant hardware and software improvements in the PIV during the last few years, the method is limited to the size of seeding particles, speed of the flow, image quality, camera frame rate, image format and robustness of image possessing algorithms.

Although there are numbers of studies in the field of coastal engineering which used LDV or PIV, there is no known study which employed both techniques simultaneously. Nezu and Onitsuka (2001) carried out LDV and PIV measurements for an open channel flow and found very good agreement between both techniques. Nakagawa and Hanratty (2001) found poor agreement between PIV and LDV methods near the wall boundaries and generally in the region of sudden changes in geometry. Hyun *et al*. (2003) compared the PIV and LDV measurements for mean

velocity and turbulence in a complex open channel and concluded that PIV could provide quantitative information about the flow structure which was not easily measured by the LDV techniques. The following sections will describe a series of PIV measurements in the wave flume, in order to study the flow fields across the nearshore. Similar hydrodynamic conditions to those of the DHI study (Chapter 4) were investigated in this work. The hydrodynamics obtained from the PIV measurements were used to quantify the mixing mechanisms in the nearshore.

5.3 Experimental Setup

The waves were generated in a flume with a rectangular cross-section and a beach slope of 1:20 in the Warwick University Water Laboratory. The flume is 25m long, 0.5m wide and the offshore water depth was set to 0.7m (Fig. 5.1). For this study, the region near to the paddles was termed 'offshore'. The offshore wave steepness, S_{op}, has been determined using the inshore wave celerity, $\sqrt{gd}$. The coordinate system has been defined such that x is positive onshore along the beach line. The z direction is defined normal to the beach line and positive is upwards. The y axis is set by the right-hand rule with $y = 0$ at the lateral mid-point of the tank, as shown in figure 5.3.

Figure 5.1 – Wave flume at Warwick Water Laboratory

The wave conditions were monitored and recorded with use of six wave gauges along the beach. Wave gauges were installed in offshore region, transient region and shallow waters in the surf zone, and used to give accurate (within 0.5mm) surface water profiles. The wave probes were re-zeroed and calibrated over 4 points [0,+100,-100,0 mm] every time the experiment was conducted by driving the probe up or down. The output voltage from each wave probe monitor was directly proportional to the probe's depth of immersion. The flume was equipped with a piston type wave-maker which included active absorption.

PIV was utilized to measure the instantaneous velocity field in a planar cross section of the observed flow across the surfzone and seawards of the breaker zone. A schematic depicting the PIV experimental setup is shown in figure 5.2.

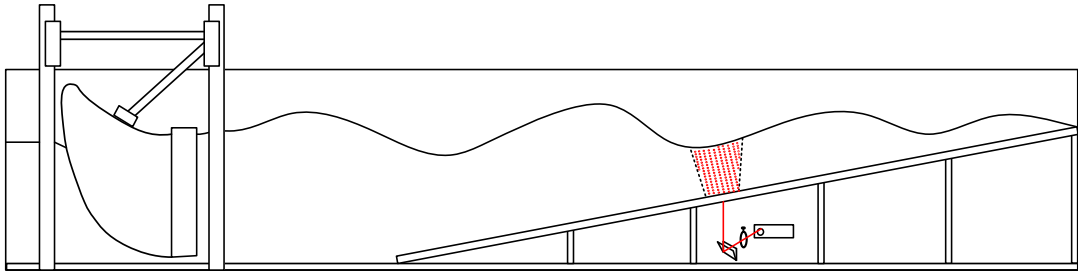

Figure 5.2 – Schematic view of the PIV experimental setup

The selection of an appropriate flow seeding is crucial to achieve high resolution data. In this study, the flow was seeded with Talisman-30ES (Plascoat) with a nominal diameter of 21.2μm and a bulk density of 0.40gr/cm^3. The seeding is almost exactly neutrally buoyant and small enough to follow the flow patterns. Also, the seeding is reflective at the wavelength of the laser used to perform the PIV measurements. The particles were added to the wave tank and mixed until they were distributed homogeneously. In order to mix the particles, the paddle was generating waves for a few minutes before the start of each round of measurement. The optimum seeding density was determined by analysing the frames prior to the measurements. About 150gr of seed particles were added to the wave tank with a volume of fluid equal to 3500litr. In order to prevent flocculation of seeding particles, Mirasol surfactant was added to the flume.

The illumination was provided by CNI Tech laser (MRL-III-655). The CNI- MRL-III-655 is a red diode laser that emits 655 nm light continuously. The output power for the laser was 1000 mW (Class 4 Laser). The beam aperture was ~5 – 40 nm in diameter. Using a series of mirrors and cylindrical and spherical lenses, the laser beam was formed into a thin light sheet with a thickness of about 2 mm passing through the middle of tank glass cross-section in the streamwise direction. Figure 5.3 shows the schematic cross-section of the PIV experimental setup.

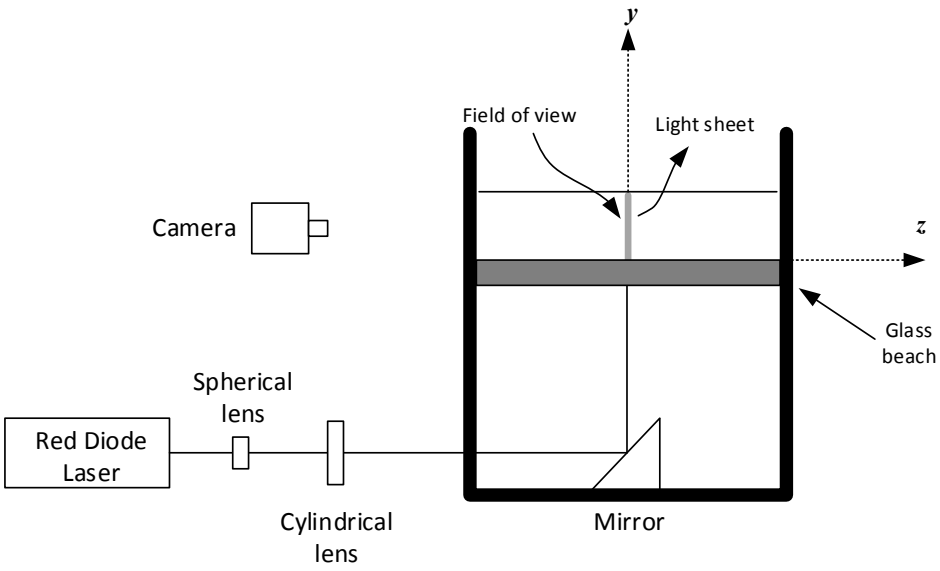

Figure 5.3 – Schematic of experimental setup from the end of the tank view point

Images of the seeded flow were obtained at a frame rate of 100 frames per second (fps) using a 14-bit Point Grey 4.1MP monochrome camera (GS3-U3-41C6M-C) with a resolution of 2048 × 2048 pixels. The camera was fitted with a lens with focal length ranging from 12 to 50mm. Figure 5.4 illustrates a schematic of the imaging set-up for the PIV tests. The camera was connected to a host computer, the image acquisition with all associated parameters were controlled with a computer algorithm. Due to hardware limitations, the image recording only took place for approximately 20 wave, depending on the wave conditions.

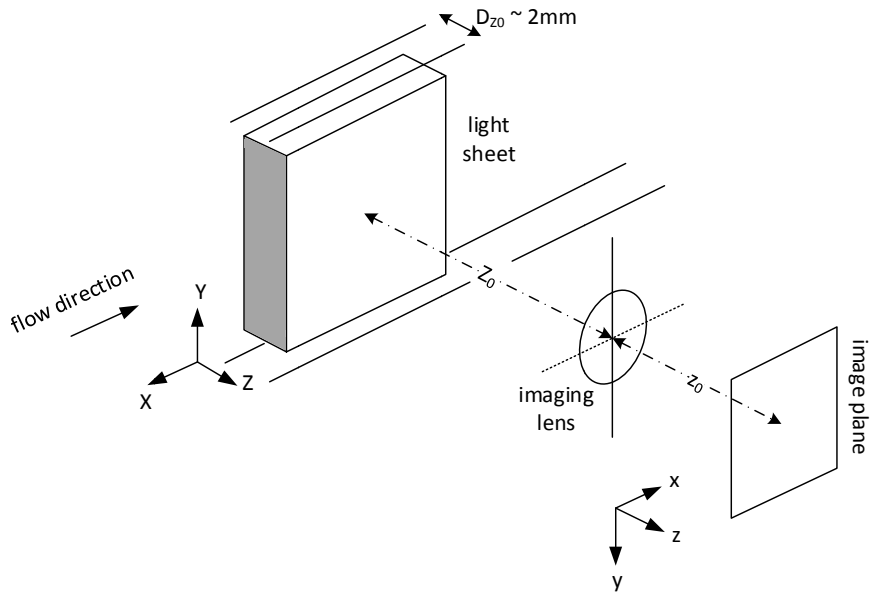

Figure 5.4 – Schematic representation of the imaging set-up in the PIV tests

5.3.1 Calibration

Prior to each set of measurements at a specific location, a calibration grid was placed on the location of the laser plane (Fig. 5.5a). Image calibration was achieved by taking pictures of a Dantec two-level uniform square grid calibration target (270×190mm). Using the calibration image, the pixel size was determined. An image of this calibration grid (Fig. 5.5b) was required to determine several parameters during the analysis phase. The parameters include, the dimensions of the Field Of View (FOV), the magnification factor (*M*) and the scale factor (*SF*).

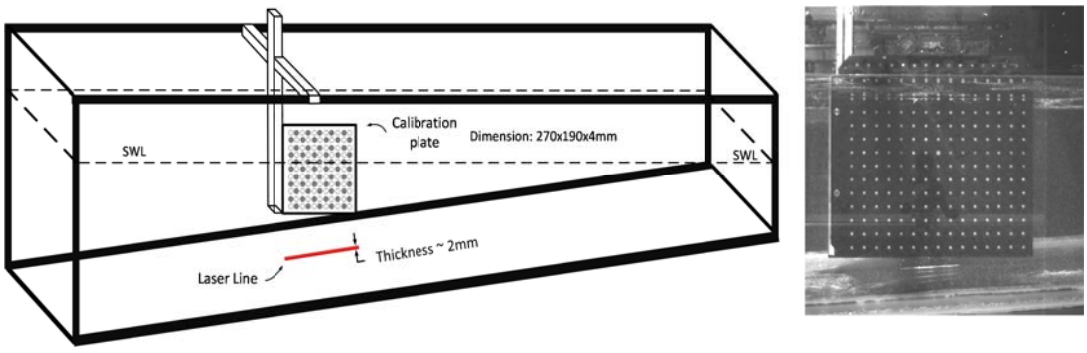

(a) (b)

Figure 5.5 – (a) Schematic sketch of calibration setup (b) calibration image

5.3.2 Test Conditions

The PIV tests were performed on the transverse sloping section of the Warwick Wave flume and the measurements were recorded for three monochromatic wave conditions with varying wave period, nominally T\{=1.2, 1.85, 2.9\}s with a constant wave height of 0.12m (nominal – offshore). The waves were designed to represent a range of the offshore wave steepnesses similar to the DHI experiments (Chapter 4). Table 5.1 summarizes the experimental conditions.

Table 5.1 – Summary of the PIV test conditions, Warwick Water Lab (2014)

Condition	S_{op} %	H_o (m)	T (sec)	x = dist. from shore (m)
1	5	0.120	1.2	1, 2, 3, 4, 5
2	3.5	0.120	1.85	1, 2, 3, 4, 5
3	2	0.120	2.9	1, 2, 3, 4, 5

The monochromatic waves were generated using a paddle type wave generator (Fig. 5.1). The wave maker and the wave parameters were controlled automatically by dedicated software. Prior to each set of measurements, the wave maker generated waves for a few minutes until the system became balanced and the seeding was well-mixed. The offshore wave height and period were also manually checked.

The PIV measurements were performed for all conditions (see Table 5.1) at five on-offshore positions x = {1, 2, 3, 4 & 5}m from the shore. The laser, optics and camera were calibrated and tested for each location before data recording.

The camera was mounded with a tripod and the FOV was selected in order to enable capturing the water column from the bed to the maximum height of the wave crest. The wave height measurements and the PIV data acquisition were simultaneously undertaken across the flume. For safety reason, the laser beam was fully shielded using a plywood chamber.

Shutter Speed

The shutter speed was selected to give the required number of exposures. It is important to consider whether the flow changes over the exposure time. After careful setting up and trial, a shutter speed of 3.486ms was chosen to perform the experiment.

Focus

Achieving a sharp focus is essential to obtain high quality PIV images. Efforts were made to achieve a sharp focus. In order to find the best focus, prior to the start of each experiment, the Dantec calibration plate was installed and aligned carefully with the laser beam and the camera focus was determined based on the calibration dots.

Exposure

Exposure is a function of laser power and lens aperture. Setting an appropriate exposure is an essential task to obtain good quality images. Large apertures can result in poor depth of field and therefore difficulties in focusing. Very small apertures can also result in larger particle images. In this study, after many trials the exposure time was determined to obtain the best field of view for each measurement location.

Following all experimental set-up procedures and careful calibration of the PIV system, 2D velocity fields were measured across the nearshore. 5800 PIV image pairs were collected for each measurement location at a frame rate of 100 images/second using a 14-bit Grasshopper-3/U3 camera with the resolution of 2048 × 2048 pixels.

5.4 PIV Data Analysis

The PIV data obtained from the laboratory measurements have been analysed by using DaVis software (Version 7.2, La Vision GmbH.). All the images were captured in Raw pixel format where image data is Bayer RAW untouched by any on board

processing. Selecting a Raw format bypasses the FPGA/colour core which disables image processing, but allows for faster frame rates. In order to proceed with the image processing and analysis of data, algorithms were developed to convert all the frames into grayscale with no changes in quality and pixels (Fig. 5.6). The greyscale frames imported to DaVis and multi-frame analysis was used to analyse the paired images and compute the vector field. The velocity vectors from DaVis software were illustrated and analysed by developing computer codes using MATLAB software.

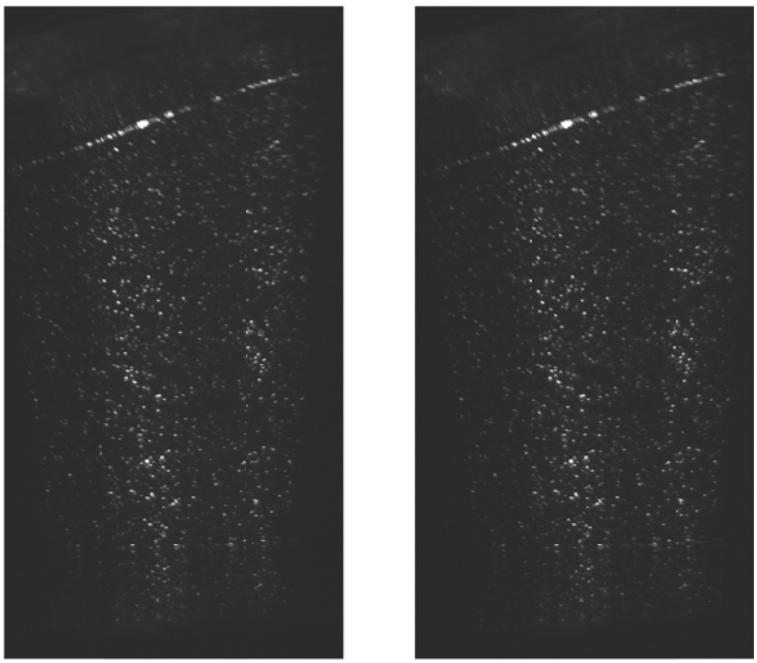

(a) (b)

Figure 5.6 – (a) Captured frame in Raw8 pixel format, (b) converted greyscale frame

The main objective of analysing the PIV recordings at medium image density is to determine the displacement between two patterns of particle images, which are stored as a two dimensional distribution of grey levels (Willert and Gharib, 1991; Adrian, 1996). Two images were captured per realization and the corresponding velocity vector field was computed using a cross-correlation technique (Keane & Adrian, 1992; Kompenhans *et al*., 1998). Cross-correlation data processing was performed using an Fast Fourier Transform algorithm. Figure 5.7 illustrates the analysis procedures using a cross-correlation technique.

Careful selection of interrogation window size in processing PIV data is essential to balance robustness with accuracy of the calculated displacement particularly in the

region of high gradients. In conventional PIV processing techniques a constant interrogation window size with a sufficient number of particles is used. The constant window size (e.g. 32×32, 16×16) is capable of capturing certain displacement gradients, but cannot follow gradients smaller than the effective spatial resolution of the algorithm (Wieneke & Pfeiffer, 2010). Therefore, algorithms with constant window size cannot perform well in the regions of strong vortices and shear flow close to surface boundaries.

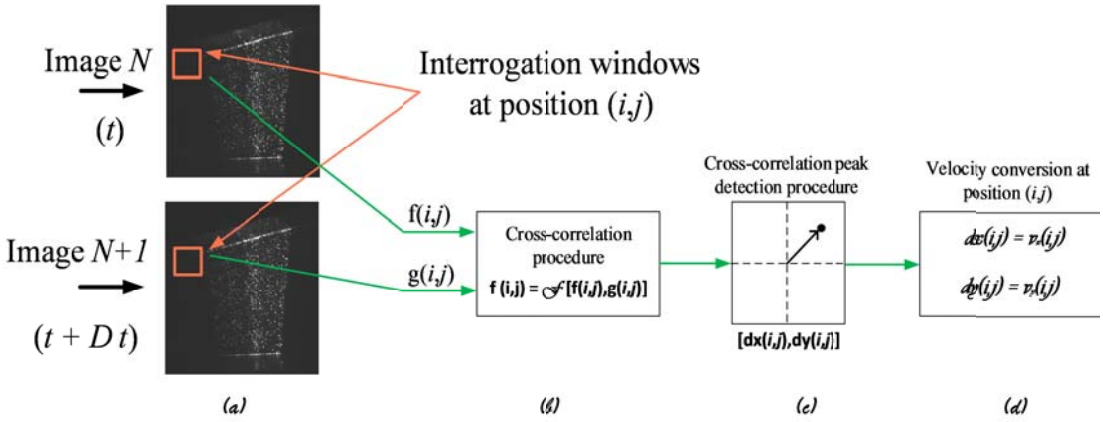

Figure 5.7 – Cross-correlation data processing procedure using an FFT algorithm (a) defining the interrogation window to subsample the main sequential image pairs; (b) cross-correlation procedure with an FFT implementation; (c) identifying the peak's location corresponding to the average shift of particles within the interrogation windows (d) converting the particle's shift to physical space and calculating the velocity vectors

In order to achieve high accuracy in data processing, a multi-pass interrogation scheme with decreasingly smaller window size was employed for the analysis. The size of the interrogation window should be large enough to ensure sufficient matching particles for robustness and accuracy (Wieneke & Pfeiffer, 2010). Three different sets of interrogation window size were tested with a weighting ratio of 1:1 in order to find the ideal interrogation size. After a few trials, the final interrogation spot size of 16x16 pixels was selected. Each pair of images processed with 50% overlap. The correlation function for both initial and final passes has been analysed by using standard functions (via FFT and no zero-padding). The velocity vectors were computed using the high accuracy mode based on Whittaker reconstruction theorem (1935).

A global range filter along with a median filter were used to remove spurious vectors. Then, the missing vectors were interpolated using the Kriging method (Chang and Liu, 1999). Since the velocity vectors are calculated based on the pixel resolution, a positional uncertainty of ± 1 pixel can occur. Therefore, in order to enhance the accuracy, a sub-pixel resolution method (Utami & Blackwelder, 1991) was adopted in the PIV data analysis algorithm. Figure 5.8 shows an example of the captured PIV image and the resulted vector fields from the data processing.

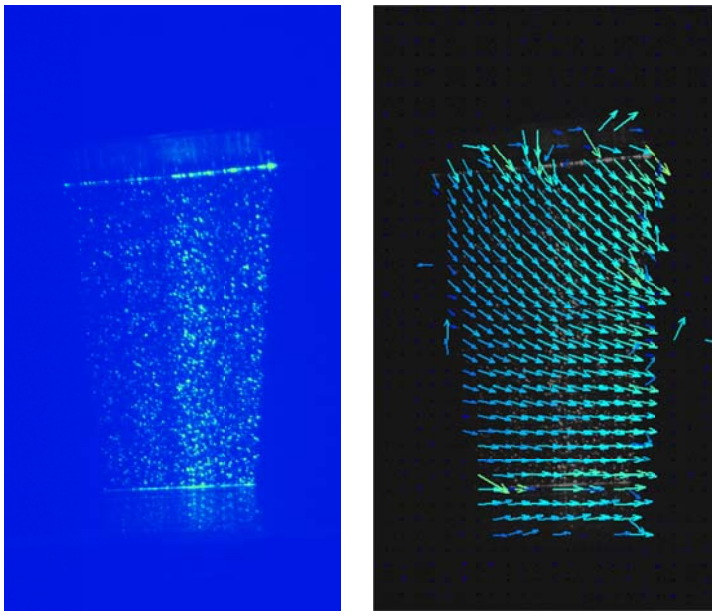

(a) (b)

Figure 5.8 – An example of PIV data processing (a) PIV unprocessed image (b) resultant velocity vector fields from processing

Figure 5.8 demonstrates that there are some reflections in the data from the glass bed of the flume and the water surface. The resultant outliers from the surface reflections of the bed and the wave crest were masked out for the post processing calculations. The vector field computed with the analysis algorithm (La Vision software) is in the format of pixels/Δt. Algorithms were developed to convert the vectors into metres per second by use of the calibration frame and determining the scale factor (*SF*).

5.5 Hydrodynamic Results of the PIV Measurements

The vector fields obtained from the PIV measurements in the nearshore and transient-offshore region are presented and discussed in this section. The focus of this work was to understand the hydrodynamic processes presented during the wave cycle, which affect the turbulent diffusion and shear dispersion mechanisms. The study presented in this chapter examines the velocity fields, turbulence structure and shear dispersion mechanisms in the shallow water column across the nearshore.

5.5.1 Velocity Field

The first section of the results focuses on the vector fields resulting from the PIV measurements. The vector fields and their temporal and spatial variations provide valuable knowledge about the mixing and dispersion mechanisms in the nearshore region. The vector fields for all measured conditions (Table 5.1) are computed and presented in this section. Moreover, the flow behaviour and the vertical structure of the flow across the nearshore region is discussed.

Vector field for monochromatic waves of H_o = 0.12m & T = 1.2sec

Monochromatic waves with an offshore wave height of 0.12m and wave period of 1.2 sec were generated in the Warwick University Wave flume on a 1:20 glass beach slope. The PIV measurements were undertaken at five on-offshore locations with 1m interval [x={1,2,3,4,5}m].

The spatial variations of flow hydrodynamics were captured at the rate of 100 frames per second. The observations from the PIV experiments indicate that for S_{op} = 5%, the incident wave crest becomes unstable and starts to break at 3m from the SWL. The temporal variations of the vector fields demonstrate strong shearing effect and the mixing exists for the locations inside the surfzone. The vector fields show that surface generated turbulence is the primary source turbulence generation inside the surfzone. Figures 5.9 and 5.10 depict the temporal variations of the velocity vectors

and their magnitude at 10 phases ($t_i = 0.1NT$ and $t_{i-\max} = T$) inside the surfzone [Fig. 5.9] and seaward of the breaker region [Fig. 5.10].

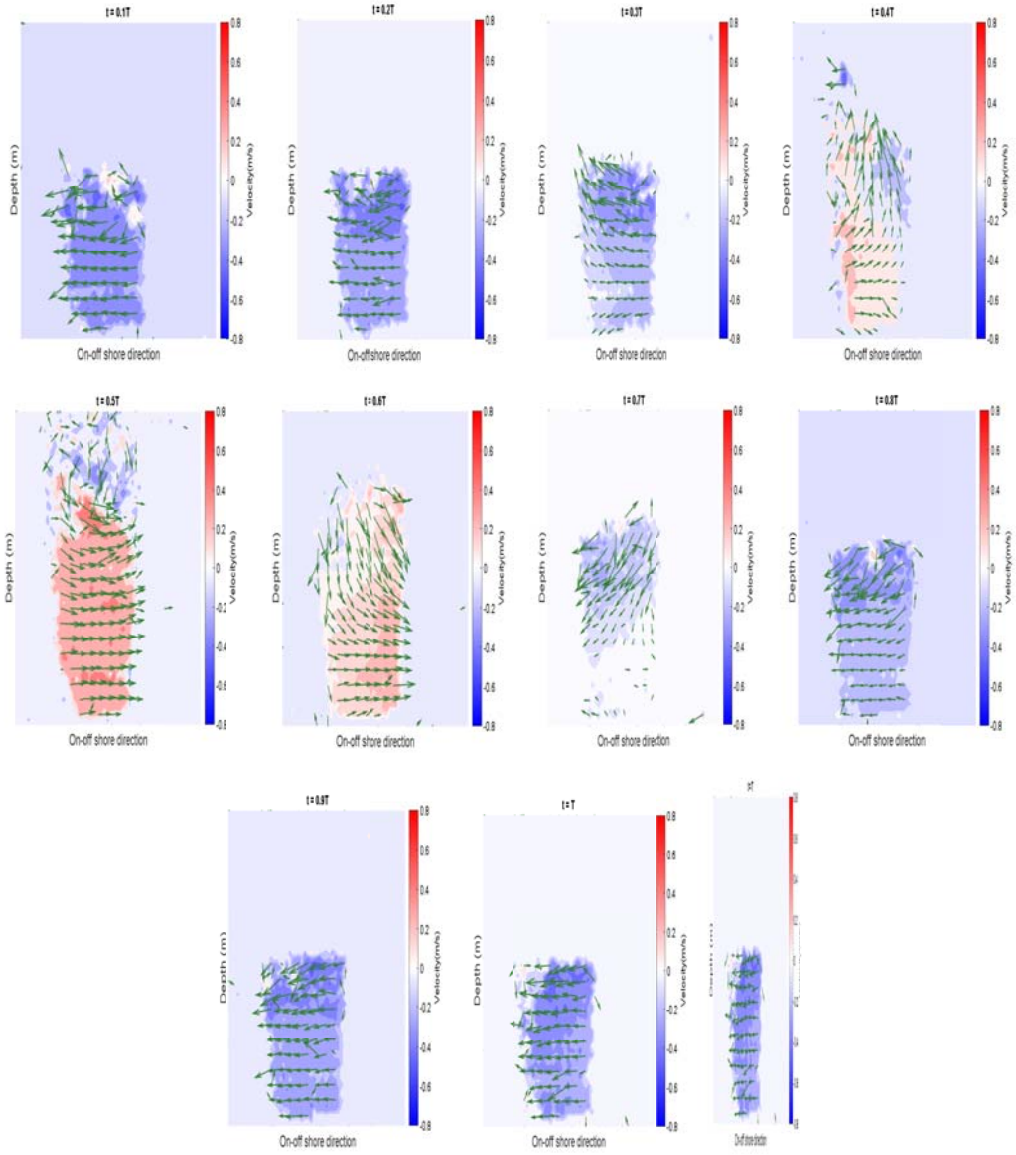

Figure 5.9 – Temporal variation of vector fields over a wave cycle in surfzone at 3m from SWL for monochromatic waves with S_{op} = 5%

Figure 5.9 shows the temporal variation of velocity vectors for the case of monochromatic waves with 5% steepness, inside the surfzone at 3m from the SWL. Contour areas in figure 5.9 show the magnitude of the velocity and the vectors

illustrate the direction of the velocity. The positive velocities indicate an onshore movement and the negative values an offshore moving flow. The analysis of the PIV vector field show that inside the surfzone, three mixing mechanisms exist due to the wave motion. These mechanisms are the diffusion and dispersion resulted from the bore and undertow activities within a wave cycle, and also the shearing effects due to the interactions between the bore and undertow. For monochromatic waves of 5% steepness at 3m, the measurements show that the duration of crest phase is 30% of a wave cycle (0.3T) where strong turbulent diffusion mechanism exist in the upper part of the water column. The shearing effects due to the bore/undertow interactions is present during 20% of the wave cycle whereas an undertow current mechanism is present in the rest of the cycle (0.5T).

The flow field illustrations indicate that a strong shearing layer with an onshore going bore and offshore moving undertow forms within the water column. This happens when the incident wave approaches the FOV, while the undertow is still moving offshore. Consequently, the shearing dispersion effects in this region are high. The surface generated turbulence in the breaker region and inside the surfzone were observed from the PIV data. The turbulence generated from the wave activities will be determined in the next section (§5.5.2).

Figure 5.10 shows the temporal variation of the velocity fields over a wave cycle at 5m from the shore. By moving from the surfzone towards the transient-offshore region, the surface generated turbulence reduces significantly and is limited only to the upper part of the water column. For locations seaward of the breaker region, the dispersive and diffusive mechanisms only exist in the upper part of the water column.

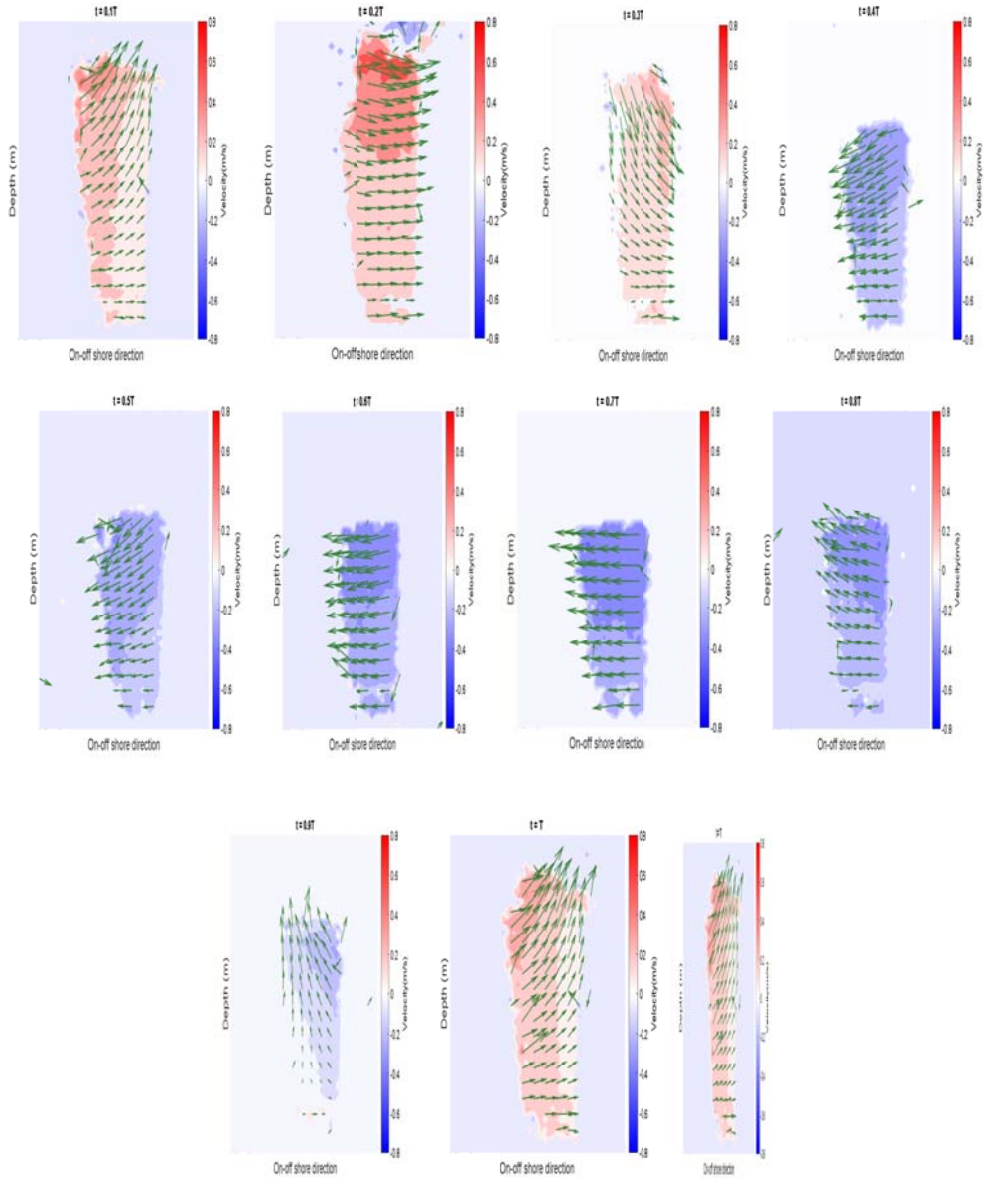

Figure 5.10 – Temporal variation of vector fields over a wave cycle at 5m from SWL for monochromatic waves with S_{op} = 5%

Vector field for monochromatic waves of H_o = 0.12m & T = 1.85sec

Regular waves with an offshore steepness of 3½% were generated in the wave flume at Warwick University, and the PIV measurements were undertaken at 5 on-offshore locations with 1m interval $x\{1,2,3,4,5\}$m. Figures 5.11 and 5.12 show the temporal variation of vector fields over a wave cycle at locations inside the surfzone and seaward of the breaker region. The observations indicate that for this condition, the incident wave crest becomes unstable and starts to break at 3.2m from the SWL.

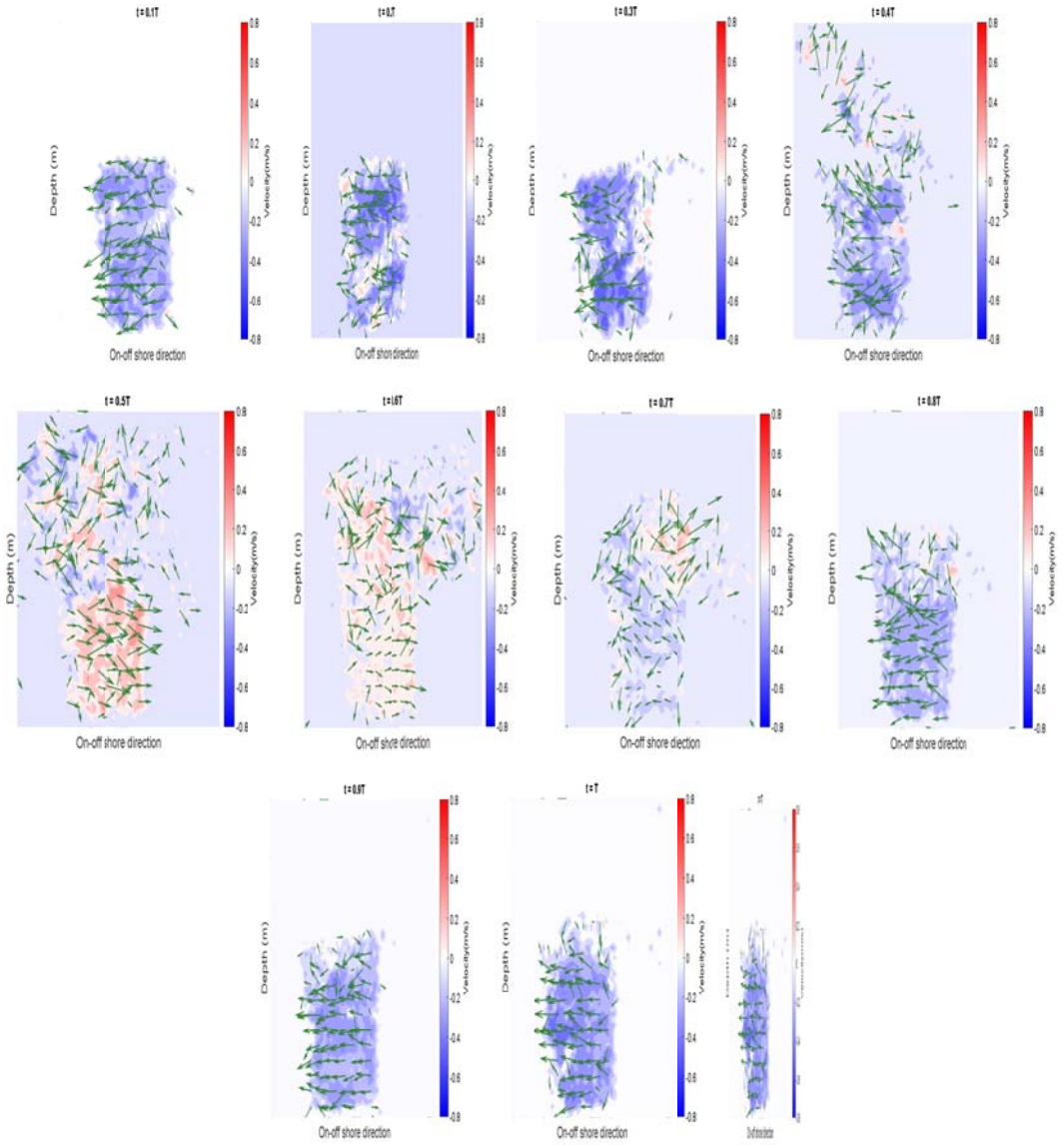

Figure 5.11 – Temporal variation of vector fields over a wave cycle at 3m from SWL for monochromatic waves with S_{op} = 3½ %

Figure 5.11 shows the temporal variation of the velocity vectors at 3m from the SWL for the monochromatic waves with S_{op} =3½%. The FOV present a location inside the breaker region. Therefore, it is expected that high turbulence generation and shearing effects exist in this location due to vertical variations of velocity over the water column. The wave breaking results in major energy loss due to the work being done in injecting turbulence and bubbles into the upper-layer of water column. Therefore, in addition to its direct impact on the wave field, wave breaking plays a significant role in determining the fluxes of energy, momentum and pollution transport in ocean. Figure 5.11 confirms that three wave mechanisms including bore, undertow and

bore/undertow interactions are the driving forces of mixing and dispersion in the nearshore.

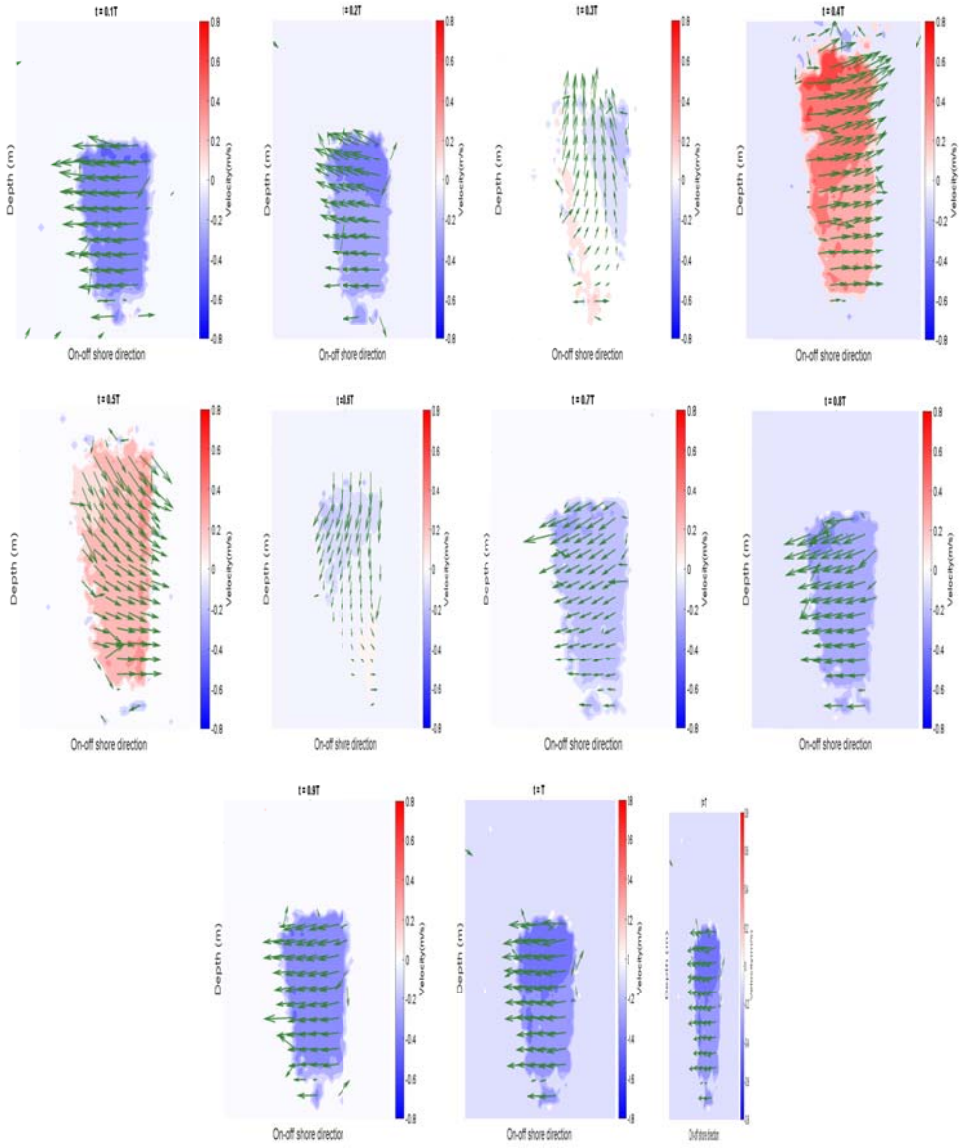

Figure 5.12 – Temporal variation of vector fields over a wave cycle at 5m from SWL for monochromatic waves with S_{op} = 3½%

Figure 5.12 shows the temporal variation of the velocity vectors for monochromatic waves with S_{op} = 3½ % seawards of the breaker region. It is evident from the vector fields illustrations that seaward of the breaker region undertow is the dominant factor which contribute to the diffusive and dispersive mechanism of mixing.

Vector field for monochromatic waves of H_o = 0.12m & T = 2.9sec

Figures 5.13 and 5.14 show the temporal variations of hydrodynamic fields for the regular waves with S_{op} = 2%. For this condition, the wave bore breaks approximately at 4m from the SWL. Therefore, the width of the surfzone is bigger in comparison to the other two conditions (S_{op} = 3½ and 5%). The results confirm that during the wave cycle wave activities in the nearshore result in three mixing mechanisms in the water column. The mechanisms include the onshore bore, the offshore undertow and the phase with high shear dispersion when the crest of the new wave collide with the undertow of previous wave. These three wave processes are responsible for turbulent diffusion and shear dispersion variations across the nearshore.

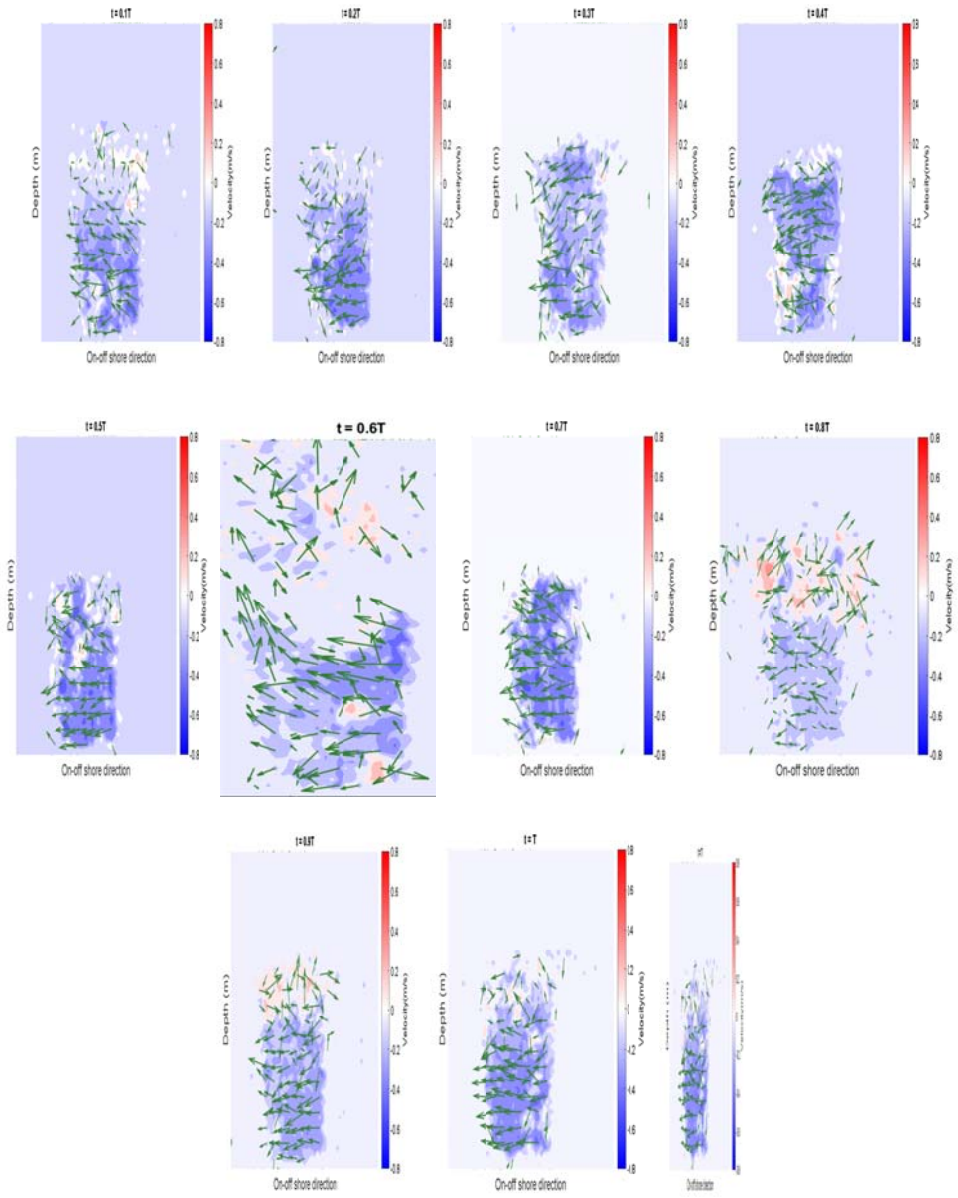

Figure 5.13 – Temporal variation of vector fields over a wave cycle at 3m from SWL for monochromatic waves with S_{op} = 2 %

Figure 5.13 illustrates the spatial and temporal variations in flow structure for the monochromatic waves of S_{op} = 2 %, inside the surfzone at 3m from SWL.

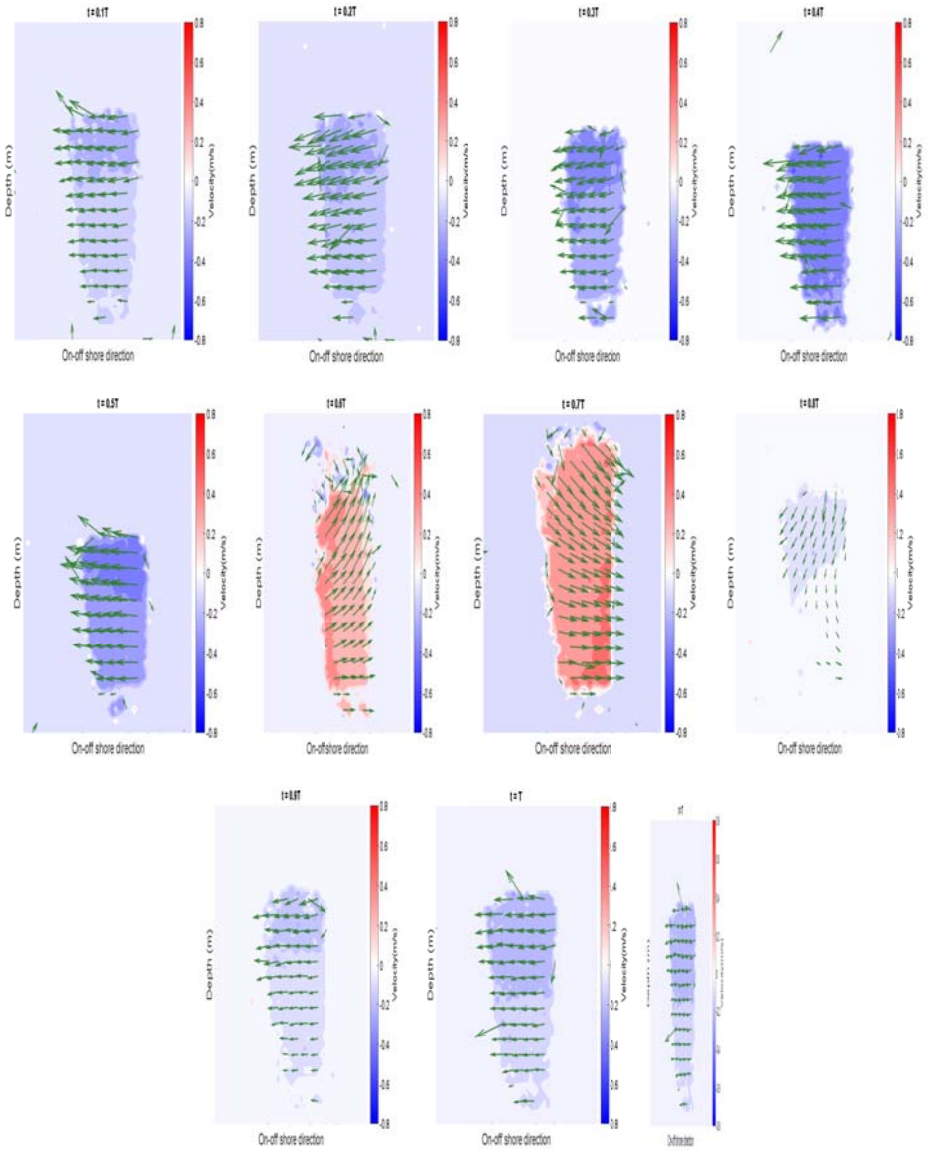

Figure 5.14 – Temporal variation of vector fields over a wave cycle at 5m from SWL for monochromatic waves with S_{op} = 2 %

Figure 5.14 depicts the temporal variations of flow hydrodynamic for the monochromatic waves with S_{op} = 2 % seaward of the breaker region at 5m from the SWL. It is evident from the figure that temporal contribution of bore mechanism at offshore locations decreases. The undertow is the main responsible mechanism for diffusion and dispersion seaward of the breaker region and the contribution of the shear dispersion, caused by the interaction of wave bore and undertow, reduces.

The velocity field (Figs. 5.9 to 5.14) obtained from the PIV measurements across the nearshore demonstrates that for all studied wave conditions, there are three general phases within the wave cycle, including the undertow moving to the offshore region, the wave bore moving onshore and the intersection between these two phases where a strong shearing mechanisms exists in the flow. The duration of these phases and the hydrodynamic structure is a function of the incident waves, the longshore currents and the geomorphology of the nearshore. For the wave conditions tested in this study, it is observed that the bore mechanism was $0.3T$ of the wave cycle inside the surfzone and the undertow mechanism was present during $0.5T$. The bore/undertow interaction phase was only present for short time (of approximately $0.2T$). In the following section, the temporal variations of the diffusive and dispersive mechanisms will be presented.

The temporal averaged vertical and horizontal velocity components were determined for all three conditions tested in this study at x={1, 2, 3, 4 & 5}m. The PIV vectors were spatially averaged for each image at eight vertical windows over the depth of the FOV (see Fig. 5.18), and then temporally averaged over the length of the experiment. Figures 5.15 to 5.17 show the temporal averaged velocities determined from the PIV data across the nearshore.

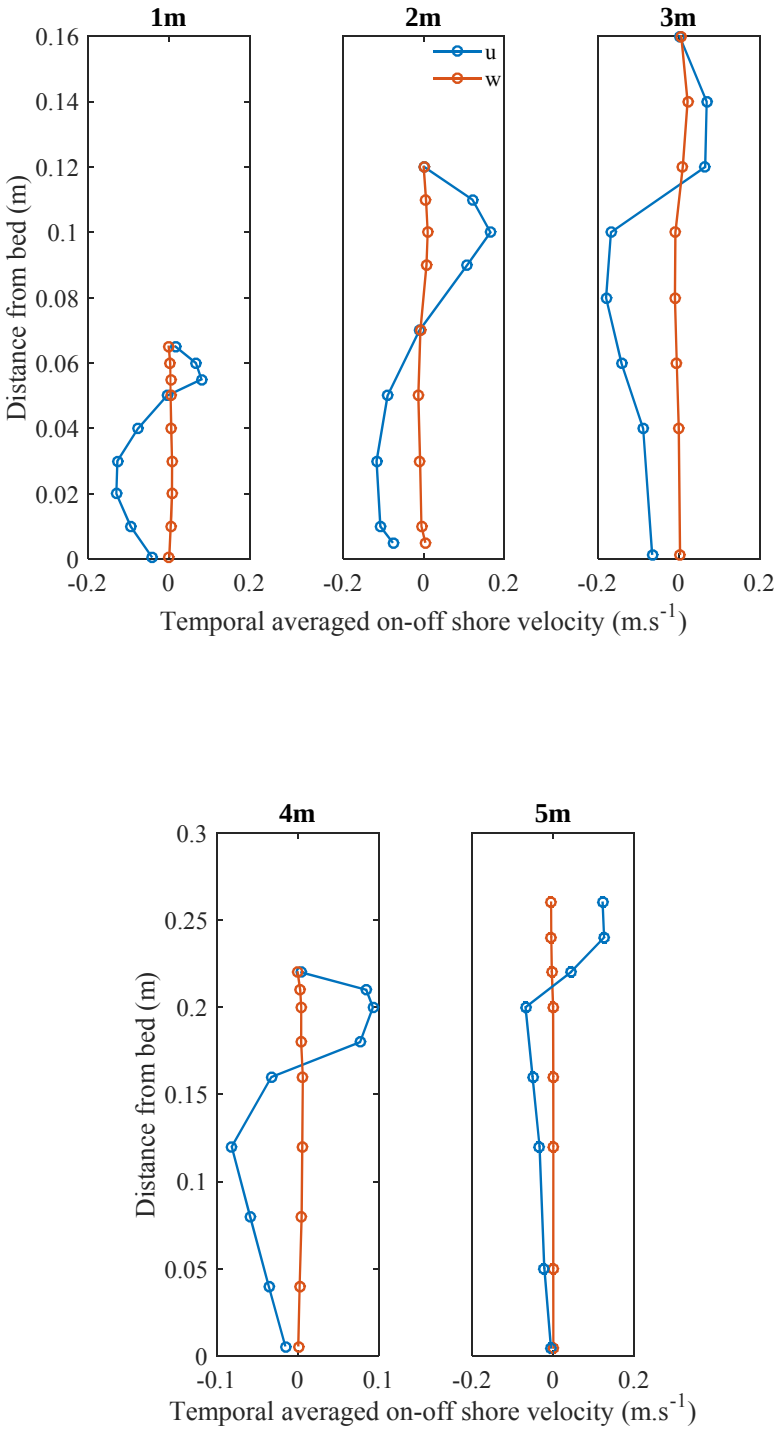

Figure 5.15 – Temporal averaged horizontal and vertical velocity components of the PIV data for monochromatic waves with H_o = 0.12m and T = 1.2sec

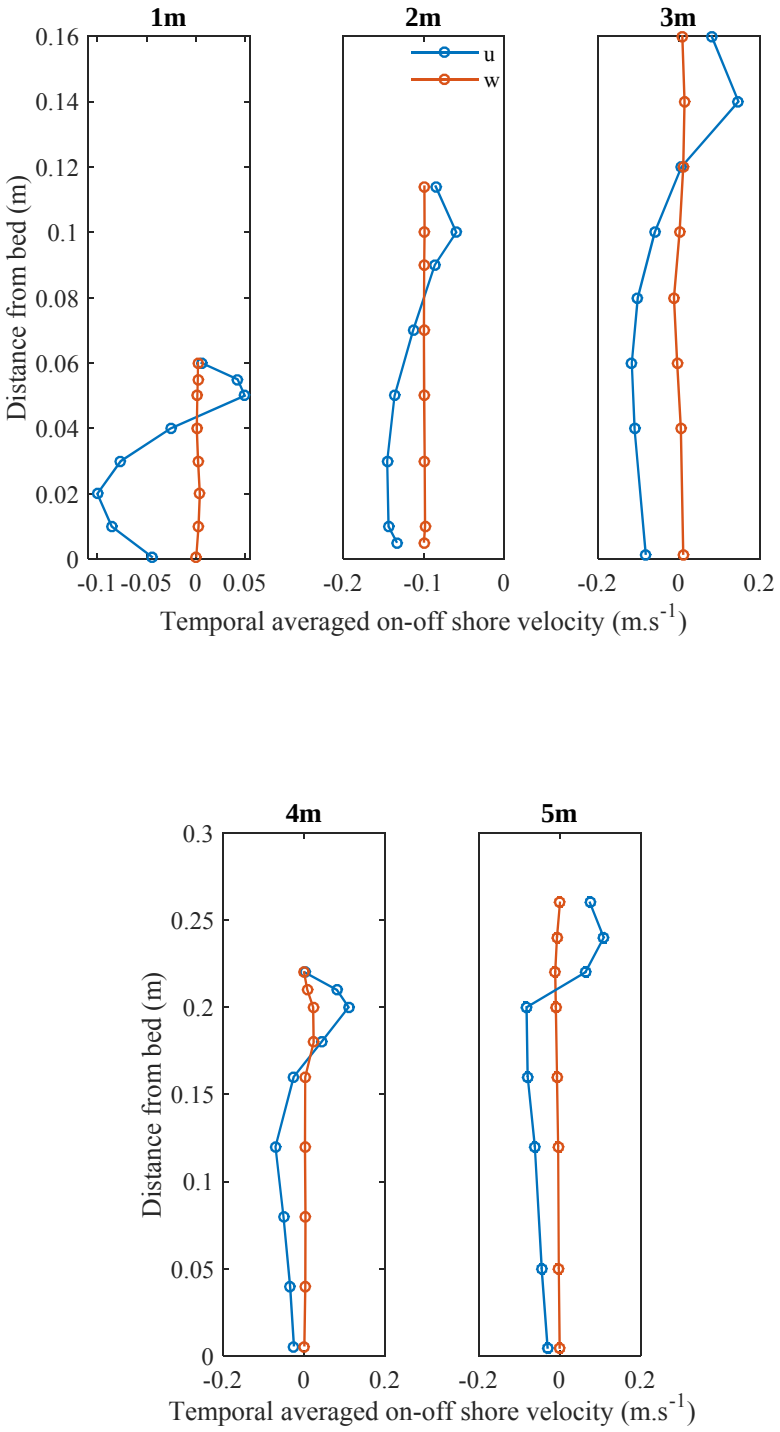

Figure 5.16 – Temporal averaged horizontal and vertical velocity components of the PIV data for monochromatic waves with H_o = 0.12m and T = 1.85sec

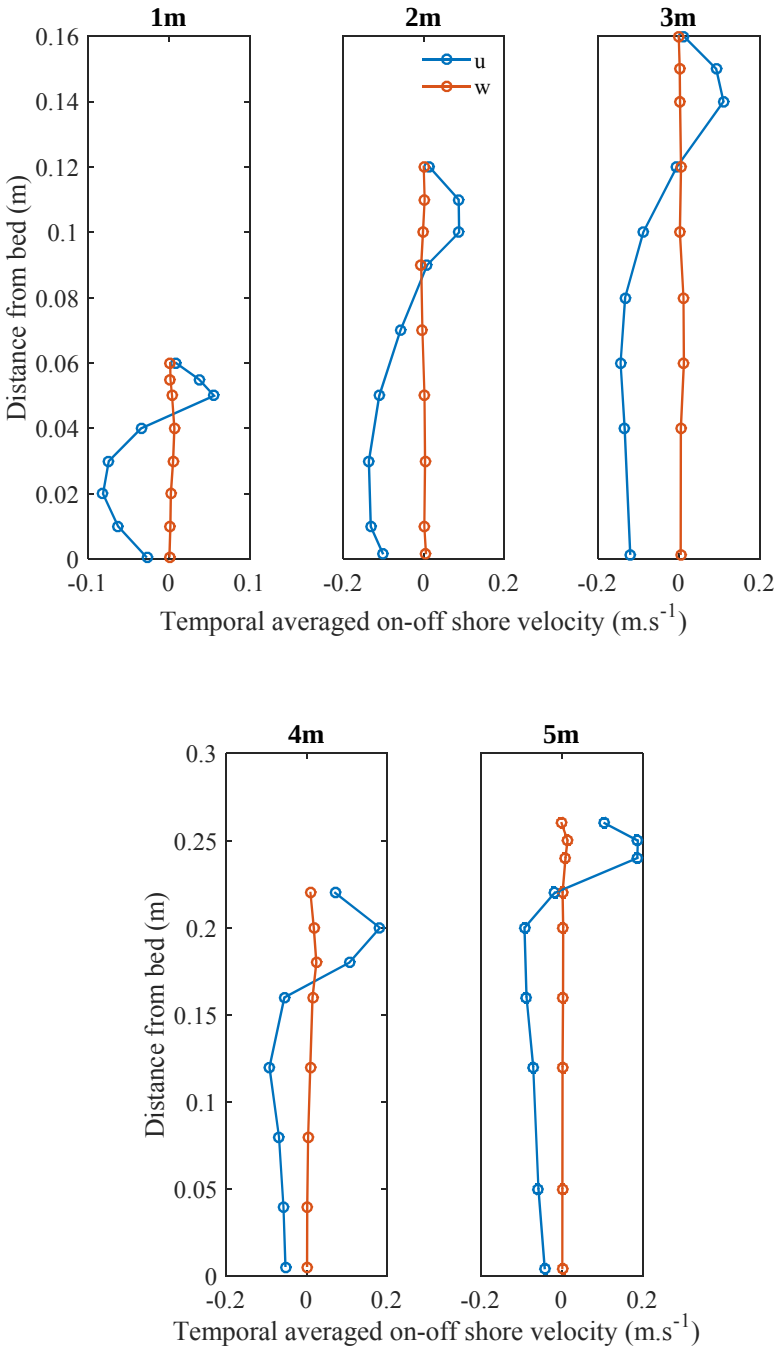

Figure 5.17 – Temporal averaged horizontal and vertical velocity components of the PIV data for monochromatic waves with H_o = 0.12m and T = 2.9sec

5.5.2 Turbulence Decomposition

Turbulence is one of the key mechanisms that influences the transport processes in the ocean and especially within the nearshore, where the incident waves shoal up and break. As discussed earlier (chapter 2 and 3), surface generated turbulence due to wave breaking phenomena is the primary mechanism for the diffusive and dispersive processes in the nearshore region.

The majority of laboratory studies in the nearshore have relied on LDV measurements [Nadaoka & Kondoh, 1982; Ting & Kirby, 1994, 1995 and 1996; Petti & Longo, 2001; Feng and Stansby, 2005, De Serio & Mossa, 2006; Shin & Cox, 2006, Feddersen, 2010; Huang *et al*., 2012]. Despite the information gained from LDV data, the technique is normally restricted to the points below the wave trough level, due to signal drop-out in the aerated region of the breaking waves. Inside the surfzone, where bubbles are generated in the water column, the acoustic signals are corrupted. Therefore, data despiking and the quality control are required to perform LDV measurements (see §4.4.1.1 for more details).

Unlike the point based measurement techniques such as LDV, PIV provides full-field two-dimensional instantaneous velocity fields. Thus, hydrodynamic measurements with PIV enables the detailed turbulence analysis of the shallow water column of nearshore region, as the TKE production can be directly evaluated with the spatial gradients obtained from the instantaneous velocity fields. The conventional LDV measurements are incapable of evaluating instantaneous spatial gradients. Over the past decade, PIV techniques have become popular for laboratory scale measurements to investigate the flow and turbulence structure under various wave climates (e.g., Chang & Liu, 1999; Melville *et al*., 2002; Govender *et al*., 2002; Kimmoun & Branger, 2007 and Huang *et al*., 2009 & 2010). In this chapter, the velocity records obtained from analysis of PIV experiments are employed to quantify the contribution of turbulent diffusion and shear dispersion in the total on-offshore mixing coefficients. The turbulent diffusion coefficients are determined based on the methodology derived in chapter 3 as a function of turbulent kinetic energy (TKE).

The measured instantaneous two dimensional flow velocities $u=(u,v)$ in the on-offshore directions consist of a solitary wave-induced component $\tilde{u}=(\tilde{u},\tilde{v})$ and a turbulent component $u'=(u',v')$. Therefore, the velocity field in mathematical notion reads:

$$u=\tilde{u}+u' \tag{5.1}$$

where the tilde denotes the wave-induced component and the prime denotes the turbulent component. There are generally two methods for separating the turbulent fluctuation which are filtering out the turbulence in spatial and temporal domains.

The first method, filters out the turbulent fluctuations in the spatial domain under the assumption that the solitary wave-induced surface flow velocity *u* is constant across the lateral dimension of the flume, due to the long-crested wave condition of the 2-D wave flume. Therefore, the wave-induced velocity components measured with the PIV technique can be defined as:

$$\tilde{u}(x,t)=\langle u(x,y,t)\rangle_{NY}=\frac{1}{Ny}\sum_{p=1}^{Ny}u(x,y,t)_p \tag{5.2}$$

where subscript *Ny* denotes the total number of velocity measurement in the *y* direction and $\langle\ \rangle_{NY}$ represents the spatial averaging in the lateral direction. Thus, the turbulent component of the flow can be defined as:

$$u'(x,y,t)=u(x,y,t)-\tilde{u}(x,t) \tag{5.3}$$

The second method, which is widely explored in turbulence decomposition from PIV data, is a temporal technique. This method works under the assumption that the coherent signal in the flow direction is induced by wave motion and the incoherent signals are assumed to be fluctuations due to the long-crested wave condition (Shaw and Trowbridge, 2001). There are several techniques for quantifying turbulence from temporal velocity data including a temporal filtering technique, ensemble averaging and spectral methods with use of Fast Fourier Transforms. Estimation of TKE based on temporal techniques were described in details in chapter 4 (§4.4.1) for analysis of the DHI hydrodynamic measurements.

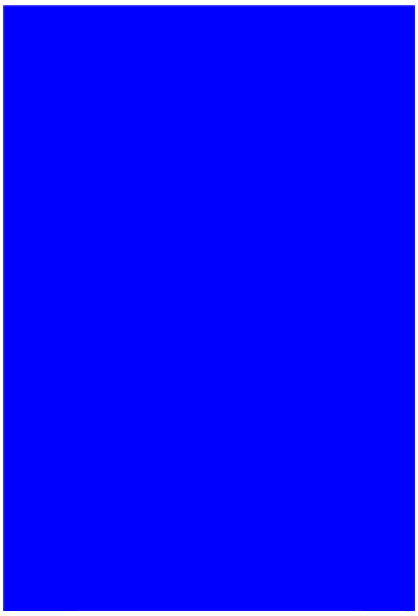

Figure 5.18 – Schematic of windowing technique for spatial averaging

In this study, the mean velocity field is obtained through the use of a windowing technique where spatial averaging was performed for 5×5 vector fields over the depth of the FOV. Figure 5.18 shows a schematic of the windowing technique used for spatial averaging. The mean and fluctuation velocity component were calculated over the depth of FOV. For those calculation cells above the still water line, no valid velocity vector exists during the undertow phases, hence the mean and fluctuation components of the velocity are zero during the undertow. In some phases, when the wave bore is approaching the FOV, those cells above the still water line could be half full with valid velocity records depending on the phase.

A filtering technique was adopted to mask out invalid/unrealistic velocity vectors due to the reflections of the laser beam from the free water surface and/or due to the reflections from the glass bed of the flume. The mean velocity field was calculated for each frame and for the duration of the PIV data.

5.5.3 Turbulent Kinetic Energy

Turbulent kinetic energy is obtained for PIV data using a windowing method in the spatial domain. Prior to the calculation of mean and instantaneous vector fields, the outlier vectors due to the reflection of laser beam from the water surface and the

glass bed of the flume were removed from the dataset. The turbulent fluctuations and TKE is calculated for each of the vertical windows (see figure 5.15) as follows:

$$u(t) = \overline{u} + u'(t) \tag{2.24a}$$

$$w(t) = \overline{w} + w'(t) \tag{2.24c}$$

where u is the velocity in the on-off shore direction and w is the vertical velocity component. Figure 5.19 is the definition sketch of so-called Reynolds' decomposition (details in §2.4.3).

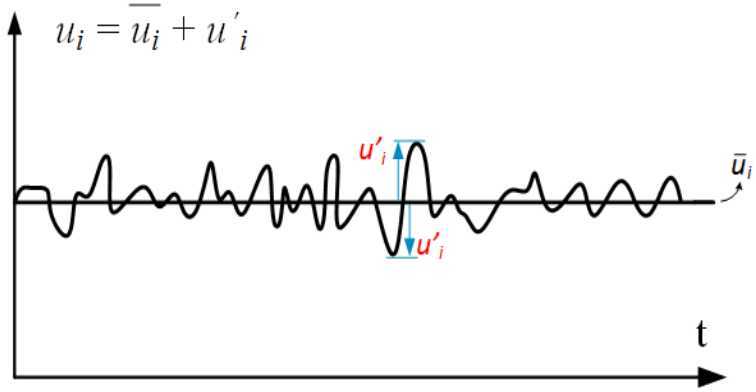

Figure 5.19 – Definition sketch of Reynolds' decomposition

The mean velocity components in on-offshore and vertical directions are then defined as:

$$\overline{u} = \int_{t}^{t+T} u(t)dt = \frac{1}{N}\sum_{1}^{N} u_i \tag{5.4}$$

$$\overline{w} = \int_{t}^{t+T} w(t)dt = \frac{1}{N}\sum_{1}^{N} w_i \tag{5.5}$$

The turbulent fluctuation for a continuous record is given by:

$$\begin{aligned} u'(t) &= u(t) - \overline{u} \\ w'(t) &= w(t) - \overline{w} \end{aligned} \tag{5.6}$$

Equation 5.6 can be rewritten for discrete points as:

$$u_i' = u_i - \overline{u}$$
$$w_i' = w_i - \overline{w} \tag{5.7}$$

Turbulent diffusion is an important mechanism in the nearshore mixing, and therefore, quantifying TKE plays an important role in understanding the magnitude of the mixing and dispersion in the turbulent flow of nearshore. Turbulent kinetic energy $\langle k \rangle^{1/2}$ can be defined as:

$$\langle k \rangle = (u'^2 + v'^2 + w'^2)/2 \tag{2.65}$$

In this study the TKE is determined from the longitudinal and vertical velocity components and it is defined according to Svendsen (1987) methodology:

$$\langle k \rangle = 1.33(u'^2 + w'^2) \tag{2.67}$$

The largest component of $\langle k \rangle$ is the turbulence generated in the stream-wise direction of the flow $\langle u'^2/2 \rangle$, and the w' component contains more energy than the v' component and is consistent with mean two dimensional flow.

In this section, the TKE is estimated based on equation 2.67 and by use of the windowing technique described earlier (Fig. 5.15). The averaged component for the velocity signal was evaluated based on equation 5.4 and 5.5. The turbulent fluctuations are determined from equation 5.7. The spatial and temporal variations of TKE were determined for all the data obtained from the PIV experiments. Figure 5.20 shows an example of TKE calculations for monochromatic waves with S_{op} = 5% in the offshore region {y = 5m}.

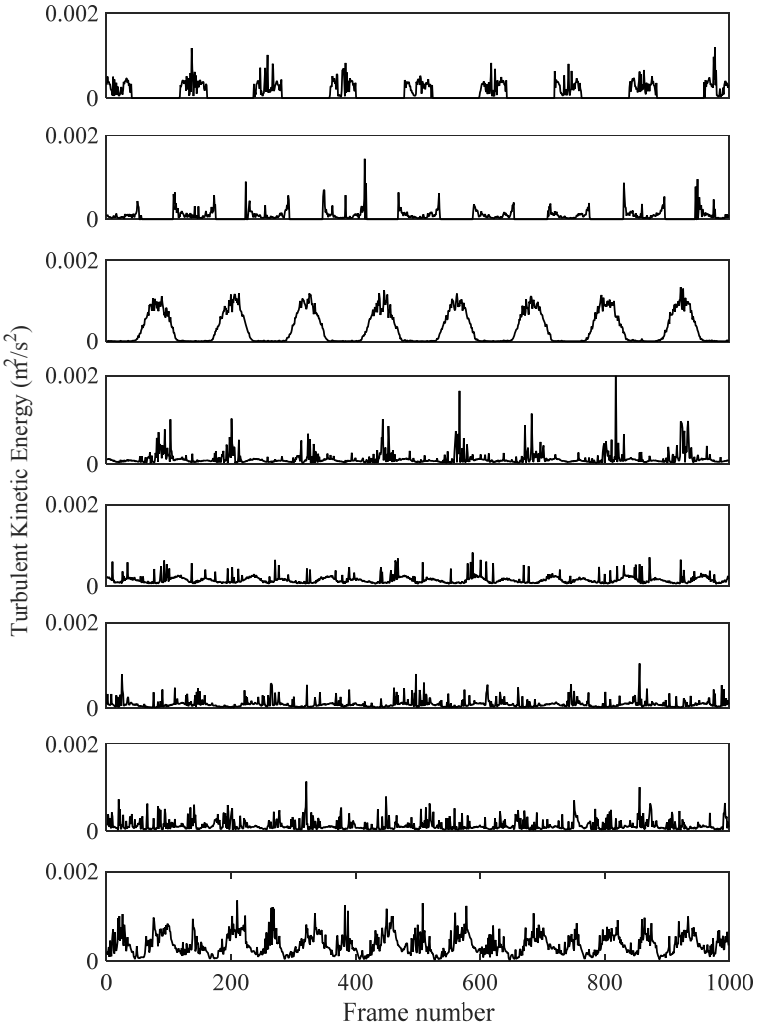

Figure 5.20 – Temporal and spatial variation of TKE in the offshore region {y=5m} for the monochromatic waves with S_{op} = 5%

Figure 5.20 illustrates the temporal variation of TKE for monochromatic waves of 5% steepness seawards of the breaker region (y =5m) for a duration of 1000 PIV images. TKE is determined for eight vertical windows covering from the bed (bottom plot) to the wave bore (top plots), where each window is representing 0.038m depth of the water column. It is evident that the magnitude of TKE is higher for the wave bore. However, TKE is zero during the undertow phase, since the water level is below mean water line and therefore no valid vectors exist in the upper part of the water column. An increased level of turbulence near the bed was observed as demonstrated in figure 5.20.

Figure 5.21 shows the temporal variation of TKE over the depth of water column for monochromatic waves of 5% steepness inside the surfzone {y=3m}. The top two windows are above the still water line. Therefore, these windows are partially full during a wave cycle when the wave crest is approaching the FOV. TKE is zero at those phases when undertow in moving offshore and thus no PIV data exists in the calculation windows. The results indicate that TKE is higher near the free surface due to wave motion and reduces towards the bed.

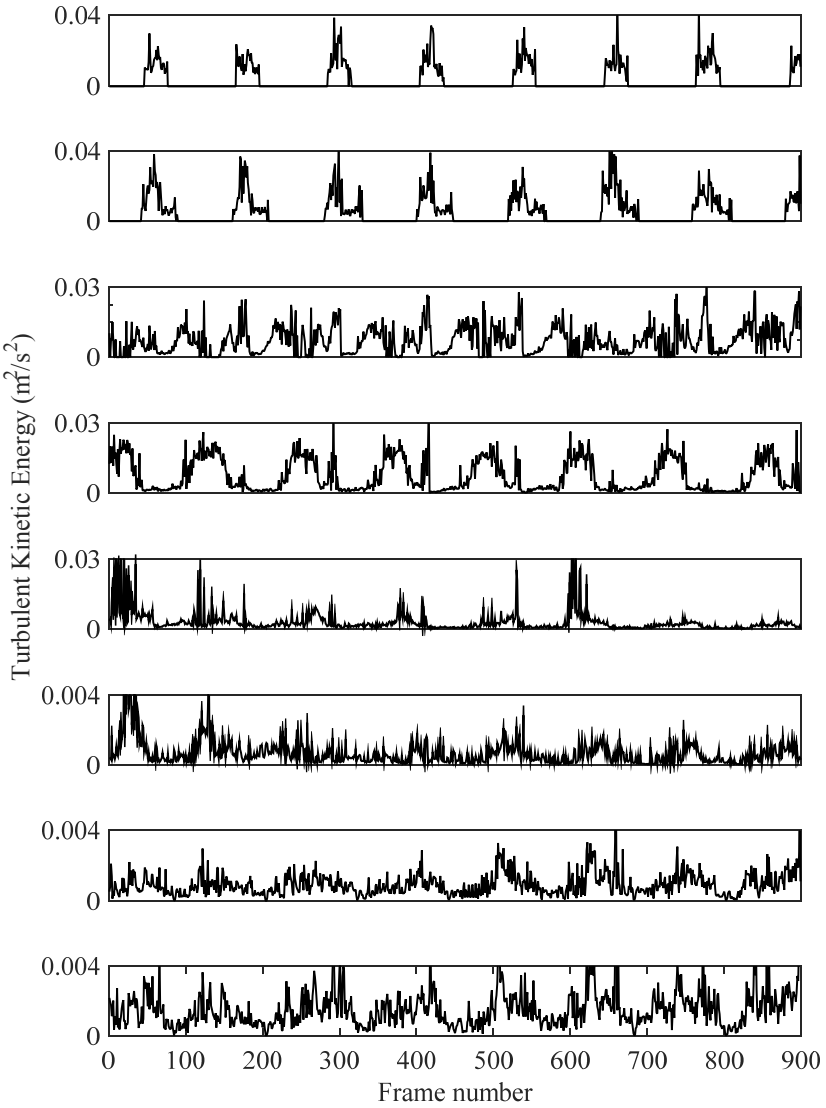

Figure 5.21 – Temporal variation of TKE inside the surfzone {y=3m} for the monochromatic waves with S_{op} = 5%

Figure 5.21 confirms that inside the surfzone, due to wave breaking and the high rate of turbulence generation and dissipation, TKE is higher in comparison with those locations seawards of the breaker region (Fig. 5.20).

The temporal variation of TKE was calculated for all the wave conditions measured during the PIV measurements and for all the locations (y ={1, 2, 3, 4 & 5}m). The results (see Figs. 5.20 and 5.21) confirm that at the bore location, there are phases of high turbulence when the wave bore approaches the measurement location (FOV). The turbulence at the bore section reduces to zero when the wave passes the FOV. It is also observed that near the bed, strong bed generated turbulence exists, especially during the undertow. The magnitude of TKE for bore and near bed was higher inside the surfzone and reduced by moving to the offshore region. For the vertical points between the wave trough level and bed, the magnitude of TKE was slightly lower than bore and bed locations. Hence, the vertical variation of TKE is small and this confirms the existing data of Svendsen (1987) and Nadaokah and Kondoh (1982).

5.5.3.1 Comparison of Measured TKE with DHI Data

The instantaneous TKE presented in §5.5.3 was temporally averaged and for each experimental condition was compared to the TKE profiles determined for LDA data (§4.4.1.2). Figure 5.22 compares the TKE values measured from the PIV data to those obtained from the LDA data.

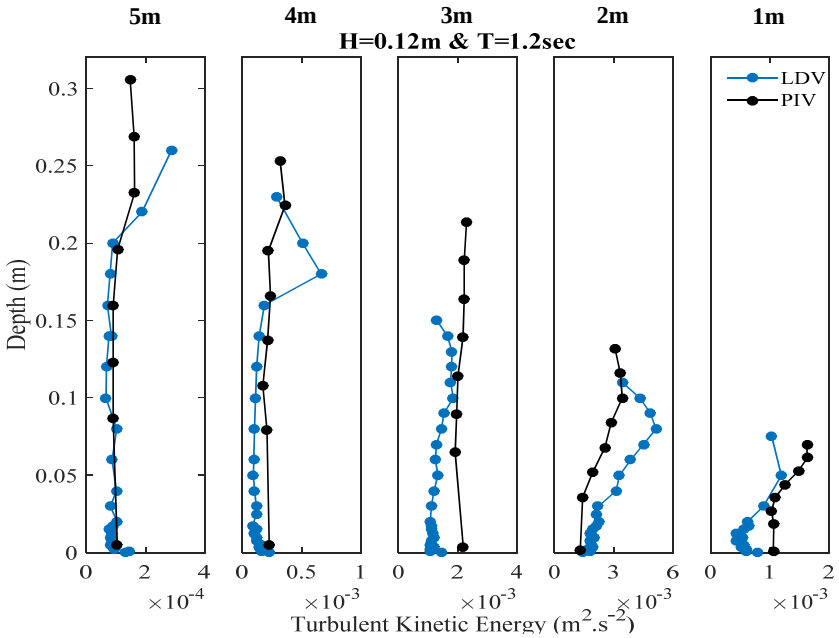
5m
4m
3m
2m
1m
H=0.12m & T=1.2sec
LDV
PIV
Depth (m)
Turbulent Kinetic Energy (m2.s-2)

(a)

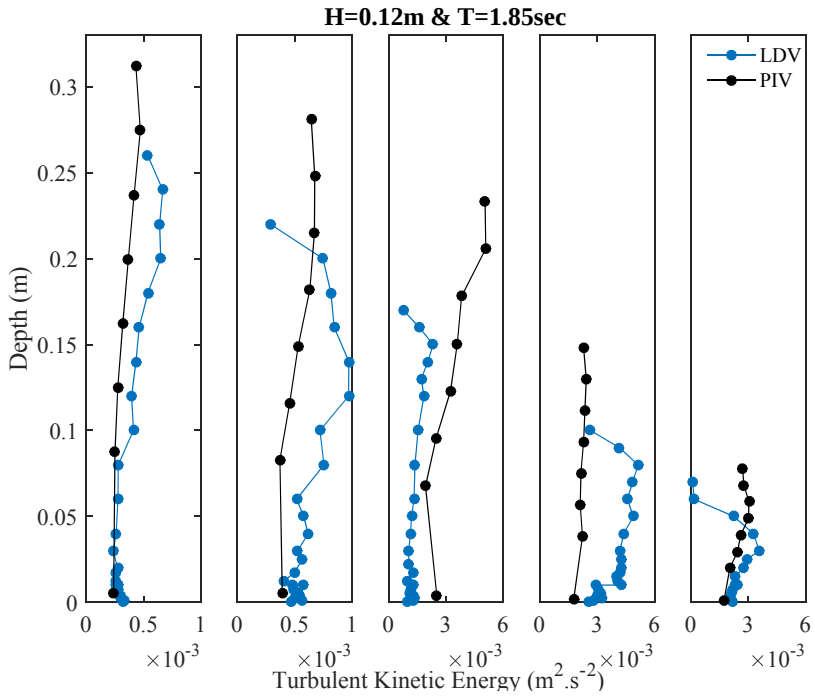
H=0.12m & T=1.85sec
LDV
PIV
Depth (m)
Turbulent Kinetic Energy (m2.s-2)

(b)

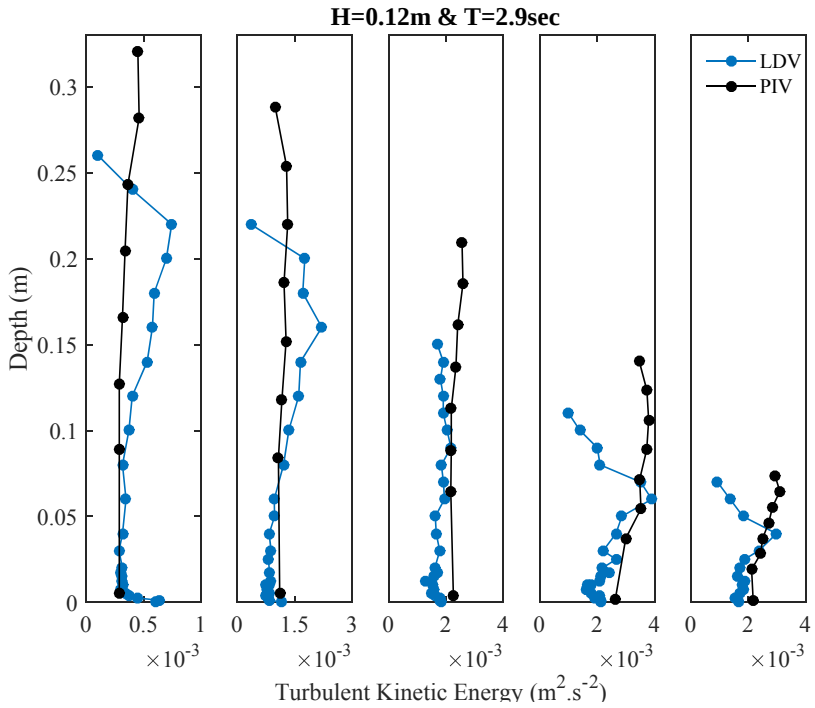

(c)

Figure 5.22 – Comparison of the TKE obtained from the PIV (-●-) and LDA (-●-) measurements for the monochromatic waves with a) S_{op} = 5%, b) S_{op} = 3 ½ % and c) S_{op} = 2%

Figure 5.22 summarizes the TKE results obtained from the PIV data and compares them to the LDA data. The figure confirms that TKE values determined for the PIV data are in good agreement with the values obtained from the LDA data (§4.4.1.2). Hence, the results are also comparable to the TKE values reported by Nadaokah & Kondoh (1982) and Svendsen (1987). For all tested conditions and locations, the turbulent kinetic energy determined for the bore section is slightly higher than the TKE of undertow part of the water column. However, the vertical variation of the TKE is very small. Turbulent kinetic energy values obtained from the PIV data demonstrate that for all wave conditions tested, the highest TKE exists at the breaker region. Also, for locations seaward of the breaker region, the magnitude of TKE drops down by ~87%.

5.5.4 Turbulent Diffusion Mechanism

The turbulent diffusion coefficient is determined for the PIV data by use of the TKE reported in §5.5.3 and turbulent length-scale (l_m) described in chapter 2 (Eq. 2.68). The diffusivity is calculated by use of a constant length-scale (l_m) across the nearshore. Figure 5.23 presents the eddy viscosity (v_t) values obtained from the PIV data for all the conditions tested, and compares them to the theoretical approach described by Svendsen and Putrevu (1994) [Eqs. 2.69 and 2.73].

$$v_t = 0.01d\sqrt{gd} \text{ ; inside the surfzone} \tag{2.69}$$

$$v_t = [0.8(\frac{d}{d_b})^{-4} + 0.2]v_{tb} \text{ ; outside the surfzone} \tag{2.73}$$

where, $v_{tb} = 0.01d_b\sqrt{gd_b}$ is the eddy viscosity at breaking point, d is depth of SWL and d_b is the depth of water at breaker point. As already discussed in chapter 2, the results of Svendsen & Putrevu (1994) theoretical formulae for eddy viscosity are highly dependent on the choice of breaker point. In this section, the breaker points were taken from laboratory data.

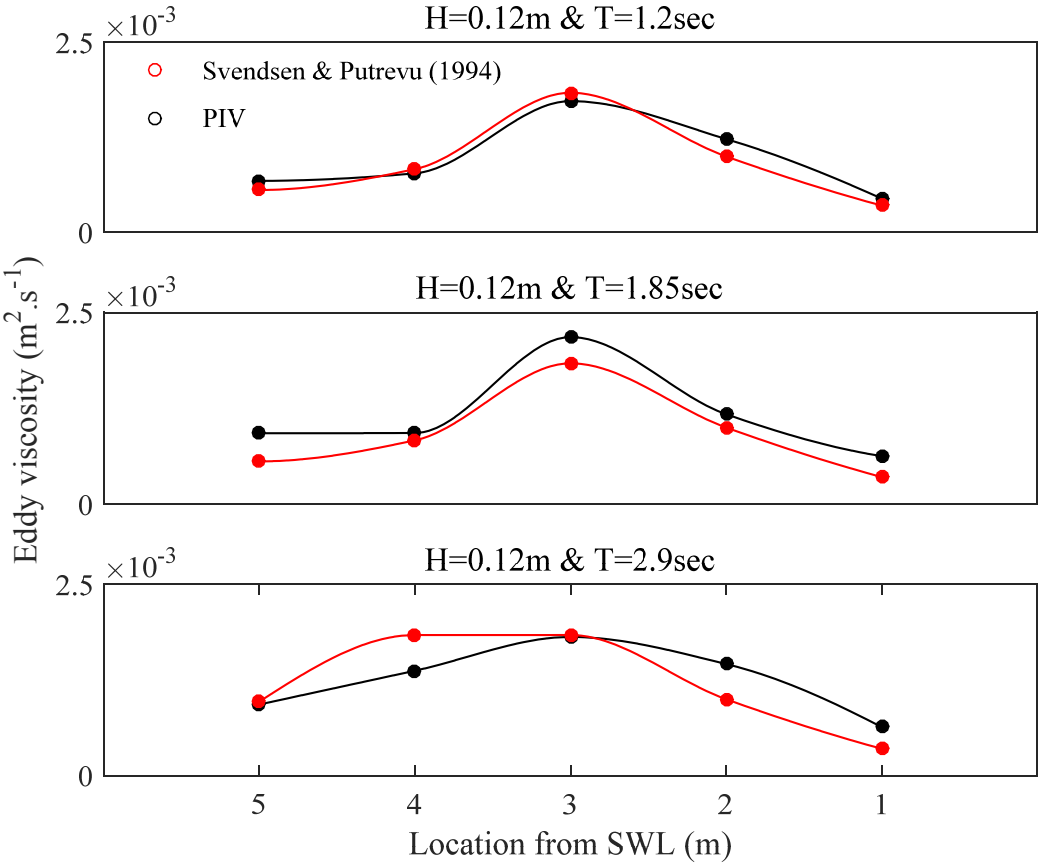

Figure 5.23 – Comparison of the diffusivities (v_t) obtained from PIV (-●-) and Theoretical approach (-●-) proposed by Svendsen and Putrevu (1994)

Figure 5.23 indicates that the diffusivity values obtained from PIV data are in good agreement with the theoretical formula (Eq. 4.11) proposed by Sevendsen and Putrevu (1994). The eddy viscosity calculated for monochromatic waves of 5% steepness was visually the best fit between the calculated and theoretical diffusivities. For 3½ % wave steepness, the PIV data is higher than theoretical relation for all locations across the nearshore. For the monochromatic waves with 2% steepness, the diffusivities obtained from the PIV data are overestimating Svendsen and Putrevu (1994) formula inside the surfzone. However, PIV diffusivities are measured lower than theoretical approach seaward of the breaker region.

The turbulent diffusion mechanism was investigated within this section. The eddy viscosity coefficients were determined from the PIV data and compared to the

theoretical values proposed by Svendsen and Putrevu (1994). The results were in good agreement with the theoretical values and follow the trend of experimental data analysis reported in chapter 4 (§4.4.2). The following section (§5.5.5) will elucidate the contribution of shear dispersion across the nearshore region from the PIV data.

5.5.5 Shear Dispersion Mechanism

The contribution of shear dispersion in the total on-off shore mixing was determined from the PIV data using the mathematical solutions of the *N*-zone model (see §3.3.2). The shear dispersion coefficients were determined for all the conditions tested in the PIV measurements. Due to the similarity of the PIV experiments and the DHI data in terms of hydrodynamic conditions, the dispersion values obtained from the PIV data were compared to the mixing coefficients obtained from the dye tracer measurements at DHI. The temporal variation of flow hydrodynamics in the water column was investigated with the PIV measurements and the results of vector computations were illustrated in §5.5.1. The analysis of PIV images has shown the existence of three principal hydrodynamic mechanisms during a wave cycle. The mechanisms include the undertow, bore and intense shearing phase due to the interactions between the undertow and bore. Figure 5.24 is the sketch of the shearing mechanisms during the wave cycle and their temporal duration based on the PIV image analysis and observations.

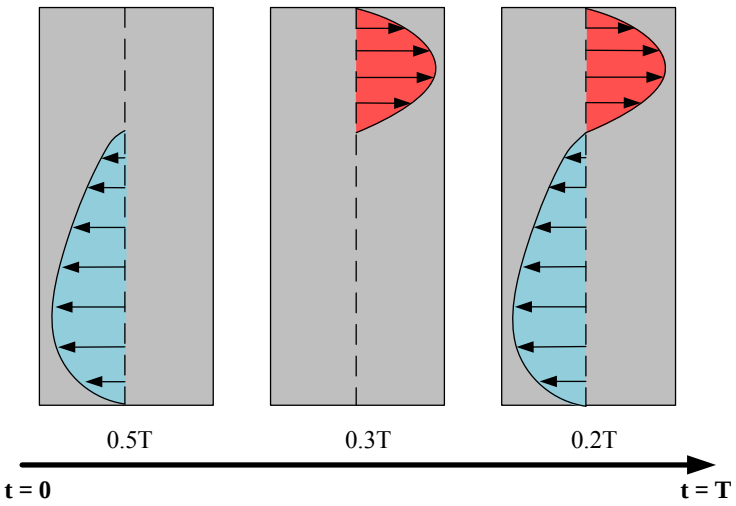

Figure 5.24 – Schematic sketch of the dispersion mechanisms during a wave cycle based on the PIV data analysis

In this section, the temporal variation of dispersive mechanisms across the nearshore were investigated by use of the PIV hydrodynamic data. The velocity input for the dispersion model is the spatially averaged vectors for each frame (0.01sec). In order to compute the velocity input for the dispersion model, at each time-step, strips of vectors in the PIV velocity matrix were selected. These vectors were located at the middle of the FOV in on-offshore directions and considered all the vectors from the bed to the wave crest. The velocity vectors were averaged for each individual row of the data and these spatially averaged velocity records were used to determine the shear dispersion with the *N*-zone model. Figure 5.25 shows a snapshot of PIV vectors and the computational procedure for obtaining the velocity profile at each time-step.

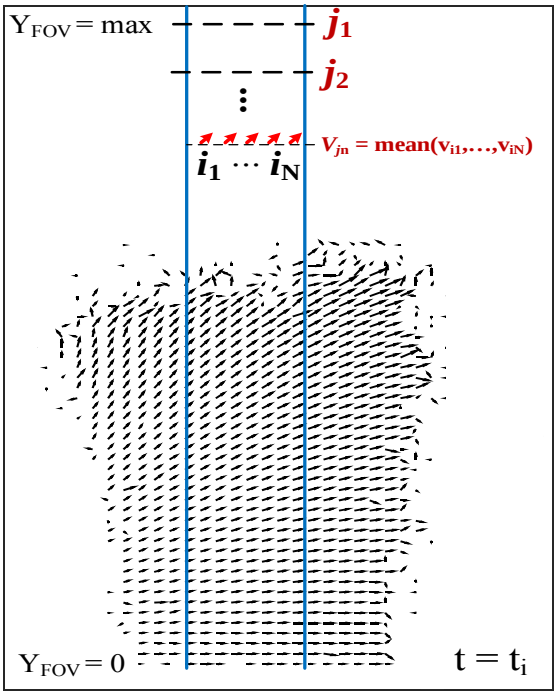

Figure 5.25 – Schematic of the shear dispersion mechanisms during a wave cycle and their temporal contribution based on the PIV data analysis

For all wave conditions and locations tested during the PIV experiments, the limits of x axis (on-offshore) were set to create a window in the middle of the FOV. Figure 5.26 shows an example of the velocity profiles computed with this method at five phases during the wave cycle for the monochromatic waves with H_o = 0.12m and T = 1.2sec inside the surfzone (y=3m).

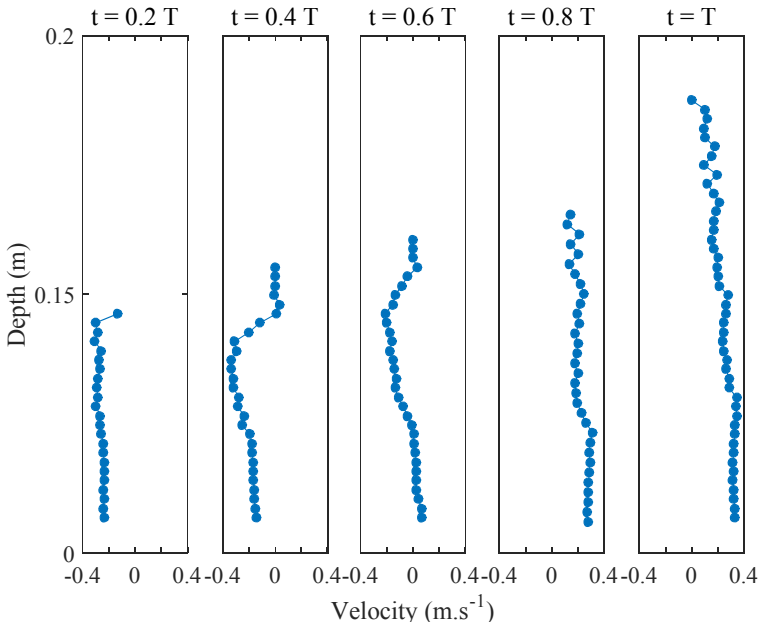

Figure 5.26 – Temporal varioation of instantanious velocity profiles at 3m from SWL for the monochromatic waves of H_o = 0.12m and T = 1.2sec

The instantanious spatially-averaged velocity profiles were computed for all of the PIV images. Figure 5.27 shows an example of vertical distribution of spatially-averaged velocity vectors for seven consequtive waves in the breaker region (y=3m) and the inner surfzone (y=2m) for the regular waves with H_o= 0.12m and T = 1.2sec.

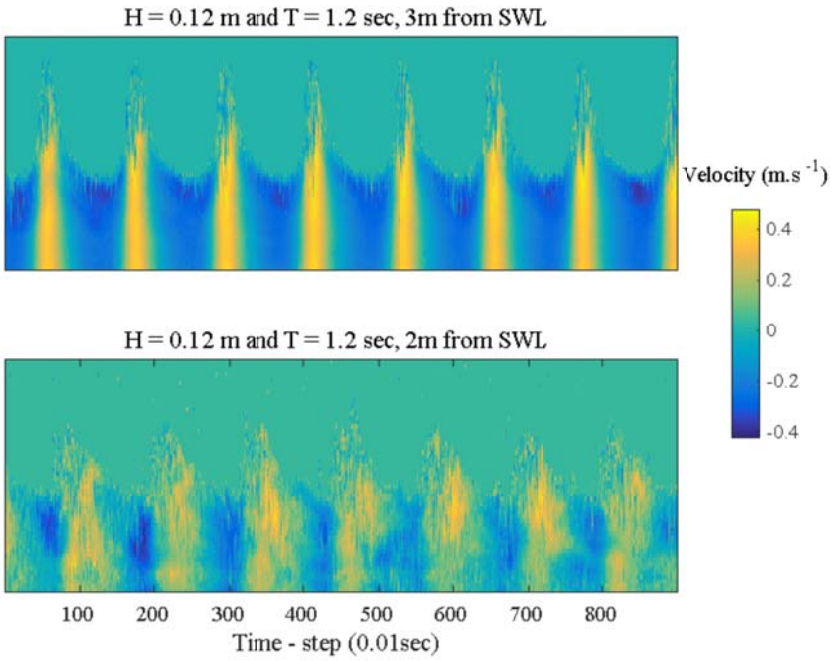

Figure 5.27 - Vertical distribution of spatially-averaged velocity over the full depth of FOV and centre of the PIV images for the monchromatic waves of H_o = 0.12m and T = 1.2sec in the breaker region (3m) and inner surfzone (2m)

The dispersion model was set to quantify the shear dispersion coefficient for each PIV image. Given that the PIV data was collected with 100 fps, each spatially-averaged velocity profile was representing 0.01sec of the wave period. The velocity profiles computed in this section have a vertically variable depth dependant on the time-step. The instantanious spatially-averaged velocity profiles and the diffusivities determined from the PIV data were the inputs of the *N*-zone model to investigate the temporal variations of the shear dispersion across the nearshore. Figures 5.28 to 5.30 show the temporal variation of shear dispersion across the nearshore for the wave conditions tested during the PIV experiments.

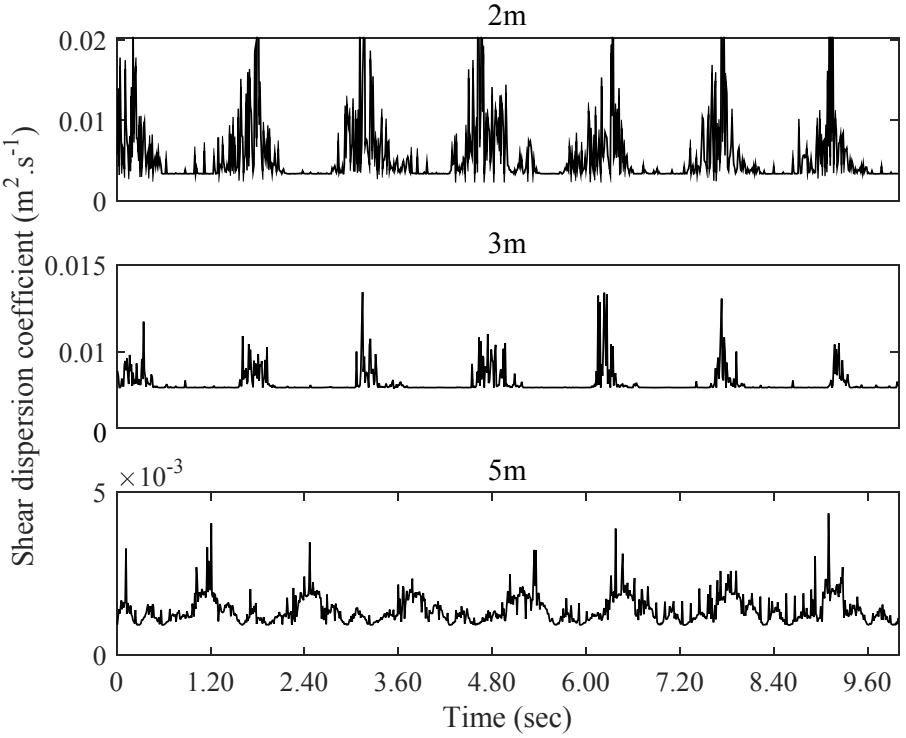

Figure 5.28 – Temporal variation of shear dispersion across the nearshore for the monochromatic waves with H_o = 0.12m and T = 1.2sec

Figure 5.28 shows the temporal variation of the shear dispersion for the monochromatic waves with 5% steepness. The shear dispersion was determined with the use of the *N*-zone model and based on the temporal variation of spatially-averaged velocity profiles from the PIV data. The temporal variations of the shear dispersion coefficients were determined for seaward of the breaker region (5m), the breaker region (3m) and the inner surfzone (2m). It is evident from figure 5.28 that the dispersive mechanisms are higher inside the surfzone in comparison to the breaker region and offshore locations. The temporal variation of shear dispersion shows that there are distinct phases within a wave cycle where an intense shearing mechanism exists, specially for the breaker region and the inner surfzone. Comparing the temporal variation of dispersion with the PIV velocity vectors show that during the undertow phase, there is a small dispersion with low fluctuations. However, the time-scale of the undertow phase is 0.5T for this condition and therefore, the contribution of the undertow mechanism in the dispersion coefficient is significant. When the wave bore approaches and exits the FOV, the dispersion fluctuations increase and decrease, respectively. The dispersion during the bore

phase showed higher values, although the temporal contribution of bore was small (0.3T). The results (Fig. 5.28) also show that a sharp increase happens over a small time durations (0.2T) which is due to the interaction between bore and undertow. The dispersion coefficients reached its peak during the undertow/bore interaction phase.

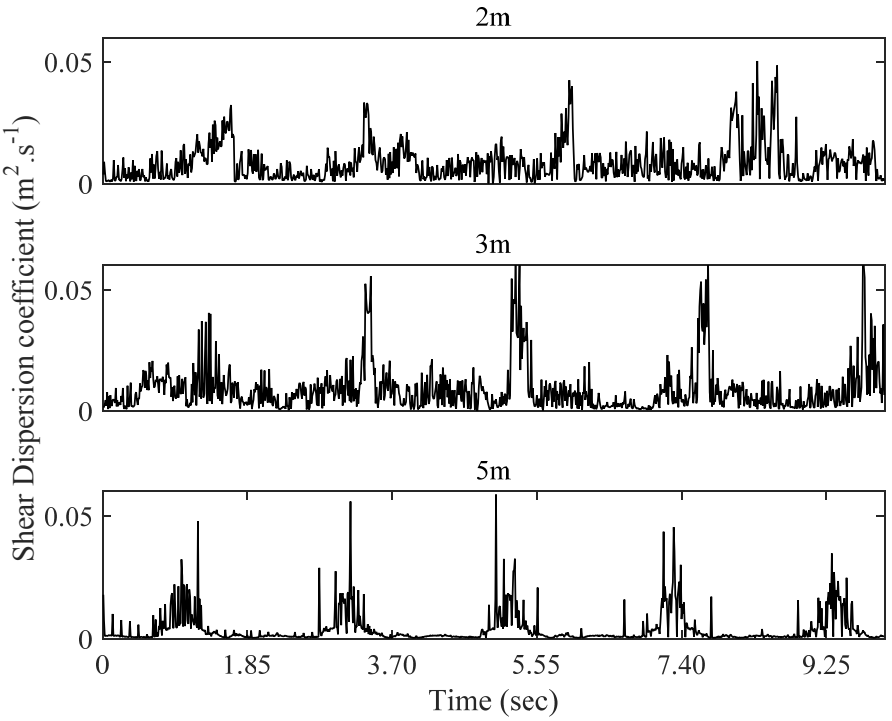

Figure 5.29 – Temporal variation of shear dispersion across the nearshore for the monochromatic waves with H_o = 0.12m and T = 1.85sec

Figure 5.29 depicts the temporal variation of the shear dispersion for the monochromatic waves with H_o = 0.12m and T = 1.85sec. The variations of dispersive mechanisms were investigated seawards of the breaker region (5m), at the breaker (3m) and the inner surfzone (2m). A comparison of the temporal variation of dispersion coeffcients with the PIV velocity vectors confirms the contribution of bore, undertow and bore/undertow interaction disperive mechanisms as described previously. The comparison between the undertow mechanisms for offshore, breaker and inner surfzone locations shows that the undetow mechanisms in the offshore region is not a significant contributor to the overall dispersion coefficients. By

moving towards the breaker region and surfzone, the contribution of undertow towards the overall dispersion coefficients is increased.

Figure 5.30 illustrates the temporal variation of the shear dispersion for the monochromatic waves with S_{op}=2%. The figure presents the temporal evolutions of the dispersion coefficients form the offshore region to the inner surfzone (5, 3 and 2m, respectively). The temporal variation of the dispersion was compared to the PIV vectors and the existance of the proposed dispersive mechanisms was confirmed. The results for the offshore location show that bore interactions with the undertow are the primary mechanisms in the overall dispersion. For this condition, the undertow mechanism results in a small contribution to the overall dispersion. The results also show that for monochromatic waves with 2% steepness, the overall dispersion varies by $4.37\times10^{-3} m^2.s^{-1}$ inside the surfzone.

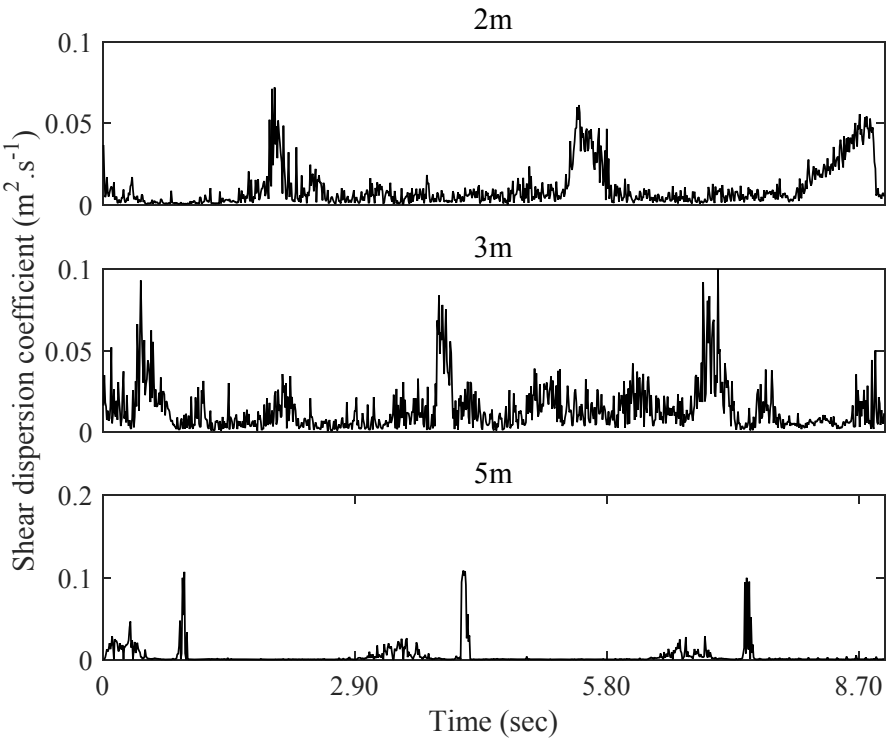

Figure 5.30 – Temporal variation of shear dispersion across the nearshore for the monochromatic waves with H_o = 0.12m and T = 2.9sec

The temporal variations of the shear dispersion were averaged over the wave period for each test case in order to obtain the overall shear dispersion coefficients. The dispersion coefficients which were determined from the PIV data, were compared to

the dispersion coefficients obtained from the analysis of the tracer measurments (§4.3.3). Tables 5.2 to 5.4 present the shear dispersion obtained from the PIV data by use of the *N*-zone model and based on the temporal variation of velocity and the depth-averaged diffusivities.

Table 5.2 – Comparison between D_y obtained from temporal variation of shear dispersion and DHI tracer measurements for monochromatic waves with S_{op} = 5%

Location from shore [m]	D_y (Total) [$m^2.s^{-1}$]	$D_{y-tracer}$ (DHI) [$m^2.s^{-1}$]
2	1.382E-02	1.195E-02
3	7.789E-03	1.261E-02
5	1.309E-03	6.930E-04

Table 5.3 – Comparison between D_y obtained from temporal variation of shear dispersion and DHI tracer measurements for monochromatic waves with S_{op} = 3½ %

Location from shore [m]	D_y (Total) [$m^2.s^{-1}$]	$D_{y-tracer}$ (DHI) [$m^2.s^{-1}$]
2	8.589E-03	8.566E-03
3	9.338E-03	8.609E-03
5	3.901E-03	1.056E-03

Table 5.4 – Comparison between D_y obtained from temporal variation of shear dispersion and DHI tracer measurements for monochromatic waves with S_{op} = 2%

Location from shore [m]	D_y (Total) [$m^2.s^{-1}$]	$D_{y-tracer}$ (DHI) [$m^2.s^{-1}$]
2	9.917E-03	1.244E-02
3	1.429E-02	1.079E-02
5	4.554E-03	1.576E-03

The comparison between the overall shear dispersion coefficients obtained from the temporal variation of dispersion and the tracer measurement indicates that the dispersion model described in work is well capable of capturing the dispersive mixing mechanisms. For the monochromatic wave conditions tested in this study the temporal contribution of the undertow mechanism in the total shear dispersion coefficient was 50% of the wave cycle, while the bore mechanism was only contributing to the overall dispersion during 30% of the wave period. The maximum shear dispersion during each cycle was achieved during the interaction between the wave bore moving onshore and the undertow going offshore. Observations show that the duration of this phase was only 20% of the wave period. Figure 5.31 summarizes the results of the shear dispersion coefficients obtained from the PIV data with use of the method described above. The dispersion coefficients were compared to the mixing coefficients obtained from DHI data (§4.3.3)

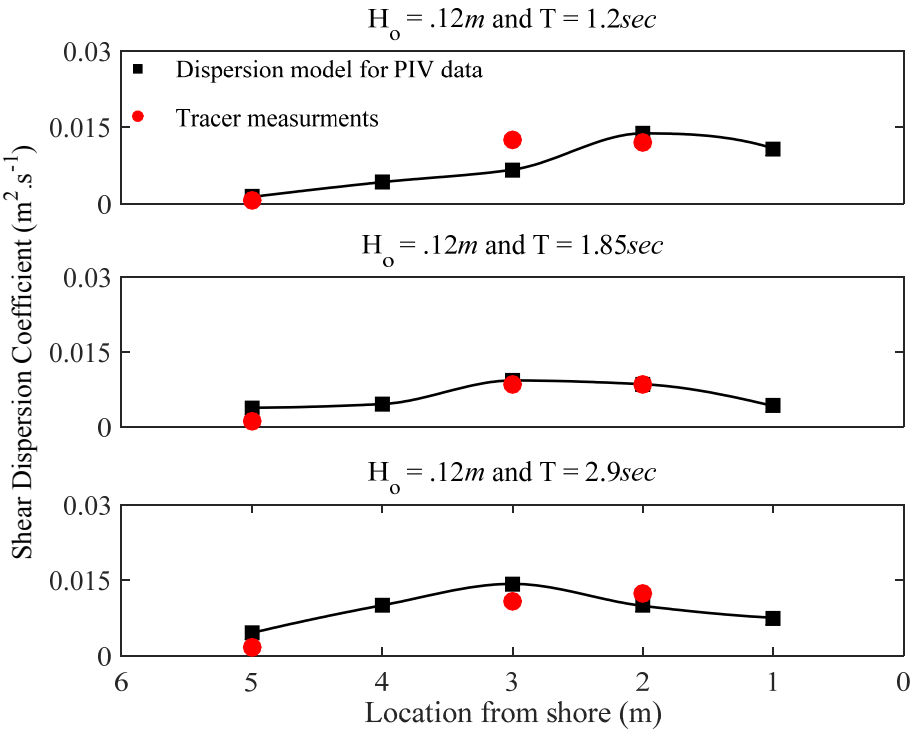

Figure 5.31 – Comparison between the dispersion coefficient obtained from the PIV data analysis and fluorometric study at DHI (§4.3.3)

Figure 5.31 shows that the dispersion coefficients obtained from the PIV data are in good agreement with the mixing coefficients determined from the fluorometric tracing study, described in chapter 4 (§4.3.3).

5.6 Summary

In this chapter, the flow hydrodynamics across the nearshore were investigated through a series of laboratory measurements with the use of Particle Image Velocimetry. The experiments were undertaken in a dedicated wave flume at the University of Warwick with a 1:20 plain beach slope and equipped with an active absorption type wave-maker. Through analysis of the PIV data, the hydrodynamic structure inside the surfzone, at the breaker region and in the offshore region were investigated. Three monochromatic wave conditions, similar to the one in the DHI study (chapter 4) were investigated. The experimental setup and data analysis techniques have been described in detail.

The spatial variation and the magnitude of the velocity across the nearshore were determined from the PIV data analysis. The flow visualisations demonstrated that, three hydrodynamic processes exist during the wave cycle which contribute to the turbulent diffusion and the shear dispersion mechanisms. The hydrodynamic processes include the undertow, the bore and the intense shearing phase caused by the collision between the incident wave bore and the undertow of the previous wave. The temporal duration of each of these hydrodynamic processes is a function of the incident wave climate.

The TKE and eddy diffusivity were determined using the PIV data. The results of TKE profiles were in good agreement with the DHI study (§4.4.1) and the existing laboratory data (Nadaokah and Kondoh, 1982; Svendsen, 1987). The eddy viscosity was determined using of TKE and a constant length-scale of $0.03d$ across the nearshore. The comparison of the eddy viscosity results with Svendsen and Putrevu (1994) theoretical values showed good agreement.

Performing PIV experiments at high data acquisition rates helped to understand and identify the hydrodynamic processes within the wave cycle. These hydrodynamic processes were used to derive a dispersion model for quantifying the contribution of the dispersive mechanisms in the overall mixing coefficients across the nearshore region. The shear dispersion coefficient was determined with the *N*-zone model described in chapter 3 (§3.4.2). Spatially-averaged velocity profiles for each PIV frame were employed with a depth-averaged diffusivity to determine the shear dispersion coefficients.

The results obtained from the dispersion model confirmed the existence of three mixing mechanisms in the nearshore including the bore, the undertow and intense dispersion phase due to the interaction of incident wave bore and reflected wave undertow. The dispersive mechanisms were identified by investigating the temporal variations of the shear dispersion and the PIV velocity vectors. The results show that, regardless of the on-offshore location in the nearshore region, the dispersion is relatively small during the undertow phase due to the small shearing effect in the water column. By approaching the wave bore towards the FOV, the results show a notable increase in the temporal fluctuations of the dispersion coefficients. These fluctuations reached their peak once the turbulent wave bore collided with the undertow of the previous wave, resulting in an intense shearing mechanism in the water column. For the three monochromatic wave conditions investigated during this study, the contribution of the undertow mechanism was 50% of the wave cycle while the bore mechanism took place over 30% of the wave period. The intense shearing mechanism of bore/undertow interaction was only present during 20% of the wave period. The results of the dispersion model developed in this chapter were compared to the tracer measurements described in chapter 4. The overall dispersion coefficients obtained from the temporal variations of the shear dispersion showed good agreement with the measured dispersion coefficients from the dye tracer data (§ 4.3.3). Inclusion of bore hydrodynamics obtained from the PIV measurements into the shear dispersion model improved the results in comparison with the dispersion model developed based on undertow velocities identified in the previous chapter (§4.4.3).

CHAPTER 6

NUMERICAL SIMULATIONS

6.1 Synopsis

This chapter focuses on the applications of numerical simulations in studying the mixing and dispersion caused by the effects of waves in the nearshore region. Eulerian and Lagrangian modelling approaches are discussed and their general features, advantages and applications for modelling hydrodynamics are compared. In this study, the capabilities of Smoothed Particle Hydrodynamics (SPH), a Lagrangian, particle-based method are explored for simulating the flow hydrodynamics in the nearshore. Background theory, some general features and advantageous of SPH type models are described. The results obtained from the SPH numerical model developed within this chapter are validated against the laboratory measurements described in chapters 4 and 5. The hydrodynamic data obtained from the SPH model is employed to quantify the temporal variation of the dispersion and diffusion mechanisms in the nearshore.

6.2 Motivation

Understanding the complicated physical processes of mixing in the nearshore region due to the effects of wave and currents is an intriguing but challenging task. The laboratory and field studies of hydrodynamics and mixing processes in the nearshore is very expensive and requires access to advanced measurement equipment. In this chapter, significant efforts have been made to develop an SPH type numerical model

to validate the mixing mechanisms postulated from PIV, LDA and tracer experiments.

6.2.1 Computational Fluid Dynamics

The aim of computational fluid dynamics is to simulate the fluid motion and the associated parameters with a degree of precision such that realistic and reliable data could be extracted from the simulations.

Computational methods are generally categorized into two primary formats of Eulerian and Lagrangian methods. Eulerian methods are formed based on the fixed spatial discretization of the fluid where all associated quantities inside the fluid are estimated at fix locations (Fig. 6.1a). However, the Lagrangian methods discretize the fluid at points, thus in this case, the fluid is described as moving particles (Fig. 6.1.b).

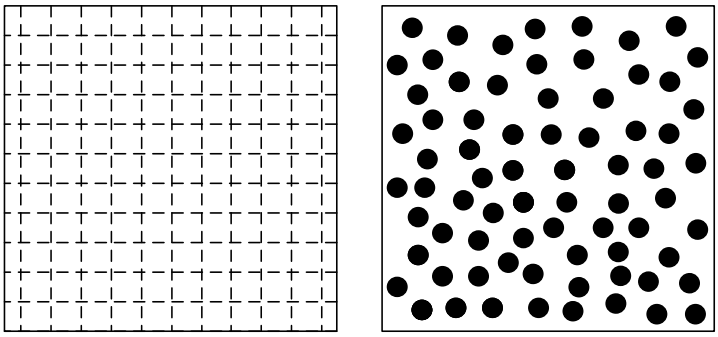

(a) (b)

Figure 6.1 – Discretization approaches in CFD simulations, a) Eulerian b) Lagrangian methods

The difference between the two approaches can be described mathematically by considering the rate of the change in quantity φ inside the fluid during its evolution:

$$\frac{\mathrm{D}\varphi}{\mathrm{Dt}} = \frac{\delta\varphi}{\delta t} + \varphi(v.\nabla) \tag{6.1}$$

Eulerian methods use the RHS of equation 6.1 for discretization of fluid, while, the Lagrangian approaches use the LHS of the equation for description of fluid motion. Table 6.1 summarizes the conservation equations in partial differential equations (PDE) form for Eulerian and Lagrangian approaches.

Table 6.1 – Governing equations of fluid motion in Eularian and Lagrangian description (adopted from Liu & Liu, 2003)

Conservation	Lagrangian description	Eulerian description
Mass	$\frac{\mathrm{D}\rho}{\mathrm{Dt}} = -\rho \frac{\partial v^{\beta}}{\partial x^{\beta}}$	$\frac{\partial \rho}{\partial t} + v^{\beta} \frac{\partial \rho}{\partial x^{\beta}} = -\rho \frac{\partial v^{\beta}}{\partial x^{\beta}}$
Momentum	$\frac{\mathrm{D}v^{\beta}}{\mathrm{Dt}} = -\frac{1}{\rho} \frac{\partial p}{\partial x^{\beta}}$	$\frac{\partial v^{\beta}}{\partial t} + v^{\alpha} \frac{\partial v^{\beta}}{\partial v^{\alpha}} = -\frac{1}{\rho} \frac{\partial p}{\partial x^{\beta}}$
Energy	$\frac{\mathrm{D}e}{\mathrm{Dt}} = -\frac{p}{\rho} \frac{\partial v^{\beta}}{\partial x^{\beta}}$	$\frac{\partial e}{\partial t} + v^{\beta} \frac{\partial e}{\partial x^{\beta}} = -\frac{p}{\rho} \frac{\partial v^{\beta}}{\partial x^{\beta}}$

In table 6.1, ρ, e, v and x are the density, internal energy, velocity and position vectors, respectively. The subscripts α and β are used to denote the coordinate directions, while the summation in the equations is taken over repeated indices.

6.2.2 Grid-based Methods

The Eularian description for grid-based models is typically represented by the finite volume method (FVM) [Versteeg & Malakasekera, 1995; Marshall *et al*., 1997; Leveque, 2002; Chen *et al*., 2003; Wang & Shen 2010; Velasco & Rendon, 2015]. In FVM, the mesh is fixed in space, whereas, the fluid moves across the grid cells. Despite difficulties of modelling irregular geometries with FVM, large deformations can be handled easily with this model since the spatially fixed mesh remains unchanged. The drawback of FVM models is in the difficulties associated with obtaining time-history (i.e., position, mass, momentum, energy, etc.) at the points

attached on the material. Also, tracking moving boundaries and interfaces is a difficult task to achieve with FVM (Liu & Liu, 2003).

The Lagrangian description of the governing equations in the grid-based approach is typically presented by the finite element method (FEM) [Wand & Hu, 1992; Li *et al*., 1999; Leveque, 2002; Li *et al*., 2013; Wei & Jia, 2014]. In the FEM, the grid is fixed to the material along the simulation and the track of the material and time-history data is known at grid points. The methods based on FEM, despite the weakness of handling large deformations, are strong in tracking moving boundary and interfaces (Liu & Liu, 2003). Thus, the applications of grid-based Lagrangian methods in computational fluid dynamics, where the deformations are relatively large, are quite limited. Table 6.2 compares different computational aspects of both Eulerian and Lagrangian grid-based methods (adopted from Liu & Liu, 2003).

Table 6.2 – Comparison of Lagrangian & Eulerian methods, (adopted from Liu & Liu, 2003)

	Lagrangian methods	Eulerian methods
Grid	Attached on the moving material	Fixed in the space
Track	Movement of any point on materials	Mass, momentum & energy flux across grid nodes and mesh cell boundary
Time history	Easy to obtain time-history data at a point attached history data at a point on materials	Difficult to obtain time-history data at a point attached history data at a point on materials
Moving boundary & interface	Easy to track	Difficult to track
Irregular geometry	Easy to model	Difficult to model with good accuracy
Large deformation	Difficult to handle	Easy to handle

6.2.3 Meshfree Methods

Applications of grid-based numerical methods are quite limited for complex fluid simulations with large deformations, mainly due to expensive computational time and elaborate mathematical procedures. On the other hand, meshfree (meshless) methods are capable of simulating complex problems with discontinuities and singularities as well as treating large deformations. The difference in meshfree approaches are mainly in the approximation techniques. Table 6.3 summarizes some of the most common meshfree methods.

Table 6.3 – Meshfree methods in chronological order (Liu & Liu, 2003)

Method	Approximation technique	References
Smoothed Particle Hydrodynamics (SPH)	Integral representation	Lucy, 1997; Gingold & Monaghan, 1977, etc.
Finite point method	Finite difference (FD) representation	Liszka & Orkisz, 1980; Onate *et al*., 1996, etc.
Element free Galerkin method (EFG)	Moving least square (MLS) approximation Galerkin method	Belytschko *et al*., 1994, 1996, 1998, etc.
Meshless local Petrov-Galerkin (MLPG) method	MLS approximation Petrov-Galerkin method	Atluri & Zhu, 1998; Atluri & Shen. 2002, etc.
Point interpolation method (PIM)	Point interpolation, Galerkin method	Liu & Gu, 1999, 2001; Gu & Liu 2001;
Meshfree weak-strong form (MWS)	MLS, PIM, collocation plus Petrov-Galerkin	Liu & Gu, 2002; 2003

6.2.4 Meshfree Particle Methods (MPMs)

In meshfree particle method, a set of finite numbers of discrete particles is employed to represent the state and the movement of the system (Liu & Liu, 2003). The MPMs perform numerical simulations of a complex problem with using connectivity of nodes instead of a pre-defined mesh for computational fluid problems. In MPM methods, each particle possesses a set of field variables such as mass, momentum, energy, position, etc., and it can also possess other variables (e.g., vorticity, etc.)

related to a specific problem. Conservation of mass, momentum and energy determine the evolution of the physical system in MPMs. Table 6.4 lists some of the typical MPMs.

Table 6.4 – Meshfree particle methods (adopted from Liu & Liu, 2003)

Method	References
Lattice Boltzmann equation (LBE)	Chen & Doolen, 1998; Qian *et al*., 2000; etc.
Particle-in-Cell (PIC)	Harlow, 1963; 1964; etc.
Marker-and-Cell (MAC)	Harlow, 1964; etc.
Fluid-in-Cell (FLIC)	Gentry *et al*., 1966; etc.
Discrete element method (DEM)	Cundall, 1987; Owen, 1996; etc.
Smoothed particle hydrodynamics (SPH)	Lucy, 1997; Gingold & Monaghan, 1977; etc.

6.3 Smoothed Particle Hydrodynamics

Smoothed particle hydrodynamics (SPH) is a meshfree, Lagrangian, particle method, which was first invented by Lucy (1977) and Gingold & Monaghan (1977) for astrophysical problems. In recent years, SPH has received huge attention from scientists and engineers for modelling free surface flow problems. SPH simulates flow motion by integrating the governing equations of fluid motion on each particle by using the Lagrangian formalism. The SPH method simulates the fluid motion based on discretization of the fluid as a continuum in discrete points (particles), which represent infinitesimal volumes of the fluid and move according to the flow's velocity field (Violeau, 2012). Particles carry individual properties along the fluid that are smoothed in the surrounding volume of each particle.

The SPH method has several advantages over grid-based approaches which make it the method of choice for simulating complex flow motions in the nearshore region. It is simple in form and all of the equations can be derived self-consistently from the basic physical principles. Hence, the complex system is relatively straight-forward to simulate (Liu & Liu, 2003). Compared to Eulerian methods, the Lagrangian nature of SPH means that changes in density and flow morphology could be automatically accounted for without the need for mesh refinement or other complicated procedures (Price, 2004). The adaptive nature of SPH makes the method very efficient as the resolution is concentrated on the regions of high density. As a result, computational effort is not exhausted on the empty region of the computational domain (Price, 2004). In the SPH method, there are no constraints imposed on the geometry of the system and thus, the initial condition could be easily defined and programmed without need of complicated meshing algorithms needed for FEMs. Finally, in the SPH method, including the other physical processes in the simulation, involves simple and unambiguous procedures.

The main drawback of the SPH method is the challenges associated with boundary condition implementation [Monaghan, 1992; Gotoh *et al*., 2001; Liu & Liu, 2003; Price, 2004; etc.]. Penetration of the fluid particles into the boundaries must be avoided with the use of appropriate boundary conditions. Also, the interpolation method used in the SPH method is very simple, hence the SPH model could be significantly affected by particle disorder. In order to overcome the interpolation problem, a gradient corrections method is developed and recommended by Bonet & Lok (1999). An important disadvantage of the SPH method compared to the grid based Eulerian methods is the relatively large computational time needed for a simulation. In recent years, extensive studies have been performed in order to overcome excessive computational times needed for SPH by adopting Graphical Processor Unit (GPU) for parallelizing the computational efforts [Darlymple *et al*., 2010; Dominguez, 2013].

SPH was developed to simulate continuum physics problems without the limitations of conventional FDM. The method was first applied for astrophysical problems [Lucy (1977); Gingold & Monaghan, 1977]. Due to the similarities of collective

movement of particles to the movement of fluid, it is possible to model fluid motion by discretizing the governing equations of the classical Newtonian hydrodynamics (Liu & Liu, 2003). The method has been shown to be robust in simulating fluid dynamics problems [Monaghan & Kocharyan, 1995; Swegle & Attaway, 1995; Monaghan, 1996; Chen *et al*., 1999; Monaghan & Kos, 2000; etc.]. In recent years, the SPH method has received more attention in coastal engineering. Table 6.5 summarizes some of the recent studies in coastal engineering problems using the SPH method.

Table 6.5 – Recent applications of SPH in coastal engineering related problems

Study	Reference
Long waves	Panizzo and Dalrymple (2004); Panizzo *et al*., (2006); Rogers and Dalrymple (2007); Li *et al*. (2012)
Sediment transport	Zou and Dalrymple (2006); Zou (2007)
Two-phase SPH	Colagrossi & Landrini (2003); Cuomo *et al*. (2006); Hu & Adams (2007); Violeau *et al*. (2007); Mokos *et al*. (2015)
Incompressible modelling of wave & run-up	Lo & Shao (2002); Ellero *et al*. (2007); Shao *et al*. (2006); Zheng (2014)
Breaking wave on coastal structures & wave impact	Gomez-Gesteira and Dalrymple (2004); Shao & Gotoh (2004); Lee *et al*. (2006); Crespo *et al*. (2007); Didier *et al*. (2014); Altomare *et al*. (2015)

6.3.1 SPH Method

This section covers the SPH method and formulation. The fundamentals of SPH and the details of the development procedures can be found in Monaghan (1982), Monaghan (1992), Liu & Liu (2003) and Gomez-Gesteria (2012) and Crespo *et al*. (2015).

6.3.1.1 Integral Interpolants

The SPH method is fundamentally based on approximating any function $A(r)$ by an integral interpolants (Eq. 6.2):

$$A(r) = \int A(r')W(r - r', h)dr' \tag{6.2}$$

where $W(r - r', h)$ is the weighting function or kernel and h is the smoothing length of weighting function. Equation 6.2, at interpolation point a can be written in discrete notation as given by equation 6.3:

$$A(r) = \sum_b m_b \frac{A_b}{\rho_b} W(r - r_b, h) \tag{6.3}$$

where m_b and ρ_b denote mass and density, respectively and the particle volume is $V_b = m_b / \rho_b$. The summation is done over all the particles (b) within the region of compact support of the kernel function, fixed by h. For position vector $r = r_a, W_{ab} = W(r_a - r_b, h)$ is the weighting function between two particles a and b. Since the derivative of a function is estimated analytically in the SPH method, the interpolation in the SPH can be obtained by ordinary differentiation without using FDM or creating a computationally expensive mesh (Liu & Liu, 2003). Equation 6.4 is derived based on the integral of equation 6.2 for a functional derivative and applying integration by parts.

$$\nabla A(r) = \sum_b \frac{m_b A_b}{\rho_b} \nabla W_{ab} \tag{6.4}$$

6.3.1.2 Smoothing Kernel (Weighting Function)

The weighting function can hugely affect the performance of SPH models and therefore the choice of smoothing kernel is crucial to satisfy the conditions such as normalization, positivity and compact support (Eq. 6.5).

Normalization	$\int_\Omega W(r - r', h)dr' = 1$		
Positivity	$W(r - r', h) \geq 0$	inside the domain Ω	(6.5)

Compact support $W(r-r',h)=0$ out of the domain Ω

The basic idea is that the kernel function W_{ab} should be decreasing monotonically with an increase in distance from particle a (Monaghan, 1992; Liu, 2003). As a result, the smoothing kernel should have a delta function behaviour as the smoothing length, h, tends to zero (Eq. 6.6).

$$\text{Delta function} \quad \lim_{h\to 0} W(r-r',h)dr = \delta(r-r') \qquad (6.6)$$

$$\text{Monotonically decreasing behaviour of } W(r-r',h)$$

Kernels depend on the non-dimensional distance between particles, q ($q=r/h$), r is the distance between particle a and b and the smoothing length, h. Smoothing length governs the size of the area around each individual particle where contribution of the rest of the particles cannot be neglected. Figure 6.2 is a definition sketch of the influence domain in SPH methods. The support domain is a circle with the radius of κh, where κ is a constant related to the smoothing function for a point at r and defines the effective area of the smoothing function.

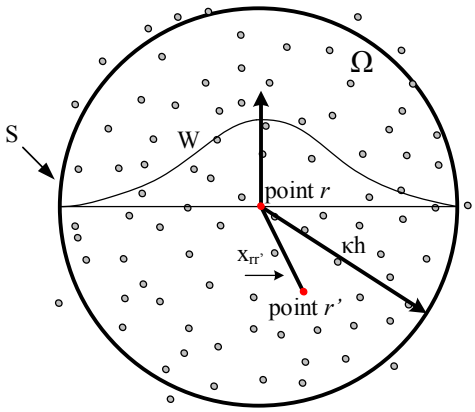

Figure 6.2 – Sketch of the influence domain in SPH model.

The smoothing function is very important in SPH, as it determines the approximation patterns and effective support domain of particles. Several kernel approximations are

proposed and tested for SPH [Monaghan, 1992; Johnson *et al*., 1996; Liu & Liu, 2003; Monaghan, 2005; etc.]. Table 6.6 summarizes the most popular kernel options widely used for SPH models.

Table 6.6 – Summary of kernel options in the SPH and their formulations

Kernel type	Formula		2D	3D
Gaussian	$W(r,h)=\alpha_D.\exp(-q^2)$	$0\le q\le 2$	$\alpha_D=\frac{1}{\pi.h^2}$	$\alpha_D=\frac{1}{\pi^{3/2}.h^3}$
Quadratic	$W(r,h)=\alpha_D.[\frac{3}{16}q^2-\frac{3}{4}q+\frac{3}{4}]$	$0\le q\le 2$	$\alpha_D=\frac{2}{\pi.h^2}$	$\alpha_D=\frac{5}{4\pi.h^3}$
Cubic Spline	$W(r,h)=\alpha_D.\begin{cases}1-\frac{3}{2}q^2-\frac{3}{4}q^3 \\ \frac{1}{4}(2-q)^3 \\ 0\end{cases}$	$0\le q\le 1$ $1\le q\le 2$ $q\ge 2$	$\alpha_D=\frac{10}{7\pi.h^2}$	$\alpha_D=\frac{1}{\pi.h^3}$
Quintic	$W(r,h)=\alpha_D.(1-\frac{q}{2})^4(2q+1)$	$0\le q\le 2$	$\alpha_D=\frac{7}{4\pi.h^2}$	$\alpha_D=\frac{7}{8\pi.h^3}$

The cubic spline function [Monaghan & Lattanzio, 1985] is similar to a Gaussian function. However, it has a narrower compact support and therefore reduces the numerical computation time, giving rise to more advantages over Gaussian kernel options. The cubic spline function has been employed in many studies as a smoothing function due to the simplicity, accuracy and computational time.

In this study, the Quintic kernel function (Wendland, 1995) has been employed for developing the SPH hydrodynamic model. The Quintic kernel function has been shown to have the best trade-off between computational cost and accuracy of model [Panizzo *et al*. 2007; Crespo, 2006; Gomez-Gesteria, 2012]. In terms of accuracy, the higher order of kernel results in a greater accuracy for the SPH scheme.

6.3.1.3 Governing Equations

The basic governing equations of fluid dynamics are based on the fundamental physical laws of conservation, including the conservation of mass, momentum and energy. In SPH, the governing equations of fluid motion are derived based on these conservation laws in Lagrangian formalism. Table 6.7 shows the conservation equations in Lagrangian form. More information on discretization procedures can be found at Monaghan (1982), Monaghan (1989) and Monaghan (1992).

Table 6.7 – SPH formulation for conservation laws of fluid motion

Conservation law	Formula	SPH formulation
Continuity	$\frac{d\rho}{dt} + \rho(\nabla . v) = 0$	$\frac{d\rho_a}{dt} = \sum_b m_b v_{ab} \nabla_a W_{ab}$
Momentum	$\frac{Dv}{Dt} = -\frac{1}{\rho}\nabla P + g + v_0 \nabla^2 v + \frac{1}{\rho}\nabla \bar{\tau}$	$\frac{dv_a}{dt} = -\sum_b m_b (\frac{P_a}{\rho_a^2} + \frac{P_b}{\rho_b^2} + \frac{\tau_a}{\rho_a^2} + \frac{\tau_a}{\rho_b^2}) \nabla_a W_{ab}$ $+ \sum_b m_b (\frac{4 v_0 r_{ab} \nabla_a W_{ab}}{(\rho_a + \rho_b)\lvert r_{ab} \rvert^2}) v_{ab} + g$
Energy		$\frac{de_a}{dt} = \frac{1}{2} \sum_b m_b (\frac{P_a}{\rho_a^2} + \frac{P_b}{\rho_b^2} + \Pi_{ab}) v_{ab} \nabla_a W_{ab}$

6.3.2 Weakly Compressible SPH (WCSPH) Approach

Commonly, SPH models enforce incompressibility of fluid in their governing equations which are based on Poisson equation and result in time-consuming solver and computationally expensive models. In this study, the SPH model used Tait's equation of state with a high speed of sound for modelling the free surface flow in the nearshore region which results in weakly compressible formulation with small density fluctuations [Monaghan, 1994].

Equation of State

Considering WCSPH formalism, an equation of state for determining the fluid pressure is needed. Monaghan (1994) methodology for the relation between pressure and density, known as Tait's equation of state (Eq. 6.7), is implemented in this research.

$$P = B[(\frac{\rho}{\rho_0})^{\gamma} - 1] \tag{6.7}$$

where ρ_0 is the reference density, taken as water density at free surface (=1000 kg/m^3), B is constant related to the bulk modulus of elasticity of fluid and γ is the polytrophic constant varying between 1 and 7 (usually 7 for water). Equation 6.7 indicates that pressure at the surface is always zero.

Weakly compressible approaches permit a speed of sound (c). The speed of sound is given by square root of the derivatives of equation of state (Eq. 6.7) with respect to density (ρ):

$$c^2(\rho) = \frac{\partial P}{\partial \rho} = \frac{B\gamma}{\rho_0}(\frac{\rho}{\rho_0})^{\gamma-1} = \frac{B\gamma}{\rho_0{}^{\gamma}}\rho^{\gamma-1} \tag{6.8}$$

$$c_0{}^2 = c^2(\rho_0) = \frac{\partial P}{\partial \rho_{\rho=\rho_0}} = \frac{B\gamma}{\rho_0} \tag{6.9}$$

where c_0 denotes the speed of sound for the reference density (at free surface). The constant B is equal to $c_0{}^2\rho_0/\gamma$ and it is a limit for the maximum change in the fluid particle's density.

6.4 The SPH Model Implementations

A brief introduction to the SPH method and the governing equations was discussed in §6.3. In this section, the SPH model implementations and the methods used to develop the model are discussed. The hydrodynamics of flow across the nearshore was modelled with the SPH for the same wave conditions generated experimentally in chapters 4 and 5. Hence, the numerical domain consists of a wave flume with 1:20 beach slope and the flume is equipped with a piston type numerical wave-maker (Fig. 6.3).

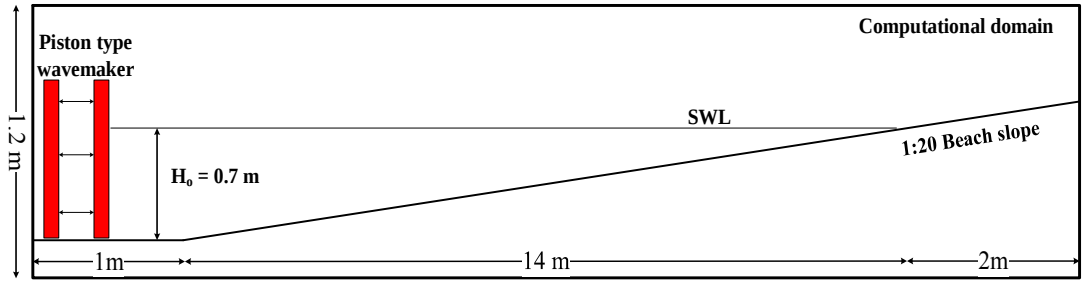

Figure 6.3 – Sketch of computational domain

Table 6.8 presents the hydrodynamic conditions simulated with the SPH model.

Table 6.8 – Simulation test cases for the SPH model

Condition	Offshore wave height (H_0) [m]	Wave frequency (f) [1/s]	Wave steepness (S_{op}) [%]
1	0.12	0.833	5
2	0.12	0.540	3½
3	0.12	0.344	2

This study employed advanced parallelization techniques with use of Graphical Processing Unit (GPU) to reduce the computational costs using Crespo *et al*. (2011) WCSPH computational technique. The numerical algorithm of SPH model developed here used CUDA (Compute Unified Device Architecture) platform for parallelizing the code on GPU. A GTX680-DC2-2GD5 GPU with 1536 CUDA core

was used for simulating the test cases (Table 6.8). The parallel architecture of GPU reduces computational time of SPH as a fully explicit Lagrangian method and therefore allows larger number of particles to be simulated up to two orders of magnitude faster than CPUs (Crespo *et al*., 2011).

The conservation laws and the basics of SPH models have been described in previous sections (§6.3). In order to improve the numerical accuracy, several techniques are employed within the SPH numerical model. The following sections (§ 6.4.1 - § 6.4.7) briefly describe the numerical schemes adopted for running the SPH code in this study.

6.4.1 Density Re-Initialization Method

In the SPH method, despite the realistic simulations, the particles exhibit large pressure oscillations [Monaghan, 1992; Liu & Liu, 2003; Crespo, 2008]. A number of studies have been performed to overcome this problem. Colagrossi & Landarini (2003) proposed a simple and computationally inexpensive approach to deal with pressure oscillations. Their methods include performing a filter over the density of particles and then correcting the particles density by re-assigning a density to each particle. There are two orders of corrections, zeroth order (Shepard filter) [Panizzo, 2004] and first order (Moving Least Squares) [Dilts, 1999; Colagrossi & Landarini, 2003; Panizzo, 2004].

In this study, the Moving Least Squares (MLS) approach is adopted for density correction. MLS is a first order correction and hence the variation of the linear density field can be exactly reproduced (Panizzo, 2004). Equation 6.10 shows the average density of particle *a* using MLS approach. Consequently, the corrected kernel is evaluated according to equation 6.11.

$$\bar{\rho}_a = \sum_b \rho_b W_{ab}^{MLS} \frac{m_b}{\rho_b} = \sum_b m_b W_{ab}^{MLS} \tag{6.10}$$

$$W_{ab}^{MLS} = W_b^{MLS}(r_a) = \beta(r_a).(r_a - r_b) W_{ab}^{MLS} \tag{6.11}$$

where the correction vector β for a two dimensional model is defined as:

$$\beta(r_a) = \begin{pmatrix} \beta_0 \\ \beta_{1x} \\ \beta_{1z} \end{pmatrix} = A^{-1} \begin{pmatrix} 1 \\ 0 \\ 0 \end{pmatrix} \tag{6.12}$$

and A is defined by equation 6.13 as:

$$A = \sum_b W_b(r_a) \tilde{A} \frac{m_b}{\rho_b} = \sum_b m_b W_{ab}^{MLS}$$

$$\tilde{A} = \begin{bmatrix} 1 & (x_a - x_b) & (z_a - z_b) \\ (x_a - x_b) & (x_a - x_b)^2 & (z_a - z_b)(x_a - x_b) \\ (z_a - z_b) & (z_a - z_b)(x_a - x_b) & (z_a - z_b)^2 \end{bmatrix} \tag{6.13}$$

The equations for three dimensions are similar but include the y direction. In this work the MLS kernel correction technique is applied every 30 time-steps to obtain more regular density distribution.

6.4.2 Kernel Re-Normalization

The computational domain of the SPH model developed for this work consists of free surface flow which is bounded by solid boundaries (Fig. 6.3). The particle's smoothing function near the free surface and the boundaries will truncate due to the absence of neighbouring particles. Therefore, a periodic kernel function correction is vital to achieve computational accuracy.

Several studies have been performed to tackle the problems associated with failing consistency of the kernel smoothing function, W [Randles & Libersky, 1996; Bonet & Lok, 1999; Bonet & Kulasegaram, 2000; etc.]. A kernel correction technique was proposed by Li and Liu (1996) to solve the kernel truncation error by correctly interpolating the polynomial function. The method was developed further by Bonet and Lok (1999), in which the gradient of kernel function was modified. Some studies also adopted the combination of these two techniques where the kernel correction is obtained by combining the gradient correction and constant kernel correction.

Kernel gradient correction technique (Bonet and Lok, 1999) has been adopted in this study to simulate the free surface flow in the nearshore region. Adopting the kernel gradient correction technique improves the evaluation model of the velocity field gradient. In order to correct the kernel, a correction matrix L is implemented in the model as follow (Eqs. 6.14 to 6.16):

$$\widetilde{\nabla} W_b(r_a) = L_a \nabla W_b(r_a) \tag{6.14}$$

where the kernel gradient must satisfy equation 6.14.

$$\sum_{b=1}^{N} \frac{m_b}{\rho_b}(r_b - r_a) \otimes \nabla W_b(r_a) = (\sum_{b=1}^{N} \frac{m_b}{\rho_b}(r_b - r_a) \otimes \nabla W_b(r_a)) L_a^T = I \tag{6.15}$$

Thus, L can be determined as:

$$L_a = (\sum_{b=1}^{N} \frac{m_b}{\rho_b} \nabla W_b(r_a) \otimes (r_b - r_a))^{-1} \tag{6.16}$$

Employing the density re-initialization and kernel re-normalization leads to an increase in the number of computations per time-step and therefore the model will be computationally more expensive.

6.4.3 Time – Stepping Algorithm

The solution of governing equations of free surface flow in Lagrangian formalism of SPH can be obtained in time with several methods. The literature indicates the need for at least a second order accurate scheme in time [Monaghan, 1989; Liu & Liu, 2003; Crespo *et al*., 2011]. Amongst the various time integrating schemes available for the SPH method, the predictor corrector algorithms proposed by Monaghan (1989), Beeman algorithm [Beeman, 1976], Verlet algorithm [Verlet, 1967] and Symplectic [Leimkhuler *et al*., 1996] are the most commonly used algorithms.

In this study, Symplectic scheme (Eq. 6.17) is employed for the time integration. In Symplectic method, the values of density and acceleration are computed initially at the middle of time-step (Monaghan, 2005). The method could preserve geometric

features which results in a better resolution for the long term solution behaviour (Crespo *et al*., 2015).

$$\begin{aligned} \rho_a^{n+\frac{1}{2}} &= \rho_a^n + \frac{\Delta t}{2}\frac{d\rho_a^n}{dt} \\ \underline{r}_a^{n+\frac{1}{2}} &= \underline{r}_a^n + \frac{\Delta t}{2}\frac{d\underline{r}_a^n}{dt} \end{aligned} \tag{6.17}$$

The subscript n represents time step and $t = n\Delta t$. Pressure is calculated for each particle at half a time-step using the equation of state. Then, $d(\omega_i \rho_i \underline{v}_i)^{n+\frac{1}{2}} / dt$ gives the velocity and therefore the position of the particles at the end of each time step is calculated by equation 6.18:

$$\begin{aligned} (\omega_a \rho_a \underline{v}_a)^{n+1} &= (\omega_a \rho_a \underline{v}_a)^{n+\frac{1}{2}} + \frac{\Delta t}{2}\frac{d(\omega_a \rho_a \underline{v}_a)^{n+\frac{1}{2}}}{dt} \\ \underline{r}_a^{n+1} &= \underline{r}_a^{n+\frac{1}{2}} + \frac{\Delta t}{2}\underline{v}_a^{n+1} \end{aligned} \tag{6.18}$$

The model will calculate $d\rho_a^{n+1} / dt$ at the end of each time step using the updated values of $\underline{r}_a^{n+1}$ and $\underline{v}_a^{n+1}$.

The SPH model has been set to run the hydrodynamic simulations for 25 consecutive waves in this study. The model was set to generate and save the output for every 0.01 second.

6.4.4 Computational Efficiency

To achieve computational efficiency, the method proposed by Monaghan and Lattanzio (1985) is employed. In this method the computational domain is divided into cells with a side length of *2h* and for a particle located inside a cell, only the interaction with the neighbouring cells are computed. Figure 6.4 illustrates a sketch of neighbouring cells in a two dimensional domain.

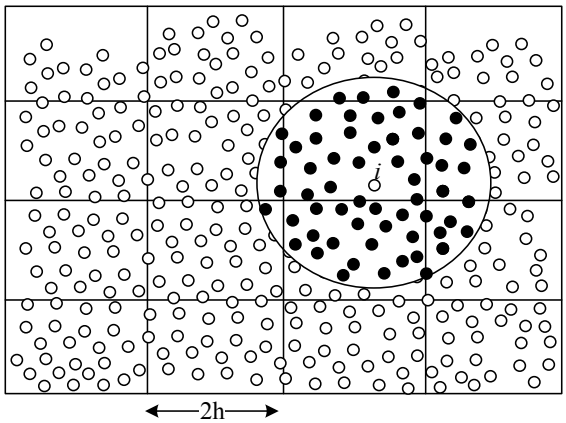

Figure 6.4 – Neighbouring particles in two dimensional domain. Particle *i* only interacts with the particles marked in black

By adopting Monaghan and Lattanzio (1985) method, the number of computations per time step reduces significantly from N_p^2 operations to $N_p.\log N_p$ (N_p is the number of particles).

6.4.5 Initial Conditions

For all three test cases considered in this work (Table 6.8), the initial velocity of fluid particles is considered to be zero. The initial density (ρ_0) of particles are assigned according to their hydrostatics pressure. Fluid particles are defined initially in a fixed position in the computational domain, using staggered grid (Monaghan & Lattanzio, 1991). This method is adopted due to the higher number of neighbouring particles being generated for each particle.

6.4.6 Boundary Conditions

The SPH method was originally developed for tackling astrophysical problems which do not consider boundaries. In coastal engineering applications, the main drawback of SPH method is the problem of particle deficiency near or on the boundary. The particle deficiency is in facet the result of the integral truncation by the boundary [Crespo *et al*., 2007]. For those particles near or on the boundary, only particles inside the boundary contribute to the summation of the particle interaction and there is no contribution from outside, as there are no particles beyond the

boundary. Due to this one-sided contribution of particles, SPH could not produce correct solutions near boundaries. Although the velocity is zero on the solid surfaces, other field variables (e.g. density) are not necessarily zero. Several studies carried out with the aim of improving SPH boundary conditions. Monaghan (1994) and Liu *et al*. (2001 & 2002) used ghost or virtual particles on the solid boundaries to produce a highly repulsive force to the particles near the boundary. Ghost particle method prevents the fluid particles from penetrating through the boundary.

Repulsive boundary condition is first introduced by Monaghan (1994) based on the assumption that particles, which forms the boundary, exert a central force on the fluid particles. Monaghan & Kos (1999) and Rogers & Darlymple (2007) further developed the repulsive boundary condition and adjust the magnitude of the force according to the local water depth and the velocity of the fluid particles normal to boundary.

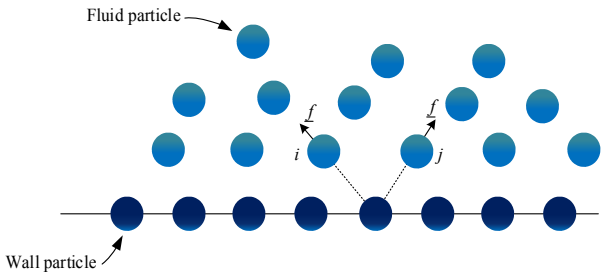

Figure 6.5 – Sketch of particle arrangement in wall boundary condition and the repulsive force between fluid and boundary particles

Dynamic boundary conditions is proposed by Darlymple and Knio (2001) and further developed by Crespo *et al*. (2007). In this method, boundary particles are forced to satisfy the same equations as fluid particles. Therefore, boundary particles must follow the continuity, momentum and energy equations as well as equation of state. However, they do not move and remain fixed in their initial place. In dynamic boundary condition, the boundary particles are organized in a staggered manner. Figure 6.6 illustrates the sketch of interaction between fluid and boundary particles in dynamic boundary condition.

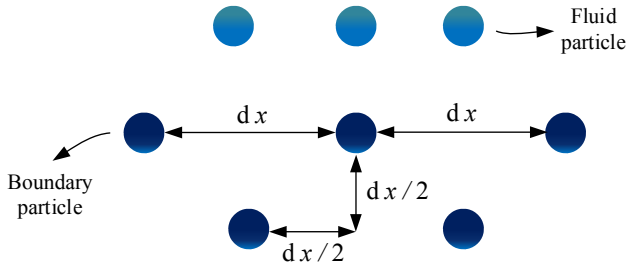

Figure 6.6 – Two dimensional sketch of interaction between fluid and boundary particles

In this study, the dynamic boundary condition (Crespo *et al.*, 2007) was implemented.

6.4.7 Numerical Wave Generator

The SPH model developed here produced long-crested monochromatic waves in the computational domain. In order to prevent the generation of spurious secondary waves, a second order wave-maker theory based on Madsen (1971) methodology was implemented.

Following Madsen (1971) theory, the piston stroke S_0 is defined based on equation 6.19:

$$\frac{H}{S_0} = \psi$$
$$\text{and } \psi = \frac{2\sinh^2(kd)}{\sinh(kd)\cosh(kd) + kd} \tag{6.19}$$

The piston movement is given by equation 6.20:

$$e(t) = \frac{S_0}{2}\sin(\omega t + \delta) + [(\frac{H^2}{32d}).(\frac{3\cosh(kd)}{\sinh^3(kd)}) - \frac{2}{\psi}]\sin(s\omega t + 2\delta) \tag{6.20}$$

Table 6.9 summarizes the numerical techniques implemented in the SPH code. More detailed descriptions, equations and references regarding SPH model employed for this study can be found in Gomez-Gesteira *et al*. (2012a, 2012b).

Table 6.9 – Summary of the numerical technique implemented for the SPH simulations

SPH model	Method	Reference
Compressibility	Weakly compressible (WCSPH) using Tait's equation of state	Monaghan (1994)
Kernel function	Quintic kernel function	Wendland (1995)
Time integration Scheme	Symplectic scheme	Monaghan (2005)
Density treatment	Delta-SPH formulation	Molteni & Colagrossi (2009)
Viscosity treatments	Laminar viscosity + SPS turbulence model	Darlymple & Rogers (2006)
Boundary conditions	Dynamic boundary condition	Crespo *et al*. (2007)
Implementation	Graphical Processor Unit (GPU)	Crespo *et al*. (2011)

6.5 Numerical Results

In this section, the hydrodynamic results obtained from the SPH model is presented. Three monochromatic wave conditions have been simulated by the SPH model (Table 6.8) to generate similar conditions as PIV and LDV measurements. The computational domain is created according to figure 6.3 and a numerical paddle type wave-maker is defined to produce shore-normal, regular long-crested waves. The developed model was initially tested with 500k particles in the computational domain. The free surface profile from the SPH simulations was compared against the experimental wave gauge from the PIV experiments. The results show that in all three test cases, the SPH model slightly overestimated the wave height elevation inside the surfzone as well as in the non-breaking region. However, at the breaking

region, the SPH model underestimated the wave height. The kinematics of incipient wave breaking region and the inner surfzone were investigated with the numerical model to elucidate the intense shear mechanism in the breaker region and the development and propagation of the turbulent bore inside the surfzone.

Upon the successful simulation of the initial SPH model and the validation against the experimental data, the final model was run for a fine resolution (~1M particles). The wave breaking location was well predicted by the finer resolution model. The trend of wave height evolution using SPH shows only insignificant deviations from the experimental data described in chapter 4. However, some discrepancies were observed in the numerical model in the region of plunger. The following section presents the result of SPH simulations.

6.5.1 Hydrodynamic Results of SPH Simulations

Monochromatic waves with H_o = 0.12m and T = 1.2sec

The SPH model described in the previous section (§ 6.4) is employed to simulate the wave hydrodynamics on a 1:20 beach profile (Fig. 6.3). The numerical model was set to run 25 monochromatic waves with an offshore wave height of 0.12m and period of 1.2sec. Figure 6.7 portrays a sequence of instantaneous SPH results for a fine particle resolution. The colour scale refers to the three dimensional Lagrangian velocity magnitudes $|u| = \sqrt{(u^2 + v^2 + w^2)}$ discretised in SPH particles form. The values of velocity magnitude ($|u|$) at the propagating crest of the breaking waves and the turbulent bore fronts are shown to reach the maximum value.

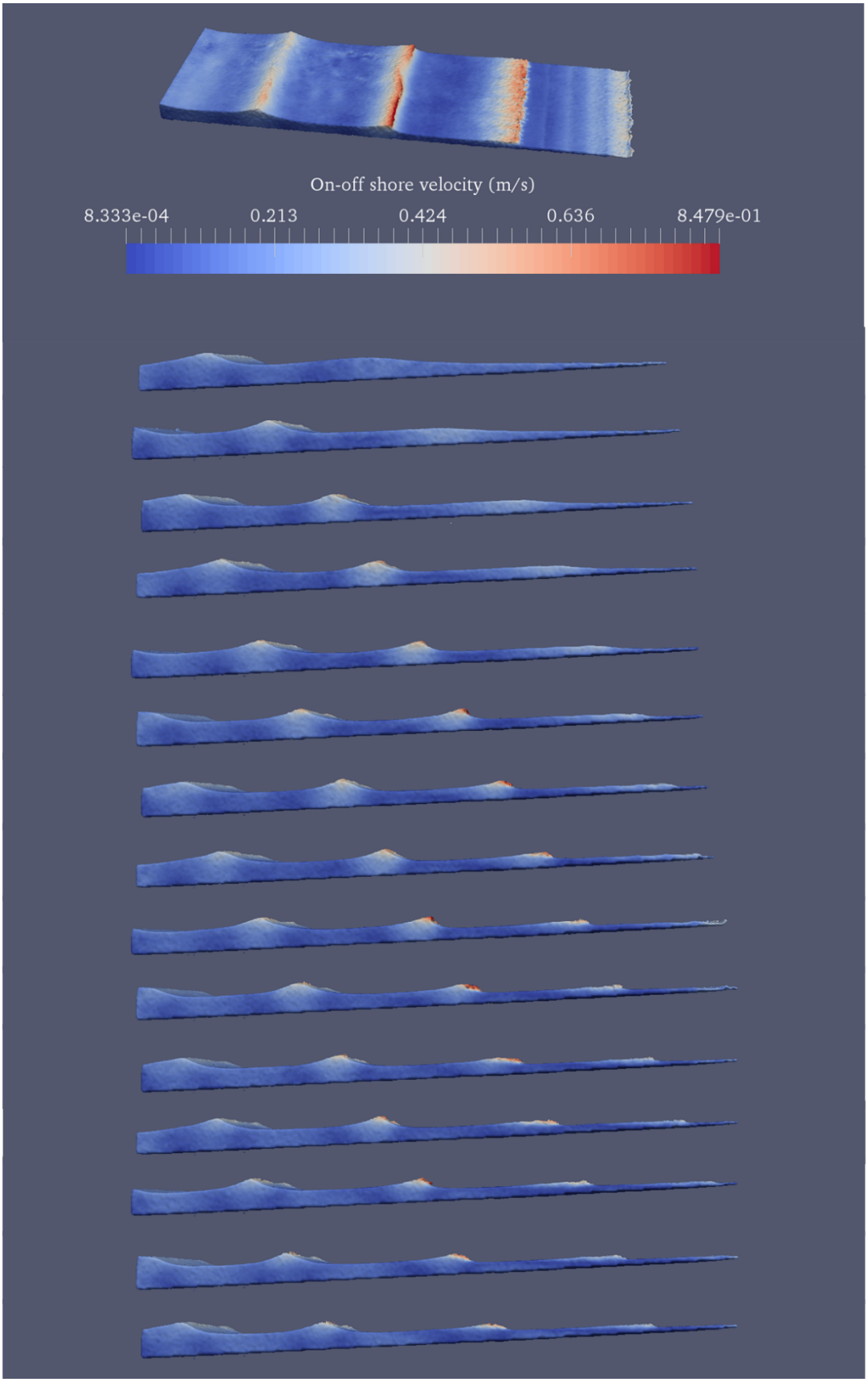

Figure 6.7 – Snapshots of SPH output for the case of monochromatic waves of H_o = 0.12m and T = 1.2sec

In order to analyse the hydrodynamic results obtained from the SPH simulation, the velocity profiles at five locations across the surfzone and seaward of the breaking region [$y = \{1, 2, 3, 4 \& 5\}$m] were extracted and investigated. A numerical algorithm was developed to calculate the temporal-averaged velocity profiles using a windowing technique over the depth of water column at every desired location. The windows were all similar in size and had square shape. The averaged velocity for each of these windows was calculated by averaging the velocity of all particles within the measurement box (window) per time-step. The total temporal averaged velocity for each window is obtained by averaging the mean velocity over the total simulation time. Figure 6.8 illustrates the windowing technique adopted for determining the velocity profiles from the SPH results. For the windows located near the free water surface profile, a portion of the computing cell was empty during a wave cycle due to the wave activities, resulting in SWL changes. To prevent biasing the results of temporal averaging, the 'NaN' velocity values were not considered for the averaging.

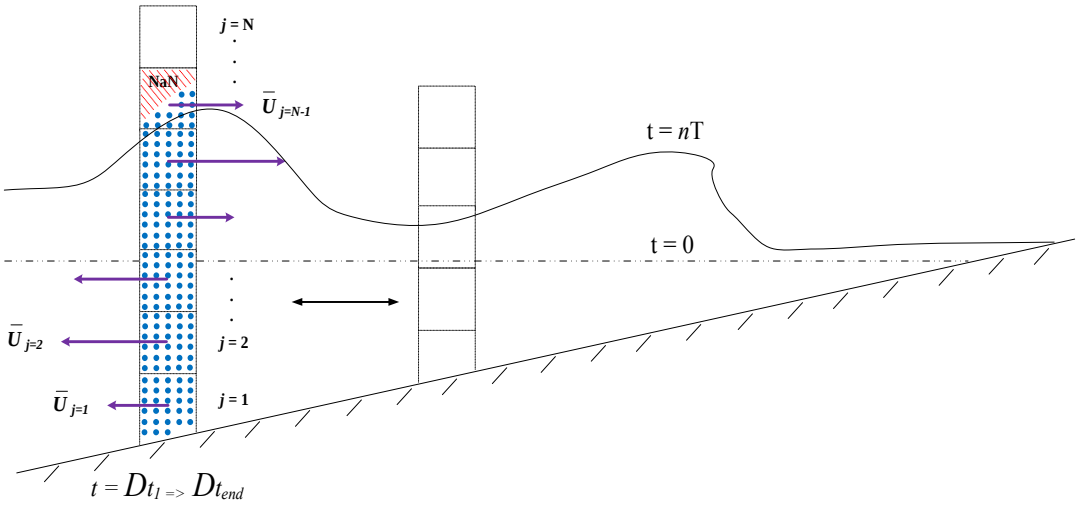

Figure 6.8 – Schematic illustration of temporal averaged velocity profiles from SPH output

The temporal averaged velocity profiles for SPH results of regular waves of 5% steepness have been calculated for five locations across the nearshore as presented in figure 6.9.

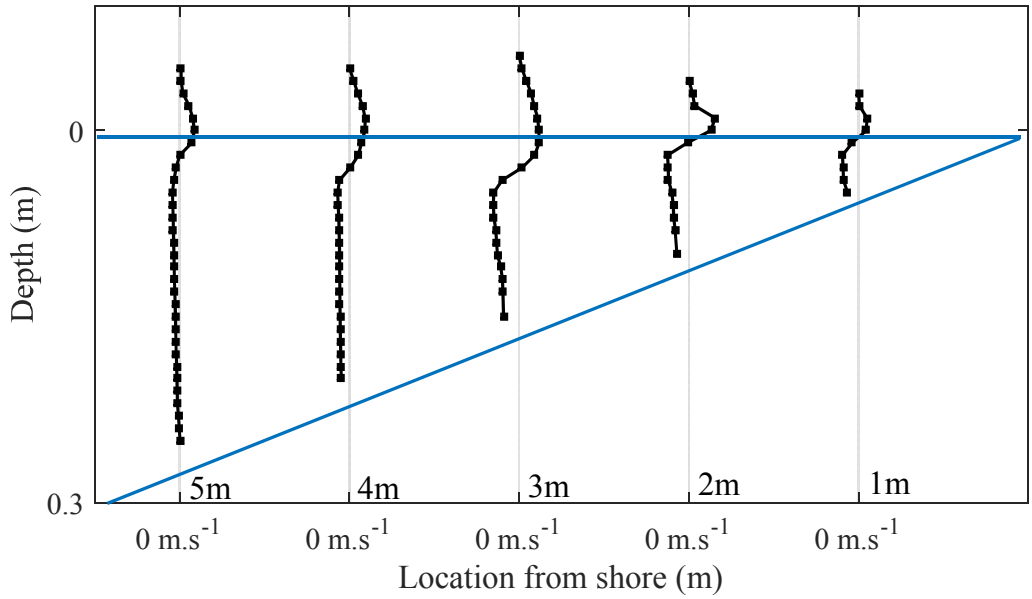

Figure 6.9 – Temporal-averaged on-offshore velocity profiles from SPH simulation for the waves of S_{op} = 5% at y = {1, 2, 3, 4 & 5}m

Monochromatic waves with H_o = 0.12m and T = 1.85sec

The SPH model described and developed in this chapter has been employed to simulate the hydrodynamics of monochromatic waves with an offshore steepness of 3½%. The numerical model was set to simulate 25 consecutive monochromatic waves with an offshore wave height of 0.12m and period of 1.85sec. Figure 6.10 represents the snapshot of numerical simulation.

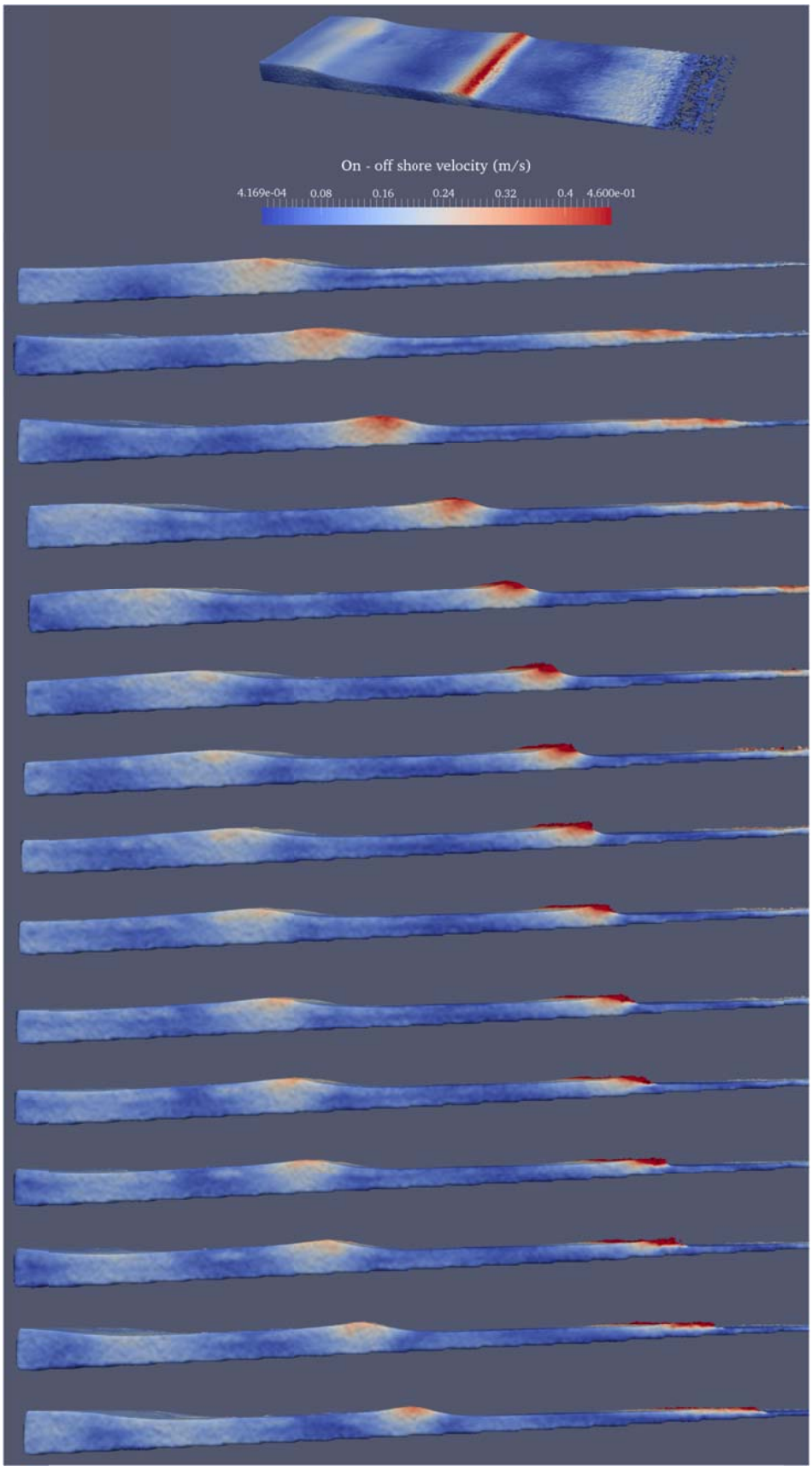

Figure 6.10 – Snapshots of SPH model output for simulation of monochromatic waves with H_0 = 0.12m and T = 1.85sec, colour scale correspond to velocity

Figure 6.10 demonstrates the nearshore wave propagation, shoaling and breaking for the monochromatic waves of 3½ % steepness, simulated by SPH model. The comparison between the hydrodynamics of the SPH model and the LDA data (§4.3.1) was satisfactory (Fig. 6.16b).

The temporal averaged on-offshore velocity profiles were determined from the SPH simulations for this case, and for five on-offshore locations with 1m intervals from SWL. The same windowing technique as described in figure 6.8 was adopted to extract temporal averaged velocities. Figure 6.11 represents the temporal averaged velocity profiles for S_{op} = 3½ %.

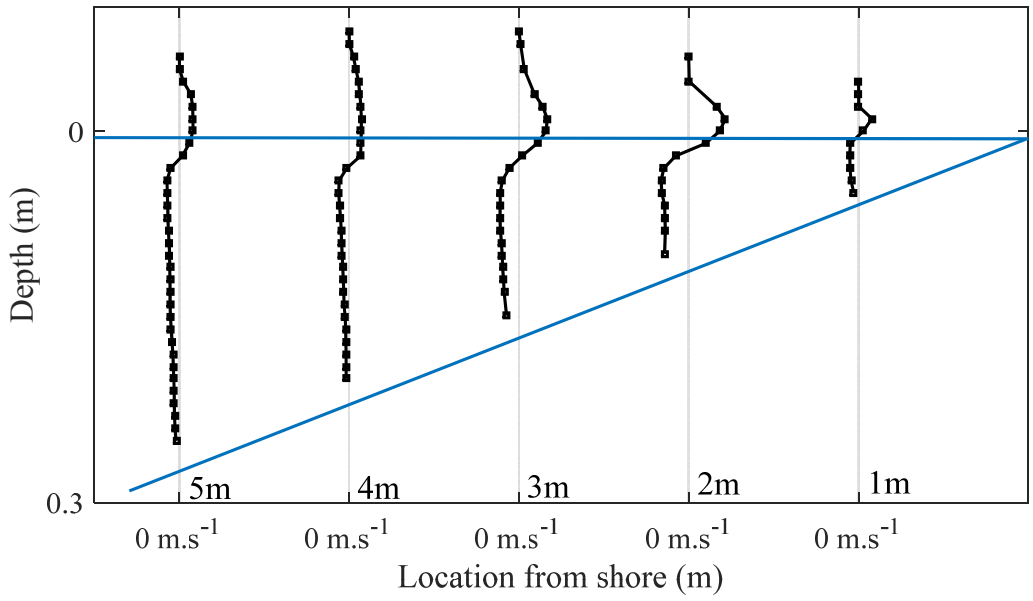

Figure 6.11 – Temporal-averaged on-offshore velocity profiles from SPH simulation for waves of S_{op} = 3½ % at y = {1, 2, 3, 4 & 5}m

Monochromatic waves with H_o = 0.12m and T = 2.9sec

The hydrodynamic results of numerical modelling with SPH for regular waves of 2% steepness is presented in this section. The numerical model was set to simulate 25 consecutive monochromatic waves with an offshore wave height of 0.12m and period of 2.9sec. Figure 6.12 shows the snapshot of the SPH numerical simulation.

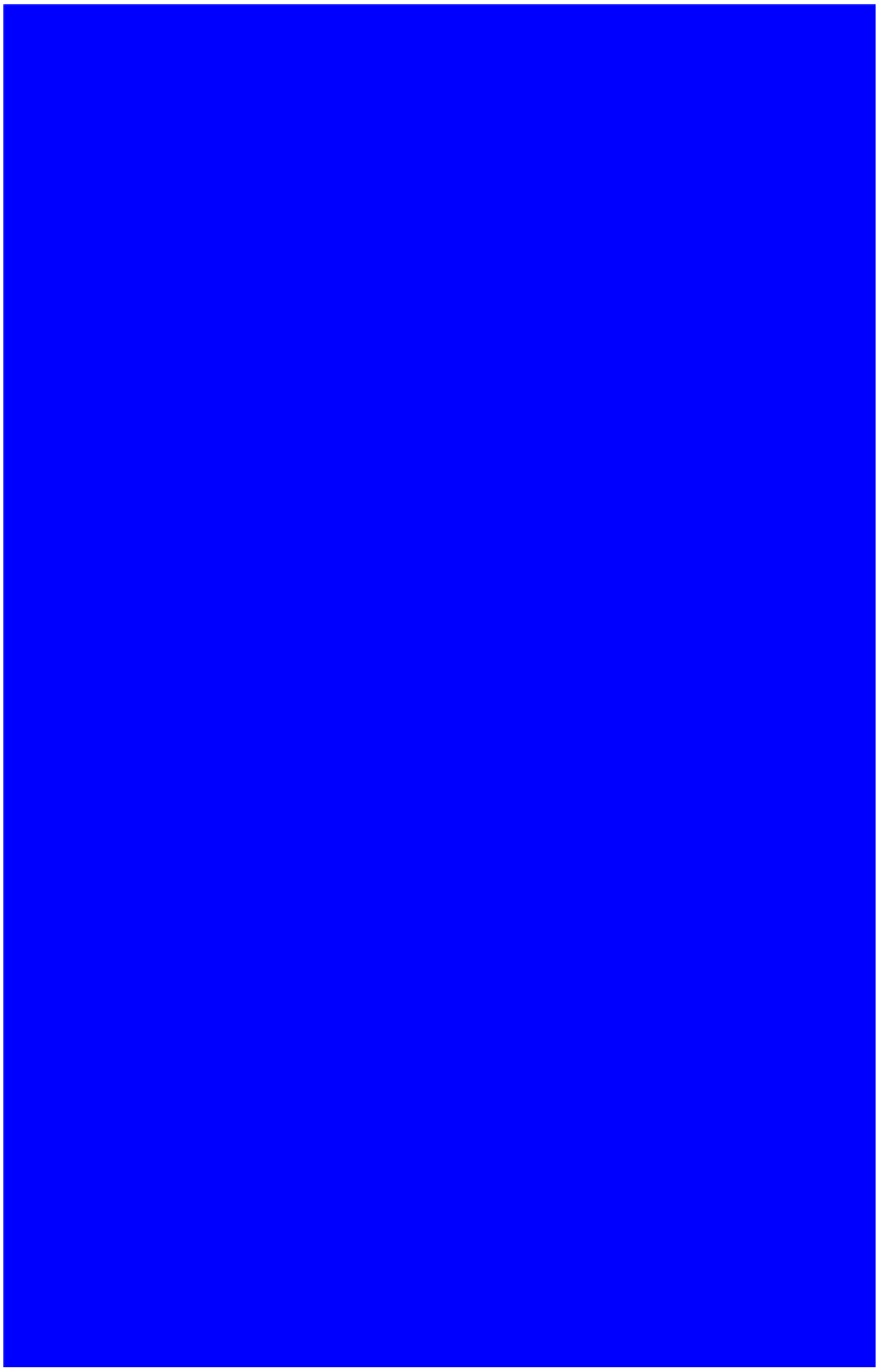

Figure 6.12 – Snapshots of SPH model output for simulation of monochromatic waves with H_0 = 0.12m and T = 2.9sec, colour scale correspond to velocity

Figure 6.12 depicts wave generation, shoaling and breaking processes simulated with SPH numerical model for the case of 2% wave steepness. The temporal averaged on-offshore velocity profiles were calculated for this test case following the methodology described in Figure 6.8.

Figure 6.13 represents the temporal averaged velocity profiles for monochromatic waves with S_{op} = 2 % for five locations inside the surfzone and seaward of the breaking region.

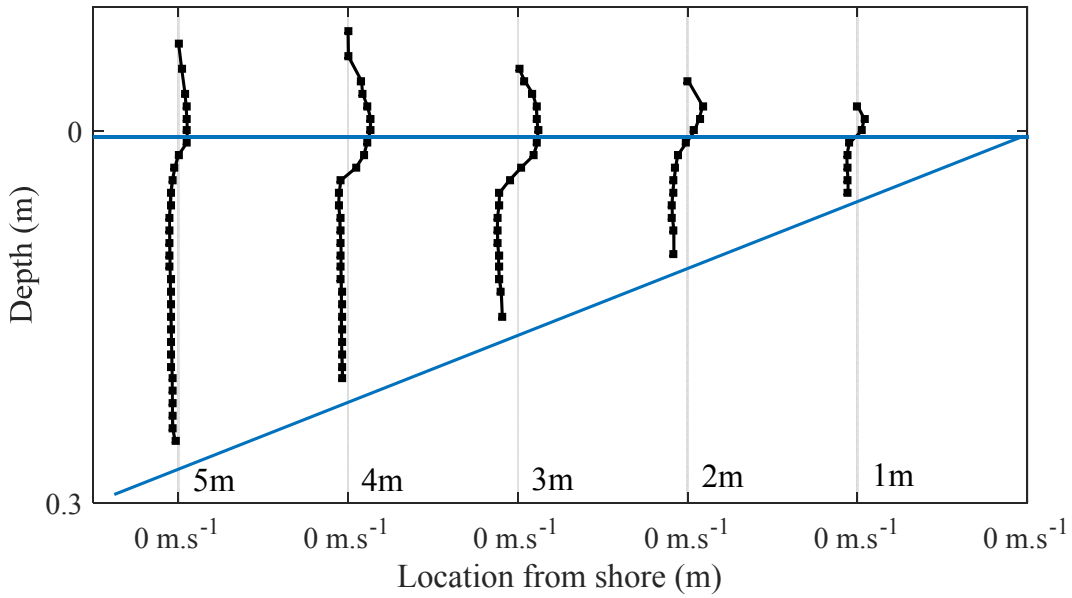

Figure 6.13 – Temporal-averaged on-offshore velocity profiles from SPH simulation for waves of S_{op} = 2 % at y = {1, 2, 3, 4 & 5}m

In this section, the hydrodynamics obtained from the SPH numerical model for the regular wave breaking on a mild impermeable slope was presented for similar conditions as for the PIV and LDA experiments. The results of the numerical model have shown that refined-resolution SPH is capable of reproducing the wave breaking process and the subsequent surfzone dynamics. Very good agreement was achieved between the numerical model and experimental data in terms of wave height profile across the nearshore and the velocity profiles. Figure 6.14 presents the comparison between on-offshore temporal averaged velocity profiles predicted by the developed SPH model and the LDA measurements in the DHI study (§4.3.1).

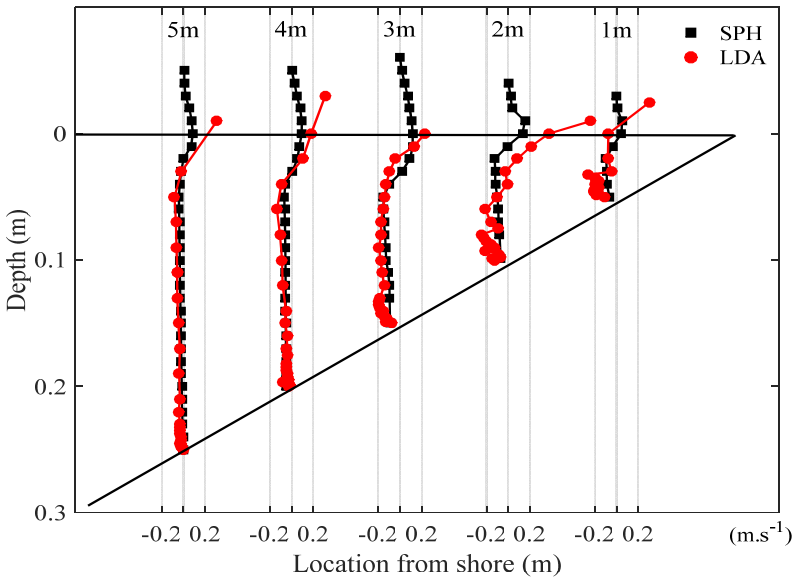
5m
4m
3m
2m
1m
SPH
LDA
0
0.1
0.2
0.3
Depth (m)
-0.2 0.2
(m.s-1)
Location from shore (m)

(a)

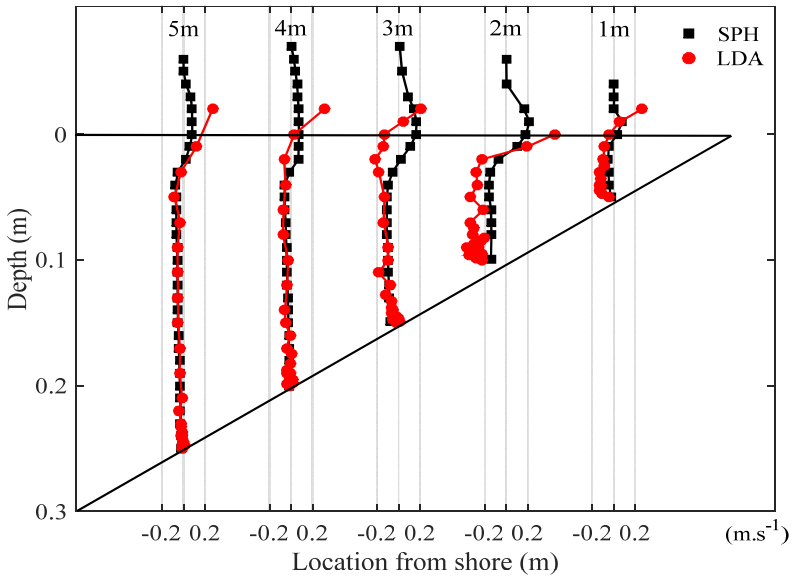
5m
4m
3m
2m
1m
SPH
LDA
0
0.1
0.2
0.3
Depth (m)
-0.2 0.2
(m.s-1)
Location from shore (m)

(b)

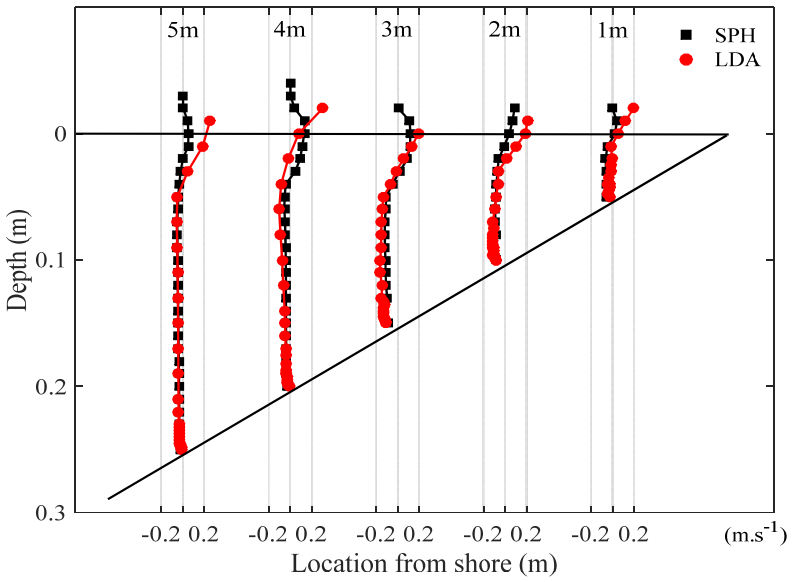

(c)

Figure 6.14 – Comparison between on-offshore temporal-averaged velocity profiles of the SPH model and the LDA measurements for monochromatic waves of a) S_{op}=5%, b) S_{op}=3½ % and c) S_{op}= 2%

Figure 6.14 compares the hydrodynamics obtained from the developed SPH model in this study, to the LDA measurements performed in the DHI experiments. The results confirm that good agreement exists between the numerical model and DHI experimental data.

6.6 Application of the SPH Hydrodynamics in Nearshore Mixing

Wave kinematics and the hydrodynamics obtained from SPH simulations are utilized to investigate the mixing coefficient in the nearshore region with using the *N*-zone model (described in §3.4.2).

The mixing coefficient was determined for five locations (y={1,2,3,4,5}m) across the nearshore with use of the SPH model hydrodynamics and depth-averaged theoretical diffusivity proposed by Svendsen and Putrevu (1994) [Eq. 2.69 and 2.73].

$$\nu_t = Md\sqrt{gd} \tag{2.69}$$

$$\nu_t = (0.8(d/d_b)^{-4} + 0.2)\nu_{tb} \tag{2.73}$$

A constant value of $M=0.03$ in equation 2.69 was adopted for the numerical analysis. For each on-offshore location across the nearshore, the temporal variations of flow hydrodynamics from the SPH model were utilized with a depth-averaged eddy viscosity value to run the *N*-zone model. To extract the velocity profile at each study location, a numerical window was defined in the SPH model. Velocity profiles were calculated by spatially-averaging particle velocities at small measurement boxes $50 \times 50\,mm$ from the bed to the top of the numerical domain. The velocity profiles were calculated for each numerical time-step. Figure 6.15 is the schematic of velocity profile calculations from the SPH simulations.

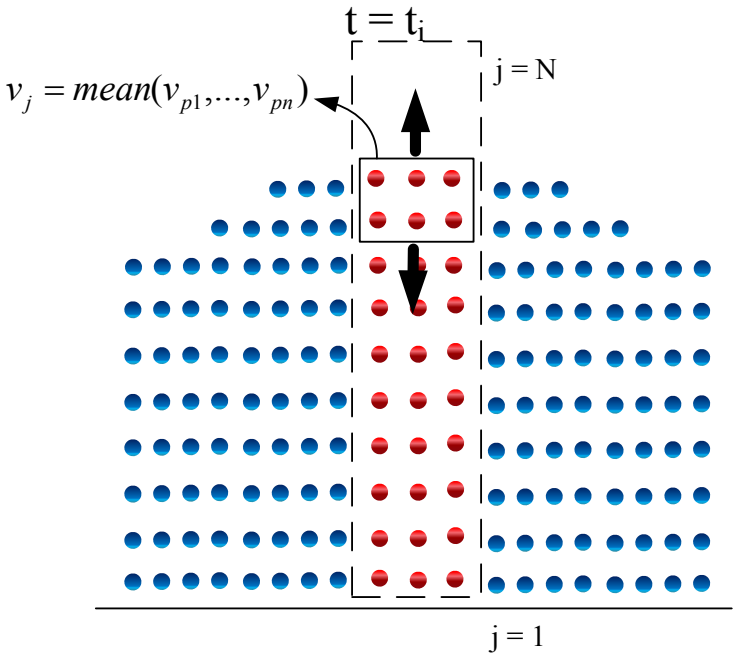

Figure 6.15 – Schematic of velocity profile measurements from SPH simulations

The mixing coefficients were calculated for the duration of the SPH numerical simulations and for all wave conditions tested in this study. Figure 6.16 shows an example of the temporal variation of mixing coefficient inside the surfzone (Fig.

6.16a), at the breaker region (Fig. 6.16b) and seaward of the breaker region (Fig. 6.16c), for the monochromatic waves of 5% steepness. The overall mixing coefficient was determined by averaging the dispersion coefficient over the length of computational time.

Figure 6.16 shows the temporal variation of the shear dispersion coefficients across the nearshore for the monochromatic waves with S_{op} =5%. For each location, the figure shows the temporal variation of D_y for 25sec of the SPH simulations (top figure).It also shows the evolution of the dispersion coefficients during a wave cycle (bottom figure). It is evident that for all locations shown in figure 6.16, the SPH model needs a few seconds until it produces steady predictions for the dispersion. The small and unrealistic fluctuations in the beginning of the SPH simulations is due to the initial conditions and the fact that the movements of the particles is yet not reached to the measurement location. The results (Fig. 6.16) show that following the initial fluctuations, the SPH model could predict the mixing coefficient with constant and regular patterns. The results for mixing coefficients confirm the existence and contributions of bore, undertow and bore/undertow collision phases within the wave cycle.

Comparison of the temporal variation of the shear dispersion with the numerical simulations shows that the shear dispersion has very small fluctuations during the undertow phase. The interaction of the incoming bore meeting the outgoing undertow, resulted in a short intense turbulent shear layer, as demonstrated by a rapid increase and decrease in the mixing over the wave cycle (Fig. 6.16 a, b and c).

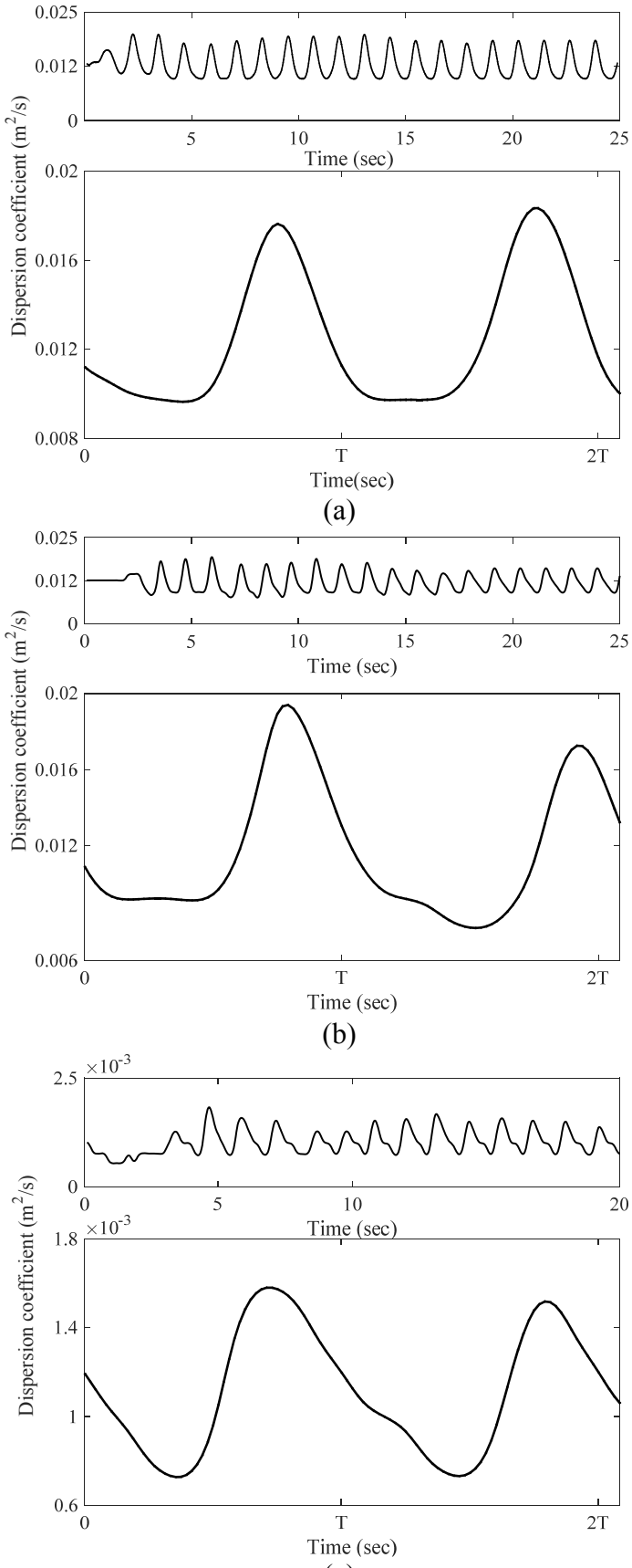

Figure 6.16 – Temporal variation of mixing coefficients obtained from SPH model for regular waves of S_{op} =5% at a) surfzone [2m], b) breaker region [3m], c) offshore [5m]

The overall mixing coefficients were quantified for all the wave conditions simulated with the SPH model. Tables 6.10 to 6.12 summarize the mixing coefficient determined by using the SPH hydrodynamics and the *N*-zone dispersion model. The overall mixing is also compared to the DHI fluorometric measurements.

Table 6.10 – The dispersion coefficients of the SPH simulations for the monochromatic waves with H_o = 0.12m and T = 1.2sec

Location from shore [m]	$D_{y\,(\mathrm{SPH})}$ $[m^2.s^{-1}]$	$D_{y\,(\mathrm{DHI})}$ $[m^2.s^{-1}]$
1	1.121E-02	N.A
2	1.200E-02	1.195E-02
3	1.220E-02	1.260E-02
4	7.100E-03	N.A
5	9.985E-04	6.930E-04

Table 6.11 – The dispersion coefficients of the SPH simulations for the monochromatic waves with H_o = 0.12m and T = 1.85sec

Location from shore [m]	$D_{y\,(\mathrm{SPH})}$ $[m^2.s^{-1}]$	$D_{y\,(\mathrm{DHI})}$ $[m^2.s^{-1}]$
1	8.400E-03	N.A
2	1.060E-02	8.566E-03
3	9.000E-03	8.609E-03
4	5.000E-03	N.A
5	1.510E-03	1.056E-03

Table 6.12 – The dispersion coefficients of the SPH simulations for the monochromatic waves with H_o = 0.12m and T = 2.9sec

Location from shore [m]	$D_{y\,(\mathrm{SPH})}$ $[m^2.s^{-1}]$	$D_{y\,(\mathrm{DHI})}$ $[m^2.s^{-1}]$
1	1.120E-02	N.A
2	1.160E-02	1.244E-02
3	1.000E-02	1.079E-02
4	6.700E-03	N.A
5	2.500E-03	1.576E-03

The mixing coefficients obtained from the temporal variation of shear dispersion from the SPH simulations (Tables 6.10 to 6.12) show that good agreement exist between the numerical model predictions and the mixing coefficients determined for

fluorometric tracer measurements of DHI study (§4.3.2). Figure 6.17 illustrates the mixing coefficient predicted by using the *N*-zone model and SPH hydrodynamics across the nearshore, and the results of the tracer data from the DHI experiment.

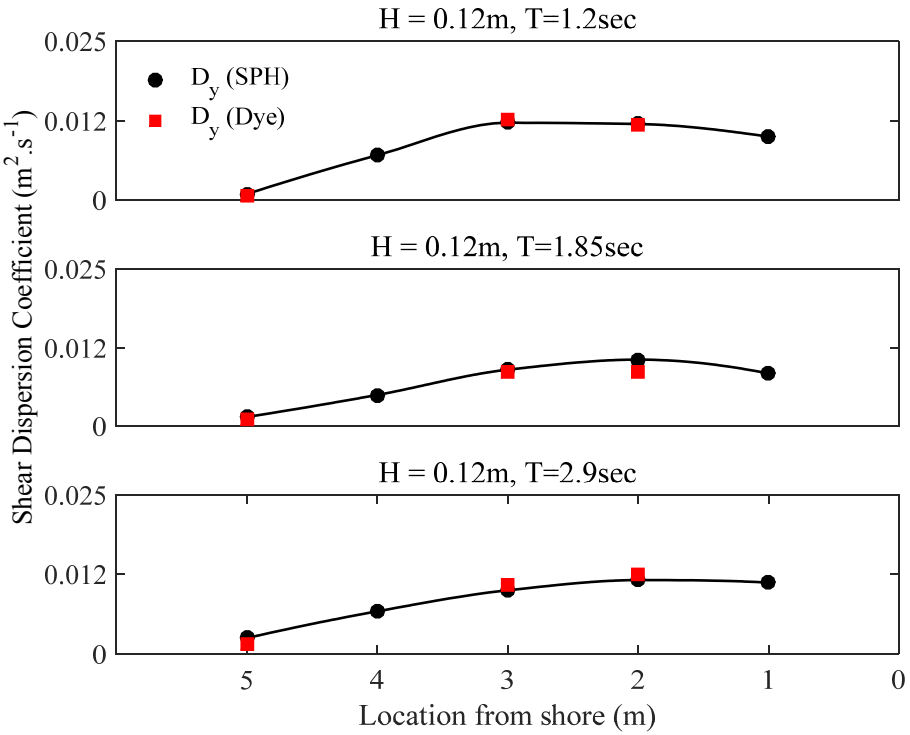

Figure 6.17 – Comparison between the overall mixing coefficients determined for the SPH model and the tracer measurement data

6.7 Summary

This chapter employed the capabilities of Smoothed Particle Hydrodynamics, a Lagrangian, and mesh-less approach to develop a numerical model for simulating wave hydrodynamics in the nearshore region. An overview of the SPH numerical model, background theory and the numerical schemes incorporated in the model were presented. The numerical method, computational domain, governing equations, initial and boundary conditions and time-stepping algorithms were briefly described throughout this chapter.

Three monochromatic wave conditions (Table 6.8) on a 1:20 smooth and impervious beach slope were simulated by the use of SPH modelling. The results of the SPH modelling were in good agreement with the LDV (chapter 4) and PIV (chapter 5) processed results. The developed SPH model was simulated with 1M particles in the computational domain. The results show that the SPH model is capable of simulating wave processes in the nearshore, such as the wave shoaling, breaking and propagation of turbulent bore.

The wave hydrodynamics from the SPH were adopted to quantify the contribution of the dispersive mechanisms on the overall on-offshore mixing coefficients. The diffusivities were implemented using Svendsen & Putrevu (1994) theoretical methodology. The *N*-zone dispersion model quantified the mixing coefficient for all the tested wave conditions (Tables 6.10 to 6.12). The temporal variation of the shear dispersion coefficients were determined to study the contribution of wave bore, undertow and intense shear phases in the overall mixing, at selected locations across the nearshore. The results of the overall mixing across the nearshore (Tables 6.10 to 6.12 and Fig. 6.17) shows that the overall dispersion in the surfzone and seaward of the breaker region are in very good agreement with the overall mixing determined from fluoromteric tracer data measured in the DHI study (§4.3.2). The results confirm that in general, intense shear layer due to the interaction of wave bore with the undertow is greater than other dispersive mechanisms. It is noticeable from the results that overall dispersive mechanism (D_y) is almost an order of magnitude greater than diffusive mechanism (υ_t), which confirms the existing theoretical and experimental data [Svendsen & Putrevu, 1994; Pearson *et al*., 2002 & 2009].

CHAPTER 7
CONCLUSIONS

This thesis presents investigations focused on understanding and quantifying the nearshore mixing processes due to the effects of waves. The context and the challenges associated with the understanding and quantifying of the nearshore mixing was described in chapter one. A detailed review on the fundamental theories and previous work on different aspects of mixing in the nearshore was presented in chapter 2. In chapter 3, nearshore mixing was described from the theoretical point of view and a framework for quantifying the overall mixing was developed. The developed theoretical model described the overall mixing coefficient as the sum of the diffusive and dispersive mechanisms due to the wave motion in the nearshore region. The diffusive mechanisms were quantified through measurements as a function of turbulent kinetic energy and the turbulent length-scale. A mathematical approach was also adopted to quantify the dispersion coefficient.

Mixing under the combined effects of waves and currents were studied in chapter 4 through measurement of hydrodynamic and fluorometric tracing experiments from a large-scale facility at the Danish Hydraulic Institute, Denmark. The data set consisted of hydrodynamic and fluorometric measurements in the nearshore region for a range of wave steepnesses between 2 and 5%. The data obtained from detailed measurements were used to examine the spreading of a solute inside the surf zone and seaward of the breaker region. The diffusion and dispersion coefficients for the hydrodynamic data were determined and the results were compared to the mixing coefficients obtained from the tracer measurements. Due to the limitation of the LDA measurement technique, no information could be obtained from the wave bore hydrodynamics. As a result, measurements were confined to the lower part of the water column.

Particle Image Velocimetry (PIV) was employed to perform a series of hydrodynamic measurements in the wave flume at the University of Warwick. Chapter 5 presented the experimental procedures and the results of the PIV measurements. The diffusive and dispersive mixing mechanisms were quantified for the PIV data. The temporal variation of turbulent kinetic energy and shear dispersion identified three distinct hydrodynamic processes during the bore, undertow and the bore/undertow interaction, which were the primary mixing mechanisms in the nearshore region (Fig. 7.1). The results showed that there was a small dispersion during the undertow phase, for the duration of approximately 0.5T. The peak of mixing for all wave conditions and especially inside the surfzone was achieved in the phase where the onshore moving turbulent wave bore interacted with the undertow of the previous offshore-going wave. The overall mixing determined for the PIV measurements were compared with the tracer studies. Good agreement was found between the hydrodynamic advective-dispersive model postulated in this work and the tracer measurements.

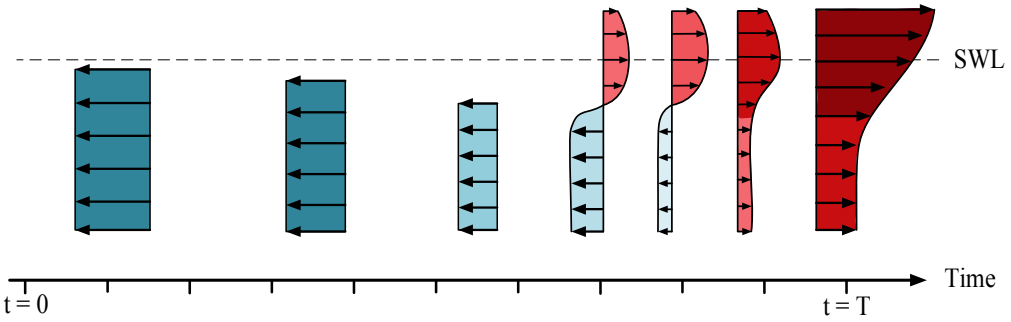

Figure 7.1 – Schematics of wave mechanisms within a wave cycle

In chapter 6, the numerical capabilities of a Lagrangian, particle-based, Smoothed Particle Hydrodynamics method were employed to simulate the wave hydrodynamics in the nearshore region. A numerical model was developed and validated against the laboratory measurements obtained from the DHI study. The numerical results for the wave hydrodynamics were employed to study the shear dispersion in the nearshore region. The instantaneous velocity profiles from the SPH simulations were utilized together with the theoretical diffusivities proposed by Svendsen and Putrevu (1994) in order to predict the overall dispersion coefficients

across the nearshore. Very good agreement was observed between the mixing determined from SPH data and the fluorometric tracer study.

This study quantified the contribution of diffusive and dispersive mixing mechanisms across the nearshore for laboratory and numerical data. The results demonstrated that the dispersive mechanisms are the primary mixing mechanism across the nearshore. Figures 7.2 to 7.4 depict the comparison between the non-dimensional diffusive and dispersive mechanisms obtained from the PIV, SPH and Dye measurements for the monochromatic wave conditions investigated within this thesis.

The variation of the diffusion coefficients across the nearshore show that the experimental data from the PIV and LDA measurements are in line with the theoretical approach proposed by Svendsen and Putrevu (1994). For all the wave conditions tested within this study, it has been shown that the diffusivity reaches its peak values in the breaker region. Seawards of the breaker region, where the wave activities and surface generated turbulence reduce significantly, the diffusive mechanism drops by approximately 85% of its peak at the breaker. It was observed that the diffusion coefficients inside the surfzone decrease by ~20% compared to the breaker region. Towards the inner surfzone and still water line, the wave activities and turbulent kinetic energy reduces, giving rise to a significant drop in the diffusivity. However, the results demonstrate that in the inner surfzone the diffusivity is still higher (~33%) than that in the offshore region.

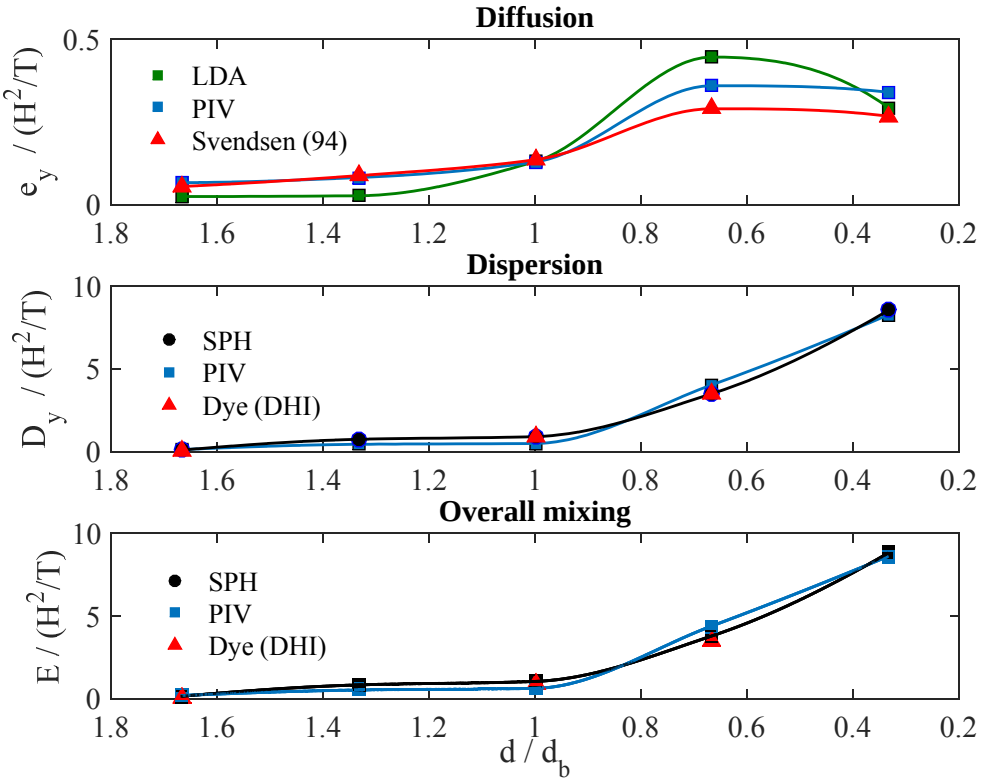

Figure 7.2 – The diffusive and dispersive mixing mechanisms for the monochromatic waves with S_{op} = 5%

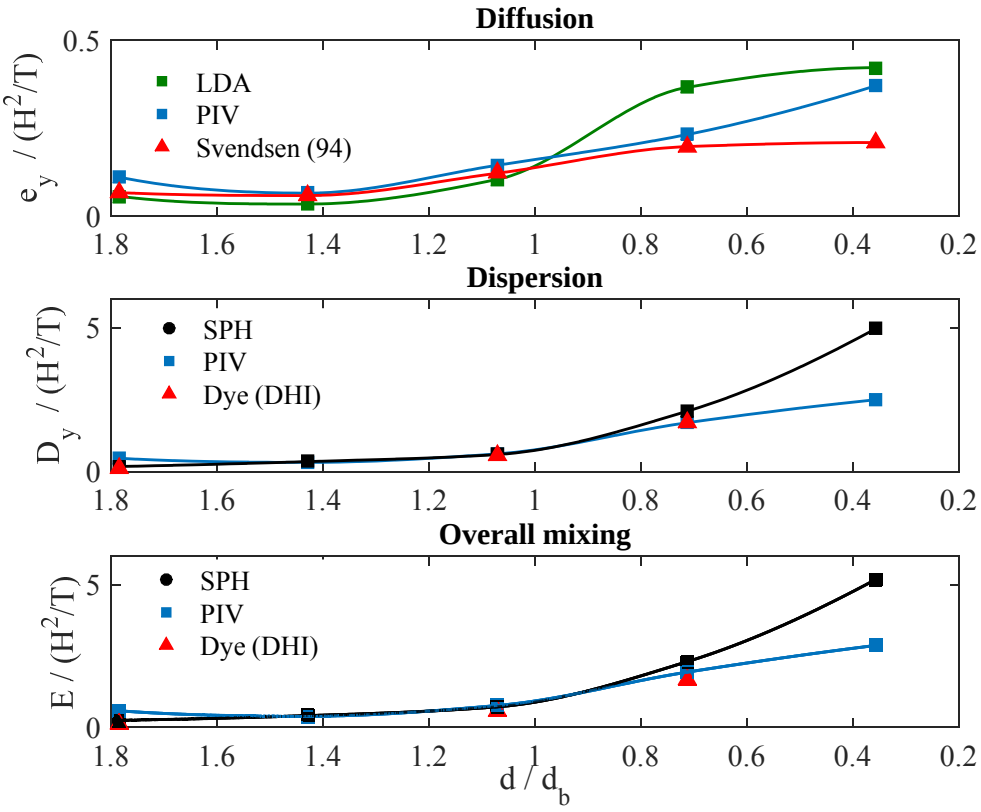

Figure 7.3 – The diffusive and dispersive mixing mechanisms for the monochromatic waves with S_{op} = 3½%

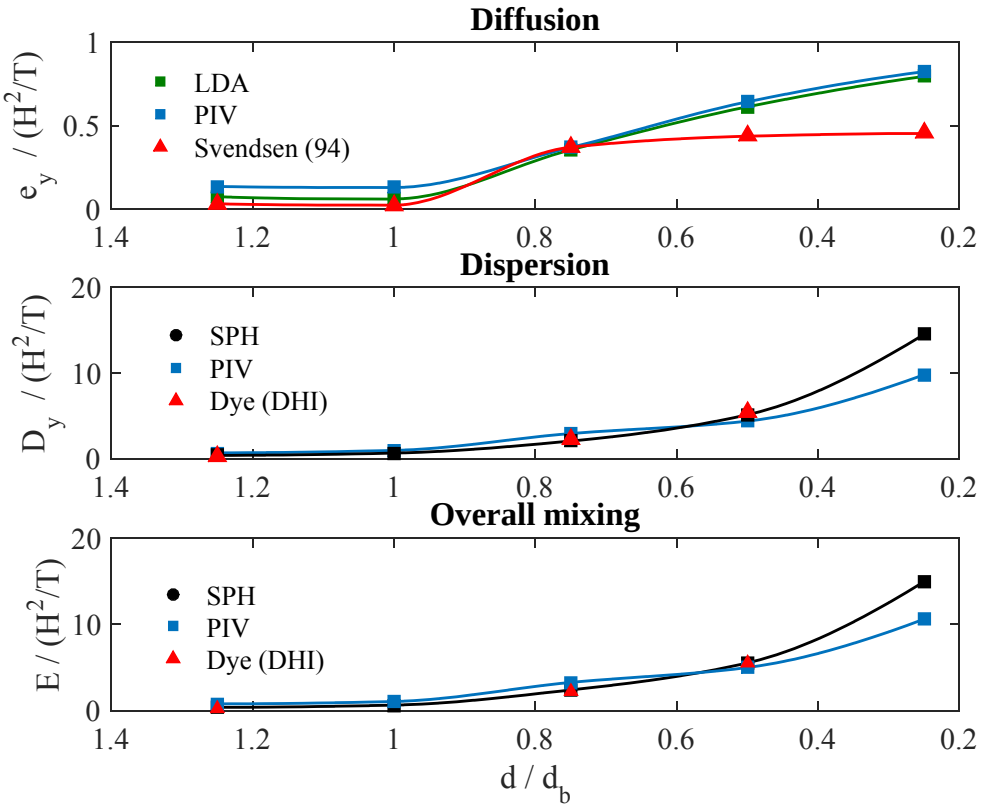

Figure 7.4 – The diffusive and dispersive mixing mechanisms for the monochromatic waves with S_{op} = 2%

In this work, the dispersive mixing mechanisms were quantified by determining the temporal variation of shear dispersion coefficients for the laboratory (chapter 4 and 5) and numerical data (chapter 6). In order to determine the dispersion coefficient, the developed dispersion model (chapter 3) utilized depth-averaged diffusivity and the localised spatially-averaged hydrodynamics across the nearshore. The dispersion coefficients determined for the hydrodynamic data have been compared with the mixing coefficients determined for the fluorometric tracer studies. The results (Figs. 7.2 to 7.4) show very good agreement between the dispersion model and the dye data. Investigating the temporal variation of dispersion mechanisms across the nearshore identified the fact that the intense mixing mechanism caused by the wave bore-undertow collision, is responsible for most of the mixing that occur. The duration of this intense mixing phase was found to be approximately $0.2T$ for the wave conditions investigated in this work. The dispersion for undertow ($0.5T$) and bore phases ($0.3T$) are relatively smaller than the bore-undertow interaction phase.

The pioneering Royal Society works of Svendsen & Putrevu (1994) identified the temporally-averaged dispersion, as a function of distance from the shore. Using a combination of experimental, mathematical, and numerical formulations, this study has identified and quantified, for the first time, the temporal and spatial dispersive mixing processes in the nearshore (over the full wave cycle), within the challenging and complex environment of the surf zone. It has been shown that the cross-shore circulation provides lateral mixing that exceeds that of the turbulence by an order of magnitude inside the surfzone.

The turbulence still remains an essential part of the flow since it is the primary driver through which the vertical mixing is responsible for defining the vertical velocity profiles, which then determines the strength of the dispersion.

7.1 Future work

This thesis has demonstrated methods to quantify the mixing and dispersion in the nearshore due to the combined effects of waves and currents through theoretical, experimental and numerical investigations. There are yet more opportunities for extending the scope of this thesis. This section presents some of these directions:

Oblique waves

Both turbulent velocity measurement and direct solute transport measurement need to be investigated for the waves approaching the nearshore from an oblique angle. The mixing mechanisms identified within this study need to be explored for the oblique waves.

Field studies

This study mainly focused on the hydrodynamic conditions across the European Union coastline (S_{op} = 2-5%). Field investigations could be carried out to have better understanding of nearshore hydrodynamics and tracer behaviour. Also, the algorithms developed within this study to quantify the turbulent diffusion and advective shear dispersion could be validated against field investigation data.

Random waves

This thesis mainly investigated monochromatic wave conditions and only one pseudo random wave condition with 3.5% steepness was investigated. The mixing and dispersion mechanisms described and quantified within this study could be further investigated under random wave conditions.

REFERENCE

AAGAARD T. & VINTHER N., 2008. Cross-shore currents in the surfzone: Rips or undertow?, J. Coast. Res., 24, 561-570.

ABARBANEL H. D. I., 1995. Analysis of observed chaotic data, Springer, New York.

ABOLFATHI S., PEARSON J. M., 2014. SOLUTE DISPERSION IN THE NEARSHORE DUE TO OBLIQUE WAVES, Coastal Eng. Proc, 1(34), waves 49.

ADDISON P. S. 1997. Fractals and chaos: an illustrated course, IOP, London.

ADRIAN R. J., 1991, Particle-imaging techniques for experimental fluid mechanics, Ann. Rev. Fluid Mech., 23, 261-304.

ADRIAN R. J., 1996, Bibliography of particle velocimetry using imaging methods: 1917-1995, Technical Report 817, University of Illinois.

AGTERBERG F.P., 1970. Autocorrelation Functions in Geology. In Geostatistics. Plenum Press, New York, 113–141.

AIRY G. B., 1845. Tides and waves. *Encyc. Metrop., Art.,* 192, 241-396.

ARNEBORG L., FIEKAS V., UMLAUF L. and BURCHARD H., 2007. Gravity current dynamics and entrainment- A process study base on observation s in the Arkona Basin, J. Phys. Oceanogr., 37, 2094-2113.

APEL J.R., OSTROVSKY L.A., SYEPANYANTS Y.A., LYNCH J.F., 2006. Internal solutions in the ocean. Technical Report, WHOI-2006-04, Woods Hole Oceanographic Institution.

BAGNOLD R. A., 1947. Sand movement by waves: some small-scale experiments with sand at very low density. *J. Inst. Civ. Engrs.,* 27, 447-469.

BATCHELOR G. K., 1967. An introduction to fluid dynamics. Cambridge University press.

BATTJES J. A., 1974. Surf similarity. Proc. 14th Int. Conf. Coastal Eng. ASCE, Copenhangen, 447–467.

BATTJES J. A., 1975. Modelling of turbulence in the surf zone. *Symp. Modeling Techniques,* Vol. 2, 1050-1061.

BATTJES J. A., 1983. Surf zone turbulence. Proc. 20th IAHR Congr., Moscow, Seminar on Hydrodynamics of Waves in Coastal Areas.

BATTJES J. A. & SAKAI T., 1981. Velocity fields in a steady breaker. J. Fluid Mech., 111, 421-437.

BATTJES J. A. & JANSEN J. P. F. M., 1986. Energy loss and set-up due to breaking of ransom waves. Coastal Engineering, 32, 569-587.

BAUMERT H. Z., & RADACH G., 1992. Hysteresis of turbulent kinetic energy in non-rotational tidal flows: A model study, J. Geophys. Res., 97, 3669-3677.

BEEMAN D., 1976. Some multistep methods for use in molecular dynamics calculations. Journal of Computational Physics, 20:130–139.

BETTERIDGE K. F. E., BELL P. S., THORNE P. D., WILLIAMS J. J., 2006. Evaluation of a triple axis coherent Doppler velocity profiler for measuring near-bed flow: A field study, J. Atmos. Ocean. Tech, 23, 90-106.

BONET J. & LOK L., 1999. 'Variational and momentum preservation aspects of Smooth Particle Hydrodynamic formulations'. Computer methods in applied mechanics and engineering 180, 97–115.

BONET J. and KULASEGARAM S., 2000. Corrections and stabilization of Smooth Particle Hydrodynamics methods with applications in metal forming simulations. International Journal for Numerical Methods in Engineering, 47:1189–1214.

BORTHWICK G. L, JOYNES S. A. 1992. Laboratory Study of Oil Slick Subjected to Nearshore Circulation. Journal of Environmental Engineering 118:6, 905-922.

BOUSSINESQ J., 1877. Essai sur la des eaux courantes (On the theory of flowing waters). *Memoires presentes par divers savants a l'Acadamie des Sciences,* Paris.

BOWEN A. J., 1969. The generation of longshore currents on a plane beach. *J. Mar. Res.,* 27(2): 206-15.

BOWEN A., 1969. Rip currents 1. Theoretical investigations. Journal of Geophysical Research, 74(23):5479-5490.

BOWEN A. & HOLMAN R., 1989, Shear instabilities of the mean longshore current: 1. Theory, Journal of Geophysical Research, 18, 23-030.

BOWEN A. J., & INMAN D. L., 1969, Rip Currents 2: Laboratory and Field observations, Journal of Geophysical Research, 74, 5479-5490.

BOWEN A. J. & INMAN D. L., 1974. Nearshore mixing due to waves and wave-induced currents. *Rapp. P.-v. Reun. Cons. int. Explor. Mer,* 167: 6-12.

BOWEN A. J., INMAN D. L. & SIMMONS V. P., 1968. Wave 'set-down' and 'set-up'. *J. geophys.* Res. 73, 2569-2577.

BOWDEN K. F., KRANUEL D. P., & LEWIS R. E., 1974. Some features of turbulent diffusion from a continuous source at sea. *Int. Symp. on turbulent diffusion in Env. Pollut.,* 18A, 315-329.

BOWLES P., BURNS R. H., HUDSWELL F. & WHIPPLE R. T. P., 1958. Exercise Mermaid, UK Atomic Energy Authority, Harwell, Report Number AERE E/R 262, published HMSO

BRADSHAW P., 1971. *An Introduction to Turbulence and its measurement.* Oxford Pergamon Press.

BRANDER R. W., 1999. Field observations on the morphodynamic evolution of a low energy rip current system, Marine Geology, 157, 199-217.

BUCKINGHAM E., 1914. On physically similar systems; illustrations of the use of dimensional equations. Physical Review 4 (4): 345–376.

BURCHARD H., 2009. Combined effects of wind, tide, and horizontal density gradients on stratification in estuaries and coastal seas, J. Phys. Oceanogr., 39, 2117– 2136.

BURCHARD H., and BAUMERT H., 1998. The formation of estuarine turbidity maxima due to density effects in the salt wedge. A hydrodynamic process study, J. Phys. Oceanogr., 28, 309-321.

BURCHARD H., CRAIG P. D., GEMMRICH J. R., VAN HAREN H., MATHIEU P-P., MEIER H. E. M., NIMMO-SMITH W. A. M., PRANDKE H., RIPPETH T. P., SKYLLINSTAD E. D., SMYTH W. D., WELSH D. J. S., WIJESEKERA H. W., 2008b. Observational and numerical modeling methods for quantifying coastal ocean turbulence and mixing. Progr. Oceanogr., 76, 399-442.

BURCHARD H., FLOSER G., STANEVA J. V., RIETMULLER R., and BADEWIEN T., 2008a. Impact of 30 density gradients on net sediment transport into the Wadden Sea, J. Phys. Oceanogr., 38, 566-587.

BURCHARD H., & HETLAND R. D., 2010. Quantifying the contributions of tidal straining andgravitational circulation to residual circulation in periodically stratified tidal estuaries. J. Phys. Oceanogr., 40,1243-1262.

BURCHARD H., HETLAND R. D., SCHULZ E., and SCHUTTELAARS H. M., 2011. Drivers of residual circulation in tidally energetic estuaries: Straight and irrotational estuaries with parabolic cross-section. J. Phys. Oceanogr., 41, 548-570.

CAMASSA R., LIN Z. & MCLAUGHLIN R. M., 2010. The exact evolution of the scalar variance in pipe and channel flow. Commun. Math. Sci. 8, 601–626.

CARLSLAW H. S. & JAEGER J. C., 1959. *Conduction of Heat in Solids.* Oxford University Press.

CENEDESE C., WHITEHEAD J.A., ACARELLI T.A., OHIWA M., 2004. A dense current flowing down a sloping bottom in a rotating fluid. J. Phys. Oceanogr., 34, 188-202.

CHADWICK A. & MORFET J., 1986. *Hydraulics in civil & Environmental Engineering,* Spon, London.

CHANG K. A., LIU P. L. F., 1998. Velocity, acceleration and vorticity under a breaking wave. Phys. Fluids 10 (1), 327–329.

CHANG K. A., LIU P. L. F., 1999. Experimental investigation of turbulence generated by breaking waves in water of intermediate depth. Phys. Fluids 11 (11), 3390–3400.

CHATWIN P. C. & ALLEN C. M., 1985. Mathematical models of dispersion in rivers and estuaries, *Ann. Rev, Fluid Mech.,* 17, 119-149.

CHEN J. K., BERAUN J. E., and CARNEY, T. C., 1999. A corrective Smoothed Particle Method for boundary value problems in heat conduction. Computer Methods in Applied Mechanics and Engineering, 46:231– 252.

CHEN C., LIU H., BEARDSLEY R. C., 2003. An unstructured grid, finite-volume, three-dimensional, primitive equations ocean model: Application to coastal ocean and estuaries. J. Atmos. Ocean. Technol. 20, 179–186.

CHIKWENDU S. C., 1986. Calculation of longshore shear dispersivity using an N-zone model, *J. Fluid Mech.,* 167, 19-30.

CHOW V. T., 1959. *Open Channel Hydraulics.* McGraw-Hill, New York.

CHRISTENSEN E. D., 2006. Large eddy simulation of spilling and plunging breakers. Coast. Eng. 53 (5–6), 463–485.

CHRISTENSEN E. D., WALSTRA D. J., EMERAT N., 2002. Vertical variation of the flow across the surf zone. Coast. Eng. 45 (1), 165–198.

CLARK D. B., FEDDERSEN F., OMAND M., and GUZA R. T., 2009. Measuring Fluorescent Dye in the Bubbly and Sediment Laden Surfzone, Water, Air, Soil Pollution.

CLARK D. B., FEDDERSEN F., and GUZA R. T., 2010. Cross-shore surfzone tracer dispersion in an alongshore current, J. Geophys. Res. Oceans, 115, C10035.

CLARK D. B., FEDDERSEN F. and GUZA R. T., 2011. Modeling surfzone tracer plumes, part 2: Transport and dispersion, J. Geophys. Res., 116, C11028.

CLARK D. B., LENAIN L., FEDDERSEN F., BOSS E., and GUZA R. T., 2014. Aerial imaging of fluorescent dye in the nearshore, J. Atmos. Oceanic Tech., 31, 1410-1421.

COLAGROSSI A., LANDRINI M., 2003. Numerical simulation of interfacial flows by smoothed particle hydrodynamics, J. Comput. Phys. 191 (2) 448–475.

COWEN E. A., SOU I. M., LIU P. L. F., RAUBENHEIMER R., 2003. Particle image velocimetry measurements within a laboratory-generated swash zone. J. Eng. Mech.-ASCE 129 (10), 1119–1129.

CRANK J., 1956. *The Mathematics of Diffusion.* Oxford University Press.

CRESPO A. J. C., DOMINGUEZ J. M., DALRYMPLE R. A., 2007. Boundary conditions generated by dynamic particles in SPH methods, CMC-Comput. Mater. Continua 5 (3)173–184.

CRESPO A. J. C., 2008. 'Application of the Smoothed particle Hydrodynamics model SPHysics to free-surface hydrodynamics', PhD Thesis. Universidade de Vigo, Department of Applied Physics.

CRESPO A. J. C., DOMINGUEZ J. M., BARREIRO A., GOMEZ-GESTERIA M. and ROGERS B. D., 2011. GPUs, a new tool of acceleration in CFD: Efficiency and reliability on Smoothed Particle Hydrodynamics methods. PLoS ONE 6 (6), e20685.

CRESPO A. J. C., DOMINGUEZ J. M., ROGERS B. D., GOMEZ-GESTERIA M., LONGSHAW S., CANELAS R., VACONDIO R., BARREIRO A., GARCIA-FEAL O., 2015. DualSPHysics: Open-source parallel CFD solver based on smoothed particle hydrodynamics (SPH), Comput. Phys. Comm. 187 , 204–216.

CSANADY G. T., 1973. *Turbulent Diffusion in the Environment.* D. Reidel, Dordrecht.

CUOMO G., PANIZZO A., and DALRYMPLE R. A., 2006. SPH-LES two phase simulation of wave breaking and wave-structure interaction. Proc. 30th Intl Conference on Coastal Engineering, 274–286.

DALRYMPLE R., 1975. A mechanism for rip current generation on an open coast, Journal Geophysical Research, ASCE, 80, 3485-3487.

DALRYMPLE R. A. and KNIO O., 2001. SPH Modelling of Water Waves. Proc. Coastal Dynamics, Lund, 779–787.

DALRYMPLE R. & LOZANO C., 1978. Wave current interaction models for rip currents, Journal of Geophysical Research, 83(C12):6063.

DALRYMPLE R., HERAULT A., BILOTTA G., and FARAHANI R. J., 2010. GPU-Accelerated SPH model for water waves and free surface flows. Proc.32nd Intl. Conf. on Coastal Engineering.

DAVIES A. M., Xing J., 2001. The influence of eddy viscosity parameterization and turbulence energy closure scheme upon the coupling of tidal and wind induced current. Estuarine, Coastal and Shelf Science, 53, 415-436.

DAVIES R. A., FITZGERALD D. M., 2004. Beaches and Coasts, Blackwell Publishing, Carlton, Victoria.

DE SILVA SAMARASINGHE J. R., BODE L., MASON L. B., 2003. Modelled Response of Gulf St Vincent (South Australia) to evaporation, heating and winds. Continental Shelf Research, Pergamon, 23, 1285-1313.

DEAN R. G. & DALRYMPLE R. A., 2002. Coastal Processes with Engineering Applications. Cambridge University Press, Cambridge, UK

DEAN R. G., 2002, 'Beach Nourishment: Theory and Practice', Advanced Series on Ocean Engineering, volume 18, World Scientific.

DEANS J. & SMITH I., 1999. Monitoring Sand Management at Glenelg and West Beach Harbours, Adelaide, [online], Department for Environment and Heritage, South Australia.

DE SERIO F., MOSSA M., 2006. Experimental study on the hydrodynamics of regular breaking waves, *Coastal Engng.,* 5, 99-113.

DE VRIEND H. J. & STIVE M. J. F., 1987. Quasi-3D modelling of near-shore current. *Coastal Engng.,* 11, 565-601.

DEWEY R. J. & SULLIVAN P. J., 1982. Longitudinal-dispersion calculations in laminar flows by statistical analysis of molecular motions. J. Fluid Mech. 125, 203–218.

DEWEY R., RICHMOND D., GARRETT C., 2005. Stratified tidal flow over a bump. Journal of Physical Oceanography 35, 1927–1991.

DIDIER E., NEVES D. R. C. B., MARTINS R., NEVES M. G., 2014. Wave interaction with a vertical wall: SPH numerical and experimental modeling, Ocean Engineering, Volume 88, 330-341, ISSN 0029-8018.

DILTS G. A., 1999. Moving-LeastSquares-Particle Hydrodynamics I. Consistency and stability. Int. J. Numer. Meth. Engineering., 44:1115– 1155.

DIXTON T., 2012. Annual survey of reported discharges attributed to vessels and offshore oil and gas installations operating in the United Kingdom pollution control zone, Advisory Committee On Protection of the Sea, Cambridge, UK.

DOMINGUEZ J. M., CRESPO A. J. C., GOMEZ-GESTEIRA M., MARONGIU J. C., 2010. Neighbour lists in smoothed particle hydrodynamics, Internat. J. Numer. Methods Fluids.

DOMINGUEZ J. M., CRESPO A. J. C., GOMEZ-GESTEIRA M., 2013. Optimization strategies for CPU and GPU implementations of a smoothed particle hydrodynamics method. Computer Physics Communications, 184(3).

DONOHO D. L., JOHNSTONE I. M., 1994. Ideal spatial adaptation by wavelet shrinkage. Biometrika, 81(3), 425–455.

DOSHI M. R., DAIYA P. M., GILL W. N., 1978. Threedimensional laminar dispersion in open and closed rectangular conduits. Chem. Engng Sci. 33, 795.

EDEN C., GREATBATCH R. J., OLBERS D., 2007. Interpreting eddy fluxes. J. Phys. Oceanogr.,37, 1282-1296.

EDEN C., GREATBATCH R. J., 2008a. Towards a turbulence model for meso-scale eddies. Ocean Modelling, 20, 223-239.

EDEN C., GREATBATCH R. J., 2008b. Diapycnal mixing by meso-scale eddies. Ocean Modelling, 23, 113-120.

EINSTEIN A., 1905. Über die von der molekularkinetischen Theorie der Wärme geforderte Bewegung von in ruhenden Flüssigkeiten suspendierten Teilchen. Ann. Phys., 17, 549.

ELDER J. W., 1959. The dispersion of marked fluid in turbulent flow. J. Fluid Mech. 5, 544-560.

ELLERO M., SERRANO M., ESPANOL P., 2007. Incomprensible Smoothed Particle Hydrodynamics. Journal of Computational Physics, 226:1731–1752.

ELGAR S., RAUBENHEIMER B., and GUZA R. T., 2005. Quality control of acoustic Doppler velocimeter data in the surfzone, Meas. Sci. Technol., 16, 1889 – 1893.

ELLIOTT A. J., BARR A. G., KENNAN D., 1997. Diffusion in Irish coastal waters. Estuarine, Coastal and Shelf Science, 11, 15-23.

ERGIN A., 1980. Surface dispersion in wave flume. J. Wtrwy., Port, Coast., and Oc. Engng., ASCE, 106, 449-467.

FALCONER R. A., LIU S. Q., CHEN Y., 1992. Application of higher order accurate schemes for advective transport in a 2-D water quality model. Proc. of the 2nd Int. Conf. of Coastal, Estuarine and River Waters, 1, 241 – 252.

FEDDERSEN F., GUZA, R. T., 2003. Observations of Nearshore Circulation: Alongshore Uniformity. J. Geophys. Res., 108.

FEDDERSEN F., TROWBRIDGE J. H., WILLIAMS A. J., 2007. 3D, Vertical structure of dissipation in the nearshore, J. Phys. Oceangr., 37, 1764-1777.

FEDDERSEN F., 2007. Breaking wave induced cross-shore tracer dispersion in the surfzone: Model results and scalings, J. Geophys. Res.,112, C0912.

FEDDERSEN F., TROWBRIDGE J. H., WILLIAMS A. J., 2007. Vertical structure of dissipation in the nearshore, J. Phys. Oceangr., 37, 1764-1777.

FEDDERSEN F., 2010. Quality controlling surfzone acoustic Doppler velocimeter observations to estimate the turbulent dissipation rate, J. Atmospheric Oceanic Tech., 27, 2039-2055.

FEDDERSEN F., CLARK D. B., GUZA R. T., 2011. Modelling surfzone tracer plumes, part 1: Waves, mean currents, and low-frequency eddies J. Geophysical Res. Oceans, 116, C11027.

FEDDERSEN F., 2012. Scaling surf zone turbulence, Geophys. Res. Letters, 39, L18613.

FEDDERSEN F., 2012. Observations of the surfzone turbulent dissipation rate, J. Physical Oceanogr., 42(3), 386-399.

FEDDERSEN F., 2013. The generation of surfzone eddies in a strong alongshore current, J. Phys. Oceanogr.

FENG T., STANSBY P. K., 2005. Streamline topography in periodic surf zone waves from LDA measurements. Measure. Sci. Technol. 16, 1929–1936.

FER I., VOET G., SEIM K. S., RUDELS B., LATARIUS K., 2010. Intense mixing of the Faroe Bank Channel overflow. Geophys. Res. Lett., 37, L02604.

FICK A., 1855. On liquid diffusion. *Philos. Mag.* 4(10), 30-39.

FISCHER H. B., LIST J. E., KOH R. C. Y., IMBERGER J., BROOKS N. H., 1979. Mixing in inland and coastal waters. New York: Academic Press.

FISCHER H. B., 1967. The mechanics of dispersion in natural streams. *J. Hyd. Div.,* ASCE, 93, 187-216.

FISCHER H. B., 1978. On the tensor form of bulk dispersion coefficient in a bounded skewed shear flow. *J. geophys. Res.,* 83, 2373-2375.

FONG D. A. & STACEY M. T., 2003. Horizontal dispersion of a near-bed coastal plume. J. Fluid Mech., 489, 239–267.

FORD R., MC INTYRE M., NORTON W., 2000. Balance and the slow quasimanifold: Some explicit results. J. Atmos. Sci., 57(9), 1236-1254.

FOX-KEMPER B., FERRARI R. & HALLBERG R. W., 2008. Parameterization of Mixed Layer Eddies. I: Theory and Diagnosis. J. Phys. Oceanogr., 38, 1145-1165.

GALVIN C. J., 1972. Wave breaking in shallow water. *Waves on Beaches,* edited by R. E. Meyer, Academic Press, New York, 413-455.

GALVIN C. J. & EAGLESON P. S., 1965. Experimental study of longshore currents on a plane beach. *Tech. Memo. Coast. Eng. Res. Cent.* Washington, 10.

GARVINE R. W., 1974. Radial spreading of buoyant, surface plumes in coastal waters. J. Geophys. Res., 89, 1989-1996.

GARVINE R.W., 1987. Estuary plumes and fronts in shelf waters: A layer model. J. Phys.Oceanogr., 17, 1877-1896.

GARVINE R.W., 2001. The impact of model configuration in studies of buoyant coastal

discharge, J. Mar. Res., 59, 193-225.

GASPAR P., GREGORIS Y., LEFEVRE J. M., 1990. A simple eddy kinetic energy model for simulations of the oceanic vertical mixing: tests at station PAPA and Long-Term Upper Ocean Study site. J. Geophys. Res., 95, 16179-16193

GENT P. R., MC WILLIAMS J. C., 1990. Isopycnal mixing in ocean circulation models. J. Phys. Oceanogr., 20, 150-155.

GENT P. R., WILLEBRAND J., MC DOUGALL T. J., McWilliams J. C., 1995. Parameterizing 31eddy-induced tracer transports in ocean circulation models. J. Phys. Oceanogr., 25,463-474.

GEORGE R., FLICK R. E., GUZA R. T., 1994. Observations of turbulence in the surf zone. J. Geophys. Res., 99, 801–810.

GERKEMA T., ZIMMERMAN J. T. F., MAAS L. R. M., VAN HAREN H., 2008. Geophysical fluid dynamics beyond the traditional approximation. Rev. Geophys., 46.

GEYER W. R., MONDEEL D. J., HILL P. S., MILLIGAN T.G., 1998. The Eel River plume during the 1997 flood: Freshwater and sediment transport, Eos Trans. AGU, 79(45).

GEYER W. R., TROWBRIDGE J. H., BOWEN M. M, 2000. The dynamics of a partially mixed estuary, J. Phys. Oceanogr., 30, 2035-2048.

GILL A. E., 1974. The stability of planetary waves on an infinite beta-plane. Geophys. Fluid Dyn, 6, 29-47.

GILL W. N., SANKARASUBRAMANIAN R., 1970. Exact Analysis of Unsteady Convective Dispersion, Proc. Roy. SOC. London, 316A, 341.

GILL W. N., SANKARASUBRAMANIAN R., 1971. Dispersion of a Non-uniform Slug in Time-Dependent Flow, Proc. Roy. SOC. London, 3224 101.

GINGOLD R. A., MONAGHAN J. J., 1977. Smoothed particle hydrodynamics: theory and application to non-spherical stars. Monthly Notices of the Royal Astronomical Society 181, 375-389.

GODA Y., 1970. A systhesis of breaker indices. Proc. Japan Soc. Civ. Engrs.. 180, 39-49.

GOMEZ-GESTEIRA M., ROGERS B. D., DALRYMPLE R. A., CRESPO A. J. C., 2010. State-of-the-art of classical SPH for free-surface flows. Journal of Hydraulic Research 48 Extra Issue, 6–27.

GOMEZ-GESTEIRA M., ROGERS B. D., CRESPO A. J. C., DALRYMPLE R. A., Narayanaswamy M., Domínguez J. M., 2012a. SPHysics - development of a free-surface fluid solver- Part 1: Theory and Formulations. Computers & Geosciences, 48, 289-299.

GOMEZ-GESTEIRA M., CRESPO A. J. C., ROGERS B. D., DALRYMPLE R. A., Domínguez J.M., Barreiro A., 2012b. SPHysics - development of a free-surface fluid solver- Part 2: Efficiency and test cases. Computers & Geosciences, 48, 300-307.

GORING D. G., NIKORA V. I., 2002. Despiking acoustic Doppler velocimeter data. J. of Hydraulic Eng., vol. 128, 117 – 126.

GOTOH H., SHIBAHARA T., SAKAI T., 2001. Sub-Particle-Scale turbulence model for the MPS method – Lagrangian flow model for hydraulic engineering. Computational Fluid Dynamics Journal 9(4), 339-347.

GOVENDER K., MPCKE G. P., ALPORT M. J., 2002. Video-imaged surf zone and roller structures and flow fields. J. Geophys. Res. 107 (C7), 3072.

GOVENDER K., MPCKE G. P., ALPORT M. J., 2004. Dissipation of isotropic turbulence and length-scale measurements through the wave roller in laboratory spilling waves. J. Geophys. Res. 109 (C08018), 5115–5124.

GRANT S. B., KIM J. H., JONES B. H., JENKINS S. A., WASYL J., CUDABACK C., 2005. Surf zone entrainment, along-shore transport, and human health implications of pollution from tidal outlets. Journal of Geophysical Research 110 (C10).

GRZECHNIK M., 2000. 'Three-Dimensional Tide and Surge Modelling and Layered Particle Tracking Techniques Applied to Southern Australian Coastal Seas', PhD thesis, Adelaide University.

GUYMER I., WEST J. R., 1988. The determination of estuarine diffusion coefficients using a fluorometric dye tracing technique. Estrarine, Coastal and Shelf Science, 27.

GUZA R. T., THORNTON E. B., 1982. Swash Oscillations on a Natural beach. Journal of geophysical research, 87(C1), 483-491.

GUZA R. T., THORNTON E. B., 1985. Observations of surf beat. Journal of geophysical research, 90, (C2), 3163-3174.

HANSEN J. B. & SVENDSEN I. A., 1984. A theoretical and experimental study of undertow. Proc. 19th Int. Conf. Coastal Engng., 2246-2262.

HARLEMAN D. R. F., IPPEN A. T., 1960. The turbulent diffusion and convection of saline water in an idealised estuary, I.A.S.H. commission of surface waters in U.S.A., 51, 362-378.

HARRIS T. F. W., JORDAN J. M., MCMURRY W. R., VERWEY C. J., ANDERSON F. P., 1963. Mixing in the surf zone. *Int. J. Air Wat. Pollut.,* 7: 649-67.

HARRIS T. F. W., 1967. 'Field and model studies of the nearshore circulation', PhD Thesis, Dept. of Physics, University of Natal.

HATTORI M., AONO T., 1985. Experimental study on turbulence structures under spilling breakers, *in the Ocean Surface,* edited by Y. Toba & Mitsuyasu, D. Rediel, Massachusetts.

HEGGE B., ELIOT I., HSU J., 1996. 'Sheltered Sandy beaches of South Western Australia', Journal of Coastal Research, 12, 748-760.

HEMER M. & BYE J., 1999. 'The swell climate of the South Australia Sea', Transactions of the Royal Society of South Australia, 123(3), 107-113.

HENDERSON F. M., 1966. *Open Channel Flow.* Macmillan, New York.

HOFMANN-WELLNHOF B., LICHTENEGGER H., COLLIN H., 1997. Global Positioning System: Theory and Practice, 4th Ed, Springer-Verlag.

HOLLY F. M., 1985. Dispersion in rivers and coastal waters. 1: Physical principles and dispersion equations, edited by P. Novak, Developments in Hydraulic Engineering, Elsevier, London, 1-37.

HORIKAWA K., 1978. An Introduction to Coastal Engineering. University of Tokyo Press.

HORIKAWA K., 1988. Nearshore Dynamics and Coastal Processes, University of Tokyo Press, Tokyo

HOWD P., OLTMAN-SHAY J., HOLMAN R., 1991. Wave Variance partitioning in the trough of a barred beach. Journal of Geophysical Research, 96(C7), 781-795.

HWUNG H. H., HWANG K. S., HIANG W. S., LAI C. F., 1998. Flow structures in swash zone. In 26th International Conference on Coastal Engineering, Reston, VA.

HU X., ADAMS N., 2007. An incompressible multiphase SPH method. Journal of Computational Physics, 227:264–278.

HUANG Z. C., HSIAO S. C., HWUNG H. H., 2009. Observation of coherent turbulent structure under breaking waves. Int. J. Polar Offshore Eng. 19 (1), 15–22.

HUANG Z. C., HWUNG H. H., CHANG, K. A., 2010a. Wavelet based vertical structure detection and length scale estimate for laboratory spilling waves. Coast. Eng. 57, 795–877.

HUANG Z. C., HWUNG H. H., HSIAO S. C., CHANG K. A., 2010b. Laboratory observation of boundary layer flow under spilling breakers in a surf zone using particle image velocimetry. Coast. Eng. 57, 343–357.

HUANG Z.C., *et al*., 2012. Dissipation of wave energy and turbulence in a barrier-reef lagoon. J. Geophys. Res. 117, C03015.

HYUN B. S., BALACHANDAR R., YU K., PATEL V. C., 2003. PIV/LDV measurements of mean velocity and turbulence in a complex open channel flow. IIHR Technical Report No424, The University of Iowa, USA.

INMAN D. L., TAIT F. J. & NORDSTROM C. E., 1971. Mixing in the surf zone. *J. geophys. Res.,* 76: 3493-3514.

IPPEN A. T., 1966. Estuary and Coastline Hydrodynamics. McGraw-Hill, New York.

JACKSON N. L., NORDSTROM K. F., ELIOT I., MASSELINK I., 2002. Low energy sandy beaches in marine and estuarine environments: a review, Geomorphology, 48, 147-162.

JAMES I. D., 1974. A non-linear theory of longshore currents. *Estrarine, Coastal and Shelf Science,* 2, 235-249.

JOHNSON D., 2004. 'The Spatial and Temporal Variability of Nearshore Currents', PhD Thesis, University of Western Australia

JOHNSON G. R., STRYK R. A., BEISSEL R. S., 1996. SPH for high velocity impact computations. Comput. Methods Appl. Mech. Engineering., 139:347–373.

JOHNSON D., STOCKER R., HEAD R., IMBERGER J., PATTIARATCHI C., 2003. 'A compact low-cost GPS drifter for use in the Oceanic Nearshore Zone, Lakes and Estuaries', Journal of Atmospheric and Oceanic Technology, 20, 1880-1884.

JOBSON H. E., SAYRE W. W., 1970. Predicting concentration profiles in open channels. *J. Hyd. Div.,* ASCE, 96, 1983-1996.

KARAMBAS T. V., 1986. On the pollutant dispersion subjected to nearshore circulation. *Proc. 3rd Int. Conf. on Environmental Pollution, Greece.*

KARAMBAS T. V., KOUTITAS C., 1992. A breaking wave propagation model based on the Boussinesq equations. Journal of Marine Engineering, 5, 159-173.

KARAMBAS T. V., 1999. Mixing in the surfzone: A theoretical approach. Coastal Engineering, 18, 1 -19.

KAY A., 1987. The effect of cross-stream depth variations upon contaminant dispersion in a vertically well-mixed current. Estrarine, Coastal and Shelf Science, 24, 177-204.

KEANE R.D., ADRIAN R. J., 1992. Theory of cross-correlation of PIV images, Applied Scientific Research, Vol. 49, 191-215.

KIMMOUN O., BRANGER H., 2007. A particle images velocimetry investigation on laboratory surf-zone breaking waves over a sloping beach. J. Fluid Mech. 588, 353–397.

KIRBY J., PUTREVU U., OZKAN HALLER H. T., 1998. 'Evolution equations for edge waves and shear waves on longshore uniform beaches', In Proceedings of the 26th International Conference on Coastal Engineering, vol 1, 203-216.

KIRONOTO B. A., GRAF W. H., 1994. Turbulence characteristics in rough uniform open-channel flow. *Proc. Instn Civ. Engrs Wat., Marit. & Energy,* ICE, 106, 333-344.

KOMAR P., 1998. Beach Processes and Sedimentation, Prentice Hall, United States

KOMPENHANS J., RAFFEL M., DIETERLE L., DEWHIRST T., VOLLMERS H., EHRENFRIED K., WILLERT C., PENGEL K., KAHLER C., SCHRODER A., RONNEBERGER O., 1998. Particle image velocimetry in aerodynamics: technology and applications in wind tunnels, Proceedings of VSJ-SPIE98, KL306, Yokohama (Japan).

KOOLE R., SWAN C., 1994. Dispersion of pollution in a wave environment. *Proc. 24th Int. Conf. on Coastal Engng.,* 3071-3085.

KRAICHMAN R. H., 1967. Inertial ranges in two-dimensional turbulence. Phys. Fluids 11, 265-277.LEE E.-S., VIOLEAU D., BENOIT M., ISSA R., LAURENCE D., and STANSBY P., 2006. Prediction of wave overtopping on coastal structures by using extended Boussinesq and SPH models. In Proc. 30th International Conference on Coastal Engineering, 4727–4740.

LEIMKUHLER B. J., REICH S., SKEEL R. D., 1996. Integration Methods for Molecular dynamic IMA Volume in Mathematics and its application. Springer.

LI S., LIU W., 1996. Moving least square Kernel Galerkin method (II) Fourier analysis. Comput. Methods Appl. Mech. Engineering., 139:159.

LIPPMANN T., HOLMAN R., BOWEN A., 1997. 'Generation of Edge Waves in shallow water', Journal of Geophysical Research, 102(C4), 8663-8679.

LIST E. J., GARTRELL G., WINANT C. D., 1990. 'Diffusion and Dispersion in Coastal Waters', Journal of Hydraulic Engineering, 116(10), 1158-1179

LIU G. R., LIU M. B., 2003. Smoothed Particle Hydrodynamics: A Meshfree Particle Method. World Scientific, 3rd printing.

LO E., SHAO S., 2002. Simulation of near-shore solitary wave mechanics by an incompressible SPH method. Applied Ocean Research, 24:275–286.

LOEWEN M. R., SIDDIQUI M. H. K., 2006. 'Detecting microscale breaking waves'. Meas. Sci. Technol. 17 (4), 771–780.

LONGO S., PETTI M., LOSADA I. J., 2002. 'Turbulence in the swash and surf zones: a review'. Coast. Eng. 45, 129–147.

LONGUET-HIGGINS M. S., 1953. Mass transport in water waves. *Proc. Cambridge Philo. Soc.,* 245, 535-581.

LONGUET-HIGGINS M. S., 1970. Long-shore currents generated by obliquely incident sea waves, parts 1 and 2. *J. geophys. Res.,* 75: 6778-6801.

LONGUET-HIGGINS M. S., 1972. Recent progress in the study of longshore currents. *Waves on Beaches,* edited by R. E. Meyer, Academic Press, New York, 203-248.

LONGUET-HIGGINS M. S., STEWART R. W., 1960. Changes in the form of short gravity waves on long waves and tidal currents. *J. Fluid Mech.,* 13, 481-504.

LONGUET-HIGGINS M. S., STEWART R. W., 1964. Radiation stress in water waves, a physical discussion with application. *Deep-Sea Res.,* 11, 529-563.

LOURENCO L., 1988. Some comments on particle image displacement velocimetry, Von Karmann Institute for Fluid Dynamics, 1988-06.

LUCY L. B., 1977. A numerical approach to the testing of the fission hypothesis. Astron. J. 82, 1013–1024.

MADSEN O. S., 1971. On the generation of long waves. Journal of Geophysical Research, 76(36), 8672–8683.

MARSHALL J., ADCROFT A., HILL C., PERELMAN L., HEISEY C., 1997. A finite-volume, incompressible Navier–Stokes model for studies of the ocean on parallel computers. J. Geophys. Res. 102, 5753-5766.

MASCH F. D., 1963. Mixing and dispersion of wastes by wind and wave action. *Int. J. Air. Wat. Pollut.,* 7:697-720.

MASSELINK G., HUGHES M., 1998. 'Field investigation of sediment transport in the swash zone'. Cont. Shelf Res. 18 (10), 1179–1199.

MASSELINK G., PATTIARATCHI C. B., 1997. The effect of sea breeze on beach morphology, surf zone hydrodynamics and sediment re-suspension, Marine Geology, 146, 115-135.

MCCABE M. V., STANSBY P. K., APSLEY D. D., 2013. Random wave runup and overtopping a steep sea wall: Shallow-water and Boussinesq modelling with generalised breaking and wall impact algorithms validated against laboratory and field measurements. Coast. Eng. 74, 33–49.

MCCOWAN J., 1894. 'On the highest wave of permanent type'. Phil. Mag. Ser. 5, 38, 351-357.

MCCREADY M. J., VASSILIADOU E., HANRATTY T. J., 1986. Computer simulation of turbulent mass transfer at a mobile interface. Am. Inst. Chem. Engrs. 32, 1108–1115.

MCDOUGAL W. G., HUDSPETH R. T., 1986. 'Influence of lateral mixing on longshore currents'. *Ocean Engng.,* 13(5), 419-433.

MCKENNA S. P., MCGILLIS W. R., 2004. The role of free-surface turbulence and surfactants in air–water gas transfer. 47 (3), 539–553.

MCKINNEY J. P., 1993. A method for locating spikes in a measured time series. Proc., 2nd Int. Symposium on Ocean Wave Measurement and Analysis, 338–393.

MCNULTY A. J., 1983. Dispersion of continuous pollutant source in open channel flow. *PhD Thesis,* University of Canterbury, Christchurch.

MEI C. C., 1989. 'The Applied Dynamics of Ocean Surface Waves'. World Scientific.

MELVILLE W. K., VERON F., WHITE C. J., 2002. 'The velocity field under breaking waves: coherent structures and turbulence'. J. Fluid Mech. 454, 203–233.

MICHELL J. H., 1893. 'On the highest waves in water'. Phil. Mag., Ser. 5, 36, 430-437.

MOKOS A. S., ROGERS B. D., STANSBY P. K., DOMINGUEZ J. M., 2015. Multi-phase SPH modelling of violent hydrodynamics on GPUs, Computer Physics Communications, ISSN 0010-4655.

MONAGHAN J. J., 1989. 'On the problem of penetration in particle methods'. J. Comp. Phys. 82, 1–9991.

MONAGHAN J. J., 1992. Smoothed particle hydrodynamics, Annu. Rev. Astron. Astrophys. 30, 543–574.

MONAGHAN J. J., 1996. Gravity currents and solitary waves. Physica D., 98:523–533.

MONAGHAN J. J., 2002. 'SPH compressible turbulence'. MNRAS 335, 843–852.

MONAGHAN J. J., LATTANZIO J. C., 1985. A refined method for astrophysical problems. Astron. Astrophys, 149:135–143.

MONAGHAN J. J., KOCHARYAN A., 1995. SPH simulation of multi-phase flow, Comput. Phys. Comm. 87,1–2225–235.

MONAGHAN J. J., KOS A., 1999. Solitary Waves on a Cretan Beach. J. Waterway, Port, Coastal and Ocean Engineering., 125:145–154.

MONAGHAN J. J., KOS A., 2000. Scott Russells Wave Generator. Physics of Fluids, 12:622–630.

MORI N., SUZUKI T., KAKUNO S., 2007. Noise of acoustic Doppler velocimeter data in bubbly flows. J. Eng. Mech.-ASCE 133 (1), 122–125.

MUNSON B. R., YOUNG D. F., OKIISHI T. H., 2002. Fundamentals of Fluid Mechanics, John Wiley and Sons Inc, U.S.A.

MURRAY A., REYDELLET G., 2002. A rip current model based on a hypothesized wave/current interaction. Journal of Coastal Research, 17(3):517{530. Okubo A., 1974, 'Some speculation on Oceanic Diffusion Diagrams', Rapp. R.-v. Reun. Cons. Int. Explor. Mer, 167, 77-85.

NADAOKA K., KONDOH T., 1982. Laboratory measurements of velocity field structure in the surf zone by LDV. Coastal Engng. Japan, 25,125-145.

NAKAGAWA S., HANRATTY T. J., 2001. Particle image velocimetry measurements of flow over a wavy wall. Phys Fluids 13:3504–3507.

NARAYANASWAMY M., DALRYMPLE R. A., 2002. 'An experimental study of surface instabilities during wave breaking'. Proceedings of the 28th International Conference on Coastal Engineering. World Scientific, Cardiff, Wales, 344–355.

NEZU I. ONITSUKA K., 2001. Turbulent structures in partly vegetated open-channel flows with LDA and PIV measurements. J. of Hydraulic Research, Vol 39, issue6, 629 – 642.

NIKORA V., 1999. Origin of the −1 spectral law in wall-bounded turbulence. Phys. Rev. Lett. 83, 734–736.

NIKORA V., GORING D. G., 2000. Flow turbulence over fixed and weakly mobile gravel beds. J. Hydraul. Eng., 126(9), 679–690.

NIKURADSE J., 1932. 'Gesetzmassigkeiten der turbulenten stromung in glatten rohrn'. Forschungsheft 356, Vereines Deutscher Ingenieure, 3.

NOKES R. I., 1986. 'Problems in turbulent dispersion'. *PhD Thesis,* University of Canterbury, Christchurch.

OLSSON D., 2004. 'Field Studies of Rip Currents in the Lee of Coastal Structures', Engineering Honours Thesis, University of Western Australia.

OLTMAN-SHAY J., HOWD P. A., BIRKENMEIER W. A., 1989. 'Shear instabilities of the mean- longshore current, 2. Field Observations', Journal of Geophysical Research, 94, C12, 18,031-18,042.

OTNES R. K., ENCHSON L., 1978. Applied time series analysis, Wiley, New York, Vol. 1.

PAL K., MURTHY R., THOMSON R., 1998. Lagrangian measurements in Lake Ontario. Journal of Great Lakes Research, 24(3), 681-697.

PATRICK D. A., WIEGAL R. L., 1954. Amphibian tractors in the surf. Conf. Ships Waves 1, 397.

PATTIARATCHI C., HEGGE B., GOULD J., ELIOT I., 1997, 'Impact of sea-breeze activity on nearshore and foreshore processes in southwestern Australia', Continental Shelf Research, v17, No.13, 15-39-1560.

PEARSON J. M., GUYMER I., COATES L. E., WEST J. R., 1997. Mixing processes due to breaking wave activity in the coastal zone. Proc. *2nd Int. Conf. Coastal Dynamics 97,* Plymouth, 197-206.

PEARSON J. M., GUYMER I., COATES L. E., WEST J. R., 2002. Effect of wave height on on-off shore solute mixing. J. Wtrwy., Port, Coast., and Oc. Engng., ASCE. 1-11.

PEARSON J. M., GUYMER I., KARAMBAS T. V., PETERSEN O. S., 2006. Laboratory investigation of Mixing in the Nearshore. Proc. 30th Int. Conf. Coastal Eng. San Diego

PEARSON J. M., ZOU Q., GUYMER I., PENG Z., 2008. Solute Dispersion in the nearshore: Laboratory and numerical results. Proc. 31st Int. Conf. Coastal Eng. Hamburg

PEARSON J. M., GUYMER I., COATES L. E., WEST J. R., 2009. On-off shore Solute Mixing in the Surf-Zone. J. Wtrwy., Port, Coast., and Oc. Engng., ASCE. Vol 135, No. 4.

PEDERSEN C., DEIGAARD R., SUTHERLAND J., 1998. Measurements of the vertical correlation in turbulence under broken waves. Coastal Engng. 35, 231–249.

PEREGRINE D. H., 1983. 'Breaking waves on beaches'. Annu. Rev. Fluid Mech. 15, 149 – 178.

PETTI M., LONGO S., 2001. Turbulence experiments in the swash zone. Coastal Eng. 43, 1–24.

POPE S. B., 2000. 'Turbulent flows'. Cambridge Univ, Press, New York.

PRANDTL L., 1952. Essentials of Fluid Dynamics. Hafner Publishing Company, New York.

PRICE D., 2004. Magnetic fields in Astrophysics. Ph.D. thesis. Cambridge University.

PROEHL J. A., LYNCH D. R., MCGILLICUDDY D. J., & LEDWELL J. R., 2005. Modelling turbulent dispersion on the North Flank of Georges Bank using Lagrangian Particle Methods, Continental Shelf Research, 25 (7-8), 875-900.

PULEO J. A., HOLLAND K. T., 2001. 'Estimating swash zone friction coefficient on a sandy beach'. Coastal Engng. 43, 25–40.

PULEO J. A., FARHADZADEH A., KOBAYASHI N., 2007. 'Numerical simulation of swash zone fluid accelerations'. J. Geophys. Res. 112 (C7).

PUTREVU U., SVENDSEN I. A., 1992. A mixing mechanism in the nearshore region. Proc. 23rd Int. Conf. on Coastal Engng, Italy, 2758-71.

RAFFEL M., WILLERT C. E., KOMPENHANS J., 1998. Particle image velocimetry. Springer.

RANDLES P., LIBERSKY L., 1996. Smoothed Particle Hydrodynamics some recent improvements and applications. Comput. Methods Appl. Mech. Engineering., 138:375– 408.

RECKTENWALD G., 2000. Numerical Methods with MATLAB, Implementation and Application, Prentice Hall, Sydney

RICHARDSON L., 1926. Atmospheric diffusion shown on a distance-neighbour graph. Proc. of the Royal Society. A110, 709-727.

RIDDLE A. M., LEWIS R. E., 2000. 'Dispersion Experiments in UK coastal waters', Estuarine, Coastal and Shelf Science, 51, 243-254.

RIPPY M. A., FRANKS P. J. S., FEDDERSEN F., GUZA R. T., MOORE D. F., 2013. Factors controlling variability in nearshore fecal pollution: Fecal indicator bacteria as passive particles, Marine Pollution Bulletin, 66, 151-157.

RIPPY M. A., FRANKS P. J. S., FEDDERSEN F., GUZA R. T., MOORE D. F., 2013. Factors controlling variability in nearshore fecal pollution: The effects of mortality, Marine Pollution Bulletin, 66, 191-198.

RIPPY M. A., FRANKS P. J. S., FEDDERSEN F., GUZA R. T., WARRICK J. A., 2013. Beach Nourishment Impacts on Bacteriological Water Quality and Phytoplankton Bloom Dynamics, Environ. Sci. Tech., 47 (12), 6146–6154.

RODI W., 1980. Turbulence models and their application in hydraulic models, IAHR, Delft.

RODRIGUEZ A., SANCHEZ-ARCILLA, REDONDO, BAHIA, SIERRA, 1995. Pollutant Dispersion in the nearshore region: modelling and measurements, Water, Science and Technology, 32(9-10): 169-178.

ROGERS B., DALRYMPLE R. A., 2007. SPH modelling of tsunami waves. In Advanced Numerical Models for Simulating Tsunami Waves and Runup.

ROGERS B., DALRYMPLE R. A., STANSBY P., LAURENCE D., 2007. Development of a Parallel SPH code for free-surface wave hydrodynamics. In SPHERIC, Second International Workshop, 111–114.

ROY M., KUMAR V. R., KULKARNI B. D., SANDERSON J., RHODES M., VAN DER STAPPEN, 1999. Simple denoising algorithm using wavelet transform. J. Am. Ins. Chem. Eng., 45(11), 2461–2466.

RUESSINK B. G., 2010. Observations of turbulence within a natural surf zone. J. Phys. Oceanogr. 40 (12), 2696–2712.

RUTHERFORD J. C., 1994. *River Mixing.* J. Wiley & Sons, Chichester, England.

RYU Y., CHANG K. A., LIM H. J., 2005. Use of bubble image velocimetry for measurement of plunging wave impinging on structure and associated greenwater. Meas. Sci. Technol. 16, 1945–1953.

SAELEVIK G., JENSEN A., PEDERSEN G., 2013. Runup of solitary waves on a straight and a composite beach. Coast. Eng. 77, 40–48.

SASAKI T., HORIKAWA K. 1978. 'Observation of nearshore current and edge waves'. In Proc. 16th International Conference On Coastal Engineering, 791-809.

SAWFORD B., 2001, 'Turbulent Relative Dispersion', Annual Review of Fluid Mechanics, Vol.33, 289-31.

SAYRE W. W., 1973. Natural mixing in rivers, edited by H. W. Shen. *Environmental Impact on Rivers,* Fort Collins, 6.31-6.37.

SCHIFF K., DORSEY J., WEISBERG S., 2001. Marine microbiological monitoring in the southern California Bight. Environ. Manage. 27, 149–157.

SCHIFF K., MORTON J., WEISBERG S., 2003. Retrospective evaluation of shoreline water quality along Santa Monica Bay beaches. Marine Environ. Res. 56, 245–253.

SCHILLER E. J., SAYRE W. W., 1975. Vertical temperature profiles on open-channel flow. J. Hyd. Div., ASCE, 101, 749-761.

SCHLICHTING H., 1968. *Boundary Layer Theory.* McGraw-Hill, New York.

SCOTT C. P., COX D. T., MADDUX T. B., LONG J. W., 2005. 'Large-scale laboratory observations of turbulence on a fixed barred beach'. Meas. Sci. Technol. 16, 1903–1912.

SHAO S., GOTOH H., 2004. Simulating coupled motion of progressive wave and floating curtain wall by SPH-LES model. Coastal Engineering Journal, 46(2):171–202.

SHAO S., JI C. M., GRAHAM D., REEVE D., JAMES P., CHADWICK A., 2006. Simulation of wave overtopping by an incompressible SPH model. Coastlab Engineering, 53:723–735.

SHAW W. J., TROWBRIDGE J. H., 2001. The direct estimation of near-bottom turbulent fluxes in the presence of energetic wave motions. J. Atmos. Ocean. Technol. 18 (9), 1540–1557.

SHIN S., COX D. T., 2006. Laboratory observations of inner surf and swash-zone hydrodynamics on a steep slope. Cont. Shelf Res. 26, 561–573.

SHORT A. D., 1985. Rip-current type, spacing and persistence, Narrabeen beach, Australia, Marine Geology, 65, 47-71.

SIMONS R. R., WHITEHOUSE R. J. S., MACIVER R. D., PEARSON J. M., SAYERS P. B., XHAO Y., CHANNEL A. R., 1995. Evaluation of the UK Coastal Research Facility. *Proc. 1st Int. Conf. Coastal Dynamics 95,* Gdansk, Poland, 161-172.

SIMPSON J. H., WILLIAMS E., BRASSEUR L. H., BRUBAKER J. M., 2005. 'The impact of tidal straining on the cycle of turbulence in a partially stratified estuary', Continental Shelf Research, 25, 51-64.

SMART P. L., LAIDLAW I. M. S., 1977. An evaluation of some fluorescent dyes for water tracing. *Water Resour. Res.,* 13, 15-33.

SOBEY R. J., BARKER C. H., 1997. Wave-driven transport of surface oil. *J. Coastal Res.,* 13(2), 490-496.

SORENSEN R. M., 1993. *Basic wave mechanics for coastal and ocean engineers.* J. Wiley & Sons, Chichester, England.

SOU I. M., COWEN E. A., LIU P. L. F., 2010. Evolution of the turbulence structure in the surf and swash zones. Journal of Fluid Mechanics, 644, 193-216.

SPYDELL M., FEDDERSEN F., GUZA R. T., SCHMIDT W., 2007. Observing surfzone dispersion with drifters, J. Phys. Oceangr., 37, 2920-2939.

SPYDELL M., FEDDERSEN F., 2009. Lagrangian drifter dispersion in the surfzone: Directionally-spread normally-incident waves, J. Phys. Oceangr., 39, 809-830.

SPYDELL M., FEDDERSEN F., GUZA R.T., 2009. Observations of drifter dispersion in the surfzone: The effect of sheared alongshore currents, J. Geophys. Res. Oceans, 114.

SPYDELL M. S., FEDDERSEN F., 2012. The effect of a non-zero Lagrangian time-scale on bounded shear dispersion, J. Fluid Mech., 691, 69-94.

SPYDELL M. S., FEDDERSEN F., 2012. Lagrangian Stochastic Model of Surfzone Drifter Dispersion, J. Geophys. Res., 117, C03041.

STANSBY P. K., FENG T., 2005. Kinematics and depth-integrated terms in surf zone waves from laboratory measurement. J. Fluid Mech. 529, 279–310.

STIVE M. J. F., WIND H. G., 1982. A study of radiation stress and setup in the nearshore region. *Coastal Engng.,* 6, 1-25.

STOKES G. G., 1847. On the theory of oscillatory waves, *Mathematical and Physical papers,* Cambridge University Press, London, Vol. 1, 314-326.

SUMER B. M., *et al*., 2011. Flow and sediment transport induced by a plunging solitary wave. J. Geophys. Res.-Oceans 116, C01008.

SUTHERLAND P., MELVILLE W. K., 2013. Field measurements and scaling of ocean surface wave-breaking statistics. Geophys. Res. Lett. 40 (12), 3074–3079.

SVENDSEN I. A., 1984. Mass flux and undertow in a surf-zone. *Coastal Engng.,* 8, 347-365.

SVENDSEN I. A., 1987. Analysis of surf zone turbulence. *J. geophys. Res.,* 92, 5115-5124.

SVENDSEN I. A. & LORENZ R. S., 1989. Velocities in combined undertow and longshore currents. *Coastal Engng.,* 13, 55-79.

SVENDSEN I. A. & PUTREVU U., 1994. Near-shore mixing and dispersion. *Proc. R. Soc. London,* Ser. A, 445, 561-576.

SVENDSEN I. A., 2005. Introduction to nearshore hydrodynamics. World Scientific. ISBN 10 981 256 142 0.

SWEGLE J. W., ATTAWAY S., 1995. On the feasibility of using Smoothed Particle Hydrodynamics for underwater explotion calculation. Comput- Mech., 17:151–168.

SYMONDS G., RANASINGHE R., 2001. On the formation of rip currents on a plane beach. In Proceeds of the 27th International Conference On Coastal Engineering volume 1, 468-481. ASCE.

SYNOLAKIS, C. E., 1987. The runup of solitary waves. J. Fluid Mech. 185, 523–545.

TAKEWAKA S., MISAKI S., NAKAMURA T., 2003. Dye diffusion experiment in a longshore, current field, Coastal Engineering Journal, World Scientific Publishing Company and Japan Society of Civil Engineers. 45(3), 471-487.

TANAKA H., WADA A., KOMORI S., TEKEUCHI I., 1980. Effects of nearshore currents on diffusion in the surf zone. *Coastal Engng. Japan,* 23, 231-50.

TAYLOR G. I., 1921. Diffusion by continuous movements. *Proc. London Math Soc.,* 2(20), 196-212.

TAYLOR G. I. 1938. The spectrum of turbulence. Proc. R. Soc. Lond. A 164, 476–490.

TAYLOR G. I., 1953. Dispersion of soluble matter in solvent flowing slowly through a tube. *Proc. R. Soc. London,* Ser. A, 219, 186-203.

TAYLOR G. I., 1954. The dispersion of matter in a turbulent flow through a pipe. *Proc. R. Soc. London,* Ser. A, 223, 446-468.

TENNEKES H., LUMLEY J. L., 1972. A First Course in Turbulence. MIT Press.

THOMANN R. V., 1973. Effect of longitudinal dispersion on dynamic water quality response of streams and rivers. *Wat. Resour. Res.,* 9, 355-366.

THOMPSON S., 1969. *PhD Thesis,* Cambridge University.

THORNTON E. B., 1970. Variation of long-shore currents across the surf zone. *Proc. 12th Int. Conf. on Coastal Engng.,* Washington, 291-308.

TING, F. C. K., KIRBY J. T., 1994. Observation of undertow and turbulence in a laboratory surzone. Coast. Eng. 24, 51–80.

TING F. C. K., KIRBY J. T., 1995. Dynamics of surf zone turbulence in a strong plunging breaker. Coast. Eng. 27, 131–160.

TING F. C. K., KIRBY J. T., 1996. Dynamics of surf zone turbulence in a spilling breaker. Coast. Eng. 24, 177–204.

TING F. C. K., 2006. Large-scale turbulence under a solitary wave. Coast. Eng. 53 (5–6), 441–462.

TING F. C. K., 2008. Large-scale turbulence under a solitary wave: Part 2 Forms and evolution of coherent structures. Coast. Eng. 55, 522–536.

TING F. C. K., 2013. Laboratory measurements of large-scale near-bed turbulent flow structures under plunging regular waves. Coast. Eng. 77, 120–139.

TOFFOLI A., BABANIN A., ONORATO M., WASEDA T., 2010. Maximum steepness of oceanic waves: Field and laboratory experiments, Geophys. Res. Lett., 37, L05603.

TROWBRIDGE J., ELGAR S., 2001. Turbulence measurements in the surf zone, J. Phys. Oceanogr., 31, 2403-2417.

TSENG R. S., 2001. 'On the Dispersion and Diffusion near Estuaries and around Islands', Estuarine Coastal and Shelf Science, v54, 89-100.

UTAMI T., BLACKWELDER R. F., 1991. A cross-correlation technique for velocity field extraction from particle visualization, Exp. Fluids, 10, 213-23.

VALIZADEH A., MONAGHAM J., 2015. A study of solid wall models for weakly compressible SPH, J. Comput. Phys. Vol 300C, 5-19.

VELASCO-SEGURA R., RENDON P. L., 2015. A finite volume approach for the simulation of nonlinear dissipative acoustic wave propagation, Wave Motion, ISSN 0165-2125.

VERLET L., 1967. Computer ''Experiments'' on classical fluids. I. Thermodynamical properties of Lennard-Jones molecules, Phys. Rev. 159 (1) 98–103.

VIOLEAU D., BUVAT C. ABED-MERIAM K., NANTEUIL E., 2007. Numerical modelling of boom and oil spill with SPH, Coastal Engineering, Volume 54, Issue 12, 895-913, ISSN.

VIOLEAU D., 2012. Fluid mechanics and the SPH method. Oxford Uni. Press. ISBN 978-0-19-965552-6.

WANG J., SHEN Y., 2010. Modelling oil spills transportation in seas based on unstructured grid, finite-volume, wave-ocean model, Ocean Modelling, Vol. 35, Issue 4, 332-344, ISSN 1463-5003.

WENDLAND H., 1995. *Computational aspects of radial basis function approximation*. Elsevier.

WESTERWEEL J., 1993a. Analysis of PIV interrogation with low pixel resolution, Proc. SPIE, 2005, Optical Diagnostics in Fluid and Thermal Flow, 624-35.

WESTERWEEL J., 1993b. Digital particle image velocimetry - theory and application, Ph. D. thesis.

WILLERT C. E., GHARIB M., 1991. Digital particle image velocimetry, Exp. Fluids, 10, 93-181.

WEIGEL R. L., 1963. Some engineering aspects of wave spectra, *Ocean Wave Spectra,* Prentice-Hall, New Jersey, 309-321.

WIENEKE B., PFEIFFER K., 2010. Adaptive PIV with variable interrogation window size and shape, 15th Int. Symp. On applications of laser techniques to fluid mechanics, Lisbon.

WINANT C. D., 1983. 'Longshore Coherence of Currents along the Southern California Shelf during Summer', Journal of Physical Oceanography, 13, 54-64.

XING J., DAVIES A. M., 2003. A model study of tidally induced suspended sediment transport in the Iberian shelf region, Estuarine, Coastal and Shelf Science, 58, 321-333.

ZEIDLER R. B., 1976. Coastal dispersion of pollutants. J. Wtrwy., Harb., Coast., Engng.,102, 235-254.

ZHENG X., MA Q. W., DUAN W. Y., 2014. Incompressible SPH method based on Rankine source solution for violent water wave simulation, Journal of Computational Physics, Volume 276, 291-314.

ZOU S., 2007. Coastal Sediment Transport Simulation by Smoothed Particle Hydrodynamics. PhD thesis, Civil Engineering, Johns Hopkins University.

ZOU S., DALRYMPLE R. A., 2006. Sediment suspension simulation under oscillatory flow with SPH-SPS method. In Proc. 30th International Conference on Coastal Engineering.